



# **The Catalysis of the Selective Electrochemical Oxidation of Hydrocarbons**

**Anna Winiwarter**

Supervisor: Prof. Ib Chorkendorff  
Co-supervisor: Associate Prof. Brian Seger

Department of Physics  
Section of Surface Physics and Catalysis  
Technical University of Denmark

**PhD Thesis**

August 2019

**Cover images**

Top: Schematic of electrochemical propene oxidation on a Pd electrode in the presence of surface adsorbates.

Bottom: Electrochemical cell. Photograph by Lisbeth Holten.

## Abstract

Decreasing prices for renewable electricity are making electrification of the chemical industry more interesting, both as a means of energy storage, and to save on non-renewable energy carriers. Such an electrochemical approach is interesting for the partial oxidation of hydrocarbons, where the catalytic challenge is to avoid formation of the thermodynamically most stable product  $\text{CO}_2$ , while providing sufficiently high reaction rates. In electrochemical processes, the driving force for the reaction is provided by applying an electrical potential, which allows for better control over reaction products and operation at room temperature.

In this thesis, I studied the electrochemical partial oxidation of propene which is highly relevant for two reasons: First, propene has two different sites for oxidation; the double bond, and the allylic carbon. This makes it ideal for mechanistic studies as different products will result from different adsorption geometries on the surface when varying reaction conditions. Second, several propene oxidation products, such as allyl alcohol, acrolein, acrylic acid, and propylene glycol are important commodity chemicals with annual production volumes of several megatons.

The catalysts used for propene oxidation experiments were high surface area Pd, Au and AuPd alloys, prepared by the hydrogen bubble template method and thoroughly characterized using XRD, XPS, SEM and LEIS. The choice of materials was based on previous literature and DFT calculations by my collaborators. Initially, electrochemical propene oxidation with *ex-situ* product analysis was carried out on Pd electrodes in acidic electrolyte. Both activity and product distribution depend on the potential, in alignment with reports from the literature. The highest activity was observed at ca. 0.9 V vs. RHE; at the same potentials, selectivity for allylic oxidation to acrolein and acrylic acid is the highest. Thorough product analysis led to the identification of two products

not previously reported under the same conditions, to the best of my knowledge: Allyl alcohol (primarily at potentials below 0.9 V *vs.* RHE), and propylene glycol (at potentials above 0.9 V *vs.* RHE). DFT modeling and allyl oxidation experiments suggest that allyl alcohol is an intermediate in the formation of acrolein, and that oxygen insertion is the rate limiting step.

Based on these results we used a combination of DFT and advanced stripping experiments with chip based electrochemical mass spectrometry (EC-MS) to show that surface coverage dictates the reaction mechanism: Propene degradation under reaction conditions leads to the formation of a layer of adsorbates which facilitates propene coordination to the catalyst solely through the allylic carbon, resulting in the observed selectivity for acrolein and acrylic acid. This surface layer can be influenced by alloying Pd with Au: Already at 10% Au content, the activity is improved, while still providing high selectivity for allylic coordination.

To further understand the nature of the adsorbed species, we performed experiments on Pd using surface-enhanced infrared absorption spectroscopy (SEIRAS). However, due to the adsorption geometry of the adsorbed species, signal intensities are very weak. Nonetheless, our results show that the degradation mechanism for propene oxidation is fundamentally different from allyl alcohol oxidation. During allyl alcohol oxidation, the surface is covered with CO. In the presence of propene, however, no CO was observed, which supports the hypothesis that oxygen insertion is the rate limiting step. SEIRAS is particularly sensitive for determination of adsorbed CO. Therefore we used CO as a probe for determining propene adsorbates. We observed that some of the adsorbed propene can be displaced by CO, while the distribution of CO between different adsorption sites is significantly altered in the presence of propene in comparison with only CO saturated electrolyte.

## Resume

De faldende priser på vedvarende elektricitet skaber en stigende interesse for at elektrificere den kemiske industri, både i form af energilagring, men også for at spare på forbruget af ikke vedvarende energibærere. Netop denne elektrokemiske tilgang er oplagt for den partielle oxidering af kulhydrider, hvor udfordringen set fra et katalytisk synspunkt, er at undgå det mest termodynamisk stabile produkt  $\text{CO}_2$ , imens man samtidig har tilstrækkelig høje reaktionshastigheder. I elektrokemiske processer leveres drivkraften til reaktionen fra det anvendte elektriske potentiale, hvilket skaber en øget kontrol over reaktionsprodukterne og muliggør reaktioner ved stuetemperatur.

I denne afhandling har jeg studeret den elektrokemiske partielle oxidering af propen, som er yderst relevant af to årsager: For det første så har propen to forskellige bindinger der kan blive oxideret; dobbelt bindingen og den allyliske kul forbindelse. Dette gør propen optimalt til mekanistiske studier eftersom forskellige bindingsgeometrier på overfladen vil skabe forskellige produkter under varierede betingelser. Derudover så er flere af propens partielle oxideringer produkter vigtige kommercielle kemikalier så som allylalkohol, acrolein, acrylsyre og propyenglycol, alle sammen med en årlig produktionsvolumen på flere megaton. Til at katalysere den partielle oxidering af propen blev der brugt katalysatorer af høj overflade Pd, Au og AuPd legeringer. Disse blev præpareret via metoden der hedder "hydrogen bubble template method" og derefter grundigt karakteriseret ved brug af XRD, XPS, SEM og LEIS. Materiale valget var baseret på eksisterende litteratur samt DFT beregninger fra mine samarbejdspartnere. Elektrokemisk propen oxidering med ex-situ produkt analyse blev oprindeligt udført på Pd elektroder i sur elektrolyt. Både aktivitet og produkt fordelingen afhænger af potentialet som også beskrevet i litteraturen. Den højeste aktivitet blev målt ved ca. 0.9 V vs. RHE; selektiviteten for allylisk oxidering til acrolein og acrylsyre var også

højest ved dette potentiale. Grundig produkt analyse førte til identificeringen af to produkter der ikke tidligere er blevet opdaget under disse betingelser: Allylalkohol (primært ved potentialer under 0.9 V vs. RHE) og propylenglycol (ved potentialer over 0.9 V vs. RHE). DFT modellering og allylisk oxidering forsøgene antyder at allylalkohol er et mellemprodukt i dannelsen af acrolein hvor ilt indførslen er det hastigheds begrænsende trin.

Ud fra disse resultater brugte vi en kombination af DFT og avanceret elektrokemiske stripping eksperimenter med chip-baseret elektrokemi-massespektrometri (EC-MS) til at vise at overfladedækningen bestemmer reaktionsmekanismen: Nedbrydningen af propen under reaktionsbetingelser fører til dannelsen af et lag af adsorbater som faciliterer propen-koordinering til katalysatoren udelukkende gennem den allyliske kul forbindelse, som resulterer i den målte selektivitet mod acrolein og acrylsyre. Dette overflade lag kan blive påvirket af legeringsdannelse mellem Pd og Au: Allerede ved 10% Au indhold bliver aktiviteten forbedret samtidig med at den høje selektivitet mod den allyliske-koordinering bevares.

For at forstå egenskaberne af de adsorbere enheder yderligere, udførte vi forsøg på Pd ved brug af "surface-enhanced infrared absorption spectroscopy" (SEIRAS), men på grund af bindingsgeometrien af de adsorbere enheder er signal styrken meget lav. På trods af dette viser vores resultater at nedbrydningsmekanismen for propen oxidering er fundamentalt forskellig fra allylalkohol oxidering. Under alkohol oxidering bliver overfladen dækket af CO, men hvis propen er tilstede ser man intet CO hvilket understøtter hypotesen om at ilt indsætningen er det hastighedsbegrænsende skridt i reaktionen. SEIRAS er særligt følsom overfor absorberet CO. Derfor brugte vi CO som en sonde til at bestemme propene adsorbater. Vi så at noget af det adsorbere propen kan blive forskubbet af CO, samtidig med at fordelingen af CO mellem de forskellige bindingsgeometrier bliver markant ændret ved tilstedeværelsen af propen i forhold til CO mættet elektrolyt.

## **Preface**

The work for this thesis was carried out at the Technical University of Denmark, Department of Physics, Section of Surface Physics and Catalysis (SurfCat) in the period between September 2016 and August 2019, including an external research stay at Stanford University, Department of Chemical Engineering, from September 2018 to November 2018.

My experimental work was carried out in close collaboration with other students. Throughout this thesis, I use the pronoun "I" to highlight the parts of the work carried out by myself, while "we" is used where no clear distinction between my work and ideas, and those of my colleagues can be made. The contributors to the work in the different parts of this thesis are stated in the respective chapters.

Anna Winiwarter  
August 2019



## Acknowledgements

The work for this thesis was funded by Innovation Fund Denmark as part of the ProActivE project. The results presented here are the outcome of close collaboration with many people supporting me along the way.

I am grateful to my supervisors Prof. Ib Chorkendorff and Assoc. Prof. Brian Seger for the opportunity of working with them and for all their support, advice and discussions, and the freedom to pursue my own ideas. I thrived in the working environment at SurfCat, full of motivated and inspiring people where I felt welcome from the first moment. I wish to thank Senior Lecturer Ifan Stephens for his supervision in the first year of my PhD, and for his continuous support after leaving the group for a position at Imperial College London in July 2017.

For most of the past three years, I worked closely together with Luca Silvioli who provided me with ideas from his DFT calculations. I thank him for the discussions and the insights and for making beautiful figures for our paper. I am very thankful to Soren Scott for getting involved in my project, for teaching me EC-MS, discussing results from the distance, for helping with Python programming and for continuously reminding me how exciting science can be, especially when I was frustrated by experimental problems.

I want to thank my collaborators Poul Georg Moses and Prof. Jan Rossmeisl for fruitful discussions and Kasper Enemark-Rasmussen for measuring many NMR samples for me.

I also want to thank all the great people at SurfCat for all their help and inspiration. I want to mention specifically Erlend Bertheussen, Stefano Mezzavilla, Kim Degn Jensen and Claudie Roy, who introduced me to experimental electrochemistry. Thomas Vagn Hogg went through all the ups and downs with me from beginning to end of this PhD

project, and helped me a great deal when I started working with FTIR spectroscopy. Ezra Clark deserves mentioning for reviving the XPS setup and for teaching me about practical XRD, XPS and LEIS analysis. I thank Suzanne Andersen, Thomas Maagaard, Niklas Secher, Mike Boyd, Erlend, Ezra, Luca and Soren for proof reading parts of this thesis and helping me with valuable suggestions to improve it, and Niklas for translating the abstract to Danish. I further thank the former and current floor managers Kenneth Nielsen, Robert Jensen, Brian Knudsen, Patrick Strøm-Hansen and Jakob Ejler Sørensen for the technical support, and Jacqueline McAnulty for assistance in the lab.

In fall 2018, I spent three months at Stanford University in Prof. Thomas Jaramillo's lab. I want to express my gratitude to Prof. Jaramillo for the opportunity of working in his lab and to all the students and post-docs in the lab who made me feel very welcome. In particular, I want to thank Mike Boyd for showing me how motivating close collaboration on a project can be, and Asst. Prof. Drew Higgins for all the discussions and support. I also acknowledge the Danish Ministry of Higher Education and Science and the Otto Mønsted Fund for supporting my stay financially.

In 2017, I participated in the competition Dance your PhD, sponsored by AAAS and Science. I really enjoyed having to think about my project from a different perspective to come up with a dance choreography showing the idea behind my research. I thank Assoc. Prof. Sebastian Horch, Henning Bo Nicolajsen and DTU Physics for providing financial support for realizing this small side project, as well as all the dancers involved. The video is available at [https://youtu.be/ET416YX\\_dMw](https://youtu.be/ET416YX_dMw).

I want to thank Suzanne and Valeria for all the coffee breaks and for reminding me that it is important to take a break and enjoy life once in a while, and all the people who I had great conversations and fun at the Friday bar with. And I thank Tangospirer, and the Tango Argentino group at DTU for giving me a chance to balance out the busy life of a PhD student with dancing and music.

Finally, I want to thank my brother Lukas for his endless patience in helping me to learn Python and my parents, for raising me in an environment full of love for science, and for their continuous support all the way. Last but not least, I thank Andrea for all his understanding, encouragement and support in the past three years, and for spotting a lot of typing errors in this thesis.

# List of publications

## Paper I

**Towards an atomistic understanding of electrocatalytic hydrocarbon oxidation: propene on palladium**

Anna Winiwarter\*, Luca Silvioli\*, Soren B. Scott, Kasper Enemark-Rasmussen, Manuel Saric, Daniel B. Trimarco, Peter C. K. Vesborg, Poul G. Moses, Ifan E. L. Stephens, Brian Seger, Jan Rossmeisl, and Ib Chorkendorff.

*Energy and Environmental Science*, 2019, **12**, 1055

\* these authors contributed equally

## Paper II

**Tuning activity in electrochemical propene oxidation by alloying Pd with Au**

Luca Silvioli\*, Anna Winiwarter\*, Soren B. Scott, Ib Chorkendorff, Brian Seger, and Jan Rossmeisl.

*in preparation*

\* these authors contributed equally

## Paper III

**Using SEIRAS and EC-MS for *in-situ* analysis of the surface adsorbates during electrochemical oxidation of propene and allyl alcohol**

Anna Winiwarter, Michael J. Boyd, Soren B. Scott, Brian Seger, Drew C. Higgins, Ib Chorkendorff, and Thomas F. Jaramillo

*in preparation*



# Table of contents

<b>Nomenclature</b>	<b>xvii</b>
<b>1 Introduction</b>	<b>1</b>
1.1 Trends in renewable electricity generation . . . . .	1
1.2 Power-to-X . . . . .	3
1.3 Outline of this thesis . . . . .	5
<b>2 Electrocatalysis and propene oxidation</b>	<b>7</b>
2.1 Electrocatalysis . . . . .	7
2.1.1 What is a catalyst? . . . . .	7
2.1.3 The role of the potential . . . . .	12
2.2 Oxidation of propene . . . . .	15
2.2.1 Choice of propene as a model system . . . . .	16
2.2.2 Current industrial processes for propene partial oxidation . . .	18
2.3 Aims of this thesis . . . . .	20
<b>3 Experimental methods</b>	<b>21</b>
3.1 Catalyst preparation . . . . .	21
3.1.1 Electrodeposition . . . . .	21
3.1.2 Chemical deposition . . . . .	23
3.2 <i>Ex-situ</i> catalyst characterization . . . . .	23
3.2.1 Scanning electron microscopy (SEM) . . . . .	24
3.2.2 X-ray diffraction (XRD) . . . . .	25
3.2.3 X-ray photoelectron spectroscopy (XPS) . . . . .	26

---

3.2.4	Low energy ion scattering (LEIS) . . . . .	27
3.3	Electrochemical performance . . . . .	28
3.3.1	Potentiostat . . . . .	28
3.3.2	Setup for electrochemical experiments . . . . .	29
3.3.3	Cleaning . . . . .	30
3.3.4	Electrochemical methods . . . . .	31
3.4	<i>Ex-situ</i> product analysis . . . . .	37
3.4.1	Gas chromatography (GC) . . . . .	37
3.4.2	High performance liquid chromatography . . . . .	39
3.4.3	Nuclear magnetic resonance spectroscopy . . . . .	40
3.4.4	Inductively coupled plasma - mass spectrometry . . . . .	42
3.5	<i>In-situ</i> product characterization . . . . .	42
3.5.1	ATR-SEIRAS . . . . .	42
3.5.2	Electrochemical mass spectrometry (EC-MS) . . . . .	45
<b>4</b>	<b>Characterization of the catalysts</b>	<b>51</b>
4.1	High surface area Pd, Au and AuPd alloy electrodes . . . . .	52
4.1.1	Scanning electron microscopy (SEM) . . . . .	52
4.1.2	X-ray diffraction (XRD) . . . . .	53
4.1.3	X-ray photoelectron spectroscopy (XPS) . . . . .	57
4.1.4	Low energy ion scattering (LEIS) . . . . .	62
4.2	Electrodes for SEIRAS experiments . . . . .	64
4.2.1	Scanning electron microscopy (SEM) . . . . .	64
4.2.2	X-ray photoelectron spectroscopy (XPS) . . . . .	65
4.3	Summary . . . . .	65
<b>5</b>	<b>Electrochemical oxidation of propene on Pd</b>	<b>67</b>
5.1	Considerations for reliable product quantification . . . . .	68
5.2	Electrochemical performance . . . . .	68
5.3	Product analysis . . . . .	70
5.4	Faradaic and non-faradaic side reactions . . . . .	72
5.4.1	Pd dissolution and homogeneous catalysis . . . . .	73
5.4.2	Surface oxidation . . . . .	74

---

5.4.3	Product stability . . . . .	78
5.5	Changing the pH to improve stability . . . . .	78
5.6	Summary . . . . .	80
<b>6</b>	<b>Desorption as a probe for surface adsorption sites - an EC-MS study</b>	<b>81</b>
6.1	CO stripping . . . . .	82
6.2	Propene stripping . . . . .	84
6.3	Site evacuation experiments . . . . .	86
6.4	Summary . . . . .	93
<b>7</b>	<b>Probing surface adsorbates <i>in-situ</i> using SEIRAS and EC-MS</b>	<b>95</b>
7.1	CO stripping . . . . .	96
7.2	Allyl alcohol oxidation . . . . .	98
7.3	Propene oxidation . . . . .	103
7.4	Pd oxidation in Ar saturated electrolyte . . . . .	105
7.5	Propene displacement with CO . . . . .	107
7.6	Summary . . . . .	109
<b>8</b>	<b>General discussion and conclusions</b>	<b>113</b>
8.1	General discussion . . . . .	113
8.2	Conclusions and outlook . . . . .	119
8.2.1	Summary and conclusions . . . . .	119
8.2.2	Outlook . . . . .	119
	<b>References</b>	<b>123</b>
	<b>Appendix A Supporting information</b>	<b>139</b>
A.1	Materials . . . . .	139
A.2	Experimental parameters . . . . .	140
A.2.1	Catalyst characterization methods . . . . .	140
A.2.2	Product analysis methods . . . . .	141
A.3	Additional figures . . . . .	143
A.3.1	Appendant to Chapter 3 . . . . .	143
A.3.2	Appendant to Chapter 7 . . . . .	144

A.4	Previously published supporting information. . . . .	147
<b>Appendix B</b>	<b>Appended publications</b>	<b>159</b>

# Nomenclature

## Roman Symbols

$a$	Lattice parameter
$c$	Speed of light in vacuum $c = 2.998 \text{ m/s}$
$D$	Force constant (related to bond strength)
$d$	Distance between lattice planes
$\Delta E$	Potential difference
$\Delta G$	Gibbs free energy
$E_A$	Activation energy
$E_b$	Binding energy
$E_k$	Kinetic energy
$F$	Faraday's constant = 96485 C/mol
$h$	Planck's constant = $6.626 \cdot 10^{-34} \text{ Js}$
$h, k, l$	Miller indices
$I$	Current
$m_{\text{eff}}$	Effective mass
$n$	Number of moles

$Q$	Transferred charge
$R$	Resistance
$\nu$	Vibrational quantum number
$z$	Number of electrons transferred

**Greek Symbols**

$\lambda$	Wavelength
$\nu$	Wavenumber
$\phi$	Workfunction
$\theta$	X-ray incident angle in XRD

**Acronyms / Abbreviations**

ATR	Attenuated total reflection
CE	Counter electrode
CV	Cyclic voltammetry
DFT	Density functional theory
ECSA	Electrochemically active surface area
EIS	Electrochemical impedance spectroscopy
FE	Faradaic efficiency
FID	Flame ionization detector
FTIR	Fourier-transform infrared spectroscopy
GC	Gas chromatography or gas chromatograph
HER	Hydrogen evolution reaction

- 
- HPLC High performance liquid chromatography
- HS-GC Static head-space gas chromatography
- ICP-MS Inductively coupled plasma - mass spectrometry
- IR Infrared (radiation)
- ISS Ion scattering spectroscopy
- IUPAC International Union of Pure and Applied Chemistry
- LEIS Low energy ion scattering
- ML Monolayer
- NMR Nuclear magnetic resonance spectroscopy
- RE Reference electrode
- RF Radio frequency
- RHE Reversible hydrogen electrode
- SEIRAS Surface enhanced infrared absorption spectroscopy
- SEM Scanning electron microscopy
- SHE Standard hydrogen electrode
- TCD Thermal conductivity detector
- UHV Ultra high vacuum
- UPD Underpotential deposition
- WE Working electrode
- XPS X-ray photoelectron spectroscopy
- XRD X-ray diffraction
- EXAFS Extended x-ray absorption fine structure



# Chapter 1

## Introduction

The aim of the following paragraphs is to provide the reader with a motivation for the work carried out for this thesis in a broader context. I will discuss current trends in renewable electricity generation, the growing need for storage of electricity and the relevance of Power-to-X. At the end, I will provide an overview of the other chapters of this thesis.

### 1.1 Trends in renewable electricity generation

Worldwide, the amount of electricity generated from renewable sources including photovoltaic and wind power has increased over the last decade, with the largest increase in Europe and the Americas [1]. This trend is motivated by the advantages of supplying a clean form of electricity, both in regards to the emission of the greenhouse gas CO<sub>2</sub>, and other airborne pollutants. The increase in installations goes hand in hand with a decrease in cost for electricity from these renewable sources, such that they can now compete with non-renewable sources such as coal. This is expressed both in the actual price of electricity, and in the energy sources on the market: For example, in Germany in 2017, wind power was shown to reduce the Day Ahead Spot Market Price by 0.94 €/MWh per GW and solar power by 0.43 €/MWh per GW [2]. This means that feeding more wind or solar power into the net reduces the average price of electricity.

Globally, the weighted average cost for electricity from onshore wind fell by 23% to 0.06 USD/kWh between 2010 and 2017 [3].

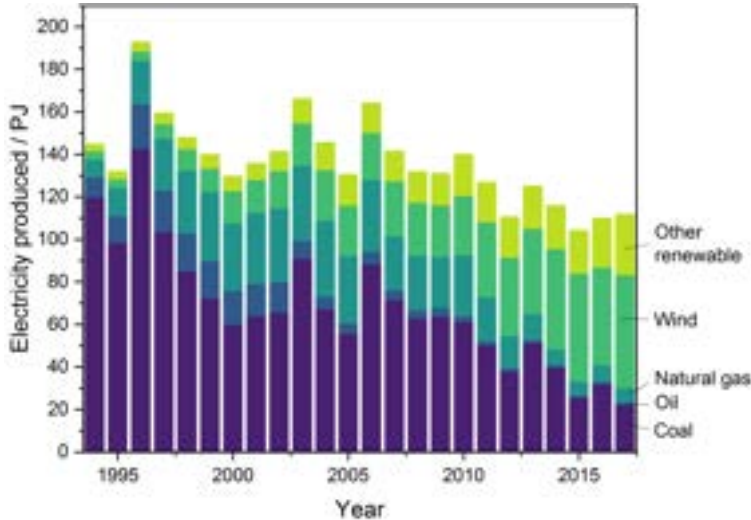


**Figure 1.1** Electricity generation from different sources in Denmark between 1994 and 2017. Data from ref. [4].

Looking at the distribution of energy sources for electricity production, an increase in renewables in recent years is evident. In Germany, for example, the installed power of renewables has been greater than the installed power of fossil and nuclear combined since 2015. The actual net electricity production from renewable sources was larger than from lignite and hard coal for the first time in 2018. [2] In the US, April 2019 was the first month where electricity generated from renewables exceeded the amount generated from coal. Figure 1.1 shows the development of power generation in Denmark since 1994: In 2012 and every year since 2014, the annually averaged power generation from renewables has been higher than from the sum of coal, oil and natural gas. This trend is expected to continue, as Denmark has stated the goal that by 2030, 100% of electricity should come from renewable sources [5].

## 1.2 Power-to-X

The main disadvantage of generating electricity from wind and solar is that they are inherently intermittent. In Figure 1.2 the wind and solar power produced in Denmark over the course of two weeks is presented, clearly showing the significant variations both on a daily level, and over periods of several days, due to weather phenomena. In order to prevent instabilities in the grid, the energy needs to be stored in some way. At the moment, for example in Denmark, this is mostly handled by trading electricity with the neighboring countries Sweden and Norway, where hydroelectric plants can be used to store excess electricity. In more extreme cases of overproduction, measures to stabilize the grid have even led to negative day-ahead electricity prices [6, 7], which are, of course, not favorable for power suppliers. Especially with the prospect of higher capacities of renewable energy, this calls for the establishing of alternative storage possibilities [8].

It is rather unlikely that there will be a single solution to solve this problem. While batteries, and possibly also other technologies such as flywheels, will undoubtedly play a significant role for short term storage [3], a system combining electrolyzers and fuel cells offers a much higher capacity, as storage of energy is decoupled from the conversion system [9].

One possibility for utilizing excess energy in peak periods is using it for production of chemicals; a concept known as Power-to-X. This possibility is discussed both in an academic setting and by policy makers. A recent analysis shows that in Denmark there is a significant potential for establishing PtX already before 2030 [8]. The electrochemical production of hydrogen, CO, ethylene and ethanol from water or CO<sub>2</sub>, respectively, can compete with processes from non-renewable sources when the electricity cost is lower than 0.04 USD/kWh [11]. In some onshore wind farms, 0.04 USD/kWh have already been achieved for extended periods in 2017 [3].

The "X" in Power-to-X stands for multiple possibilities: gas (e.g. H<sub>2</sub>, CH<sub>4</sub>), liquids or fuels (e.g. methanol, ethanol, replacement for currently used airplane fuels), chemicals, etc. The most developed of these technologies is water electrolysis for production of hydrogen gas, which can be used directly as a fuel, or be used for example together with nitrogen to produce ammonia, or in combination with CO to

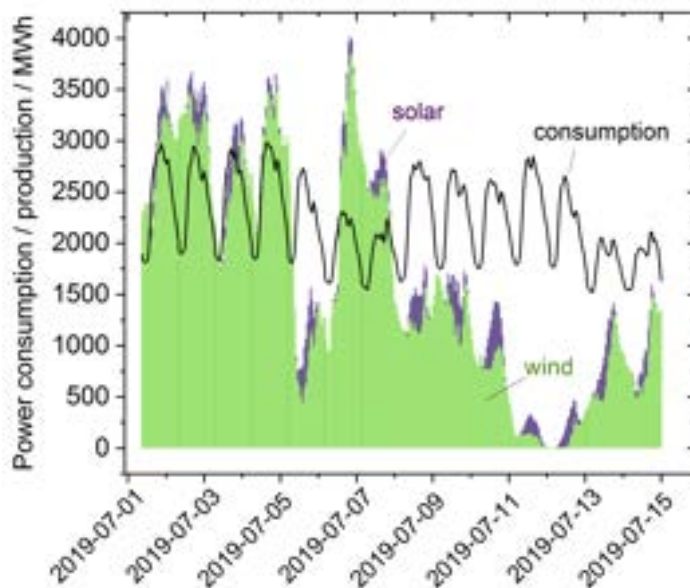


**Figure 1.2** Electrical power consumption and production from wind and solar power over a two-week period in July 2019, Price area DK1 (Jutland and Fyn), Denmark. Contributions from wind and solar are stacked for easier comparison with the consumption. Data from ref. [10].

make chemicals/fuels using conventional, thermochemical processes [12]. In recent years, also electrochemical reduction of  $\text{CO}_2$  to CO and other compounds has received increased interest [13, 14]. Considering that chemicals (both commodity and fine chemicals) are more valuable products than fuel, Power-to-Chemicals is a particularly attractive option, as the higher costs of establishing a new technology can more easily be compensated for [11, 13, 15]. Besides being a means of storing energy, using electricity can also have a great beneficial influence on the production of fine chemicals: complicated, multi-step organic synthesis routes can be shortened while providing high selectivity and reducing the amount of waste produced [16, 17]. Also simpler reactions such as the oxidation of simple hydrocarbons or alcohols to aldehydes and acids can benefit from using electrochemical methods [18–20]. Applying a potential to drive the reaction rather than high temperatures gives a good control over the reaction parameters and allows for mild reaction conditions. The formation of the thermodynamically most favorable product,  $\text{CO}_2$ , can be prevented in this way, and the selectivity towards the

goal products increased. In addition to this, fuel cell technology based reactors are scalable, and would allow for decentralized production [21].

Climate change and the need to reduce global CO<sub>2</sub> emissions has become a hot topic in political discussions this year, both in Denmark and abroad. In the public discussion, however, the main focus of means to reduce both the consumption of fuels and the overall greenhouse gas emissions is on the transport sector. Much progress has been made in this field. A recent economic analysis highlights how cars which run on renewable electricity are already cheaper to operate than conventionally fueled cars considering the gained mobility per money paid [22]. Nonetheless, it is often overlooked that the industrial sector actually consumes 50% of global energy carriers, of which 44% are combusted (the rest is used as starting material) [23]. The IPCC reports that 28.5% of global greenhouse gas emissions come from the industry of which 10.6 percentage points come indirectly from electricity [24]. This means that there is a high potential for reduction of the industry's CO<sub>2</sub> footprint, if electric energy from renewable sources is used instead of burning fossile energy carriers [25]. Using electrocatalysis to convert CO<sub>2</sub> to ethanol, formic acid and CO could even be net-CO<sub>2</sub>-negative [11]. With the motivation presented in the paragraphs above I would like to point out, however, that even without considering climate change, which is undoubtedly one of the great challenges of our times, electrification of the chemical industry can be beneficial purely from a financial point of view.

In this work, the electrochemical oxidation of propene to important commodity chemicals such as acrolein, acrylic acid, and propylene glycol was investigated. The background and prior literature for this reaction is discussed in detail in the following chapter.

### **1.3 Outline of this thesis**

In Chapter 2, first an introduction to general concepts in catalysis is given, followed by a summary of the state-of-the-art of electrochemical oxidation of propene. At the end of the chapter, I specify the aims of this thesis.

Chapter 3 provides an introduction to the experimental methods used throughout the thesis.

In Chapter 4 the catalysts that were used for the experiments in the latter chapters are characterized with complementary *ex-situ* methods.

The next three chapters deal with three different experimental approaches aimed at studying different aspects of electrochemical propene oxidation: In Chapter 5, high surface area Pd electrodes and different chemical analysis methods are used to determine the dependence of product distribution on the potential. In Chapter 6, desorption products under different conditions are followed by electrochemistry-mass spectrometry. Differences between Pd, Au and AuPd alloys are discussed. Lastly, in Chapter 7, surface enhanced infrared spectroscopy is used to probe surface adsorbates on Pd electrodes *in-situ*.

In Chapter 8, I aim at relating the results presented in Chapters 4 to 7 to derive some main conclusions about the mechanism of electrochemical propene oxidation. Finally, I discuss possible directions for future research.

## Chapter 2

# Electrocatalysis and propene oxidation

The first part of this chapter serves as a brief introduction to general concepts in (electro)catalysis that are helpful for the understanding of the results presented later on. Any reader familiar with the field may skip Section 2.1. The second half of the chapter aims at providing an overview of the state-of-the-art of electrocatalytic oxidation of propene.

### 2.1 Electrocatalysis

#### 2.1.1 What is a catalyst?

The IUPAC Gold Book defines a catalyst as "A substance that increases the rate of a reaction without modifying the overall standard Gibbs energy change in the reaction" [26]. The difference in Gibbs free energy between a reactant and a product of a chemical reaction is the thermodynamic driving force for the reaction to occur. As a chemical reaction involves changing the configuration of atoms and the formation or breaking of bonds, the reacting molecules typically have to go through a transition state that is energetically less favorable than the initial state. The energy necessary to reach this transition state is termed activation energy ( $E_A$ ). A catalyst has an effect on reaction kinetics (*i.e.* the reaction rate) by interacting with reactants, as shown in Figure 2.1.

Thereby it provides an alternative reaction pathway *via* a metastable intermediate with a lower activation barrier ( $E_{A,1}$  in the schematic). A good catalyst is both *active*, *i.e.* reaction rates are high, and *selective* towards the reaction of interest, *i.e.* the rate of potential side reactions is minimized.

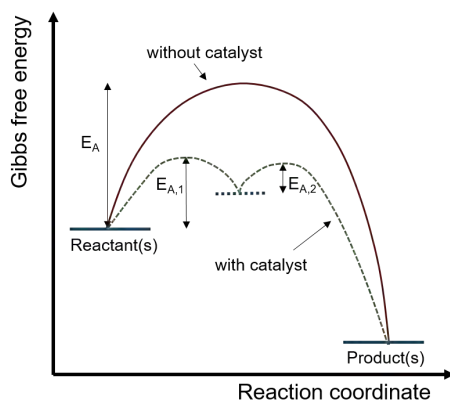


**Figure 2.1** Schematic drawing of the effect of a catalyst on the energy landscape of a reaction. The catalyst lowers the effective activation barrier for the reaction to occur by providing a different pathway from reactant to product.

One can differentiate between homogeneous catalysis where the catalyst is in the same phase as the reactants, and heterogeneous catalysis where the catalyst is in a different phase, most commonly solid [27]. In the following, the main focus will be on heterogeneous catalysis.

### Basic mechanisms of surface reactions

Heterogeneous catalysis on solid catalysts occurs on surfaces and involves adsorption of at least one reactant. This adsorption to the surface lowers the kinetic barrier for the reaction to occur. Depending on whether only one or several reactants adsorb, it is differentiated between three main classes of reaction mechanism. These are illustrated schematically in Figure 2.2 considering the simple reaction of two reactants  $A + B \longrightarrow AB$  :

- The **Langmuir-Hinshelwood** mechanism involves separate adsorption of both reactants, diffusion and reaction on the surface, and desorption of the product molecule.
- The **Eley-Rideal** mechanism, where only one reactant is adsorbed, which then directly reacts with the other reactant, followed by desorption of the product.
- The **Mars-Van Krevelen** which is essentially a variation of the Langmuir-Hinshelwood mechanism, except that here one of the reacting atoms comes from the lattice of the catalyst. Such a mechanism is typical for oxidation reactions on oxide surfaces.

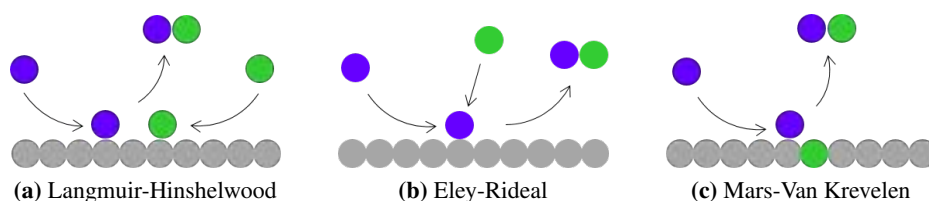


**Figure 2.2** Schematic of the basic mechanisms of surface reactions.

The different mechanisms are naturally governed by different kinetic laws, *i.e.* different dependencies on surface concentrations, which allows for determination of the mechanism for a specific reaction. This is important, as knowing the mechanism is crucial for developing an optimal catalyst for the reaction: While for an Eley-Rideal-type reaction only one adsorbate has to be considered, for a reaction following a Langmuir-Hinshelwood mechanism, the adsorption of both reactants has to be balanced to allow for high reaction rates [27]. Catalyst design is the topic of the next section.

### 2.1.2 The Sabatier principle and rational catalyst design

At the beginning of the 20th century, based on extensive work in organic synthesis, Paul Sabatier proposed what is now known as the Sabatier principle [28]: To maximize the reaction rate a catalyst needs to bind the reactants strong enough to have an effect on the intra-molecular binding strength, but not too strong to hinder dissociation and

release of the product after the reaction. This principle can be visualized by plotting a measure for the reaction rate (*e.g.* the current density) as a function of a measure for the interaction with the catalyst (*e.g.* the adsorption energy). Both at high and low binding strength the reaction rate is low, with a maximum at intermediate strengths. Such a volcano plot for the hydrogen evolution reaction, one of the two partial reactions of electrochemical water splitting, is shown in Figure 2.3 as an example.

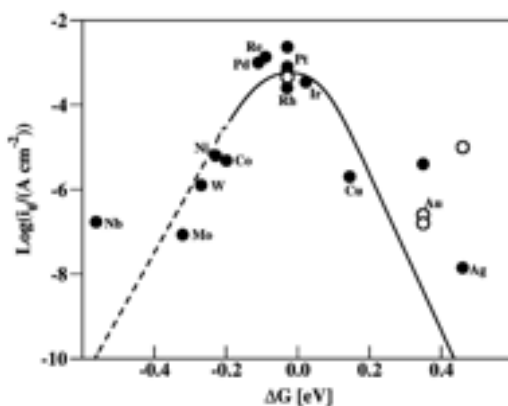


**Figure 2.3** Volcano plot for the hydrogen evolution reaction on transition metals: exchange current density as a function of the Gibbs free energy of adsorption of hydrogen. Ni and Co bind hydrogen too strongly, Ag and Au too weakly to be efficient catalysts. Pt, the best single metal catalyst for hydrogen evolution, lies at the top of the volcano. Reprinted with permission from ref. [29]. Copyright 2010 American Chemical Society.

### Tuning adsorption energies

In order to find the optimal catalyst for a reaction, it is therefore crucial to be able to determine the adsorption energies of the intermediate(s) on different materials. While in some cases it is possible to determine adsorption strength or related parameters experimentally, computational methods are a powerful tool to screen a large number of possible catalyst materials. The theoretical basis for the calculation of adsorption energies lies in the Newns-Anderson model, also known as the d-band model. Chemisorption of an adsorbate on a transition metal is established by interaction of electrons in both the sp-band and the d-band of the metal with the molecular orbitals of the molecule. The degree of the interaction is determined by the degree of filling

of molecular states with electrons from the metal. This degree is directly related to the position of the d-band center of the transition metal and the molecular orbitals before adsorption. The position and width of the d-band is an inherent property of the transition metal depending primarily on the filling degree of the d-band (the more electrons, the more localized the d-orbitals are around the core) and the width of the d-band (the larger the atoms, the more overlap, the broader the d-band) [27].

To obtain adsorption properties beyond the pure metals, several ways have been described how surface modification, for example by bulk alloying or deposition of metal adsorbates, can change the catalytic properties [30]:

**Change of electronic properties:** Adatoms or (surface) alloy atoms change the electronic properties of the neighboring atoms directly. As width and position of the d-band depend on the distance between atoms in the lattice, the electronic structure can also be influenced indirectly by putting a strain/stress on the lattice, for example by alloying. In an alloy with full miscibility the lattice constant changes linearly with composition (Vegard's law), therefore the d-band width and center will also change linearly [31]. Such an electronic effect was for example achieved by alloying Pt with different metals such as Co or Ni [32, 33], Sc or Y [34], or different lanthanides [35], to improve the oxygen reduction reaction. In all these examples a compressively strained Pt overlayer is formed. This strain shifts the d-band center of Pt and reduces the oxygen binding energy such that the catalytic activity is improved.

**Bifunctional catalysts:** Foreign atoms on a surface can also simply act as separate sites with different adsorption properties, which can be beneficial in more complicated reaction mechanisms involving several surface adsorbates. Two reactants with different adsorption properties can in this way adsorb at the surface at the same time enabling the reaction to proceed. This effect is used for example to improve ethanol oxidation catalysts: In PtSn alloys the higher affinity of Sn (compared to Pt) for oxygen is suggested as a possible mechanism for the observed reduction in CO poisoning of the catalyst [36, 37].

**Ensemble effects:** For many reactions the adsorption geometry is crucial. By blocking certain adsorption geometries, unfavorable reaction pathways can be

prevented, increasing the selectivity towards the goal product. An example for such an effect is the high selectivity for  $\text{H}_2\text{O}_2$  achieved for oxygen reduction on Pt-Hg surface alloys [38]. Every other Pt surface atom is covered by a Hg atom effectively hindering the dissociative adsorption of  $\text{O}_2$ , which would lead to the full reduction to  $\text{H}_2\text{O}$ .

### Scaling relations

The hydrogen evolution reaction, for which the volcano plot is discussed above, is a very simple reaction involving only two steps. Most reactions, however, involve larger molecules that can bind to a surface with different moieties in different configurations. This leads to many different volcano-type relationships for the different reaction steps and molecules. Nevertheless, binding to the surface through the same atom, despite a different overall structure, is usually similar energetically. Binding through several atoms can be approximated by a linear combination of the individual atoms. These scaling relationships allow for the reduction of a complicated, multistep reaction to a few parameters which make computational methods a powerful tool to predict the behavior of new materials and reactions important for catalysis research [39]. At the same, time scaling relations can also be a limit to further improvement of a catalyst. A way to circumvent these limitations can then be to use bifunctional catalysts or to take advantage of ensemble effects as described above [40].

Considering scaling relations and different ways of influencing catalyst properties gives a large parameter space to tune the catalyst to reach optimal performance for a reaction [34]. Computational catalyst screening was not part of the work presented in this thesis. Nonetheless, since I closely collaborated with Luca Silvioli who carried out DFT calculations, such considerations were important for the choice of which system to test experimentally.

#### 2.1.3 The role of the potential

The considerations above are derived for heterogeneous catalysts. The reaction discussed in this thesis, however, is an electrochemical reaction, which is a spatially separated redox reaction that involves charge transfer across an electrolyte/electrode

interface [41]. The driving force of a chemical reaction – the difference in chemical potential which is the derivative of the Gibbs free energy at constant pressure and temperature – can, for a given system, be influenced by temperature and pressure. For an electrochemical reaction there is an additional parameter: the potential applied at the electrode. The difference in Gibbs free energy is related to the difference in applied potential according to the following equation:

$$\Delta G = -zF\Delta E \quad (2.1)$$

The reversible potential of a reaction, on the other hand, can be calculated from the Gibbs free energy of reaction using the same relationship.

In this way, the potential applied to an electrode has an influence on which reactions can take place and is therefore an important tool to steer selectivity in electrochemical reactions. Compared with thermochemical reactions it gives an additional parameter for tuning the reaction thermodynamics in addition to changing the temperature. This is shown in a more illustrative way in Figure 2.4: By applying a potential to the electrode, the energy level of the electrons at the electrode is changed in relation to the molecular orbitals of the reacting molecule. If the electron energy level is shifted above that of a vacant molecular orbital, electron transfer to the molecule (*i.e.* reduction) occurs. On the other hand, if the electron energy in the electrode is lower than for an occupied molecular orbital, electrons can be transferred to the electrode and the molecule is oxidized.

The reversible potential which can be calculated using Equation 2.1 is the thermodynamic potential for the reaction. At this potential the reaction is reversible, *i.e.* the reaction rate of forward and backward reaction are equal. By lowering or increasing the potential, this equilibrium can be shifted towards reduction or oxidation. However, for most reactions, kinetic limitations make it necessary to increase the driving force further by applying additional potential to achieve measurable reaction rates, which is termed overpotential. If an electrode now lowers this overpotential by interacting with the molecules which are to be reduced/oxidized, it acts as an electrocatalyst. In other words, an electrocatalyst is simply a catalyst that catalyzes an electrochemical reaction at the surface of the electrode.

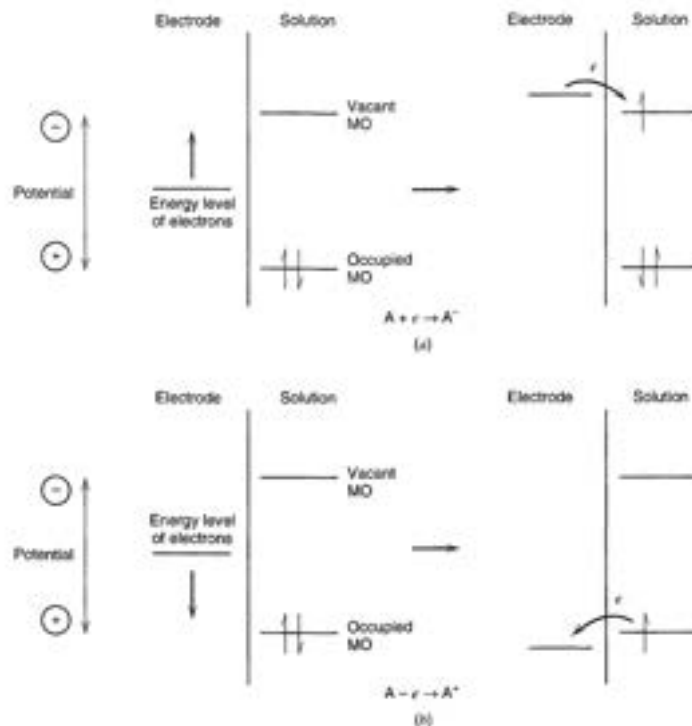


**Figure 2.4** Schematic of the electron transfer during a reduction (a) and an oxidation reaction (b) of an organic molecule in solution. Figure reprinted with permission from ref. [41]. Copyright 2001 John Wiley & Sons, Inc.

Not only kinetic limitations at the electrode can result in an overpotential, however. If the reaction rate is high, the electrolyte around the electrode can be depleted of the reactant. The reaction is now limited by diffusion of reactants rather than reaction kinetics. This regime has to be avoided if the activity of a catalyst should be tested.

### Referencing the potential

For any electrochemical reaction both a reduction and an oxidation reaction are necessary. Therefore, experimentally, a potential difference can only be measured/applied over an electrochemical cell consisting at least of two electrodes and an electrolyte in between. The equilibrium potential of the reaction  $2\text{H}^+ + 2\text{e}^- \rightleftharpoons \text{H}_2$  at a Pt electrode at 1 atm  $\text{H}_2$  and a  $\text{H}^+$  activity of 1 was defined as zero for practical purposes,

and is termed standard hydrogen electrode (SHE) [41]. This potential is defined at pH 0, making it inconvenient for comparison of different pH. The reversible hydrogen potential ( $E_{RHE}$ ) is the potential at a Pt electrode at 1 atm  $H_2$  independent of pH and defined as:

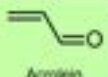
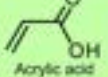
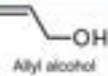
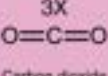
$$E_{RHE} = E_{SHE} - 0.059 * pH \quad (2.2)$$

As both reference electrodes are inconvenient to use, usually other half-cells with a stable potential are used as reference electrodes, such as Hg/HgSO<sub>4</sub> or Ag/AgCl.

## 2.2 Oxidation of propene

The work presented in this thesis is dedicated to the electrochemical partial oxidation of propene.

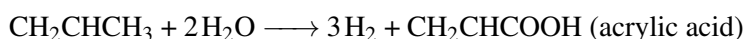
There are many different partial oxidation products; an overview of the structures of the most important ones is given in Figure 2.5. The major challenge is to partially oxidize propene with high selectivity towards a goal product, while preventing the overoxidation to the thermodynamically most favorable product: CO<sub>2</sub>.

 Name Rev. Pot. (V/RHE)	 1,2-propylene oxide (2-methyloxirane)	 Acrolein (prop-2-en-1-al)
2 0.65	4 0.25	
 Propene	 Propylene glycol (propan-1,2-diol)	 Acrylic acid (prop-2-enoic acid)
0 NA	2 0.41	6 0.19
 Isopropanol (propanol)	 Propionaldehyde (propanal)	 Allyl alcohol (prop-2-en-1-ol)
0 NA	2 0.15	2 0.38
 Propane	 Acetone (propanon)	 3X Carbon dioxide
-2 0.51	2 0.00	18 0.10

**Figure 2.5** Overview of the main propene oxidation products and the respective reversible potentials for their formation from propene. Figure by Luca Silvili, reprinted from Paper I.

## Reaction products

Propene oxidation products can be divided into two different groups, depending on the location of the insertion of oxygen into the molecule: Oxidation of the allylic carbon leads to the formation of allyl alcohol, acrolein and acrylic acid:



On the other hand, when oxidizing the double bond, propylene oxide is formed, which can be hydrolyzed to propylene glycol:



This two-fold reactivity makes propene an interesting target for mechanistic studies of electrochemical partial oxidation reactions of hydrocarbons. In the following, first an overview of the current state-of-the-art of electro-oxidation of propene is given. This is followed by a short summary of current industrial processes for the production of the propene oxidation products presented above. While the mechanisms behind these processes are not directly comparable to the electrochemical approach, I hope to provide a context for the industrial relevance of an electrochemical process.

### 2.2.1 Choice of propene as a model system

As illustrated in the previous section, propene is an interesting model molecule for studying partial oxidation reactions, because of the availability of two different reaction sites on an otherwise simple molecule. Analyzing the product distribution is therefore a simple approach towards understanding the interaction of the molecule with the catalyst and elucidating mechanistic details.

The electrochemical partial oxidation of propene has been the focus of a few studies over the past seven decades. Different catalyst materials and different reaction

conditions (alkaline and acid aqueous solutions, and fuel-cell-type reactors with liquid or solid electrolyte) have been tested. Over the course of time, both electrochemical methods, and methods to probe reaction products have been developed significantly, which can make direct comparison difficult.

In alkaline environment, high selectivity towards propylene oxide and the hydrolyzed product propylene glycol has been reported on silver [42] and stainless steel electrodes [43–45]. Based on the studies on stainless steel, NiOOH was tested, but while it is active for allyl alcohol oxidation, it proved not to be able to activate propene [46]. Noble metal catalysts were tested in acidic conditions: Platinum in aqueous electrolyte gives CO<sub>2</sub> as the only product and is therefore not suitable as a catalyst for partial oxidation [47, 48]. On gold, the major product is acetone [49, 50]. An early study using Pd and Pd-Au catalysts reports the formation of acetone, acrolein, ethanal, acetic acid, acrylic acid and malonic acid in different ratios depending on the precise conditions. In contrast to all others, in this study, the catalyst consists of dispersed nanoparticles, and the partial pressure of gas phase oxygen is used to regulate the potential [51]. Later, Pd was also tested with an externally applied electrical potential: The main products from these experiments were acrolein, acrylic acid, acetone and CO<sub>2</sub> with acetone being formed homogeneously from corroded Pd<sup>2+</sup> in solution [52]. Otsuka et al. [53] used a fuel cell set-up and found mainly acrolein and acrylic acid at lower potentials, but increasing amounts of acetone and CO<sub>2</sub> at higher potentials. Despite suggesting a reaction mechanism involving Pd<sup>2+</sup>, the concentration of Pd ions was determined in neither of the studies. Only one study reports the formation of propylene oxide under acidic conditions on Pt in a fuel-cell type reactor [54]. The fact that the contact of the product with the acidic electrolyte is very brief is probably the reason why propylene oxide was not hydrolyzed to propylene glycol immediately.

There are also a few studies where instead of direct electrochemical oxidation of propene at the catalyst surface, first another reactant is oxidized electrochemically, which then oxidizes propene in a second step. One such approach is to use halogen ions (chloride, bromide) in the electrolyte which are oxidized to the respective dihalogen molecules. These then react with propene in a similar mechanism as in the chlorohydrin process [55, 56] (see Section 2.2.2). Furthermore, producing hydrogen peroxide *in-situ* to oxidize propene has been proposed, but has only been used for the oxidation of allyl

alcohol so far [57]. Partial propene oxidation has also been tested successfully in fuel cell-type reactors with solid oxide electrolytes [58, 59].

### 2.2.2 Current industrial processes for propene partial oxidation

Many partial oxidation products of propene are of significant industrial relevance: For example propylene oxide is produced at an annual volume of 9.81 Mt, (2016) [60], propylene glycol at 2.56 Mt (2017 prognosis) [61], acrylic acid at 7.66 Mt, (2016) [60], and acetone at more than 6 Mt (2014) [62]. Different approaches are used in the industry to achieve high conversion and selectivity towards the target product. An overview of the commercially most relevant processes is given in Figure 2.6.

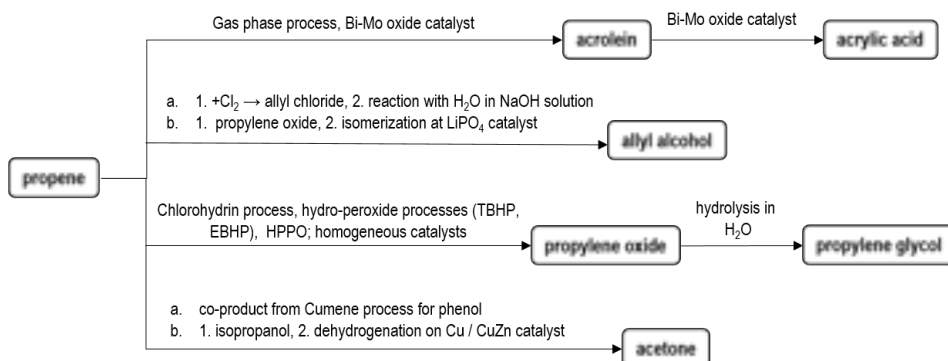


**Figure 2.6** Overview of the commercially most relevant processes towards important propene oxidation products [61, 63–68].

**Acrolein** is produced in a gas phase process at 300–400 °C and near-atmospheric pressure by oxidation with oxygen over bismuth-molybdate catalysts. **Acrylic acid** is produced in a similar process from acrolein. The catalysts are complex multi-component systems with different additives (for example Co, Ni, P, Sb, W, or K). Conversion of propene is typically 93–98% with 85–90% selectivity towards acrolein in the first step. The rate determining step in this reaction is the abstraction of H from the allylic carbon. The mechanism is a Mars-Van Krevelen-type mechanism involving lattice oxygen from the catalyst. Additives help to tune the redox-properties of the molybdate [63–65].

For the epoxidation of the double bond to **propylene oxide**, no gas phase process has been established yet. In contrast to ethylene oxide, where epoxidation on a Ag-based

catalyst yields good selectivity, propene oxidation on Ag results in poor conversion and a large amount of side products. This is due to the abstraction of the allylic proton by oxygen bound to the surface, resulting in the formation of acrolein and further oxidation to CO<sub>2</sub> [69, 70]. Instead, there are three main processes currently used in the industry [67, 71]:

The Chlorohydrin process, where chlorine gas and propene are mixed in water to produce propene chlorohydrin. In a second step the epoxide is formed by treating the chlorohydrin with equimolar amounts of sodium- or calcium hydroxide, resulting in large amounts of salt waste.

Hydro-peroxide processes, where an organic precursor is oxidized to its hydroperoxide (the most relevant being *tert*-butyl hydroxyperoxide (TBHP) and ethylbenzene hydroperoxide (EBHP)), which then reacts with propene on a homogeneous catalyst to form propene oxide and an alcohol. The viability of these processes depends highly on the marketability of the alcohol side product.

The Hydrogen-peroxide propylene oxide (HPPO) process is a comparatively new process where propene is directly oxidized with hydrogen peroxide in the presence of titanium silicalite (TS-1).

**Propylene glycol** is produced from propylene oxide by hydrolysis in water [61]. **Allyl alcohol** is made from propene using one of two 2-step processes: One way is the conversion to allyl chloride with chlorine gas, followed by hydrolysis in aqueous NaOH solution. Alternatively, propene oxide can be isomerized on LiPO<sub>4</sub> [66].

The vast majority of **acetone** is currently produced as a by-product of the Cumene process for production of phenol. Benzene is converted to cumene by reaction with propene with an acidic zeolite catalyst. Cumene is then oxidized to cumene hydroperoxide and cleaved to phenol and acetone using sulfuric acid as catalyst. A second relevant process is the dehydrogenation of isopropanol on Cu or brass catalysts [62, 68].

For all reactions, various alternative processes exist, but they are of negligible commercial relevance. Nevertheless, it is worth mentioning that there is at least one process for electrochemical oxidation of propene to propylene oxide by Kellogg and Shell which was at the stage of a pilot process in 2009 [72].

## 2.3 Aims of this thesis

The work in this thesis was started using Pd as catalyst, as it is the only catalyst where a significant change in product distribution as a function of potential had been reported. These previous studies do not report an analysis of the processes on the surface. In this thesis I therefore want to contribute to a more detailed understanding of the relationship between product distribution and surface processes.

Specifically, I aim at providing an answer to the following questions:

1. What is the effect of varying experimental conditions (particularly the potential) on the product distribution in propene oxidation on high surface area Pd catalysts? Can we reproduce the results from the literature [52, 53]? (Chapter 5)
2. What is limiting the reaction? Are there spectator species adsorbed at the surface under reaction conditions and do they have an influence on the reaction mechanism? Can we influence the activity by alloying Pd? (Chapter 6)
3. Which information can we get from surface enhanced infrared spectroscopy (SEIRAS) to help understanding the reaction mechanism? (Chapter 7)

Additionally, in order to answer the above questions appropriately, I aimed at developing a method for reliable quantification of reaction products (Chapter 5), and at establishing a versatile synthesis method for high surface area Pd and Pd alloy electrodes (Chapters 3 and 4).

# Chapter 3

## Experimental methods

In order to study propene oxidation on Pd in as much detail as possible, I used a wide variety of different experimental methods for characterization of the catalyst *in-situ* and *ex-situ*, as well as several different methods for product quantification. In this chapter I will give a short introduction to the theoretical background of the different techniques. Experimental details on the equipment and conditions I used, as well as a summary of materials used are given in Appendix A.

### 3.1 Catalyst preparation

Catalyst synthesis was not the primary goal of this thesis. Therefore the important aspects of catalyst preparation were good reproducibility, speed and low complexity of the process, as well as versatility, while still giving representative results for the catalyst material. For *in-situ* techniques, there is an additional constraint that the resulting material needs to be suitable for the respective technique. All catalysts used in the experiments presented in this thesis were prepared using either electrochemical or chemical deposition on an inert substrate.

#### 3.1.1 Electrodeposition

Reaction rates of electrochemical propene oxidation are significantly lower than for example of alcohol oxidation or CO<sub>2</sub> reduction. To still be able to quantify products

reliably using similar experimental equipment and methods, the surface area of the catalyst should be high, as also discussed in Chapter 5. Metals that are good hydrogen evolution catalysts can be deposited using the hydrogen-bubble-template method [73, 74]: Here the metal is deposited at a very negative potential together with rigorous hydrogen evolution. The hydrogen bubbles at the surface lead to metal deposition around the bubbles, resulting in a high surface area, sponge-like structure which I termed "foam".

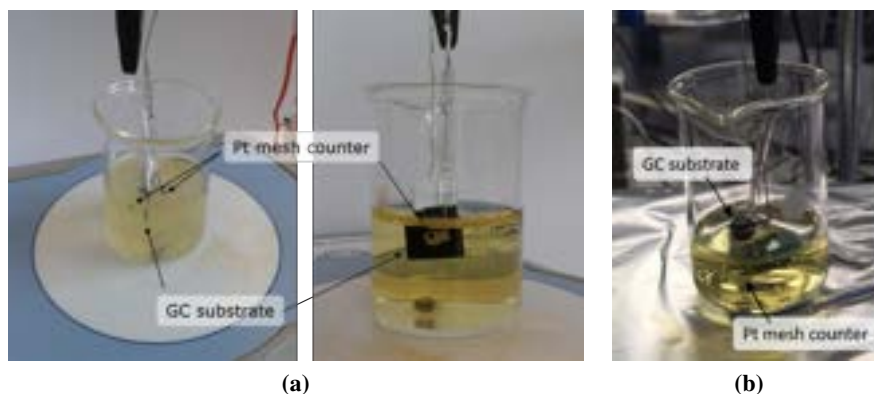


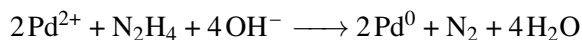
**Figure 3.1** Electrode configuration for Pd deposition in a beaker using the hydrogen bubble template technique. a) Deposition on a glassy carbon sheet: Left picture shows the electrode while depositing, right picture shows the position of the counter electrode from the side. b) Deposition on a glassy carbon stub for EC-MS experiments.

I carried out the depositions in a small glass beaker using Pt mesh as a counter electrode. The deposition solution was 2 mM PdCl<sub>2</sub> in 2 M H<sub>2</sub>SO<sub>4</sub> for Pd electrodes. For alloy electrodes Au salt (NaAuCl<sub>4</sub>) and Pd salt was used in the ratio desired in the catalyst, summing up to a concentration of 2 mM. Glassy carbon plates (for the bulk experiments) or stubs (for EC-MS) were used as substrate due to their inactivity as a propene oxidation catalyst, and because Pd foil would intercalate large amounts of hydrogen during the deposition. The electrode was attached to a piece of Pt wire and wrapped with Teflon tape to prevent contact of the wire with the electrolyte. The most reproducible results were achieved by folding the mesh to form a small ball and placing it close to the middle of both sides for the substrate, as shown in Figure 3.1. It was critical for reproducibility to ensure the same distance between working and counter

electrodes (I used a ruler), and rigorous stirring to remove the evolving hydrogen and increase mass transport. To improve adhesion of Pd to the substrate, first a thin layer was deposited without hydrogen evolution at -1 V applied voltage. Then the porous film was deposited at -4 V between working and counter electrode for 3 min. For all alloy electrodes the first step was omitted to avoid preferential deposition of Au at lower overpotential. No Pt from the counter electrode was detected with XPS or LEIS on any tested electrode.

### 3.1.2 Chemical deposition

The SEIRAS technique requires a defined morphology of the catalyst film deposited on an ATR crystal (see details in Section 3.5). Such a SEIRAS active morphology was obtained by electroless deposition of Pd nanoparticles onto a Si prism [75]: First the native oxide layer was removed from the Si substrate by etching with  $\text{NH}_4\text{F}$  buffered HF. Then a primary layer of Pd seeds was deposited from 1 wt.% HF + 1 mM  $\text{PdCl}_2$  solution applied to the Si crystal surface for 90 s. The seed solution was removed by careful rinsing with millipore water. The nanoparticles were then deposited from a 1:2 mixture of plating solution A (0.018 g  $\text{PdCl}_2$  + 0.048 g ethylenediamine in 5 mL 0.01 M HCl) and solution B (4 ml  $\text{H}_2\text{O}$  + 1 ml 29%  $\text{NH}_3$  + 0.03 g hydrazine monohydrate). The plating solution was mixed just before deposition, applied to the substrate, and rinsed off after ca. 5 min. Palladium is reduced autocatalytically by reaction with hydrazine according to the following equation [76]:



Conductivity of the films was tested using a multimeter and, if necessary, the deposition was repeated until the resistance across the film was below ca. 10  $\Omega$ .

All SEIRAS films used for the experiments shown in Chapter 7 were prepared by Michael Boyd.

## 3.2 *Ex-situ* catalyst characterization

The catalysts were characterized extensively *ex-situ* before and after the electrochemical experiments using scanning electron microscopy, x-ray diffraction, x-ray photoelectron

spectroscopy and low-energy ion scattering. These techniques are introduced in the following.

### 3.2.1 Scanning electron microscopy (SEM)

In scanning electron microscopy, images are generated by scanning a focused electron beam over a sample surface and recording a response signal. The intensity of the signal for each spot is recorded and an image generated. The electrons interact with the sample and generate electrons and photons from elastic and inelastic scattering processes. Elastic scattering produces backscattered electrons (BSE), that are high in energy ( $> 1$  keV). Due to the high energy the information depth is comparatively large (usually 50-300 nm, depending on the sample). Secondary electrons (SE) are electrons from the outer electron shells which are released in inelastic scattering processes. They are much lower in energy (ca. 50 eV), and the information depth is therefore lower (5-50 nm). Different relaxation mechanisms of the excited atoms lead to the generation of element specific x-ray photons or Auger electrons. The electrons and photons from the different processes are measured using different detectors: BSE detectors are usually semiconductor-based and placed around the beam source. SE are detected using an Everhart-Thornley detector where they are accelerated towards the detector with a bias (around 250 V) to enhance collection efficiency. X-ray photons are most often detected with a silicon-drift detector, where all energies are detected simultaneously (energy dispersive spectroscopy-EDS). As the backscattering depends on the electron density of the interacting atom, BSE images give a contrast between atoms of different atomic number. EDS gives element specific information and can be used to generate elemental maps. However, the information depth of the x-rays is even larger than for BSE. The amount of SE that escapes the sample depends very much on the morphology: at tips and edges more electrons can escape than on a flat surface or from valleys. SE-imaging is therefore important for imaging the 3D-structure of electrodes (in 2D).

To avoid charging of the surface, the sample needs to be sufficiently conductive. This is usually given for metallic specimen. At atmospheric pressure, the mean free path of electrons is too short for sufficient signals, therefore for conventional SEM, high vacuum is necessary in the analysis chamber [77]. All SEM images in this thesis are secondary electron images recorded in high vacuum.

### 3.2.2 X-ray diffraction (XRD)

X-ray diffraction (XRD) is a bulk technique to determine the crystal structure of a solid. The wavelength of x-rays is on the same order of magnitude as the distance between lattice planes in crystalline materials. Inelastic scattering of x-rays with the atoms in the lattice can be seen as reflection at the lattice planes, as sketched in Figure 3.2. Depending on the wavelength and the distance between the lattice planes, this leads to constructive and destructive interference of the x-rays that are in-phase. Constructive interference is given according to Bragg's law:

$$n\lambda = 2d\sin\theta, \quad n = 1, 2, 3, \dots \quad (3.1)$$

Where  $\lambda$  is the wavelength of the x-rays,  $d$  the distance between the lattice planes and  $\theta$  the incident angle of the x-rays.

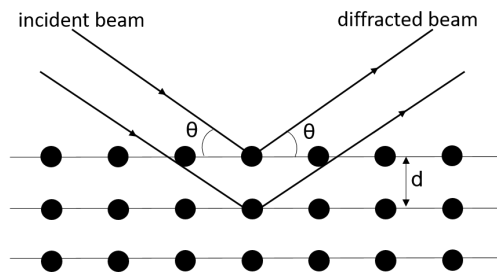


**Figure 3.2** Bragg diffraction of an x-ray beam in a crystal lattice. Figure adapted with permission from ref. [78]. Copyright 2006 John Wiley & Sons Inc.

In a conventional XRD scan, the sample is exposed to x-rays of a certain wavelength (usually generated by accelerating electrons towards a metallic target with high voltage in an x-ray gun). The incidence angle is varied, and the diffracted beam intensity recorded as a function of the angle  $2\theta$ . For a cubic lattice, the distance between the lattice planes is related to the lattice parameter  $a$  and the Miller indices  $(h, k, l)$  of the reflecting plane according to the equation:

$$d_{hkl} = \frac{a}{\sqrt{h^2 + k^2 + l^2}} \quad (3.2)$$

Depending on the crystal structure there are some "forbidden peaks", *i.e.* peaks for certain lattice planes will canceled out because of destructive interference with additional planes. Hence, from a x-ray diffractogram, the crystal structure can be determined based on the pattern of reflecting lattice planes and the lattice parameter  $a$ , characteristic for a material, can be determined from the peak position. Therefore, XRD is also very useful for determining effects which directly influence the lattice parameter such as alloy formation (more details in Section 4.1.2), or determining strain and stress of the lattice. A limitation of XRD is that the presence of sufficiently large crystalline structures is required. If the structures are smaller than ca. 100 nm, incomplete destructive interference will lead to peak broadening [27].

### 3.2.3 X-ray photoelectron spectroscopy (XPS)

X-ray photoelectron spectroscopy (XPS) is one of the most commonly used methods for determining catalyst composition and chemical environment, due to its surface sensitivity and the possibility to determine the chemical states of the elements present.

The inelastic interaction of x-ray photons with a material can excite photoelectrons: The kinetic energy  $E_k$  of the ejected electron is related to the energy of the photon  $h\nu$ , the electron's binding energy in the material with respect to the Fermi level  $E_b$  and the workfunction of the instrument  $\phi$  according to:

$$E_k = h\nu - E_b - \phi \quad (3.3)$$

This is shown schematically in Figure 3.3.

A related process leading to electrons with a similar kinetic energy is the Auger process, also illustrated in Figure 3.3. The hole left behind by excitation of a core electron to the vacuum is filled by an electron from a higher energy shell. The surplus energy excites another electron to the vacuum - the Auger electron. This means that in an XPS spectrum there will usually be peaks related to Auger transitions. An important difference between photo- and Auger electrons is that the kinetic energy of the latter does not change with photon energy [27].

To ensure good signal-to-noise ratio and no energy discrimination, conventional XPS analysis is carried out in UHV conditions at pressures around  $10^{-9}$  mbar. X-rays

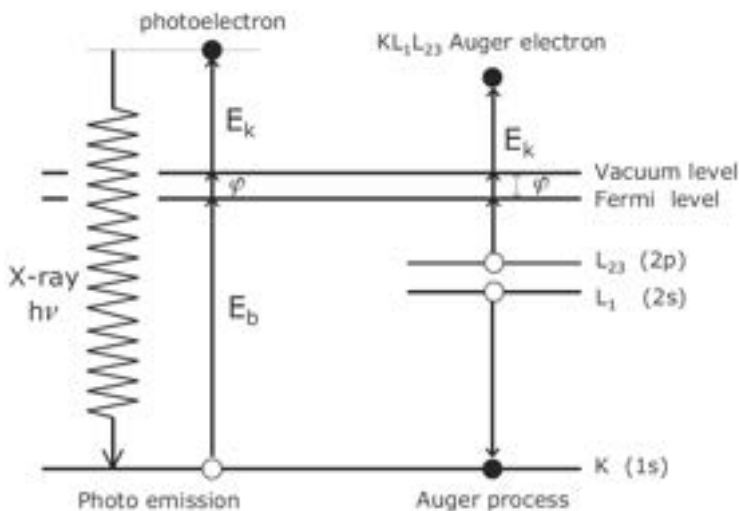


**Figure 3.3** XPS and Auger processes. Reprinted with permission from ref. [27]. Copyright 2003 WILEY-VCH Verlag GmbH & Co. KGaA,

are generated in an x-ray gun using Al or Mg anodes. The most common analyzer for high resolution applications is a hemispherical electron energy analyzer. Here the electrons travel through two concentric hemispheres with a varying voltage applied, so electrons of a specific energy reach the detector at the other end of the hemisphere.

### 3.2.4 Low energy ion scattering (LEIS)

Low energy electron spectroscopy (LEIS), also known as ion scattering spectroscopy (ISS), is an intrinsically highly surface sensitive method which only probes the top monolayer of atoms.

In LEIS, the sample surface is bombarded with low energy noble gas ions (most commonly He, Ne or Ar). When they elastically interact with the surface they lose energy only related to the mass of the atoms present directly at the surface. Based on conservation of energy and momentum, the kinetic energy of the ions after the impact ( $E_{k,o}$ ) is related to the initial energy  $E_{k,i}$ , the scattering angle  $\alpha$  and the masses of surface atom  $M_s$  and ion  $M_{ion}$  according to:

$$\frac{E_{k,o}}{E_{k,i}} = \left( \frac{\pm \sqrt{M_s - M_{ion} \cdot \sin^2 \alpha} + M_{ion} \cdot \cos^2 \alpha}{M_s + M_{ion}} \right)^2 \quad (3.4)$$

The energy calculated using Equation 3.4 is the maximum possible kinetic energy of the ions after interaction with the surface. Usually, detected energies are lower due to phonon losses or lattice effects even on a perfectly clean surface. The ion energy is analyzed in the same type of hemispherical analyzer as used in XPS, except that the polarization of the hemispheres has to be inverted to account for the positive charge of the ions.

Interaction with atoms below the surface is rare due to the low energy of the ions and the chance to detect such ions after interaction is even lower as they lack the energy to escape the surface. This makes LEIS a powerful tool to determine the composition at the surface.

However, the differentiation of atoms of similar atomic number, especially for higher masses, is very difficult. The use of heavier ions can help, but comes at the cost of additional surface damage. Also, quantitative analysis is difficult, because the ion yield differs highly from element to element and would require extensive calibration with pure materials.

### 3.3 Electrochemical performance

The most important characterization of an electrocatalyst is the measurement of its activity for the reaction(s) of interest. In this section, I will briefly introduce the techniques used in this thesis and define parameters which are used to measure the performance.

#### 3.3.1 Potentiostat

For the electrochemical experiments, very precise control and measurement of potential and current are crucial. A potentiostat with 3-electrode configuration was used for all experiments in this thesis. In this configuration, a working electrode (WE, where the reaction of interest takes place), a counter electrode (CE, where the counter reaction takes place to close the electric cycle), and reference electrode (RE, with a known,

stable potential) all immersed into the electrolyte are connected to a potentiostat. The potentiostat controls the chosen parameters through a complex system of feedback loops. In chronoamperometry, for example, a constant, defined potential between the RE and the WE is established by varying the current between the WE and the CE [79]. The RE is separated by a high impedance to prevent any reaction from taking place.

The terms anode, cathode, and positive/negative current can be confusing, since different conventions are used in different fields of electrochemistry. The following definitions are used throughout this thesis:

**Anode:** Electrode where the oxidation reaction takes place, *i.e.* where the reactant loses electrons.

**Cathode:** Electrode where the reduction reaction takes place, *i.e.* where the reactant gains electrons.

**Anodic current = positive current:** current where the reactant at the WE is being oxidized and electrons flow from the WE to the potentiostat.

**Cathodic current = negative current:** current where the reactant is being reduced at the WE and electrons flow from the potentiostat to the WE.

### 3.3.2 Setup for electrochemical experiments

A sketch of the cell and setup used for the electrochemical experiments presented in Chapter 5 is shown in Figure 3.4 a. I used a custom made 3-compartment glass cell with a 3-electrode configuration, as described previously [80, 81]. The compartment containing the working electrode is separated from the counter electrode by a commercial Nafion membrane and from the reference electrode by a glass frit. In this way, the electrolyte volume is minimized, and reaction of products at the counter electrode is prevented. The working compartment is connected to gas loop, which can operate in "purge" and in "loop" mode. Gas is introduced to the electrolyte through a glass tube ending in a frit, for better dispersion. In purge-mode, the gas passes through the cell and the loop and then exits the system through an exhaust. In loop mode, the gas is continuously moved through the cell and the gas loop by a pump. In this way, the electrolyte is constantly replenished with reactant gas, while gaseous products can

accumulate over time, allowing for much higher product sensitivity. At the same time, the bubbling also improves mass transport. For all experiments shown in this thesis, the working compartment was filled with 13 mL electrolyte. A Hg/HgSO<sub>4</sub> reference electrode (Schott Instruments) was used together with a Pt-mesh counter electrode. The reference electrode was calibrated every time a new batch of electrolyte was prepared by measuring the open circuit potential *versus* a Pt wire immersed in the electrolyte saturated with hydrogen at atmospheric pressure. All potentials given in this thesis are corrected to the RHE scale.

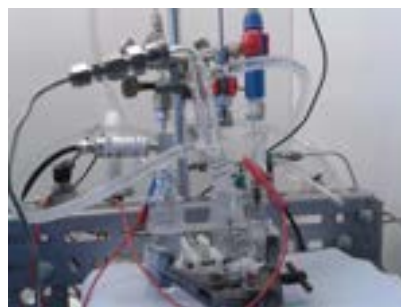
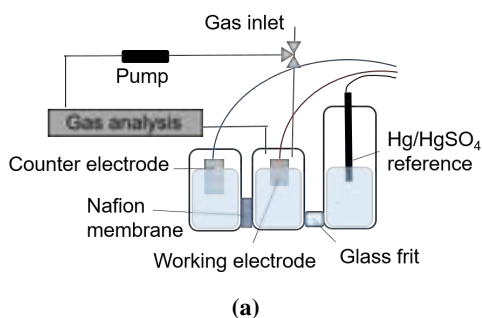


**Figure 3.4** Setup used for the experiments presented in Chapter 5. a) Schematic drawing. b) Photograph of the cell during an experiment.

### 3.3.3 Cleaning

In order to avoid the influence of metal or organic contaminants from water, glassware or the working environment, care was taken to work at high cleanliness. All glassware was initially cleaned by immersion first in piranha solution (30% H<sub>2</sub>O<sub>2</sub> and H<sub>2</sub>SO<sub>4</sub> conc. mixed at a ratio 1:3) over night and then *aqua regia* (HNO<sub>3</sub> conc. and HCl conc. mixed at a ratio 1:3) over night, and by immersion in *aqua regia* regularly to remove Pd dissolved during the reaction. After acid treatment, the acid was removed by rigorous rinsing with millipore water (5-10 times), followed by boiling in millipore water for 1 h.

The electrode substrates were cleaned in a similar way by immersion in *aqua regia* for ca. 30 min, rinsing, and 3 times sonication in millipore water for at least 5 min each.

### 3.3.4 Electrochemical methods

#### Electrochemical impedance spectroscopy (EIS)

In electrochemical impedance spectroscopy the response of the system to a low-magnitude alternating potential of different frequencies is probed. Different processes (such as electron conduction in a conductor, ionic conduction, charge transfer processes, or mass transport) will have an influence on the system's impedance at different frequencies, depending on the timescale for the process to adapt to the changes in potential. For example, the ohmic resistance across the system can be obtained from the high frequency response, while the charge-transfer resistance of electrochemical reactions shows at lower frequencies. To analyze the data, usually an equivalent circuit using elements such as resistors, capacitors and inductances is constructed to model the frequency response of the electrochemical system. The most basic equivalent circuit for an electrochemical cell is shown in Figure 3.5. A resistor modeling the ohmic resistance is in series with a capacitor and a resistor in parallel, resembling the double layer charging and the charge transfer of the electrochemical reaction [82].

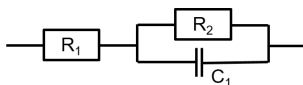


**Figure 3.5** Simple equivalent circuit for EIS used to determine the ohmic resistance across the cell.

Electrochemical impedance spectroscopy is a very powerful technique for the characterization of electrochemical processes. However, accurate modeling requires deep knowledge of the technique and the reaction. I only used it to determine the ohmic resistance across the system. A more detailed description of the technique is therefore out of the scope of this thesis.

#### Ohmic drop compensation

Due to the ohmic resistance of the electrolyte, the potential measured between WE and RE does not correspond to the actual potential at the surface. The difference is given as

a function of current  $I$  and ohmic resistance  $R$  according to the following equation [41]:

$$E_{appl} = E_{actual} - IR \quad (3.5)$$

The ohmic resistance was determined by measuring EIS spectra in the double layer region and fitting the equivalent circuit shown in Figure 3.5 to the data. The "manual IR compensation" function in the potentiostat software EC-Lab was used to compensate for 85% of the ohmic drop. The remaining 15% was considered negligible due to low current and low resistance for most experiments.

### Chronoamperometry

In chronoamperometry, a constant potential is applied to the WE and the resulting current between WE and CE is measured as a function of time [41].

I used this technique primarily to test the effect of the potential on the products that are formed during propene oxidation. In this context I used two parameters to quantify the results: the faradaic efficiency and the partial current density towards the individual products, which are defined in the following.

As any conversion in an electrochemical reaction entails a current, the measure for kinetics in electrochemical reactions is usually the current. To normalize to the actual number of surface sites, the total current is normalized to the surface area, ideally to the electrochemically active surface area (ECSA). Faraday's law of electrolysis gives the relationship between transferred charge ( $Q$ ) and moles of molecules converted ( $n$ ) from the number of electrons transferred per mole,  $z$ :

$$n = \frac{Q}{zF} \quad (3.6)$$

From the concentration of the different products in gas phase and electrolyte, and the respective volumes, the number of moles can be calculated. Using Equation 3.6, the charge towards each product can be calculated.

The **faradaic efficiency** (FE) is a measure of how much of the charge transferred across a system is used for the formation of the different products. Ideally, the sum of the FE of all products should be 100%, to be sure that no faradaic reactions at the

electrode are overlooked. It is calculated by relating the charge towards the product of interest to the total charge transferred according to:

$$\text{FE} = \frac{Q_{\text{product}}}{Q_{\text{total}}} \cdot 100\% \quad (3.7)$$

The total charge  $Q_{\text{total}}$  is calculated by integrating the current trace over the entire reaction time. The FE is an important measure for *selectivity* of a reaction.

The **partial current density** is a measure of the *activity* towards a certain reaction product. It is also calculated from the charge calculated using Equation 3.6, by dividing by the total time of the experiment,  $t$ . In this thesis, I only show partial current density normalized to the electrode surface area, ECSA (see below):

$$\text{partial current density} = \frac{Q_{\text{product}}}{t \cdot \text{ECSA}} \quad (3.8)$$

Since the concentration was only determined at the end of the experiment, the partial current density is an average over the total time of the experiment and does not provide information about possible changes with time.

For the chronoamperometry experiments, I purged propene at a constant potential, where no reaction was expected (0.4 V) for 5 min (experiments at pH 3) or 10 min. The gas supply was set to loop mode at a slight overpressure of 0.2 bar, to prevent air seeping in through small leaks, which might be present. Then the potential was stepped up to a final potential (between 0.7 and 1.2 V vs. RHE, see Chapter 5) and held for 30 min (experiments at pH 3) or 60 min. At the end of the reaction time the product concentrations in gas and liquid phase were determined using the techniques described in Section 3.4.

### Cyclic voltammetry

In linear sweep voltammetry, the potential is changed linearly with time at a defined scan rate while measuring the resulting current. In cyclic voltammetry, when reaching the final potential, the potential is swept back at the same rate to the initial potential to close the cycle, which can then be repeated [41]. An example of two consecutive cycles is shown in Figure 3.6. Of course, it is also possible to start a cycle by decreasing the potential, or to start the cycle between the minimum and maximum potential. The

current response gives information about oxidation and reduction reactions occurring at the WE at different potentials. The most common representation is to plot the current as a function of potential, as shown in Figure 3.7. The advantage of this representation is that it eases the comparison between the anodic and cathodic part of related reactions, for example the oxidation and the reduction of the electrode surface.

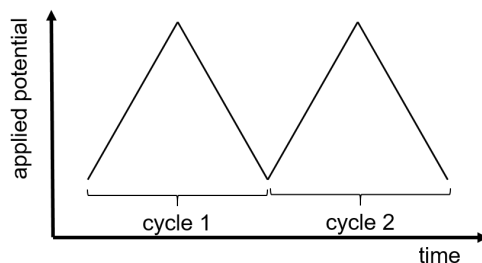


**Figure 3.6** Sketch of the potential profile of two consecutive cycles in cyclic voltammetry as a function of time.

There are many possibilities of how to use cyclic voltammetry to study reaction kinetics. In this thesis I used cyclic voltammetry primarily for determination of the electrochemically active surface area as discussed below, and in EC-MS experiments. Details about how CVs were used in connection with EC-MS are given together with the results in Chapter 6.

### Surface area estimation

To be able to compare results between different catalysts, the determination of the activity per active surface site is important. I used three methods to estimate the electrochemically active surface area (ECSA) of the individual electrodes.

**In CO stripping**, a full monolayer of CO is adsorbed to the surface at a potential where no other processes occur. After removal of non-adsorbed CO from the electrolyte, the potential is scanned anodically and CO is removed from the surface in form of CO<sub>2</sub>:



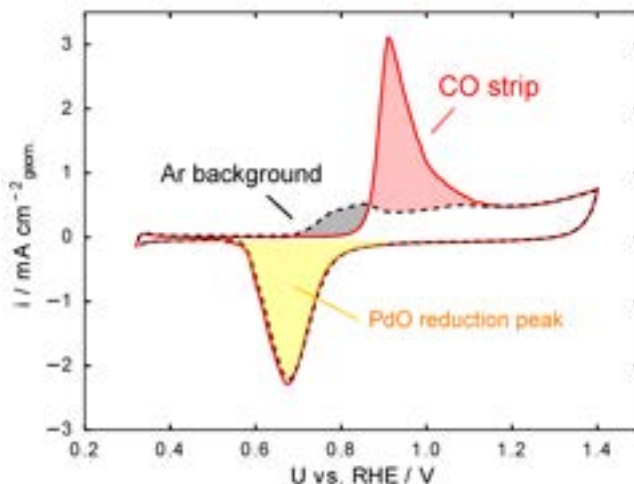


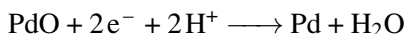
**Figure 3.7** Cyclic voltammetry for surface area determination. The full line shows the first cycle after adsorption of a ML of CO on a Pd surface in 0.1 M HClO<sub>4</sub>, with a clear CO oxidation peak at ca. 0.9 V. The dashed line shows the consecutive background cycle in Ar, where all current is due to ad- and desorption processes of species originating from the electrolyte, characteristic for the electrode material.

From the integrated current, the amount of CO that was originally on the surface can be calculated using Faraday's law of electrolysis (Equation 3.6). A CO stripping cycle is shown in Figure 3.7 (red line). The black dashed line shows the second cycle in Ar after removal of the adsorbed CO. There is a significant oxidative current in the same potential range as the CO oxidation due to oxidation of Pd. To account for this contribution, the integrated current between 0.6 and 1.2 V vs. RHE of the second cycle in Ar was subtracted from that of the first cycle [83].

In this thesis, a charge of  $410 \mu\text{C}/\text{cm}^{-2}$  Pd is assumed for a full CO strip [83]. This assumes the adsorption of one CO molecule per Pd atom, which is not necessarily true, as the preferred adsorption of CO is in the bridge position between two Pd atoms at lower CO partial pressures [84–87]. Nevertheless, the same value was used in all experiments, providing comparability at least between the experiments presented here, and is also commonly used in the literature. An important requirement for CO stripping is, of course, the adsorption of a known

amount of CO (greater than zero). This is given for example for Pt and Pd, but not for Au [88].

**Oxide reduction** is another method to determine the surface area. Alternatively to covering the surface with CO, the electrode is oxidized up to a potential where it can be assumed that one ML of oxide is formed. For Pd, the oxide reduction peak between 0.4 and 0.9 V *vs.* RHE is much more well-defined than the oxidation feature; it is therefore more precise to use the integrated reduction feature instead. This is also shown in Figure 3.7. Here, the reaction of interest is the following:



I used this method for surface area estimation to avoid contamination of the gas loop with CO, which would have affected the quantification of CO<sub>2</sub> as reaction product of propene oxidation. As there is no clear consensus in the literature at which potential a full monolayer of PdO is formed [88, 89], instead of assuming coverage of 1 ML at a certain potential, I calibrated the PdO reduction peak area at 50 mV/s scan rate up to 1.4 V *vs.* RHE to the surface area determined by CO stripping on four different electrodes. The calibration data is shown in Appendix A. Based on this calibration, a charge of  $-482 \mu\text{C}/\text{cm}^{-2}$  was used.

**Double layer capacitance** is a third alternative to determine electrode surface area which is often used if defined reactions like CO stripping or oxide reduction can not easily be performed. When applying a potential to an electrode, ions from the solution will move towards the surface, resulting in a current proportional to the surface area similar to a plate capacitor. From CVs at different scan rates in the double layer region (*i.e.* in a potential region where no electrochemical reactions take place), the surface area of the electrode can be determined [90]. In this thesis, I used a simplified approach, where I determined the current in a small potential window at 50 mV/s and calibrated this current to the surface area determined by CO stripping on the same electrode. This approach was used to estimate the surface area for the electrodes used in the experiments at pH 3. While the double layer capacitance depends heavily on material and reaction conditions, it has been reported that for Au and Pd the same capacitance was

obtained under similar conditions, justifying the use of this method for these alloys [91, 92].

Oxide reduction was used to estimate the surface area for each high surface area Pd electrode used for the experiments at pH 1 shown in Chapter 5, and for the EC-MS experiments on Pd. The calibrated DL capacitance was used for the Pd electrodes measured at pH 3. For the alloy electrodes used in the EC-MS experiments, CO stripping was used to estimate the number of Pd sites on the surface. The ECSA was then used to calculate the ECSA normalized current density for each experiment.

### 3.4 *Ex-situ* product analysis

Both gas and liquid products of propene oxidation were quantified after chronoamperometry to determine selectivity and activity towards the different products. Despite using high surface area catalysts and low electrolyte volume, the concentrations were very low due to low intrinsic activity of the tested catalysts (in the low  $\mu\text{mol/L}$  range), requiring sensitive analytical methods. While generally most of the products are measurable with most of the techniques introduced below, I used different techniques with higher sensitivity towards different products to optimize detection limits.

#### 3.4.1 Gas chromatography (GC)

In gas chromatography, the gaseous analytes are carried through a column by an inert carrier gas such as Ar or He. The column is filled (packed column) or coated (capillary column) with a material that interacts with the analyte, depending on its chemical properties. In this way, analyte molecules that interact more with the column take longer to reach the end of the column than those which interact less. Thus, compounds with different properties can be separated from each other. For example, if the column is coated with a polar material, polar molecules, such as alcohols, will have longer retention times (exit the column later) than apolar compounds, *e.g.* hydrocarbons. In addition to the interaction, there is also a size effect, as larger, heavier molecules take longer to pass through the column due to stronger van-der-Waals forces.

At the end of the column there is a detector which, based on certain properties of the molecules, produces a signal that is proportional to the quantity of the analyte. The gas chromatograph (GC) used for the work in this thesis is equipped with two detectors connected to different columns for the detection of different analytes:

**A Flame Ionization Detector (FID):** Here the gas exiting the column is ionized in a hydrogen flame. These ions are accelerated in an electric field and the resulting ion current is recorded. The requirement for detection using this detector is that the analyte molecule is not fully oxidized. Very good sensitivity is given for organic molecules. CO and CO<sub>2</sub> can also be determined, if they are converted to CH<sub>4</sub> with H<sub>2</sub> over a Ni catalyst in a methanizer before reaching the detector.

**A Thermal Conductivity Detector (TCD),** which works if the analyte has a different thermal conductivity than the carrier gas. Here, the thermal conductivity between two cells – one where the column exhaust passes through, and a reference cell where carrier gas passes through – is compared. I used a TCD for the determination of H<sub>2</sub> and air components.

The retention time depends on column parameters, such as coating material and length, but also on carrier gas flow, pressure, and column temperature. It is only molecule-specific under the right conditions. Also, the intensity of the detector signal depends on the molecule itself. Extensive calibration is therefore necessary [93]. All calibrations used for analysis shown in this thesis are given in the Supporting Information to Paper I in Appendix A.

In the setup described in Section 3.3.2, the gas loop is directly connected to an injection loop, where a defined volume of the gas is injected into the column. As the signal is proportional to the actual number of molecules, the pressure in the gas loop has an influence on the signal intensity. Therefore, the pressure in the loop was determined and the signal normalized to a standard pressure, before determining the concentration.

### **Static head-space gas chromatography (HS-GC)**

Gas chromatography is not restricted to analytes that are gaseous at room temperature, as long as they are brought to the gas phase before they reach the column. This is conventionally done by direct, fast evaporation of a liquid sample in a hot inlet.

Alternatively, a method called head-space sampling can be used, where a gas-tightly closed vial containing the liquid sample is heated to a temperature below the boiling point of the matrix. Analytes that have a lower boiling point than the solvent and/or are not well soluble will concentrate in the head space over the liquid. A sample from the gas in the head space can then be injected into the GC, where the analyte concentration will be increased in comparison with the liquid phase. The sensitivity of the method for a compound can be estimated from its Henry constant in the solvent. A large compilation of Henry constants is available from Sander [94].

In addition to better sensitivity for trace components compared to conventional direct injection, this HS injection also protects the inlet and the column from salt deposition from the electrolyte and damage by overloading the column with water. Unfortunately, this method does not work for non-volatile propene oxidation products such as acrylic acid and propylene glycol. Also, poor results were obtained for acrolein, since the high temperature increased the speed of degradation processes dramatically, impairing sufficient reproducibility. Isopropanol could be detected, but due to its high polarity, the sensitivity was low. Good analytical results were obtained for acetone and propanal.

### 3.4.2 High performance liquid chromatography

The basic principle in high performance liquid chromatography (HPLC) is the same as in GC: An analyte is transported through a column, and can be detected at the end of the column after a certain retention time depending on the chemical properties, the size of the analyte, and the resulting interaction with the column material. In HPLC, instead of a carrier gas, a liquid solvent (eluent) is used to carry the analyte through the column. This adds an additional set of parameters, as the polarity of the eluent now plays an additional role, and the retention time will in essence depend on the ratio between interaction of the analyte with the eluent and the column [93].

I used 5  $\mu\text{M}$   $\text{H}_2\text{SO}_4$ , *i.e.* a very polar eluent, in combination with an apolar column. This means that polar products such as acids and alcohols are expected at short retention times, while apolar compounds, such as acrolein and dissolved propene, will interact more strongly with the column and less with the eluent and therefore take longer to reach the detector. The HPLC system I used is equipped with two types of detector:

**A Diode Array Detector (DAD)**, suitable for the detection of any molecules absorbing light in the UV-VIS range down to 190 nm. This is given for example for organic molecules with  $\pi$ -electron systems, such as the double bond in propene, allyl alcohol and acetone or the conjugated double bonds in acrolein and acrylic acid. The diode array allows for recording of a complete UV-VIS spectrum as a function of time. To obtain maximum sensitivity for quantification, the wavelength with the maximum absorption should be chosen for each analyte. The intensity is referenced to a wavelength region where no absorption of eluent or analytes is expected.

**A Refractive Index Detector (RID)** can be used for analytes which do not absorb light in the UV-VIS range, but have a refractive index sufficiently different from the eluent. This is given for example for alcohols like ethanol, propanol, isopropanol and propylene glycol in comparison with dilute  $\text{H}_2\text{SO}_4$ . However, the sensitivity is generally not as high as for DAD signals. Therefore propylene glycol quantification is not possible at the low concentrations observed in the propene oxidation experiments.

Like with the different detectors in the GC, a suitable detector has to be selected based on the properties of the analyte. In each case the signal intensity is a linear function of the concentration (within some limits), which can therefore be determined from the integrated signal after a suitable calibration. HPLC analysis was used for quantification of acrolein and acrylic acid. For the experiments at pH 3 shown in Chapter 5 also allyl alcohol concentration was determined using HPLC.

### 3.4.3 Nuclear magnetic resonance spectroscopy

The basis of nuclear magnetic resonance spectroscopy are the magnetic properties of atomic nuclei. The main prerequisite for a nucleus to be active for NMR spectroscopy is that the spin quantum number  $I > 0$ . From this follows that there are more than one magnetic quantum numbers according to  $-(2I + 1) < m < (2I + 1)$ .

If an external magnetic field is applied to such an atom, the magnetic moment of the nucleus will align parallel or antiparallel to the field. The potential energy of the nuclei in the magnetic field is proportional to the magnetic moment which is in turn

proportional to the magnetic quantum number and therefore quantized. The energy difference between these states is in the range of radio frequency (RF) electromagnetic radiation. Therefore, the nuclear spin can be excited when exposing a sample in a sufficiently strong magnetic field to radiation in this energy range.

The local magnetic field around a nucleus depends on its precise chemical environment. The energy required for excitation will therefore depend on chemical environment and thus contain information about chemical bonds and other atoms around the nucleus of interest. In addition to that, the alignment of the spin of neighboring atoms will also influence excitation energy, which results in multiplet splitting of the signal, giving information about the number of neighboring atoms. Both the chemical shift and the multiplet splitting make NMR a powerful method for determining the structure of molecules [95].

While also some isotopes of other atoms show NMR activity, in this thesis I only used  $^1\text{H}$ -NMR.  $^{13}\text{C}$ -NMR, for example, is also relevant for determining the structure of organic molecules, unfortunately due to the low natural abundance of  $^{13}\text{C}$ , it is not sensitive enough to give reasonable signal at the low concentrations encountered here.

In principle the signal in NMR is proportional to the number of nuclei that are being probed. This means that if an internal standard with a known concentration is added, quantification of the other analytes is possible. Nevertheless, the excited state of some nuclei decays more slowly than that of others. For reliable quantification, the same number of nuclei has to be excited both for the standard and the analytes, which is only given if the time between two pulses is long enough for all nuclei to relax. To reduce the measurement time, the time between two pulses is optimized for the standard only and an external calibration with the analytes of interest is made to account for the effective decrease in analyte signal due to saturation. One challenge of  $^1\text{H}$ -NMR in aqueous solution is that the concentration of proton nuclei of water is orders of magnitude higher than that of the analytes'. This can be suppressed by saturating the transition of these nuclei by applying a RF-pulse in the frequency corresponding to the signal of  $\text{H}_2\text{O}$  just before the multi-frequency pulse. This technique of water signal suppression was used for all samples.

Quantitative NMR was used for quantification of propylene glycol, isopropanol and allyl alcohol.

### 3.4.4 Inductively coupled plasma - mass spectrometry

In inductively coupled plasma - mass spectrometry (ICP-MS), the sample is first vaporized in a nebulizer and ionized in an Ar plasma. The masses of the ions are then analyzed using a quadrupole mass analyzer, where they are separated according to their mass-to-charge ratio ( $m/z$ -ratio). Due to the harsh ionization conditions, organic molecules will be fragmented entirely, however this method is suitable for the determination of dissolved metals in solution. It is intrinsically very sensitive and suitable for the quantification in the ppb range [96].

ICP-MS was used to quantify catalyst corrosion, *i.e.* dissolution of Pd and Au.

## 3.5 *In-situ* product characterization

*In-situ* product characterization has the advantage of probing reaction products while the reaction is occurring. This means that ideally reaction intermediates can be observed. However, instrumentation is challenging and special electrochemical cells and catalyst configurations are required. I used two different *in-situ* methods in the work presented in this thesis: IR spectroscopy and EC-MS. They are introduced in the following.

### 3.5.1 ATR-SEIRAS

With attenuated total reflection - surface-enhanced infrared absorption spectroscopy (ATR-SEIRAS), organic species adsorbed on the catalyst surface can be detected.

#### FT-IR spectroscopy

Infrared spectroscopy probes the vibrational modes of chemical bonds. Atoms in a molecule can move relative to each other. For a diatomic molecule this can be illustrated by two balls connected by a spring. As quantum mechanics apply, the quantized potential energy levels of such a system can be calculated approximately by treatment as a harmonic oscillator. The energy levels for the vibrational quantum numbers  $\nu = 1, 2, 3, \dots$  can then be expressed as following [97]:

$$E_{\nu} = h\nu_0 \left( \nu + \frac{1}{2} \right) \quad (3.9)$$

With the fundamental frequency  $\nu_0$  depending on an effective force constant  $D$  (related to the bond strength) and the effective mass  $m_{\text{eff}}$  according to:

$$\nu_0 = \frac{1}{2\pi} \sqrt{\frac{D}{m_{\text{eff}}}} \quad (3.10)$$

Where effective mass  $m_{\text{eff}}$  is given from the masses of the two atoms  $m_1$  and  $m_2$ :

$$m_{\text{eff}} = \frac{m_1 m_2}{m_1 + m_2} \quad (3.11)$$

In IR spectroscopy, instead of energy, usually wavenumbers  $\nu$  are used, related to the energy by  $\nu = E/(hc)$ .

The energy between different vibrational modes of a molecule is in the range of IR radiation. According to the equations above, the energy required for a specific transition depends on the bond strength and the respective masses. However, not all transitions are allowed. For an harmonic oscillator only transitions of  $\nu = \pm 1$  are allowed. (This is extended to transitions of  $\nu = \pm 1, \pm 2, \pm 3, \dots$  when considering that the approximation with an anharmonic oscillator is more appropriate for molecular vibrations, however, these higher harmonics are low in intensity.) Importantly, excitation of a vibrational mode is only possible, if there is a change in dipole moment during the vibration [98].

Typically, the signal intensity is given in absorbance units (AU). The absorbance is defined from the ratio of the intensity of the incoming and the outgoing light ( $I_0$  and  $I_s$ , respectively) by:

$$A = -\log_{10} \left( \frac{I_s}{I_0} \right) \quad (3.12)$$

### **Attenuated total reflection (ATR)**

Attenuated total reflection (ATR) can be used to limit the penetration depth of the IR signal into the sample. A crystal with a high refractive index is used, which is illuminated from the backside at an angle to achieve total reflection at the surface. The electromagnetic field perpendicular to the beam penetrates through the interface with exponential decay in energy; thereby probing only the first few micrometers of the sample on top of the crystal. When studying electrochemical reactions this has twofold

advantage: (1) if the catalyst is positioned on top of the optical crystal, only species very close to the surface are probed and (2) the problem of very low intensities due to absorption of the surrounding water is circumvented [98].

### **The SEIRA effect**

Surface enhanced infrared absorption (SEIRA) is an effect observed on some transition metal surfaces (for example Au, Pt, Pd, Cu, and others) with a rough morphology consisting of islands or nanoparticles smaller than the wavelength of light [99]. On these surfaces, the intensity of the infrared light is locally enhanced resulting in a significantly enhanced IR absorption signal of 10-1000 times for molecules in close vicinity of/bound to the surface. The effect is ascribed to the excitation of surface plasmons (quantized oscillations of electrons) from the metal nanoparticles by IR radiation which in turn excite the vibrational states of adsorbed molecules. Thereby the signal from molecules adsorbed at the surface is significantly enhanced compared to molecules in solution enabling high surface sensitivity. The enhancement is greatest for vibrations where the change in dipole moment is normal to the surface, while vibrations parallel to the surface cannot be detected (surface selection rule) [100].

### **Experimental setup and data treatment**

A custom made electrochemical cell (Kel-F) was mounted directly to the FT-IR accessory (see Figure 3.8 b). A Si ATR crystal was used directly as substrate for the working electrode (see Section 3.1). A sketch of the cell is shown in Figure 3.8 b: Gases were introduced through a glass rod with a glass frit for dispersion. The working electrode was contacted *via* Au foil (not in contact with the electrolyte), a graphite rod was used as counter electrode and a Ag/AgCl electrode (Accumet) as reference electrode.

Absorbance spectra were acquired using the software Omnic (version 9.6). Where necessary, contributions from CO<sub>2</sub> and gaseous H<sub>2</sub>O from varying gas impurities in the optical system of the IR instrument were manually corrected after acquisition by subtracting scaled spectra of CO<sub>2</sub> and H<sub>2</sub>O gas separately, followed by baseline correction. For difference spectra the difference between absorbance spectra was

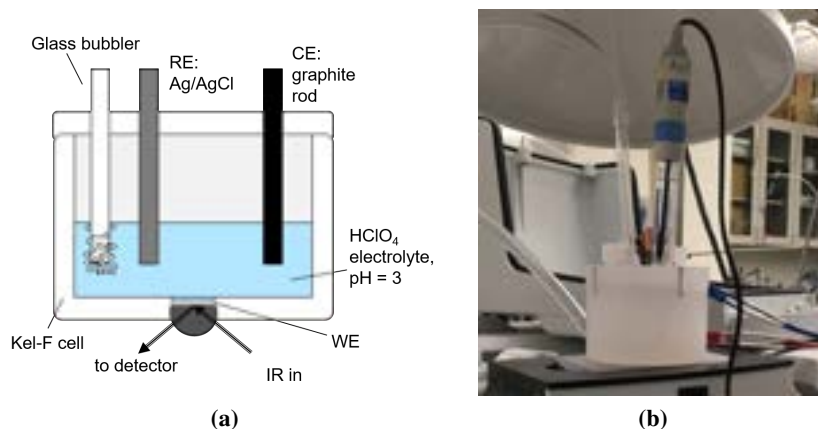


**Figure 3.8** Electrochemical cell setup used in the SEIRAS experiments

calculated directly without correction for gas contributions. Data treatment was carried out using the software Spectragryph, version 1.2.10d [101].

### 3.5.2 Electrochemical mass spectrometry (EC-MS)

In electrochemical mass spectrometry (EC-MS), a mass spectrometer is coupled to an electrochemical cell in a way to enable detection of reaction products desorbing from the electrode on-line, *i.e.* with good time resolution. In this way the dependence of products and reaction intermediates can be followed as a function of potential, for example during cyclic voltammetry.

Several designs have been used to achieve this, such as DEMS (differential electrochemical mass spectrometry) where the catalyst is sputter deposited onto on a Teflon membrane which serves as the interface to the mass spectrometer [102, 103] or OLEMS (on-line electrochemical mass spectrometry) where a porous Teflon tip on a glass rod is brought into close vicinity of an electrode [104].

In the design used for the experiments presented here, instead of a porous Teflon membrane, a silicon based membrane chip is used as the interface between liquid phase and vacuum. A cross sectional scheme of this chip is shown in Figure 3.9. The electrolyte is separated from a gas supply capillary by a membrane consisting of a dense system of holes with 2.5  $\mu\text{m}$  diameter, small enough so that the aqueous

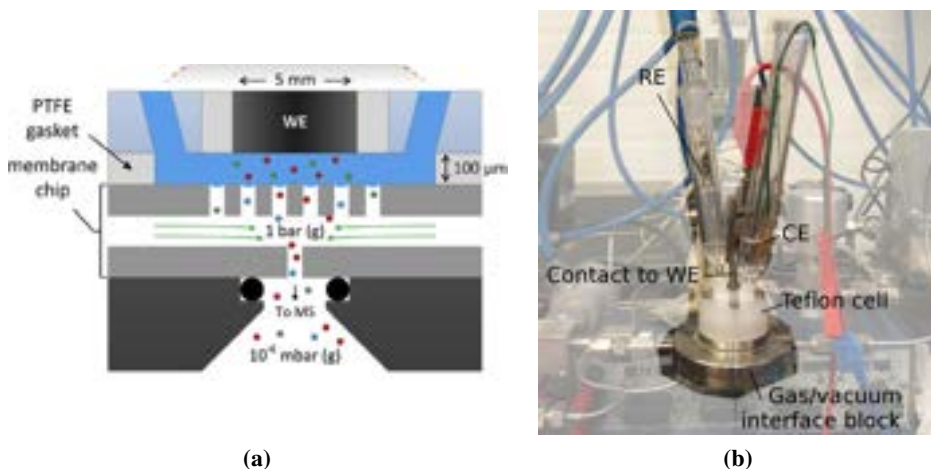


**Figure 3.9** EC-MS Setup. a) Reprinted with permission from ref. [105]. Copyright 2018 Elsevier Ltd. All. b) Photograph of the electrochemical cell mounted to the interface block with counter and reference electrode.

electrolyte will not penetrate as long as the the pressure difference between above and below the membrane does not exceed 0.3 bar. Different gases can be introduced through the capillary which is in equilibrium with the thin layer of electrolyte above the membrane. The connection to the mass spectrometer is through a separate capillary designed such that the flux through the capillary allows for optimal performance of the mass spectrometer. The system is described in detail in ref. [105]. A stagnant thin layer cell was employed in all experiments. The working volume was defined by a PTFE gasket of 100  $\mu\text{m}$  thickness, resulting in an active electrolyte volume of 2  $\mu\text{L}$ . For more details regarding the setup see ref. [105–107].

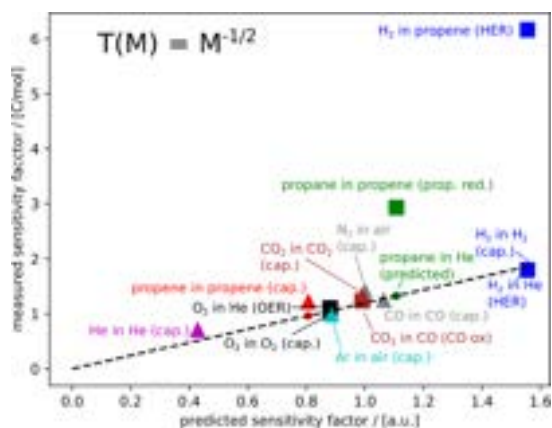
### Calibration

The high collection efficiency in EC-MS allows for the quantification of sub-mono-layer amounts of reaction products. Nevertheless, the current response of the mass spectrometer has to be calibrated for the different compounds. Soren Scott devised a method with which to predict the sensitivity factors for different molecules with an accuracy of 20% based on the ionization cross section of a molecule  $\sigma_i$ , its mass

spectrum and a reference calibration of a known molecule (I used O<sub>2</sub>) to determine constants related to the mass spectrometer and the membrane chip. The predicted sensitivity factor  $f_M^i$  for mass fragment M of analyte i is then given as follows [107]:

$$f_M^i = k \sigma_i \frac{I_M^i}{\sum_{M_j} I_{M_j}^i} M^{-1} \quad (3.13)$$

where  $M$  is the mass to charge ratio of interest and  $I_{M_j}^i$  is the intensity of the mass fragment  $j$  in the mass spectrum of molecule  $i$ . The proportionality factor  $k$  is determined by calibration with a known molecule. The proportionality of the sensitivity factor to  $M^{-1}$  was determined experimentally.



(a)

Molecule	primary M
H <sub>2</sub>	2
He	4
N <sub>2</sub>	28
CO	28
C <sub>3</sub> H <sub>8</sub>	29
O <sub>2</sub>	32
Ar	40
C <sub>3</sub> H <sub>6</sub>	41
CO <sub>2</sub>	44

(b)

**Figure 3.10** a) Universal calibration curve. Figure by Soren Scott, reprinted with permission from ref. [107]. b) Primary mass fragments ( $M$ ) used for the quantification of the molecules shown in a. C<sub>3</sub>H<sub>6</sub> is propene, C<sub>3</sub>H<sub>8</sub> is propane.

In Figure 3.10, a number of measured sensitivity factors is plotted *versus* the predicted sensitivity factors. Most points fall on a line, except for two: hydrogen evolution and propene reduction to propane in propene. This is due to the sensitivity of the mass spectrometer changing significantly in the presence of propene, for reasons that are not entirely clear to us. In the EC-MS experiments shown in this thesis, propane was quantified in the presence of He as a carrier gas, but not propene. Therefore we decided that the more accurate calibration factor would be the one predicted in He.

The EC-MS data shown for pure Pd electrodes was collected before the prediction of sensitivity factors was developed. Hence, a calibration factor based on the calibration in propene was used here, which means that the propane signals are likely underestimated roughly by a factor 2. A more detailed discussion of sensitivity factors is out of the scope of this thesis, but is described thoroughly in Soren Scott's PhD thesis [107].

Another challenge when quantifying propene and propane is that the mass spectra largely overlap, as shown in the reference spectra from NIST in Figure 3.11. For propane quantification  $m/z$  signal 29 was chosen, as it does not contain a contribution from propene. However it overlaps with a contribution from CO (not shown). Propene was quantified using  $m/z$  41, which overlaps with a mass fragment from propane; as does  $m/z$  44, the main mass fragment for the quantification of  $\text{CO}_2$ . To account for these overlaps, the calculated mass fluxes were corrected by subtracting the contribution from the other molecule by observing other masses of the other molecules at the same time. For example, ca. 12% of the intensity of the propane signal measured at  $m/z$  29 will be measured at  $m/z$  41 due to fragmentation of propane. To determine how much of the  $m/z$  41 signal is due to propene flux, 12% of the mass 29 signal has to be subtracted from the  $m/z$  41 signal.

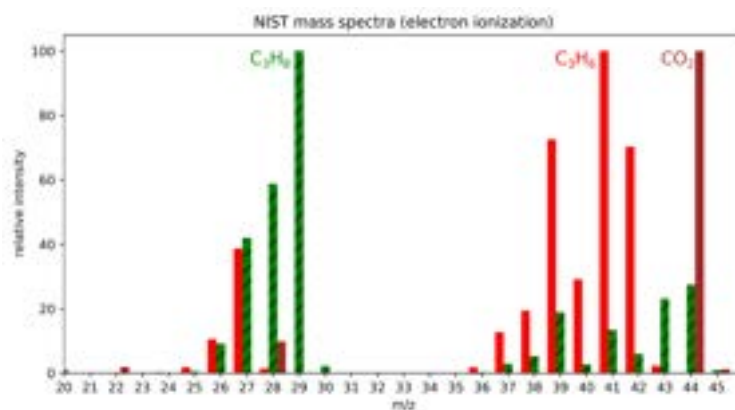


**Figure 3.11** Mass spectra for propene ( $\text{C}_3\text{H}_6$ , red), propane ( $\text{C}_3\text{H}_8$ , green hatched) and  $\text{CO}_2$  (brown) from NIST. [108]. Figure by Soren Scott, reprinted with permission from ref. [107].

All data analysis was carried out using a Python package written by Soren Scott, which contains functions for both the calibration using experimental and predicted sensi-

tivity factors, and correction for overlapping masses and is available at <https://github.com/ScottSoren/>.



## Chapter 4

# Characterization of the catalysts

The aim of this chapter is to provide an overview of the physical characteristics of the electrodes, which are used in the tests of their electrocatalytic performance in the following chapters. The catalyst samples were characterized using several complementary *ex-situ* methods before and after electrochemical measurements. Catalyst preparation was not the main focus of my work presented in this thesis. Nevertheless, the characterization serves to verify that the electrochemical experiments were carried out on defined catalysts and that they were not significantly altered during the experiment. Also, post-analysis can help in the interpretation of the results from electrochemistry.

The first part of this chapter is devoted to the samples prepared by the hydrogen bubble template method. The characterization results from the pure metal and alloy electrodes used in the experiments discussed in Chapter 6 are shown in the following, but they are representative also for the Pd electrodes for the experiments in Chapter 5. The second part of this chapter focuses on the electrodes prepared by chemical deposition for the SEIRAS experiments shown in Chapter 7. Characterization of these electrodes was carried out by Michael Boyd.

The preparation methods for both types of electrodes were introduced in Section 3.1. A short introduction to the individual characterization techniques is given in Chapter 3, experimental details are given in Appendix A.

## 4.1 High surface area Pd, Au and AuPd alloy electrodes

The hydrogen bubble template method was used as a versatile method to obtain high surface area electrodes of different compositions. The determination of morphology using SEM, and a brief comparison with electrochemically active surface area is shown in the first part of this section. Alloy composition and homogeneity were analyzed with XRD, XPS and LEIS, as shown in the second part of this section.

### 4.1.1 Scanning electron microscopy (SEM)

The morphology of the electrodes gives a first indication of the surface area. SEM images of samples of different composition (as prepared) are shown in Figure 4.1 at two magnifications. I use the term "foam" for these structures due to the morphology of the pure Pd electrodes to differentiate from bulk metal and thin film electrodes.

While the deposition parameters were very similar for all samples, there are clear differences in morphology: Au foam is comparatively smooth, while the other compositions exhibit a needle-like structure. The higher the Pd content, the smaller, and the more needles are present. CVs on Pd, and Pb-UPD on Au (not shown) resemble those of the respective polycrystalline metal foil. Therefore a homogeneous distribution of surface facets on those samples is assumed, despite the differences in morphology. The actual electrochemically active surface area differed between the compositions from a roughness factor of around 4-5 for Au and Au rich samples to around 20 for Pd rich and up to 40-50 for Pd electrodes, as determined from the double layer capacitance. This was accounted for in the treatment of the electrochemical data, as described in Section 3.3.

The electrodes were also analyzed after electrochemistry. For bulk electrochemistry experiments, where the samples were mainly exposed to a constant potential, the morphology did not change. The electrodes used in EC-MS suffered a more harsh treatment of repeated potential cycling. The needles in the Pd rich sample clearly smoothed over the course of the experiment, and the film partially scaled off. Pure Pd foam could not be analyzed after the EC-MS experiments, as it repeatedly scaled off the substrate. Changes in electrochemical performance were only observed for pure Pd (here the surface area decreased over the course of the experiment, as evident from a

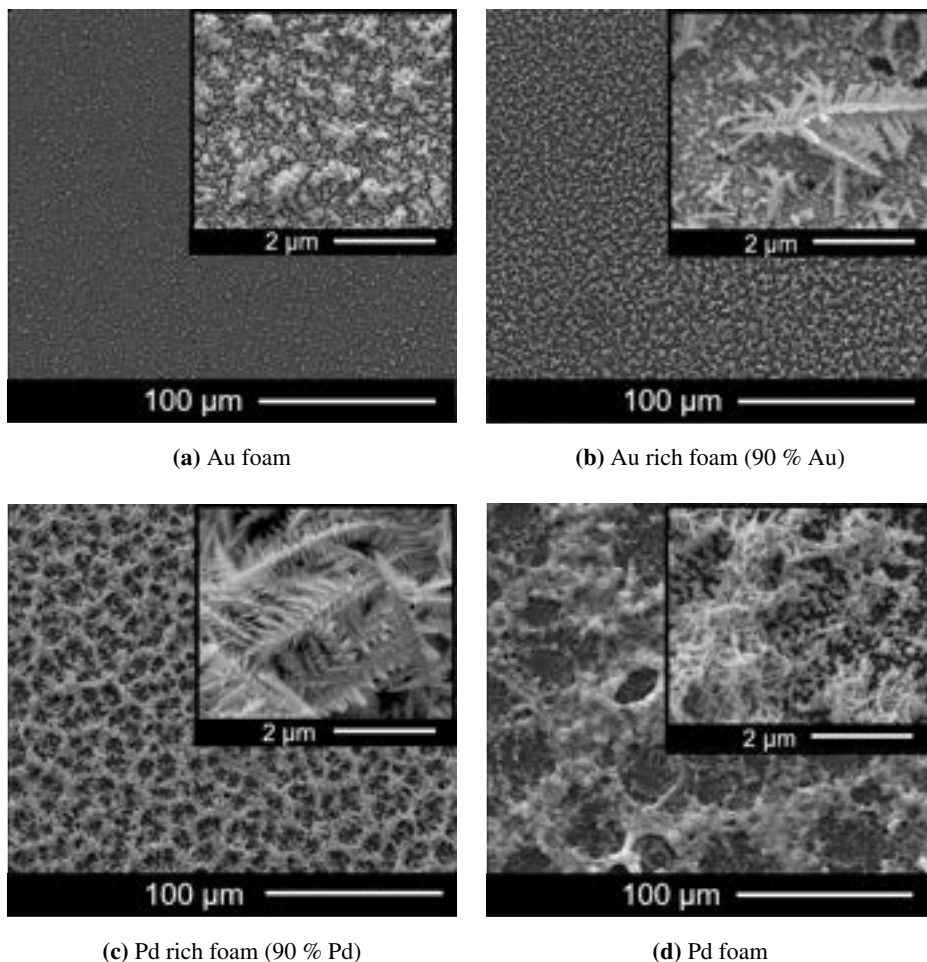


**Figure 4.1** SEM images of Pd, Au and AuPd foams of different composition prepared by the hydrogen bubble template method (as prepared).

decrease in Pd reduction charge with time). For this reason, the changes in morphology were not considered important for the outcome of the experiments.

#### 4.1.2 X-ray diffraction (XRD)

An important concern when co-depositing Au and Pd from the same solution for making alloy electrodes was that, instead of a homogeneous solid solution, areas with high Pd

or high Au concentrations would form. X-ray diffraction measurements were carried out to test whether there was more than one phase present in the samples. Grazing incidence geometry was used to maximize the signal from the catalyst film compared to the glassy carbon substrate. Full XRD patterns between  $35^\circ$  and  $90^\circ 2\theta$  are shown in Figure 4.2. The signal-to-noise ratio is not optimal, which I attribute to alignment difficulties for the porous films. For all samples, only one set of peaks is observed, corresponding to the solid solution of the respective composition. The broad peaks at ca.  $43^\circ$  and  $78^\circ 2\theta$  originate from the glassy carbon substrate.

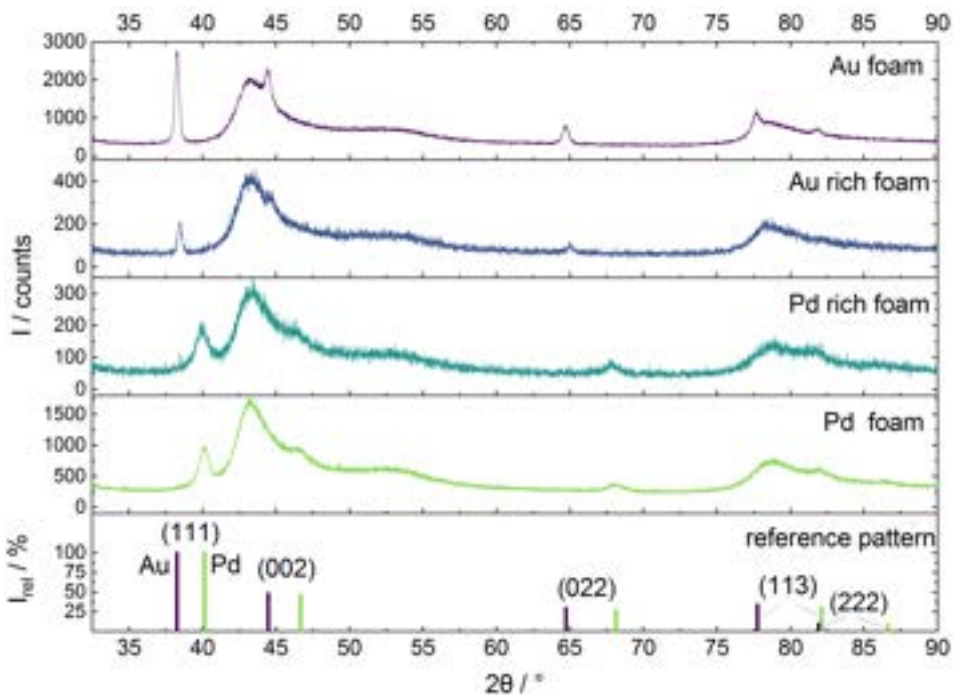


**Figure 4.2** XRD patterns of as-prepared Pd, Au and AuPd foams of different composition recorded in grazing incidence geometry. The broad peaks at  $43^\circ$  and  $78^\circ 2\theta$  originate from the carbon substrate.

In order to determine the peak position more accurately, more detailed scans of the region of the (111) reflex between  $37^\circ$  and  $42^\circ 2\theta$  were recorded and are shown in Figure 4.3. From these scans it is evident that, despite the poor signal-to-noise ratio in the full scan, no additional phases of Au or Pd present in significant amounts were

missed, as these would manifest in additional (111) peaks in the shown region. The peak position of the pure metal foams agrees well with the literature values. The shape of the peak of Pd and Pd rich foam is much broader than for Au and Au rich foam. The peak broadening probably originates from the smaller crystallite size of these samples (see Figure 4.1).

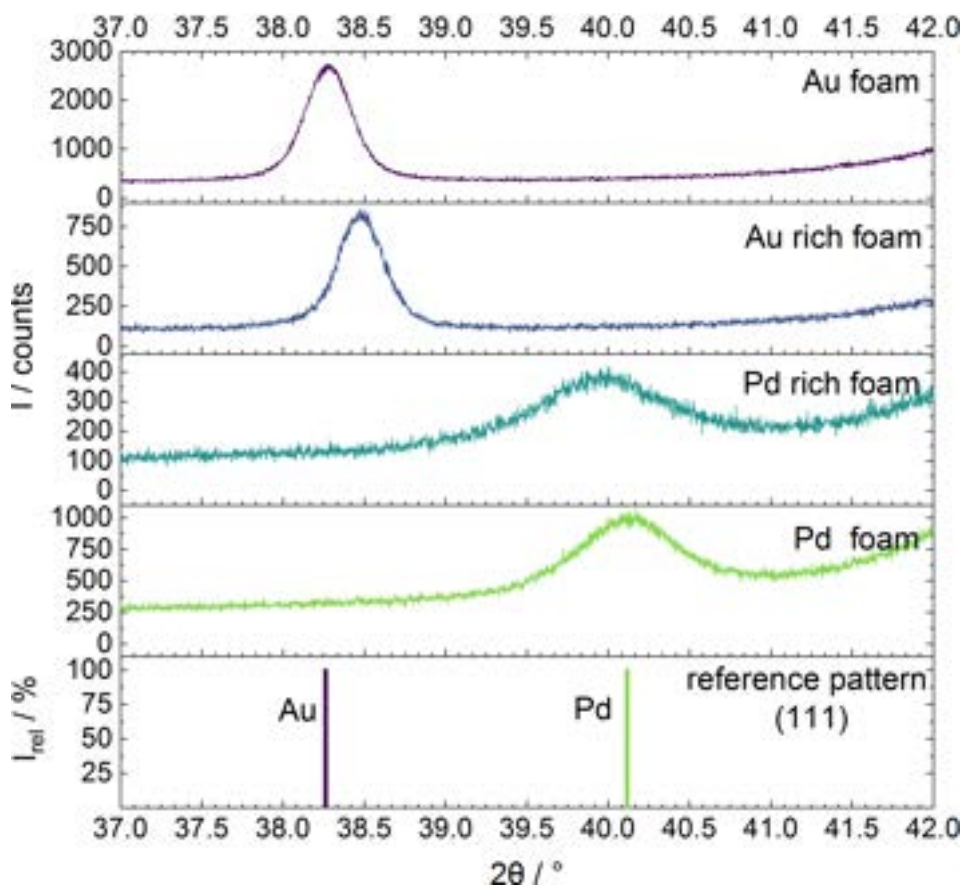


**Figure 4.3** Detailed scan of the (111) reflex of as-prepared Pd, Au and AuPd foams of different composition recorded in grazing incidence geometry.

The peak maxima of the (111) reflex peaks were used to determine the composition of the alloy. A good approximation of the lattice constant in a solid solution is that it is proportional to the concentration of the components according to Vegard's law (here applied to an AuPd alloy with the composition  $\text{Au}_{(1-x)}\text{Pd}_x$ ) [109]:

$$a_{Au_{(1-x)}Pd_x} = (1-x) a_{Au} + x a_{Pd} \quad (4.1)$$

Using this relationship and the peak positions of the pure metals, the bulk composition of the alloys was determined and is shown in Table 4.1. The compositions correspond very well to the ratio of Au/Pd salt in the deposition solution, indicating that despite different redox potentials for the alloy components, the alloy composition can be tuned by using precursor salts in the same ratio as desired in the metal.

**Table 4.1** Peak positions of XRD (111) reflexes shown in Figure 4.3 and Au content calculated from the differences in peak positions using Vegard's law.

Sample	Au content nominal	Peak position	Au content from Vegard's law
	%	$^{\circ} 2\theta$	%
Au foam	100	38.25	100
Au rich foam	90	38.46	89
Pd rich foam	10	38.87	11
Pd	0	40.06	0

An important disadvantage of XRD is that it cannot give information on the distribution of alloy components directly on the surface due to its bulk-probing nature, as evident from the large signal from the substrate. Nevertheless, the results indicate a good distribution of alloy components.

### 4.1.3 X-ray photoelectron spectroscopy (XPS)

While XRD gives good information about the phases present in the bulk, it is not a surface sensitive technique. For the electrocatalyst, however, it is important to know the composition of the surface, since this is where the reaction will take place. Better surface sensitivity is given in XPS measurements. Survey spectra of the samples used for the EC-MS experiments are presented in Figure 4.4. Except for Pd foam, also spectra of the samples after electrochemistry (rinsed with Millipore water) are shown, which do not differ significantly from the initial spectra. No XPS data is available for the Pd sample after electrochemistry in the EC-MS setup, as the film repeatedly scaled off when dismantling the cell. The spectra presented were recorded after brief sputtering with Ar (3 times for 5 s each), to remove the major part of electrolyte and adventitious carbon still present on the sample. This might also have removed possible contaminants from the surface. As the purpose of this characterization was the composition analysis rather than screening for contaminants, this was not investigated further. For analysis of the samples before sputtering, see Section 4.1.4. The spectra mostly exhibit features related to Au and Pd, as well as O and C, which can be expected from samples that had been exposed to air. There are some peaks that can be assigned to K and Cl, which originate from the deposition solution containing  $\text{KAuCl}_4$  and  $\text{PdCl}_2$ .

For determination of the ratio Au:Pd, detailed scans of the most intense core level transitions were recorded. Here is where XPS analysis of the Au-Pd system becomes challenging, as peaks overlap extensively. Not only does the Pd 3d doublet peak, which is usually used for Pd analysis, overlap with Au 4d (energy range 330-360 eV), but also Au 4f (usually used for Au) overlaps with Pd 4s (range 80-95 eV), and Pd 3p overlaps both with Au 4p and O 1s (range 520-580 eV). The signals from all other transitions are significantly weaker, which makes them unsuitable for analysis of small amounts of an alloy component. To be able to use the same peaks for all compositions, I therefore chose to use the range between 325 to 360 eV despite the overlap. I deconvoluted the contributions from Au 4d and Pd 3d by fitting using the software Casa-XPS. The recorded spectra are co-plotted with the fits in Figure 4.5. A Shirley background was fitted over the entire energy range of the spectra (325-360 eV). While pure Au could be fitted satisfyingly using one set of peaks (Figure 4.5 a), for Pd three sets were necessary, even for a freshly prepared sample (Figure 4.5 b). Pd forms a native oxide layer as

soon as it is exposed to air. In addition to the oxide, the presence of satellite features makes the third set of peaks necessary [110]. Better fitting results can be obtained for Au when recording the spectra over a broader energy range, however, I realized this too late for the samples presented here. The use of asymmetric peaks was necessary both for metallic Au and Pd, which introduces inaccuracies for the quantification due to the nature of the fitted function [111]. For the two alloy compositions, fitted spectra from before and after electrochemical measurements are shown in Figure 4.5, second and third row, respectively. The peak positions of one of the fitted doublet peaks ( $4d^{3/2}$  for Au,  $3d^{3/2}$  for Pd,  $PdO_x$  and  $PdO_{x(sat)}$ ) and the calculated concentrations of the components are given in Table 4.2. The concentrations were calculated using the relative sensitivity factors built into the analysis software (Casa-XPS).

The Pd feature at highest binding energies was assigned to being a  $PdO_x$  satellite rather than  $PdO_2$  due to the high binding energies compared to the other Pd peaks. The peak positions resemble the reference data reasonably well. The determined concentrations agree with those derived from XRD measurements within experimental inaccuracy, and corroborate that the composition can easily be tuned by changing the metal ion concentration in the deposition solution. Interestingly the Pd concentration for both the Au rich and the Pd rich sample increased in the course of the electrochemical experiments. Also, the rather harsh electrochemical treatment the samples were exposed to leads to an increase in Pd oxidation state even after transport through air. While the latter was to be anticipated, the surface enrichment with Pd is a rather surprising result. As Pd is the less noble component, preferential dissolution was expected [112]. Nevertheless, it is likely that Pd is pulled out to the surface if exposed to propene or CO during the electrochemical experiments, due to a higher carbon affinity, as has been observed previously [113].

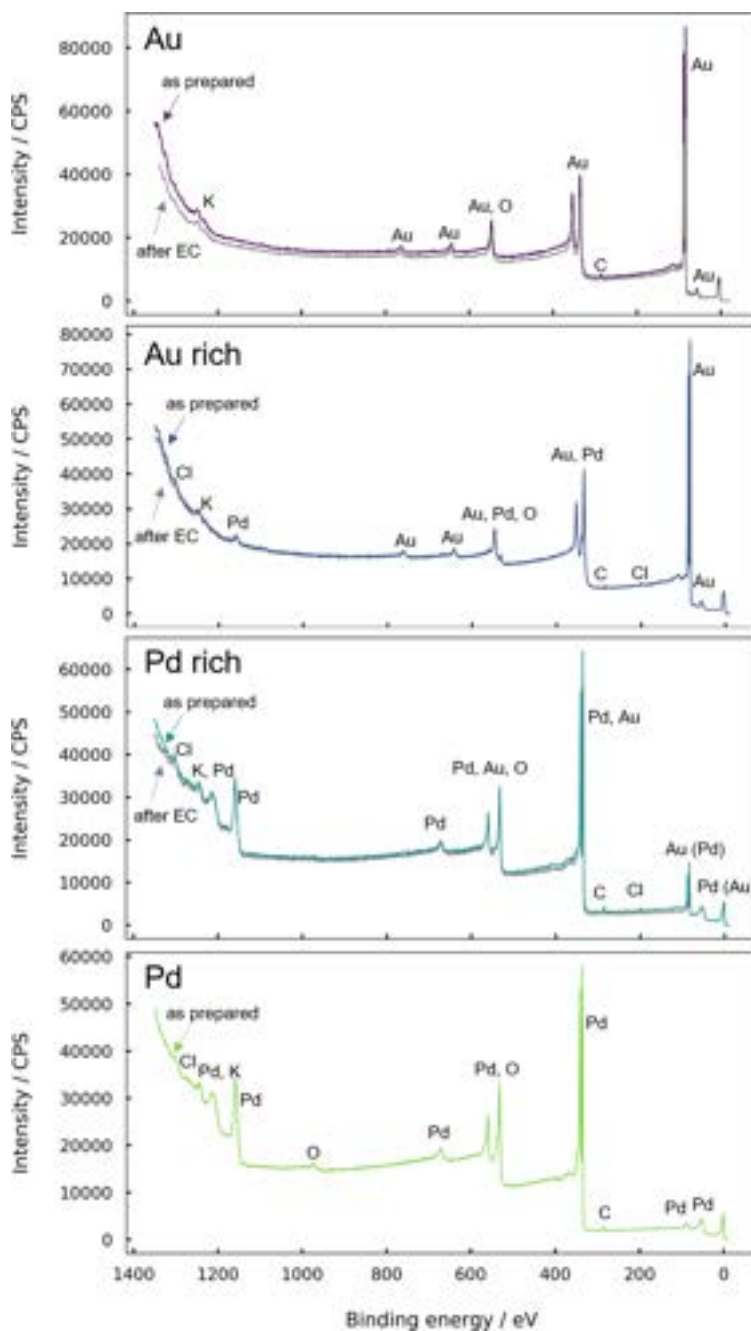


**Figure 4.4** XPS survey scans of Pd, Au and AuPd samples of different composition, as prepared and after experiments in the EC-MS setup. All samples were sputter cleaned with Ar before recording the spectra. Spectra shift was corrected to C 1s at 284.6 eV

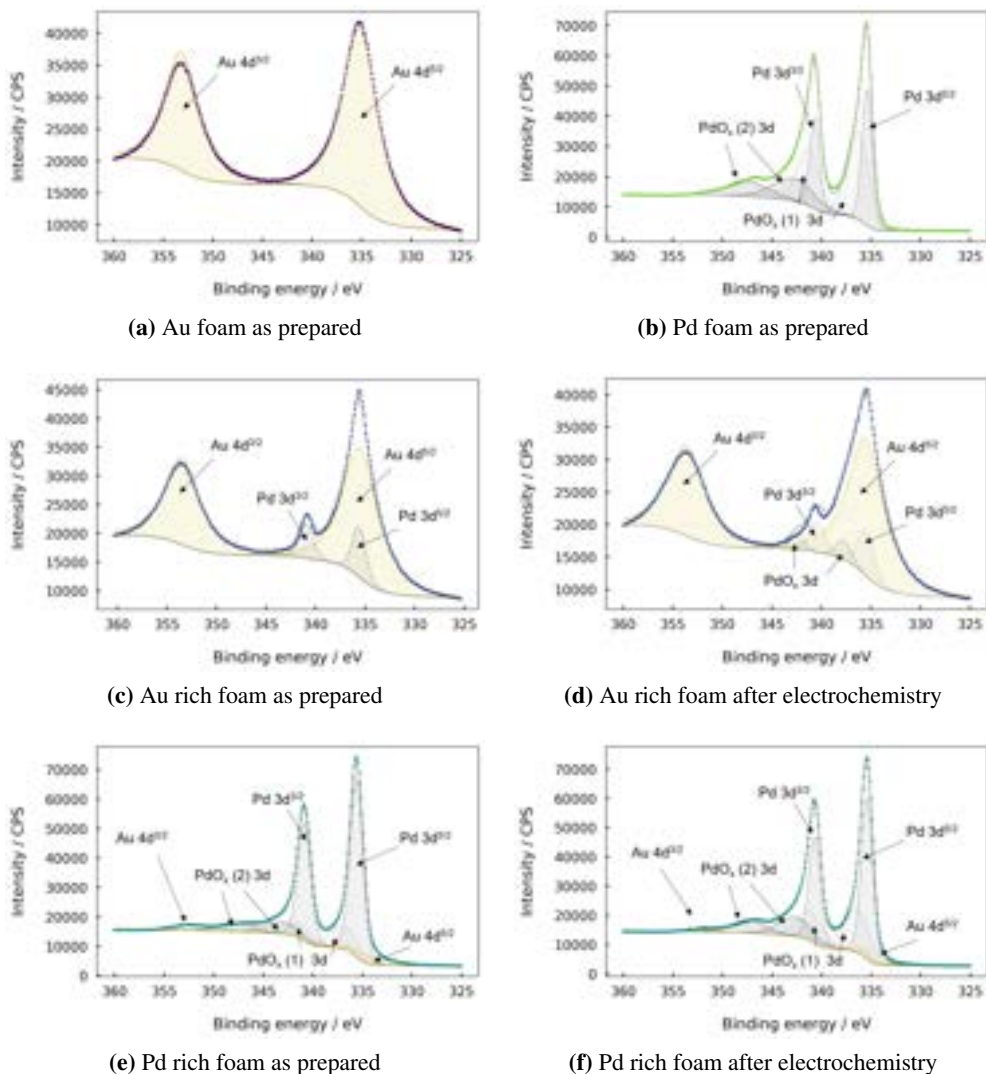


**Figure 4.5** XPS core level scans in the Au 4d/Pd 3d region of Pd, Au and AuPd samples of different composition, as prepared and after experiments in the EC-MS setup. All samples were sputter cleaned with Ar before recording the spectra. Experimental values are shown as circles; dotted lines show the Shirley background, full lines the fits for the respective components. Spectra shift was corrected to C 1s at 284.6 eV.

**Table 4.2** Peak position and concentration of components calculated from the fitted XPS spectra shown in Figure 4.5. The peak position shown corresponds to  $4d^{3/2}$  for Au, and  $3d^{3/2}$  for Pd,  $PdO_x$  and  $PdO_{x(sat)}$ . Spectra shift was corrected to C 1s at 284.6 eV. The literature reference values are taken from the NIST database [114]. The last two columns give the percentage of Au and Pd species, disregarding the contribution from the satellite features. See text for details.

Sample	Au		Pd		$PdO_x$		$PdO_{x(sat)}$		$\Sigma Pd$		$\Sigma Au$	
	pos.	%	pos.	%	pos.	%	pos.	%	pos.	%	pos.	%
Lit. reference	353.2	-	340.3	-	342.4	-	345.8	-	-	-	-	-
Au foam	353.2	100	-	-	-	-	-	-	-	-	100	-
Au rich foam	353.5	85.6	340.9	14.4	-	-	-	-	-	14.4	85.6	-
Au rich foam post EC	353.7	81.1	340.5	13.9	342.5	5.0	-	-	-	18.9	81.1	-
Pd rich foam	352.6	7.2	340.9	64.4	341.6	17.7	347.7	10.7	91.9	8.1	-	-
Pd rich foam post EC	352.0	2.88	340.7	50.5	341.2	29.8	347.4	16.9	96.5	3.5	-	-
Pd foam	-	-	340.7	32.5	341.3	45.5	347.5	22.0	100	-	-	-

#### 4.1.4 Low energy ion scattering (LEIS)

Even more surface-specific information than from XPS can be obtained from LEIS, which is intrinsically highly surface sensitive. LEIS spectra were recorded before and after electrochemistry. Spectra before and after Ar sputtering to remove C, O, and electrolyte residues from the surface are shown in Figure 4.6 left and right column, respectively. The vertical lines show the energy where peaks from the main components and major contaminants were to be expected. The energies were calculated using the LEIS online calculator [115] assuming an ion energy of 950 eV (instead of 1000 eV, which was used) and 135 ° scattering angle. A lower ion energy was chosen for the calculation for better visibility of the peak assignment. Using the correct ion energy, the theoretical lines correspond to the high-energy onset of the peaks rather than the peak maxima, since various losses are not accounted for in the calculation. Before sputtering, the metal signal is reduced due to the presence of C at the surface (broad peak around 150 eV). On the alloy foams, the minor component is only visible after sputter cleaning. While there is no clear difference between before and after electrochemistry for Au rich foam (Figure 4.6 c and d), the Au signal on the Pd rich foam is decreased significantly after electrochemistry. This agrees with the data from XPS presented above. The S and Cl present originate from the deposition solution ( $\text{SO}_4^{2-}$  based), or the electrolyte. Quantitative analysis was not carried out, due to the difficulty of determining sensitivity factors for the different components. In addition, it is not clear to what extent the high roughness of the samples affects the accuracy of the measurements. Nevertheless, these spectra show that both Pd and Au are present at the surface of the alloy samples before and after electrochemistry, and that all samples are free of major impurities. A quantitative investigation of a possible gradient in composition, for example with angle-resolved XPS, could provide further insights [116]. However, I refrained from doing such an analysis as high inaccuracy due to the surface roughness can be expected. Moreover, as will be discussed in detail in Chapter 6, the distribution of atoms on the surface is more interesting than the average composition in terms of the catalytic properties. None of the methods used in the present chapter is suitable to obtain such information.

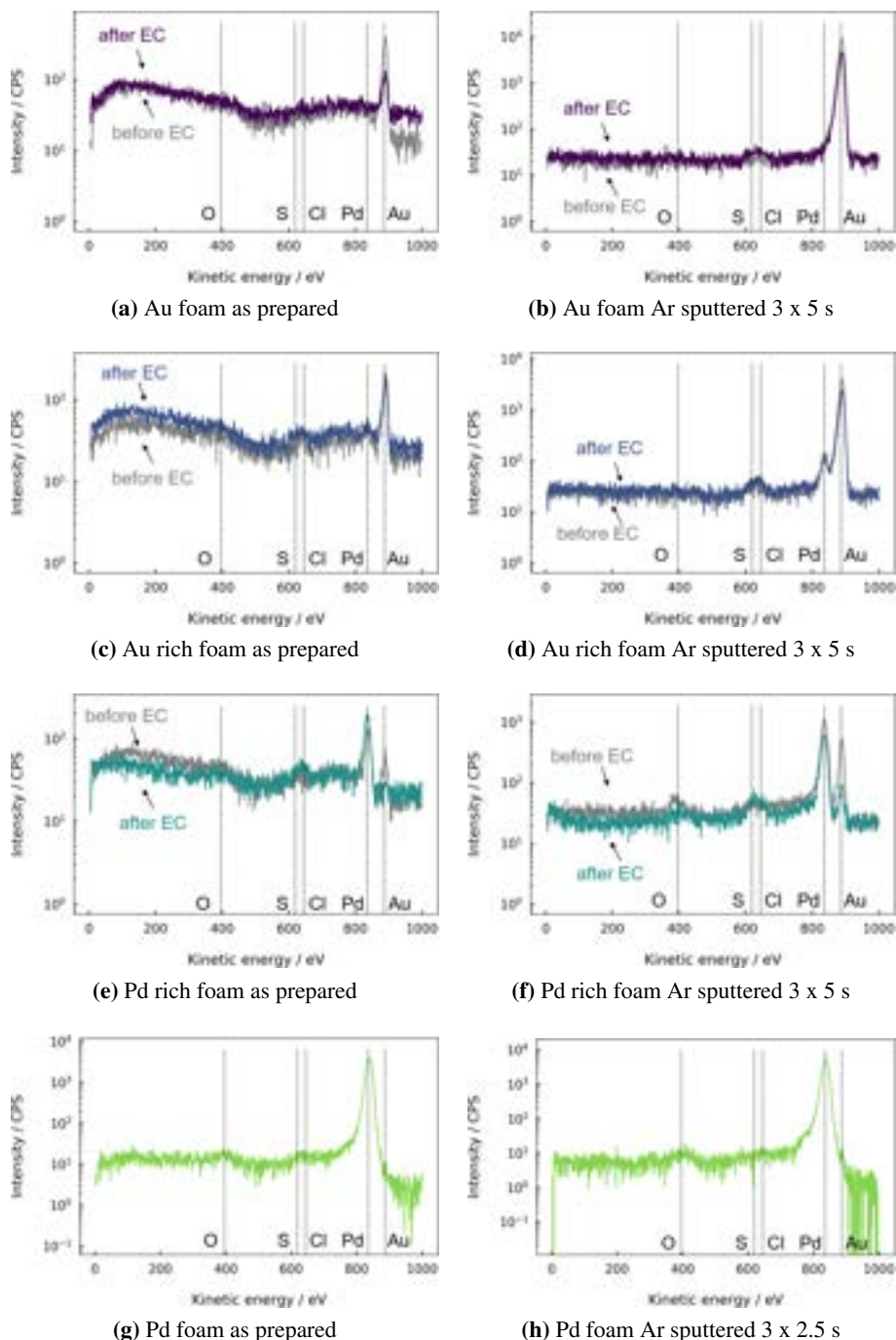


**Figure 4.6** LEIS on Pd, Au and AuPd foams, before and after EC (except Pd), as prepared (left) and Ar sputtered (right). The sputtering time was different for the Pd sample, as a different filament was used resulting in an increased sputter yield at the same Ar pressure.

## 4.2 Electrodes for SEIRAS experiments

### 4.2.1 Scanning electron microscopy (SEM)

As mentioned in Section 3.5, SEIRAS requires a particular, rough morphology, which can be obtained for example by chemical deposition of nanoparticles. While the only way to reliably verify SEIRAS activity is to measure IR spectra on a film *in-situ* after adsorption of a suitable probe molecule such as CO, SEM images can give an indication whether a suitable morphology has been obtained. SEM images before and after electrochemical measurements on a Pd film for SEIRAS are shown in Figure 4.7. The as-prepared film exhibits homogeneously sized nanoparticles (ca. 100-150 nm in diameter) which are uniformly distributed over the surface. The observed particle coalescence is required to obtain sufficient conductivity across the sample, as the Si substrate is not conductive. After a series of experiments involving potential cycling, the morphology changes as the particles gradually merge, see Figure 4.7 b, likely due to dissolution and re-deposition effects. Instabilities of the sample were also observed in the IR spectra in form of increasing signals from water over time (see Chapter 7). Unfortunately, also the SEIRA activity of the film is affected, which can be seen in changing intensity of repeated CO strips on the same sample, which impedes reliable quantitative analysis of the intensities.

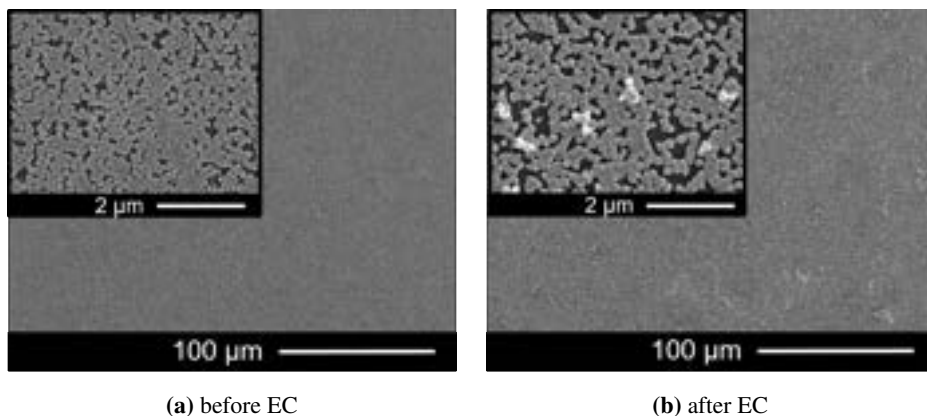


**Figure 4.7** SEM images of Pd SEIRAS film before and after electrochemical experiments. Images acquired by Michael Boyd.

### 4.2.2 X-ray photoelectron spectroscopy (XPS)

As SEIRAS experiments were only carried out on Pd electrodes, XPS was used primarily to confirm that the film was clean and free of impurities which could affect the catalytic properties. Figure 4.8 shows a survey scan on a Pd SEIRAS film: Only features from Pd, O and C are present. No Si is visible in the survey scan, despite visibility of the substrate in SEM, however, traces of Si can be seen in a detail scan (not shown).

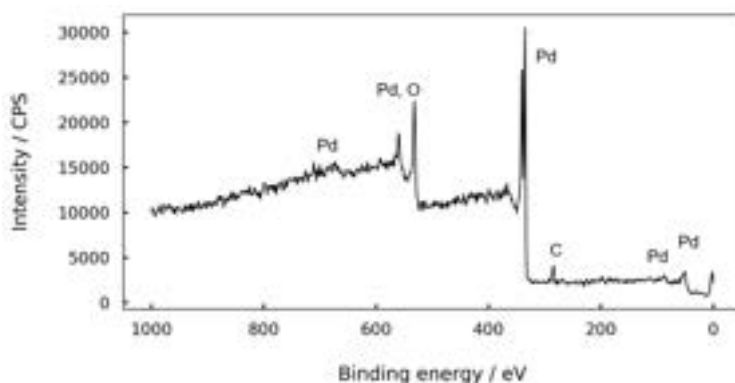


**Figure 4.8** XPS survey scan of Pd SEIRAS film (as prepared). Spectrum acquired by Michael Boyd.

## 4.3 Summary

In this chapter, I presented the *ex-situ* analysis of Au-Pd electrodes using complementary methods. The morphology determined by SEM differs for the different compositions, but shows high surface area structures for all samples. XRD indicates the formation of homogeneous alloys with a bulk composition similar to the metal ratio in the deposition solution, which is confirmed with XPS analysis. LEIS spectra confirm the presence of both Au and Pd on the very surface of the alloy samples, before and after electrochemistry.

Characterization of SEIRAS samples shows the presence of Pd nanoparticles, ca. 100-150 nm in size. The morphology changes during electrochemical testing, which is also evident from the IR data shown in Chapter 7.



## Chapter 5

# Electrochemical oxidation of propene on Pd

In this chapter, I discuss the results of experiments focused on the electrochemical bulk oxidation of propene on Pd. Most of the data presented here was included in Paper I in the main text and supporting information (see the appendices). All the results shown here are from experiments that I conducted myself, however, most interpretation of results was done together with the co-authors of the article. All potentials in this chapter are reported *versus* RHE.

The primary goals of the experiments in the present chapter were the following:

- To develop a set of analytical methods to be able to reliably quantify propene oxidation products with high sensitivity.
- To determine which propene oxidation products are formed at Pd electrodes.
- To determine the effect of varying the experimental conditions – primarily the applied potential – on the product distribution.
- To relate the findings to previous literature studying the same system (in particular [52, 53])

## 5.1 Considerations for reliable product quantification

The first goal stated above, to develop reliable analytical methods, is crucial to meet the other three goals. The importance of sensitive analytical techniques has recently been highlighted in the field of electrochemical reduction of CO<sub>2</sub>, described for example in references [117–119]. There are several important aspects to be considered: First, that the ratio between electrode area and electrolyte volume should be as high as possible. I addressed this by using high surface area electrodes prepared with the hydrogen bubble template method to increase the surface-to-electrolyte ratio (for *ex-situ* characterization see Chapter 4). Secondly, very sensitive analytical methods are required for the product analysis of trace amounts. A third aspect is to consider reactions in the electrolyte that might overshadow a correct interpretation of the results [118, 120, 121]. To this end, I tested product stability over time and reactions with metal ions dissolved from the catalyst. (see Section 5.4.1). For the experiments shown in this chapter, different analytical methods were used for different compounds, to compromise in the most effective way between sensitivity and waiting time until the analysis could be carried out: Acetone and propanal concentrations were determined using HS-GC, acrolein and acrylic acid were determined using HPLC, and NMR was used for allyl alcohol, propylene glycol and isopropanol. For experimental details see Chapter 3. Later the HPLC method was expanded to allyl alcohol and the HS-GC method modified to be able to quantify isopropanol at lower concentrations. These newer calibrations were used for the experiments at pH 3.

A detailed description of the development of analytical tools is out of the scope of this thesis. Calibration curves for all the compounds are shown in the Supporting Material of Paper I, Appendix A.

## 5.2 Electrochemical performance

CVs on high surface area Pd recorded in Ar and propene saturated electrolyte (0.1 M HClO<sub>4</sub>) are shown in Figure 5.1. In Ar, the voltammogram agrees well with literature data: Pd oxidation onset is at ca. 0.65 V. Two oxidation waves peaking at ca. 0.8 and 1.1 V can be distinguished, which suggests the presence of a range of surface facets

[122–125]. In the presence of propene, the primary surface oxidation is inhibited; the onset of oxidation in the anodic sweep is significantly increased to almost 0.9 V. The peak at 1.1 V is more pronounced than without propene. The oxide reduction feature at ca. 0.7 V in the cathodic part of the cycle is slightly smaller in the presence of propene. For this reason we interpret the additional oxidation current in propene saturated electrolyte as originating from the electrochemical oxidation of propene.

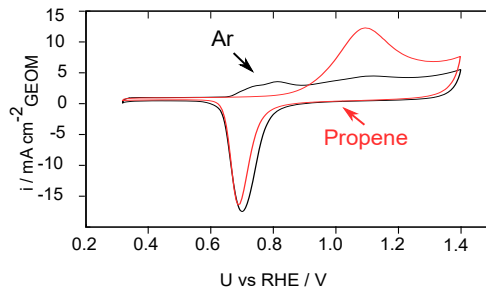
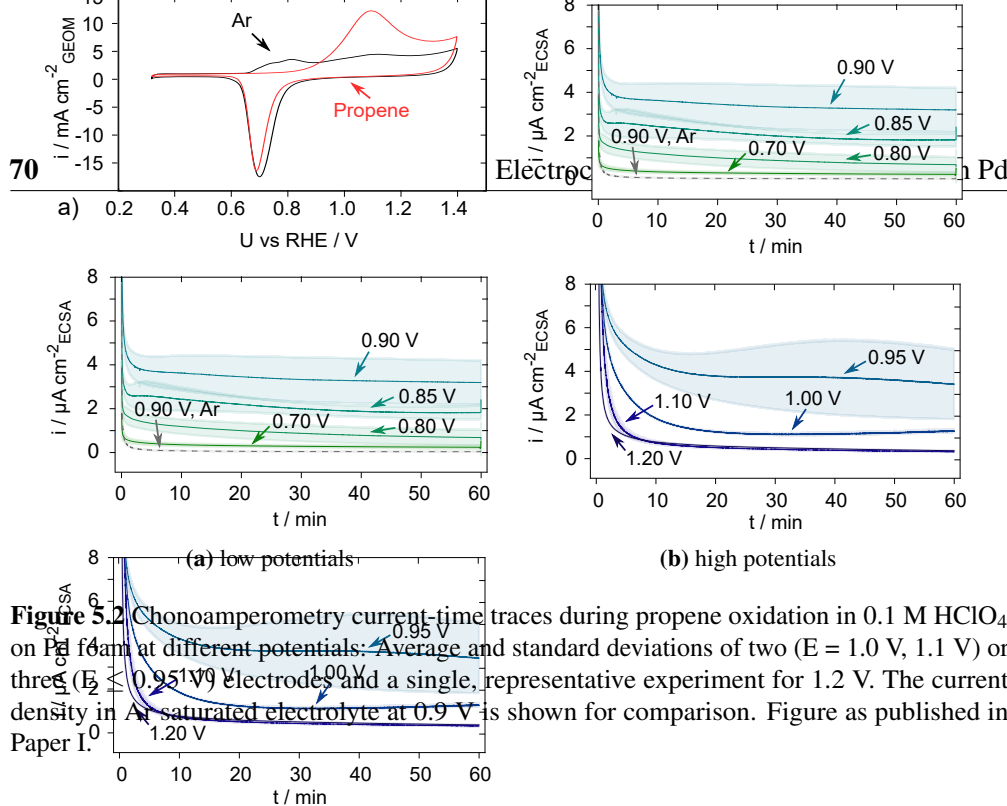


**Figure 5.1** Cyclic voltammograms in Ar and propene saturated 0.1 M  $\text{HClO}_4$  between 0.3 and 1.4 V, scan rate 50 mV/s. Figure as published in Paper I.

The CVs in Figure 5.1 suggest electrochemical activity of Pd for propene oxidation in the range between 0.7 and 1.2 V, which agrees with results from the literature [52, 53]. To study the reaction products, steady state electrolysis experiments were conducted: After purging with propene at a potential where no reaction was observed (at 0.4 V), the potential was stepped up to different final potentials in the range where propene oxidation was expected, and products were accumulated over 1 h.

The current-time traces for these experiments are shown in Figure 5.2. The current density was normalized to electrochemical surface area as described in Section 3.3. Generally, there is a large initial drop and steady state current densities are low and indicate a low reaction rate, compared to, for example, allyl alcohol oxidation [126]. There is a maximum in steady state current densities between 0.90 and 0.95 V; at the same potentials, the experimental uncertainty is the highest. Possible causes of this behavior and implications are discussed in the following sections.



### 5.3 Product analysis

Figure 5.3 shows the faradaic efficiency and the partial current density (subfigures a-c, and d-f, respectively) for seven different reaction products. They are grouped according to concentration and desirability: the top panels show the main product acrolein, the middle panels show the "desired" secondary products allyl alcohol, acrylic acid and propylene glycol, and the bottom panel the "undesired" products  $\text{CO}_2$ , dissolved Pd and acetone. Acetone is considered "undesired" because it is not a direct electrocatalytic product (as will be shown below). In addition to these substances, also isopropanol and propanal were detected. The prior is a product of the acid catalysed hydrolysis of propene. The concentrations of the latter were so low that no differences could be measured between the different conditions (see supporting information of Paper I, Appendix A). For the other seven products there is a clear dependence of reaction rates on the potential. The highest partial current densities for all products except propylene glycol were measured in the same potential range where also the total current density was the highest: allyl alcohol current density peaks at  $0.85 \text{ V}$ , acrolein and acrylic acid at  $0.9 \text{ V}$ . No propylene glycol could be detected at potentials below  $0.95 \text{ V}$ . Meanwhile, going to higher potentials, the partial current density, as well as the faradaic efficiency, towards this product increase with potential, reaching the highest values

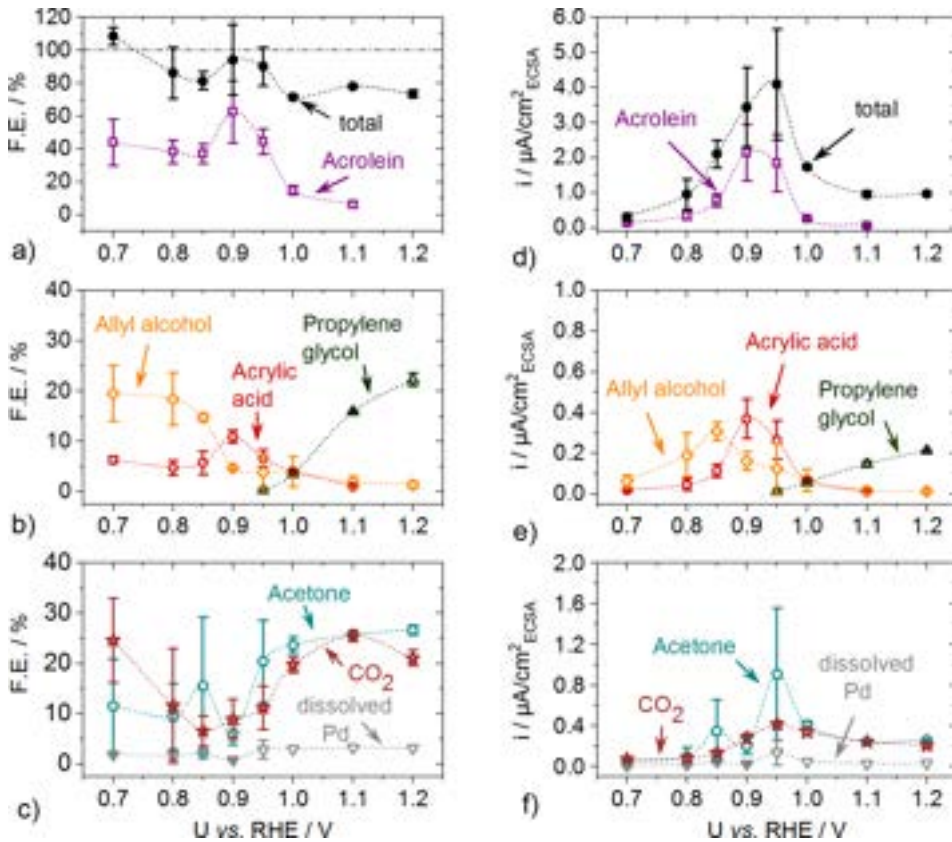


**Figure 5.3** Faradaic efficiency (left) and partial current density (right) for propene oxidation products from CAs at different potentials in 0.1 M HClO<sub>4</sub> as shown in Figure 5.2. The products were grouped according to concentration and desirability (see text). Different y-scales were used for better readability. Figure as published in Paper I.

at the highest potential tested: 1.2 V. In contrast to the other three products of major interest, for the formation of propylene glycol the double bond is oxidized, and not the allylic carbon. This indicates a change of the reaction mechanism when increasing the potential. Propylene glycol has, to the best of my knowledge, only been reported as a product of propene electrooxidation in alkaline conditions on catalysts such as Ag and stainless steel [42–44].

There are several possible causes for this change of mechanism: (1) the reaction simply requires a larger driving force (the reversible potential is higher than for the allylic oxidation products, see Figure 2.5), (2) the reaction is catalyzed by Pd oxide

rather than Pd, or (3) there are other, non-straightforward reasons why the coordination geometry to the surface depends on the potential. While (1) and (2) likely play a role, we found strong evidence why reason (3) is important, which will be the subject of Chapter 6.

To the best of my knowledge, this is the first time allyl alcohol is described as an intermediate product of electrochemical propene oxidation. The faradaic efficiency towards this alcohol is significant at low potentials (up to 0.8 V) while it decreases at the same time as the FE for acrolein and acrylic acid increases. This is a strong indication that allyl alcohol is the first step in the oxidation of the allylic carbon. I further investigated the role of this intermediate by directly oxidizing allyl alcohol; these results are presented in Chapter 7.2.

The partial current densities and faradaic efficiency for undesired products  $\text{CO}_2$  and dissolved Pd exhibit an expected dependence on the potential: At higher potentials, more propene is fully oxidized to  $\text{CO}_2$ . There is a maximum of partial current density at 1.0 V. At higher potentials, the surface is expected to be partially oxidized (see discussion below). Even though there is no direct evidence, competition between propene and oxygen for surface sites at this potential could rationalize lower current density at higher potentials. The relation between Pd dissolution and acetone formation are discussed in detail below.

Despite great efforts to ensure accurate product quantification and reproducible conditions for the electrochemical experiments, there are high standard deviation in product faradaic efficiency and partial current density. For lower potentials, this is attributed to lack of significant quantities of products (see Appendix A), while at intermediate potentials, we hypothesize that the error is due to the instability of the electrode at these potentials, which resulted in unaccountable changes in electrode surface area.

## 5.4 Faradaic and non-faradaic side reactions

In order to draw reliable conclusions about a reaction mechanism from the chronoamperometry data presented above, it is important to understand all processes happening at the electrode and in the electrolyte. That non-faradaic reactions can play an important

role in electrochemical processes has been shown for example for CO<sub>2</sub> reduction [120, 127], or for the oxidative formation of dimethyl carbonate using Cu [121].

I measured small amounts of isopropanol in all samples at different concentrations (ca 1% of liquid products at 0.9 V), but without a clear dependence in the potential. The acid catalyzed hydrolysis of propene is, in fact, well known [128]. The varying concentration is likely related to insufficient removal of propene in the solution after the electrolysis. As the concentration of isopropanol was determined by NMR, the times between reaction and product determination varied for the different samples, leading to a range of reaction times. When trying to oxidize isopropanol under similar conditions, the current was lower than in the presence of propene and no oxidation products were found in the solution (data not shown). The reaction is therefore considered not significant. Even though the oxidation of isopropanol is well known to occur on Pt electrodes in acidic medium [129], the rates are low on Pd [130].

Two other side reactions, the non-faradaic formation of acetone and faradaic oxidation of Pd, are discussed in the following.

#### 5.4.1 Pd dissolution and homogeneous catalysis

As mentioned above, acetone is counted as a non-desired product because it is not produced *via* a direct electrocatalytic process.

Previous literature has described acetone being formed by a homogeneous reaction of Pd<sup>2+</sup> with propene [52, 53]. This spontaneous reaction proceeds through a Wacker-type mechanism ( $\Delta G = -167$  kJ/mol) [53]:



The partial current density of acetone formation shown in Figure 5.3 f follows the same trend as the release of Pd<sup>2+</sup> ions to the solution. To further corroborate this hypothesis I tested the formation of propene reaction products by purging propene through an electrolyte solution (0.1 M HClO<sub>4</sub>) containing different amounts of Pd<sup>2+</sup> ions. The concentrations determined after 1 h of reaction time are shown in Figure 5.4.

The acetone concentration increases linearly with the Pd<sup>2+</sup> concentration. The slope is close to 1 indicating there is a full conversion within the reaction time. At a Pd<sup>2+</sup> concentration of 100 mM and higher, Pd nanoparticles formed, as evident

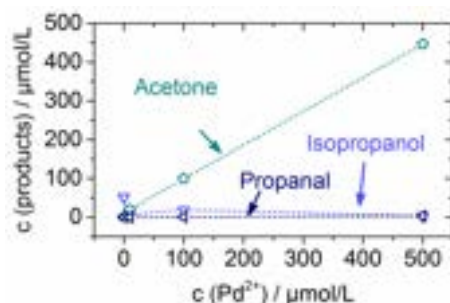


**Figure 5.4** Reaction products of the homogeneous reaction of propene with different amounts of  $\text{Pd}^{2+}$  ions in 0.1 M  $\text{HClO}_4$ . Figure as published in Paper I

from discoloration of the solution and formation of a precipitate. Since some  $\text{Pd}^{2+}$  was found in the electrolyte after chronoamperometry at all potentials, it is a fair assumption that the majority of acetone from the electrochemical experiments is produced by the Wacker mechanism. Two other products were also detected in the solution: Isopropanol (from acid catalysed hydrolysis of propene, as mentioned before) and propanal, which is a known minor side product of Wacker oxidation of propene. [131]

Otsuka et. al [53] claim that, in their system, Pd reduced in the Wacker process is re-oxidized at the electrode, closing the catalytic cycle. I did not observe such reoxidation when applying a potential positive of the reversible potential of Pd oxidation to a glassy carbon electrode in the presence of  $\text{Pd}^{2+}$  ions in solution (see Appendix A). Therefore, I consider acetone an undesired product in the context of propene oxidation of Pd.

### 5.4.2 Surface oxidation

From the current density-time traces shown in Figure 5.2 a difference in the shape between the traces at potentials below 0.90 V vs. RHE is evident. A different view on the same data is shown in Figure 5.5: The current density and the charge density (a and b, respectively) after 1, 3, 10 and 55 min of reaction time are plotted *versus* the potential. Here, the differences in current development as a function of time are even more evident. At lower potentials, the major initial current density drop occurs in the first minute, since the change in current density between minute 1 and minute 55 is small. Starting at 0.95 V and above, there is a significant drop in the first 10 min until a quasi-steady state current density is reached. At 0.90 to 0.95 V, there is a maximum in current density

both after 1 min and at steady state, incidentally in the same potential region where the transition between fast and slow initial oxidation is observed. This indicates that at strongly oxidizing potentials there is an initially dominant reaction which affects the surface in such a way that the high current densities at intermediate potentials can not be maintained despite the higher driving force at these higher potentials. At the same time this reaction does not play a role at potentials below 0.9 V.

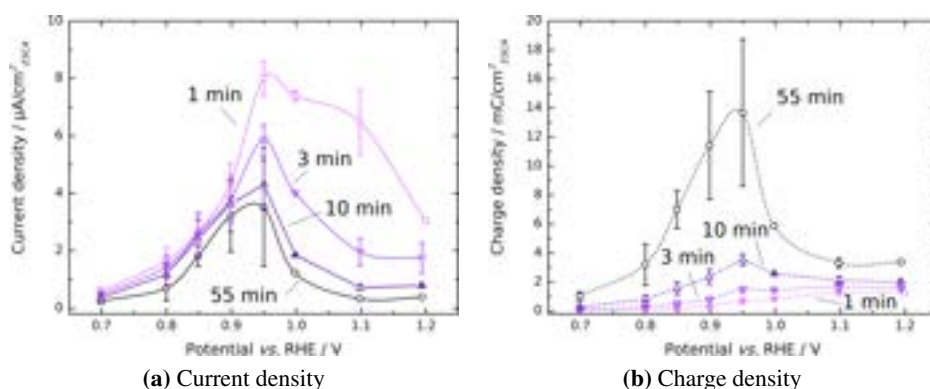


**Figure 5.5** Chronoamperometry data from Figure 5.2 in a different representation: (a) current density and (b) charge density (accumulated charge per surface area) after 1, 3, 10 and 55 min of reaction time plotted *versus* the potential. As in Figure 5.2, average and standard deviation of 2-3 measurements is shown. Figure from the Supplementary Material of Paper I.

The equilibrium potential for the oxidation of Pd at pH 1 is 0.91 V *vs.* RHE [132]:



The formation of a surface oxide at these higher potentials is therefore likely. The total faradaic efficiency (shown in Figure 5.3 a) is significantly below 100% for all experiments at potentials above 0.95 V. Since the current density at these potentials is small, I estimated whether Pd oxidation could account for the missing charge. To this end, I carried out Pd oxidation experiments under similar conditions as the propene oxidation experiments, except that propene was replaced by Ar. At the end of the chronoamperometry, I determined the amount of Pd oxide at the surface by reducing the oxide in a linear sweep at a low scan rate down to 0.4 V. The reduction charge per surface area as a function of oxidation potential is shown in Figure 5.6 a. For

the electrodes that were used in the propene oxidation experiments, I estimated the theoretical charge necessary for the formation of one monolayer PdO. Assuming an atom density of  $1.26 \cdot 10^{15}$  atoms/cm<sup>2</sup> (corresponding to the average over low index facets), a charge of 404  $\mu\text{C}$  is required to oxidize 1 cm<sup>2</sup> Pd to PdO. The calculated charge for the formation of 1 ML PdO on the different electrodes, based on their experimental ECSA, is shown in Figure 5.6 b together with the total, measured charge transferred in the propene oxidation experiments on the same electrodes.

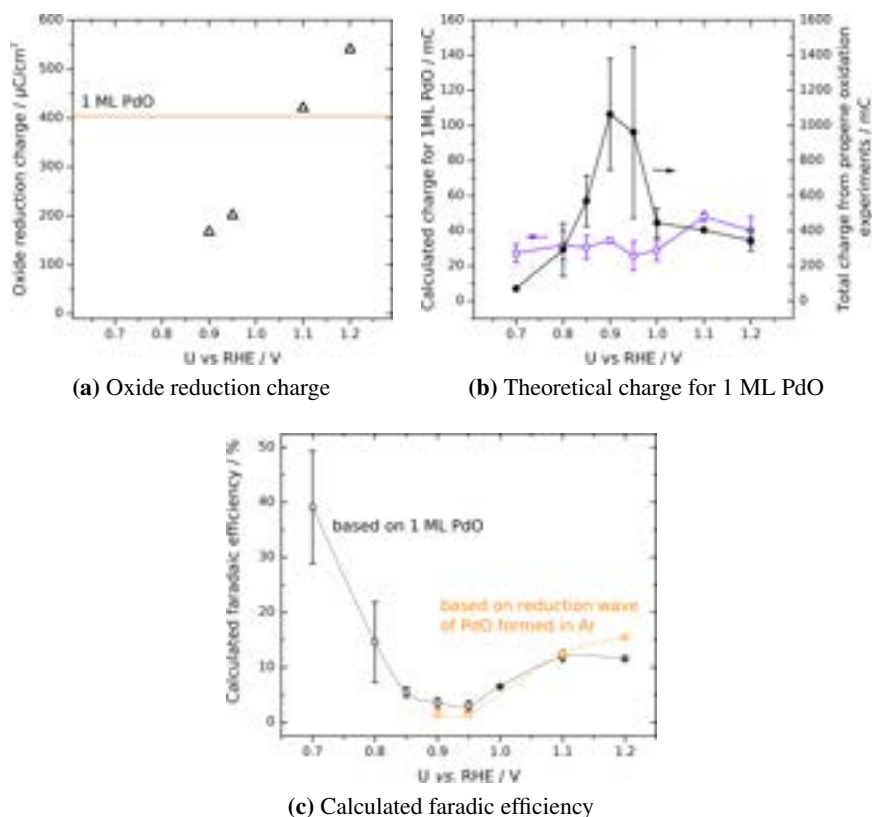


**Figure 5.6** Estimations of formation of surface oxides: a) Oxide reduction charge after oxidation of Pd in 0.1 M HClO<sub>4</sub> for 1 h at different potentials. b) Calculated charge for the formation of 1 ML PdO for the electrodes used in propene oxidation experiments based on the surface area. c) Faradaic efficiency for the formation of PdO as determined experimentally (data from panel a) and for formation of 1 ML PdO (panel b). For details see text. Figure from the Supplementary Material of Paper I.

From these data, I calculated two theoretical values for the faradaic efficiency for Pd oxidation: (1) the FE for the formation of 1 ML of PdO, and (2) the FE assuming the same amount of Pd oxide formation in the presence of propene as in Ar. Here I used the oxide reduction charge from the Pd oxidation experiments (Figure 5.6 a) and projected this on the surface area measured on the actual electrodes in the same way as the calculations for 1 ML. The faradaic efficiencies are co-plotted in Figure 5.6 c. Due to the low charge transferred at low potentials, formation of 1 ML PdO would correspond to very high FE. However, at these potentials propene oxidation products account for most of the charge and Pd oxidation is unlikely, meaning that below 0.85 V *vs.* RHE, the PdO faradaic efficiency is definitely overestimated. At potentials above 0.9 V, on the other hand, the charge for the formation of 1 ML oxide fits well with the actual oxide formation in Ar. Between 1.0 and 1.2 V, where only 80% of faradaic efficiency are accounted for, Pd oxidation could contribute an additional 10-15%. Also, the formation of a ML of oxide can be an explanation for the differences in the current drop in the CA experiments at low and high potentials: At higher potentials, initially there is a higher current, due to formation of an oxide layer. Later, the oxide layer prevents propene oxidation, resulting in a lower current than at intermediate potentials despite the larger driving force. At low potential, Pd is not oxidized, therefore the steady state current density is reached faster. This analysis is in accordance with detailed studies of Pd oxidation in acid, where dissolution of Pd was observed between 0.8 and 0.95 V [133, 134], while above 1.0 V growth of an oxide layer is described [134]. However, a charge of more than 1 mC/cm<sup>2</sup> is transferred in the first minute at 1.1 and 1.2 V which corresponds to more than 2 ML of PdO, while in the Pd oxidation experiment only a bit more than 1 ML of PdO were formed. The CVs shown in Figure 5.1 suggest that Pd oxidation is inhibited in the presence of propene, making it unlikely that more oxide is formed in propene than in Ar. It is therefore likely that there is another oxidative process occurring at the same time as the Pd oxidation. In Chapter 6, I will discuss the role of surface adsorbates in steering the reaction mechanism. Initial stripping of organic adsorbates of the surface could account for the missing initial charge.

### 5.4.3 Product stability

During the calibration of the analytical methods for product quantification, I observed significant decrease in acrolein concentration over time using HPLC. In the NMR spectra, additional peaks showed up and increased concurrently with acrolein degradation. Using advanced NMR analysis, Kasper Enemark-Rasmussen was able to assign these additional peaks to 3-hydroxypropanal and propane-1,3,3-triol which are presumably formed through acid catalyzed hydrolysis of the double bond. The detailed analysis is shown in the supporting information of Paper I. Product degradation despite best efforts to carry out the analysis directly after reaction and related underestimation of the product concentrations might contribute to the low faradaic efficiency in some of the experiments.

## 5.5 Changing the pH to improve stability

According to the Pourbaix diagram of Pd, the dissolution of Pd at low pH depends on the pH beyond the pH dependence of the SHE scale that is accounted for by using the RHE scale [132]. Pd dissolution, and the related acetone formation, should thus be decreased at less acidic pH. Moreover, acid catalyzed formation of isopropanol and degradation of acrolein should be reduced at higher pH, as well as the related decrease in surface area over the course of the experiment.

Therefore I carried out a set of experiments at pH 3 using 0.001 M HClO<sub>4</sub> with 0.099 M NaClO<sub>4</sub> to provide sufficient electrical conductivity, at 0.7, 0.9 and 1.1 V, to probe the three different regimes seen at pH 1.

The current-time traces of these CA experiments are shown in Figure 5.7 a. At all three potentials, the current density is the same as observed at pH 1 at the respective potential, suggesting that there are no fundamental differences.

In Figure 5.7, the faradaic efficiencies for different propene oxidation products at pH 3 are shown. The FE towards acrolein, and the other products of allylic oxidation is the highest at 0.9 V, while at 1.1 V there is a high selectivity for acetone and CO<sub>2</sub>. Like the current density, also the faradaic efficiencies are very similar to those at pH 1. While the FE for Pd ions in solution was similar, the FE towards acetone at low and intermediate potential was lower than at pH 1. At 1.1 V, however, it was very similar,

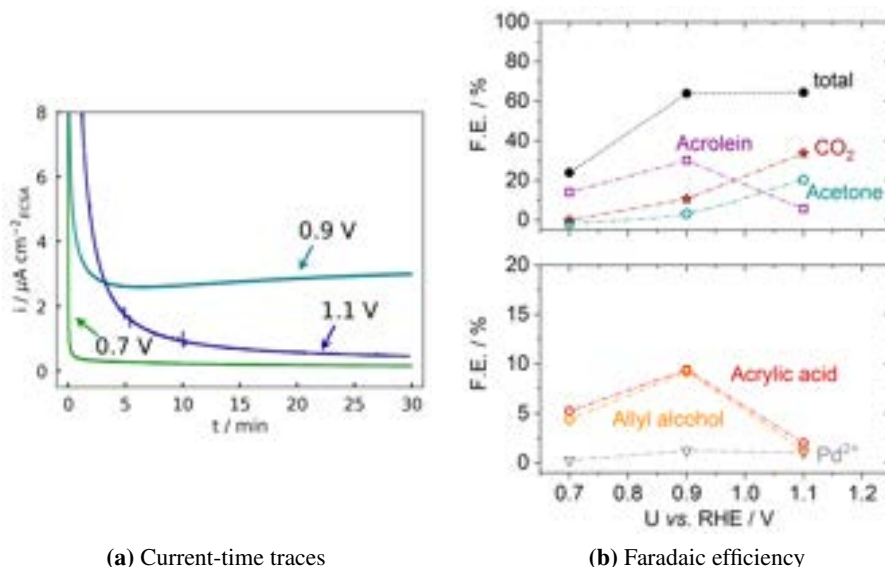


**Figure 5.7** Propene oxidation on Pd foam in 0.001 M  $\text{HClO}_4$  with 0.099 M  $\text{NaClO}_4$ , pH 3. Note the different y-scale on the plots in (b) for better readability.

which could indicate that an electrocatalytic mechanism might play a role at these potentials after all.

At neither of the three potentials, 100% faradaic efficiency could be achieved. At 0.7 V vs. RHE, despite the low total FE, the missing charge corresponds to less than 5  $\mu\text{M}$  products (assuming a 2 electron process). As the concentrations are very low, the missing charge is probably due to quantification inaccuracy. Propylene glycol was not quantified for these experiments, as NMR analysis was not available. Assuming similar amounts of propylene glycol and surface oxidation, as at pH 1, 100% FE can be reached for 1.1 eV. At 0.9 V the largest absolute amount of charge is missing, which can only partially be explained with the same arguments as at the other potentials. Nevertheless, these observations are an important prerequisite for the *in-situ* experiments shown in Chapter 6, which were carried out at pH 3 to prevent catalyst dissolution as much as possible. Especially during potential cycling, a significant stabilization of the catalyst was observed at higher pH.

## 5.6 Summary

In this chapter, I presented propene oxidation experiments on high surface area Pd electrodes at different potentials.

- In total six different partial oxidation products were identified: Allyl alcohol, acrolein and acrylic acid; propylene glycol, acetone and propanal. In addition to these, Pd<sup>2+</sup> ions, the full oxidation product CO<sub>2</sub>, and isopropanol, where the latter is formed in solution by acid catalyst hydrolysis of propene. Detailed analysis of the relation between acetone and Pd ions suggests that acetone is not an electrocatalytic product, but is formed in a homogeneous reaction with dissolved Pd.
- Allylic oxidation reaches a maximum in activity and selectivity at ca. 0.9 V vs. RHE. At higher potential propylene glycol is formed with increasing activity, indicating a mechanistic shift towards oxidation of the double bond.
- Two new products for the propene oxidation on Pd could be identified: allyl alcohol and propylene glycol. In contrast to the reports by Otsuka et. al [53], re-oxidation of Pd after formation of Acetone was not observed. On the other hand, the dependence of product distribution on potential was confirmed [52, 53].

## Chapter 6

# Desorption as a probe for surface adsorption sites - an EC-MS study

I showed in Chapter 5 that there is a significant decrease in the propene oxidation current over time. Such a behavior has been described for the oxidation of hydrocarbons and oxygenates on noble metal catalysts, and was usually attributed to the formation of poisoning adsorbate species on the surface [135, 136]. In the current chapter, following questions are addressed:

- Can we find evidence for adsorbates present at the surface under propene oxidation conditions, which poison the surface? If so, what is their effect on activity and selectivity?
- Can the poisoning be reduced, and a higher activity be achieved while maintaining selectivity towards oxidation of the allylic position by using Pd alloys, in particular by isolating single Pd atoms in an inert matrix to promote allylic coordination?

The first question originated directly from my observations from Chapter 5. It led to a series of experiments using EC-MS which was initiated by Soren Scott. These experiments on Pd were carried out and analyzed by Soren and constitute a main part of Paper I. We developed a hypothesis about the reaction mechanism in close collaboration with Luca Silvioli, who was concurrently performing DFT calculations on the same

system. Our experimental results were used to refine his model, while we used the results from the model to devise experimental procedures. While showing the DFT results is out of the scope of this thesis, I will refer to them where we drew significant insights from them. They are all shown in Paper I (Appendix B).

Later, in an attempt to answer the second question, I extended the experimental series by carrying out similar experiments on Au electrodes and AuPd alloys with low amounts of Pd in Au (Au rich, 10% Pd), and low amounts of Au in Pd (Pd rich, 90% Pd). This alloy system was chosen based on an initial suggestion by Luca. Pd binds carbon too strongly, resulting in poisoning. Alloying with Au leads to both electronic and ensemble effects on the catalyst properties [137]: The compressive strain of the surface induced by the larger Au atoms leads to a downshift of the d-band center, and therefore weaker binding to the adsorbates [138]. On the other hand, Pd atoms on Au surfaces have been demonstrated to improve selectivity in the case of reactions where adsorption geometry is crucial, such as  $\text{H}_2\text{O}_2$  formation, vinyl acetate production and selective hydrogenation of butadiene [137, 139, 140]. The experiments on AuPd alloys are part of Paper II.

All samples were prepared using electrodeposition as described in Section 3.1. Non-electrochemical characterization of these electrodes is shown in Chapter 4. As in the previous chapters, all potentials are given *versus* the reversible hydrogen electrode (RHE).

## 6.1 CO stripping

One of the most basic experiments demonstrating the possibilities of EC-MS is performing CO stripping: Desorption of gaseous reaction products is monitored at the same time as the electrochemical current is measured. The procedure is described in Section 3.3. CO stripping was used to electrochemically characterize the different electrode compositions.

CO stripping cycles on the four different sample compositions are shown in Figure 6.1. The CO strip on pure Pd resembles CO strips on Pd as reported in the literature reasonably well (for example ref. [83]): H ad- and absorption is blocked by CO on the surface in the first cycle, and a large oxidative peak is observed starting at ca. 0.9 V vs.

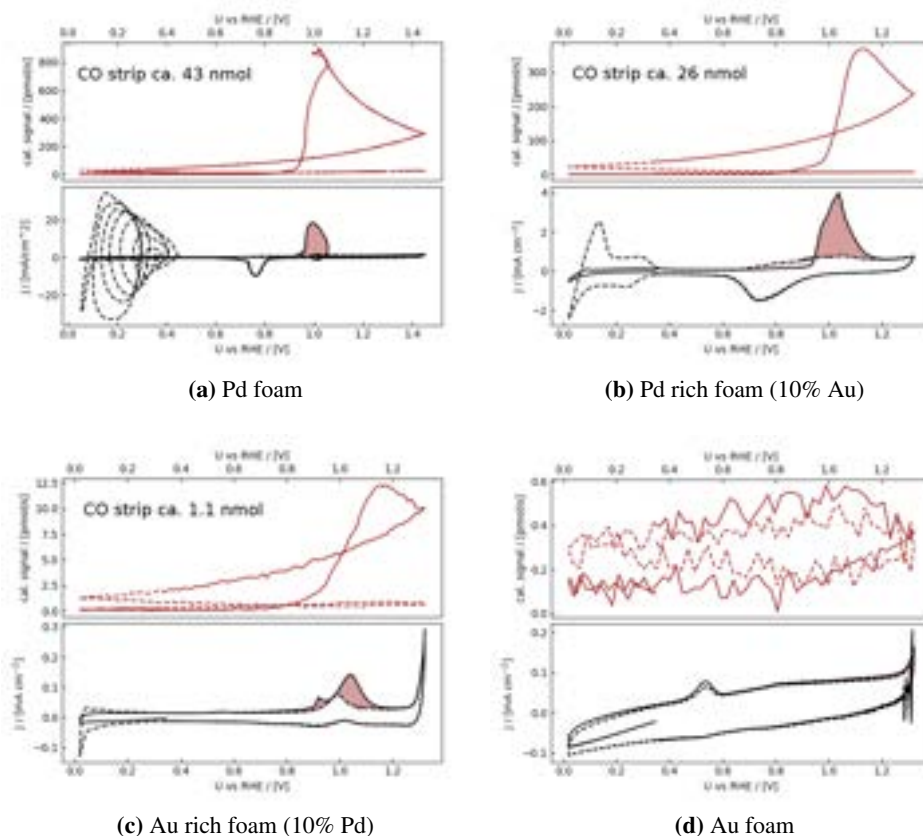


**Figure 6.1** CO strips on four different high surface area electrodes (Pd, Pd rich, Au rich and Au) plotted conventionally as a function of potential. The top panels show the  $m/z$  44 trace from the mass spectrometer, the bottom panels the geometric current density measured at the same time. Full line: 1st cycle after CO adsorption, dashed line: 2nd cycle. All experiments were performed in 1 M  $\text{HClO}_4$ , scan rate of 10 mV/s for Pd, Pd rich and Au rich, 20 mV/s for Au electrodes.

RHE, concurrently with an increase in intensity of the  $m/z$  44 trace corresponding to  $\text{CO}_2$ . The oscillations at the upper end of the CO stripping peak and in the hydrogen absorption region are experimental artifacts (see ref. [107]). The presence of 10% Au does not alter the general behavior significantly compared to pure Pd. However, the lower surface area/number of available Pd sites effectively prevents the oscillations observed on Pd. With 10% Pd in Au, there is a clear reduction of the size of the CO

stripping feature and of hydrogen adsorption. In addition to the features on surfaces richer in Pd, here, Pd oxidation and reduction features are present at ca. 1.0 V *vs.* RHE. The anodic current feature is split in two, but unfortunately this is not resolved in the m/z 44 feature. On Au foam, no CO was found to be adsorbed after purging CO from the electrolyte, as expected [141–143]: No stripping current was observed and there is also no significant increase in m/z 44 signal. The anodic feature around 0.55 V *vs.* RHE is known on Au electrodes and has been attributed to anion induced (by  $\text{ClO}_4^-$ , or  $\text{Cl}^-$  impurities) lifting of surface reconstructions [144–148]. Note that there is also no current related to H adsorption or HER in the tested potential range. The peak position of the CO oxidation current is shifted slightly towards more positive potentials the higher the Au content, as has been reported for well-defined alloy thin-films on Au(111) single crystal electrodes [149].

In general, the m/z 44 traces only decrease slowly in the cathodic part of the first cycle. This is an artifact due to generally slow diffusion of  $\text{CO}_2$  leading to a longer response time [105]. The problem is exacerbated on the high surface area electrodes used in this set of experiments, due to a larger distance between the electrode surface and the membrane.

I use the amount of  $\text{CO}_2$  coming off in the CO strip as a probe for the actual number of Pd surface sites on the alloy samples, as no adsorption of CO on Au is expected. The whole  $\text{CO}_2$  peak was integrated for this purpose, taking into consideration the long diffusion times. The surface area of the Pd sample decreased significantly over the course of the experiments. Therefore, the desorbing  $\text{CO}_2$  was estimated from the Pd surface area, which was in turn calculated from the Pd reduction charge of a blank cycle recorded close to the time of the respective experiment. I reduced the anodic potential limit for the other experiments to minimize the reduction of surface area by dissolution, resulting in better stability.

## 6.2 Propene stripping

We carried out propene stripping experiments in a similar manner as CO stripping: First, propene was adsorbed by introducing the gas while holding the potential constant, then the carrier gas was changed to He and propene was removed from the electrolyte. When

the signal had dropped sufficiently (after 15-20 min) a stripping cycle was performed by first going cathodic to +0.1 V *vs.* RHE and then going anodic to +1.4 V *vs.* RHE. An example of such a stripping cycle as a function of time is shown in Figure 6.2 a. Here the dosing potential was 0.65 V *vs.* RHE.

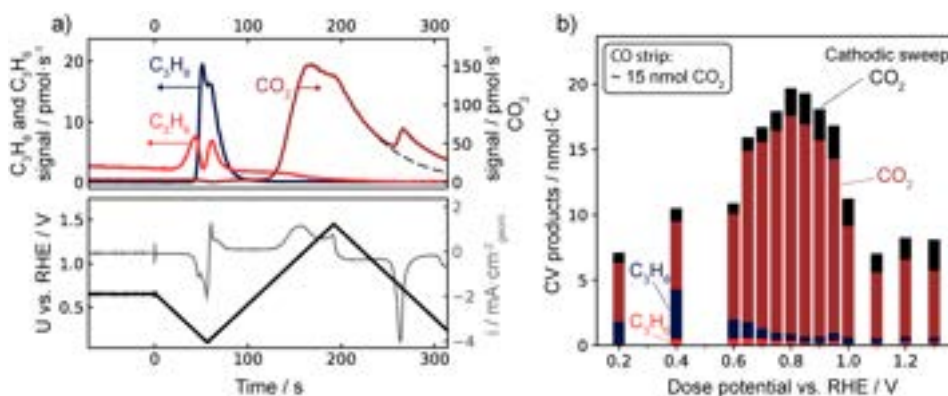


**Figure 6.2** Propene stripping on Pd. a) Propene is dosed at constant potential (here 0.65 V, dosing not shown) and non-adsorbed propene purged out. The potential is scanned first cathodically to 0.1 V, then cycled between 0.1 V and 1.4 V, while desorption of propene ( $C_3H_6$ ), propane ( $C_3H_8$ ) and  $CO_2$  is monitored. Note the different scaling on the left and right y-axes. b) Integrated desorption products observed at different dosing potentials.  $CO_2$  desorbing in the anodic and subsequent cathodic cycle is quantified separately. Figure by Soren Scott, reprinted from Paper I.

A small amount of the adsorbed propene comes off cathodically as propane (reduced) and propene (unaltered). There is a decline in propene desorption with a concurrent peak in propane desorption at the most negative potential. The reason for this behavior is not perfectly clear. The majority of the adsorbates can only be removed by going sufficiently anodic and stripping them off oxidatively in form of  $CO_2$ . Interestingly there are two separate  $CO_2$  maxima in the anodic and in the cathodic sweep, which has been observed before for allyl alcohol oxidation [126, 150]. We further tested how the adsorption potential would influence the amount and distribution of gases desorbing in the stripping cycle, as shown in Figure 6.2 b. When adsorbing propene in the range between 0.90-0.95 V *vs.* RHE, the amount of  $CO_2$  desorbing is the largest, which is incidentally also the potential region with the highest selectivity towards acrolein.

From these experiments we concluded that there are several types of propene adsorbates present on the surface: Weakly bound adsorbates which desorb unaltered as propene, weakly bound species that can be reduced to propane, and strongly bound species, which can only be removed oxidatively. In accordance with predictions from DFT, we propose that the latter species originates from degenerative adsorption of propene, where the C–C bonds are broken and stable  $\text{CH}_x$  species remain on the surface.

We further hypothesized that these surface adsorbates have an influence on how propene coordinates to the surface. While vinylic coordination is more stable according to DFT, the adsorption is also more cumbersome and requires more space on the surface. Allylic coordination, on the other hand, is energetically less favorable, but if the surface is highly covered by other adsorbates, it could be forced to this coordination due to sterical hindrance. This is illustrated in Figure 6.3. Based on DFT calculations, we assume that allylic oxidation requires adsorption in the allylic coordination. Hence, the high surface coverage at intermediate potentials, as evident from the large amount of  $\text{CO}_2$  desorption in stripping after adsorption at these potentials, could enforce allylic coordination, and thereby be responsible for the high selectivity towards acrolein at these potentials.

To investigate this further we devised the "site evacuation" experiments described in the following section.

### 6.3 Site evacuation experiments

As described in the previous section, based on propene stripping experiments and DFT modeling, we hypothesize that selective poisoning of the surface has an influence on the propene adsorption geometry, where low coverage allows for vinylic coordination, while high coverage forces propene to adsorb in the allylic position.

In order to test this hypothesis, we devised an experimental sequence using EC-MS which we termed "site evacuation" experiments. We assume that the amount of propane ( $\text{C}_3\text{H}_8$ ) desorbing in the cathodic part of a propene stripping cycle corresponds to the amount of propene bound through the vinylic position, while the amount of propene ( $\text{C}_3\text{H}_6$ ) desorbing corresponds to the amount of propene bound more weakly

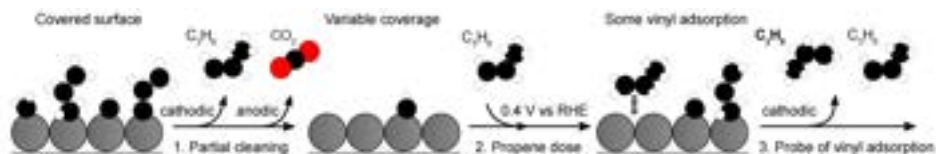


**Figure 6.3** Illustration of the three steps of a site evacuation experiment. Figure by Soren Scott, published in Paper I.

and possibly through the allylic position. This means that we can test the availability of these sites by adsorbing propene and observing the cathodic desorption. We can then vary the surface coverage at the beginning of the adsorption phase, by choosing different anodic potential limits (cleaning potentials), which leads to the removal of different amounts of surface adsorbates in form of  $\text{CO}_2$ . Figure 6.3 illustrates the different steps in the experiment and the expected surface coverage schematically. One full cleaning-dosing-desorption cycle on Pd is shown in Figure 6.4: First, the surface is cleaned by performing a linear sweep up to the cleaning potential and back down to 0.4 V vs. RHE, a dose potential at which no production of liquid products is expected, which would accumulate in the electrolyte. Then the electrolyte is exchanged, in order to remove any liquid products that might have formed in the previous anodic sweep. Second, propene is dosed again at constant potential (0.4 V vs. RHE). Then the carrier gas is switched back to He, and the remaining propene is purged out. Finally, a cathodic sweep is performed where the desorption of propene and propane is monitored.

The results of the site evacuation experiments on Pd, Au-Pd alloys and Au are shown in Figure 6.5. On Pd (Figure 6.5 a), post-dose propane clearly follows the trend of  $\text{CO}_2$  desorption, while post-dose propene is not affected by the coverage of the surface. This supports our hypothesis: at lower coverage, the adsorption through the vinylic moiety is preferred, while at high coverage it is hindered. The fact that the allylic adsorption is not increased at low coverage supports that it is not simply an effect of site availability.

DFT modeling by Luca Silvioli presented in Paper I, shows that the adsorption of propene on Pd is generally very strong. For purely vinylic adsorption on a clean Pd(111) surface there is a driving force for dissociation of propene; allylic adsorption is stabilized by additional vinylic coordination. The kinetic barriers for oxidation at the

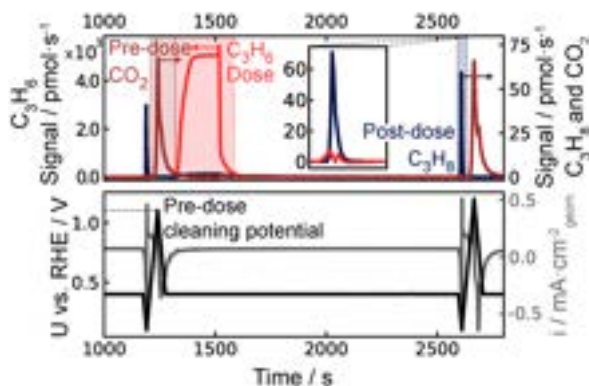


**Figure 6.4** One cycle of a site evacuation experiment measured on Pd: The surface is cleaned (pre-dose  $\text{CO}_2$ ), propene is dosed and purged out at constant potential and finally post-dose  $\text{C}_3\text{H}_6$  and  $\text{C}_3\text{H}_8$  are measured (inset). This procedure was repeated with different cleaning potentials, see Figure 6.5. Figure by Soren Scott, published in Paper I.

allylic position are generally very high. Luca then simulated a surface covered with adsorbates by adding CO to the surface as a model adsorbate. The result is that the vinylic co-adsorption together with allylic adsorption is prevented, which reduces the kinetic barriers for the reaction towards allylic oxidation products significantly. We interpret this as further support of the hypothesis that on Pd, selectivity towards the allylic propene oxidation products allyl alcohol, acrolein and acrylic acid is given by the partial coverage of the catalyst surface with degradation products. Nevertheless, as the catalyst has to be sufficiently poisoned by the reaction, this limits the reaction rate substantially.

The second reactant besides propene that is required for the reaction is oxygen. We proposed a Langmuir-Hinshelwood-type reaction mechanism with adsorbed  $\text{*OH}$  and  $\text{*O}$  species on the surface, motivated by several observations: The onset of propene oxidation activity corresponds to the onset of OH adsorption calculated by DFT (see Paper I), and the Pd oxidation onset in the experimental CVs. Also, the oxidation of Pd is shifted towards higher potentials in the presence of propene (see Figure 5.1), which is typical for competitive adsorption of two reactants, known for example from CO oxidation [105, 136, 151].

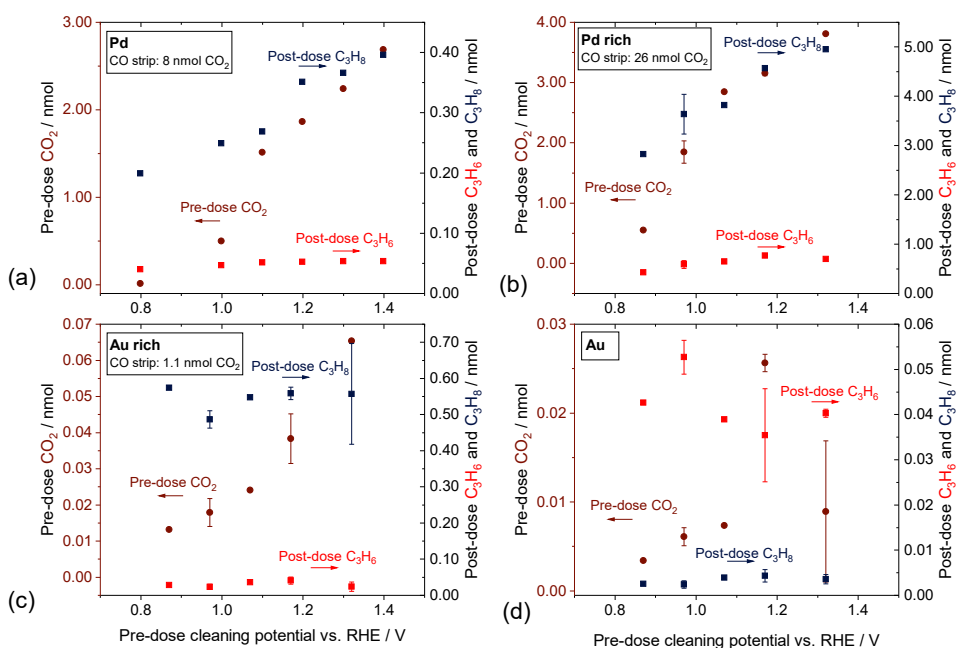


**Figure 6.5** Site evacuation experiments. The integrated  $\text{CO}_2$  coming off in the cleaning step (circles) is shown on the left y-axis; propene ( $\text{C}_3\text{H}_6$ ) and propane ( $\text{C}_3\text{H}_8$ ) desorbing in the cathodic strip (squares) are shown on the right y-axis. Data in (a) is given as published in Paper I (for error bars the reader is referred to the original figure in Appendix B). Note the different scales on the axes. Error bars are given where more than one point was recorded on the same sample. All experiments were performed in 1 M  $\text{HClO}_4$ , scan rate 10 mV/s for Pd, Pd rich and Au rich, 20 mV/s for Au.

Taking this into consideration in Paper I, we suggest approaches how one could design a catalyst to optimize for higher reaction rates while maintaining high selectivity: We want to reduce poisoning from propene degradation products by choosing a less carbophilic catalyst. At the same time, we want to provide adsorption sites for allylic adsorption. Also, the catalyst should be reasonably stable under reaction conditions. We concentrated our efforts on the system AuPd: Here Au, both less oxophilic and less carbophilic than Pd, can act as an inert matrix in which single Pd atoms or small islands

are embedded as active sites. Au, in contrast to other materials, is reasonably stable even at oxidizing potentials in an acidic environment [152].

I carried out site evacuation experiments on Au and two different compositions of AuPd alloys. Our idea was that Pd atoms surrounded by only Au atoms would not show a propane desorption behaviour dependent on the carbon coverage, because the degenerative adsorption mechanism resulting in high surface coverage would be inhibited. While in this case we assume that Au is an inert matrix and only Pd interacts with propene, Au has been described as a catalyst for the electrochemical oxidation of propene to acetone [49]. Thus, it is important to test the adsorption behavior of pure Au. Finally, I also tested how the presence of small amounts of Au in a Pd matrix would affect the interaction with propene. Ideally, a defined system with a defined surface composition, such as a single crystal, should be used for these experiments. Unfortunately, tests on flat surfaces prepared by sputter deposition showed too low activity for comparison between different samples (results not shown). Therefore, I used high surface area samples, as characterized in Chapter 4. As XRD results (Section 4.1.2) showed the presence of only one phase with a change in lattice constant as expected from Vegard's law for the respective compositions, I assumed statistical distribution of the atoms in the lattice.

The alloy compositions at the ends of the alloy spectrum were chosen to make it safe to assume that on the Au rich foam, the majority of Pd atoms on the surface is surrounded by Au atoms, and on the Pd rich foam the majority of Au atoms is surrounded by Pd. The mixing enthalpy for Au and Pd is slightly negative, suggesting that island formation should not be expected [149, 153, 154]. Assuming a purely statistical distribution, according to Maroun et al. [149], the percentage of dimer sites should be between 15 - 22% for a minority atom content of 7 - 15%. However, they and others observed a significantly higher number of Pd monomers [139, 149, 155–157]. Mobility of surface atoms under reaction conditions can be expected in the presence of gases and when changing the potential [158], especially during repeated oxidation and reduction of the surface by potential cycling. Agglomeration of Pd at the surface has been observed in the presence of CO [113] and even during HER [159]. Nonetheless, Maroun et al. observe, that Pd dimers are necessary to enable hydrogen adsorption [149]. Assuming the current from the hydrogen desorption feature between 0.05 and

0.4 V vs. RHE in the anodic part of the CV shown in Figure 6.1 is a measure for the number of Pd sites with at least one Pd neighbor, while the CO strip probes all available Pd sites, it is possible to estimate the amount of Pd dimers on the surface. On the Au rich foam, this is ca. 17% at the beginning of the experiment, and only ca. 3% at the end of the experiment. This indicates that there is no coalescence of Pd atoms in the course of the electrochemical testing, but rather the opposite. However, the surface was cleaned by repeatedly cycling the potential before this measurement, during which the structure could have changed. The distribution of Pd atoms on the Au rich surface is further discussed in Section 8.

The results of the site evacuation experiments on Pd rich, Au rich and Au foam are shown in Figure 6.5 b-d. Note that the electrochemical surface area varied between the samples, and that the scaling of the axes differ. Note also that the calibration of the mass spectrometer was done differently for Pd, resulting in the underestimation of propane roughly by a factor 2 (see Section 3.5). Nevertheless, neither the variations in surface area, nor in different calibration factors are substantial enough to rationalize the differences in ad- and desorption behavior. The general behavior of Pd rich foam is similar to pure Pd (Figure 6.5 a): Post-dose propane desorption correlates with pre-dose CO<sub>2</sub> desorption, while post-dose propene desorption is not affected on a similar scale. On Au rich foam, on the other hand, neither propene nor propane desorption depend on the amount of CO<sub>2</sub> stripped off in the cleaning step. Pure Au shows a different behavior: The maximum of CO<sub>2</sub> stripped off is already reached at lower potentials. Propene desorption does not depend on the cleaning potential, but no propane desorption is observed.

The observations on the Au rich catalyst are in agreement with the hypothesis that on a surface where Pd is surrounded by Au, adsorption of propene through the vinylic position should not depend on the coverage. Nevertheless, there is still more adsorbate desorbing in form of propane than in the form of propene. This indicates that the vinylic position is still involved in surface adsorption, or is at least accessible for participation in a reaction. Previous studies showed that the main product of propene oxidation on Au is acetone, which is hypothesized to be a product of vinylic coordination with the surface [49]. It seems like sterical hindrance is really necessary to force the allylic coordination.

In contrast to pure Au, in the presence of Pd, H-UPD is observed in the probed potential range (see also the CO strip in Figure 6.1), and reduction to propane is possible. Nonetheless, on Au, propane formation could be observed at lower potentials (same onset potential as HER, data not shown), suggesting that the presence of hydrogen on the surface plays a role in the reaction [160, 161]. However, a decrease in propene desorption on Pd and Pd rich electrodes at the potential minimum (see Figure 6.2 a) could indicate that at sufficiently negative potentials, also propene in allylic coordination can be hydrogenated. Hence, from the present results the reason for the lack of propene desorption from Au cannot be elucidated.

For a more quantitative comparison of the behavior of the different alloy compositions, I normalized the desorbing propene, propane and CO<sub>2</sub> from the site evacuation experiments to the amount of CO<sub>2</sub> coming off in the CO strip as a measure of how many Pd atoms there are on the surface. The normalized data is shown in Figure 6.6. The more Au there is on the surface, the higher is the amount of propene and propane which desorb per Pd atom. On the other hand, the more Pd there is, the more CO<sub>2</sub> per Pd comes off in the cleaning. Propane desorption scales with CO<sub>2</sub> coming off for pure Pd and for 90% Pd, but not for 10% Pd.

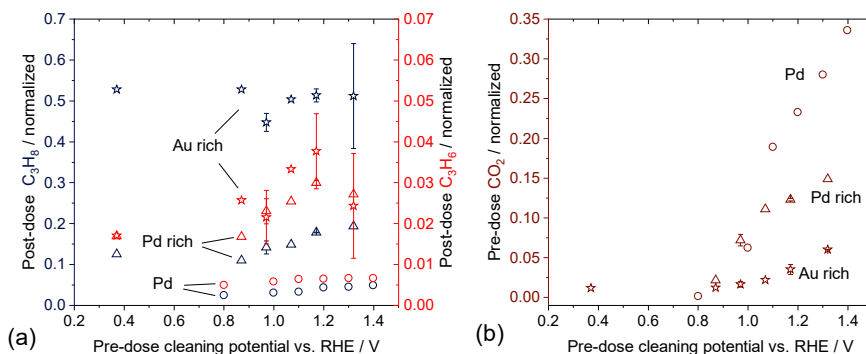


**Figure 6.6** Data from Figure 6.5 normalized to CO<sub>2</sub> coming off in CO strip as a measure of the Pd surface area for easier comparison between the different samples. a) Propane (C<sub>3</sub>H<sub>8</sub>, left y-axis) and propene (C<sub>3</sub>H<sub>6</sub>, right y-axis) desorption in the cathodic cycle. b) CO<sub>2</sub> desorption in the anodic cycle. Note the different scaling of the axes.

Adding only 10% of Au to the surface reduces the degradation of propene on the surface significantly (less CO<sub>2</sub> is released per Pd surface area in the anodic strip);

therefore more sites both for allylic and vinylic coordination are available, resulting in a higher desorption rate of both propene and propane per Pd atom. It is unlikely that the Au atoms play a significant role, since the adsorption of propene on Au is much lower than on Pd. Nevertheless, the the number of allylic adsorption sites is only altered slightly by cleaning the surface, suggesting that also here, allylic coordination only occurs where the surface is covered sufficiently to sterically hinder vinylic coordination. On 90% Au and 10% Pd, propene desorption is 5-10 times higher per Pd atom than for the other compositions. The total number of moles of propene, propane and CO<sub>2</sub> desorption in one cycle is on the same order of magnitude as the amount of CO<sub>2</sub> from the CO strip. Nevertheless, the absolute number of post-dose propane desorption on pure Au is also on a similar order of magnitude (Figure 6.5). An underestimation of available Pd sites is not expected as a CO strip at the end of the series of propene experiments suggested a slight reduction in Pd sites (data not shown). Hence, it cannot be excluded as such that adsorption on Au also plays a role here.

## 6.4 Summary

In this chapter, I described a series of experiments in which we used the desorption of CO<sub>2</sub>, propene and propane as a measure of different types of propene adsorption to Pd, Au and AuPd alloy surfaces.

- On pure Pd, under conditions relevant for the oxidation of propene, we found that the surface is covered by degenerated propene adsorbates. The number of adsorption sites for vinylic adsorption can be increased by removing surface adsorbate oxidatively. At the same time sites for allylic adsorption are not affected. The highest number of surface adsorbates was found in the same potential region where activity and selectivity towards allylic oxidation is the highest. DFT results suggest that the kinetic barriers for oxidation in the allylic position are significantly lowered in the presence of the surface adsorbates due to steric effects. This suggests that the surface adsorbates formed *in-situ* limit activity, but are crucial for selectivity towards allylic oxidation.

- Alloying Pd with 10% Au decreases the degradation and results in a higher availability of site both for allylic and vinylic coordination in comparison with Pd. The effect of removing adsorbate is still the same. Nevertheless, this indicates that the activity of Pd towards allylic oxidation can be improved by alloying, while maintaining selectivity.
- On an Au surface with 10% Pd, the coverage with degenerated propene species is very low compared to alloys with a higher Pd content. Also, cleaning the surface does not have an effect on either propene or propane desorption. We still see significant propane desorption per Pd atom indicating reactivity of the vinylic bond. On pure Au, the interaction with propene is even smaller. No propane desorption is observed, which is likely due to the lack of H on the surface in the tested potential range.

## Chapter 7

# Probing surface adsorbates *in-situ* using SEIRAS and EC-MS

In Chapter 6, I discuss how surface adsorbates play a role in the selectivity of electrochemical propene oxidation. Poisoning of the surface is also well known for electrochemical oxidation of alcohols [135, 136]. For allyl alcohol oxidation on Pd, CO has been described as such a poisoning species based on detailed experiments using DEMS [126]. It was observed to form especially at potentials cathodic of the potentials necessary for oxidation towards acrolein and CO<sub>2</sub>. With the work presented in the current chapter we want to corroborate this analysis with direct evidence of CO on the surface observed with SEIRAS, and discuss how the degradation mechanism for allyl alcohol oxidation on Pd relates to that of propene oxidation. In particular, I aim at exploring following questions:

- CO poisoning during allyl alcohol oxidation was observed indirectly using DEMS [126]. Can we detect and measure this poisoning CO intermediate during allyl alcohol oxidation using SEIRAS?
- Can we directly observe surface adsorbates during propene oxidation? Do they differ from what we see for allyl alcohol?
- Can we use CO as a probe to determine the presence of surface adsorbates?

All Pd films used in SEIRAS experiments were prepared and characterized by Michael Boyd. *Ex-situ* characterization of these electrodes is shown in Chapter 4. I performed the experiments shown in the present chapter and carried out the data analysis. Michael helped by developing the electrochemical cell and doing all necessary acid cleaning. He was also involved in planning the experiments and discussing the results. Soren Scott helped carrying out and analyzing the EC-MS experiments.

The bulk allyl alcohol experiments, were included in Paper I. The rest of the data presented in the present chapter will be shown in Paper III.

As in the previous chapters, all potentials in this chapter are reported *versus* the reversible hydrogen electrode (RHE).

## 7.1 CO stripping

CO stripping was performed to verify the SEIRA activity of the Pd films [75]. As in EC-MS, CO stripping is a useful tool to test and demonstrate the possibilities of the method. The procedure was the same as described in Section 3.3: The electrolyte (0.001 M HClO<sub>4</sub> + 0.099 M KClO<sub>4</sub>, pH 2.85) was saturated with CO while holding the electrode at 375 mV where no CO oxidation was expected. After adsorption for 10 minutes, CO was purged out with Ar at constant potential for 30 minutes. Then the potential was scanned up to 1.4 V and IR spectra were recorded simultaneously. The CV is shown in Figure 7.1, the IR spectra in Figure 7.2. Each spectrum was recorded over ca. 30 s, therefore, at the employed scan rate of 2 mV/s, they resemble an average over 60 mV. In Figure 7.2, the first line from the bottom shows the spectrum in CO saturated solution before purging with Ar. The large peak at 1960 cm<sup>-1</sup> can be assigned to the C–O stretch vibration,  $\nu(\text{C–O})$ , of CO bound in bridge position, and the small feature at 2060 cm<sup>-1</sup> to on-top bound CO [75]. The on-top feature almost disappears when decreasing the CO concentration in the electrolyte by purging with Ar. When increasing the potential, a shoulder appears at the low-wavenumber side of the  $\nu(\text{C–O})$  bridge mode, which can be attributed to CO bound in a three-fold hollow site [75]. Before completely disappearing at 1065 mV, at 1005 mV all CO remaining on the surfaces is bound in the hollow site with a peak maximum at ca. 1925 cm<sup>-1</sup>. A small shift of the bridge peak maximum from ca. 1945 to 1960 cm<sup>-1</sup> is observed between

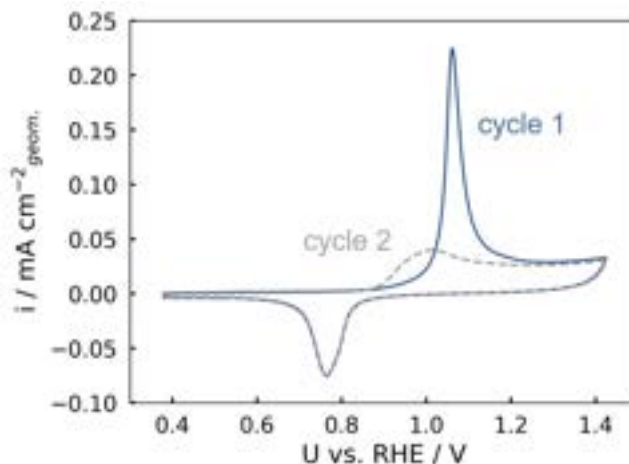


**Figure 7.1** CO stripping on a Pd SEIRAS film in 0.001 M HClO<sub>4</sub> + 0.099 M KClO<sub>4</sub>, pH 2.85: Cycle 1 shows the CO oxidation feature. Cycle 2 was performed immediately after and shows the oxidation and reduction features expected for a Pd electrode.

375 and 940 mV due to the Stark effect [75]. The broad feature at 3000-3600 cm<sup>-1</sup>, which increases with intensity on potential cycling is due to O-H stretch vibrations ( $\nu(\text{O-H})$ ) of water. The broadening is due to H bonds between water molecules. The feature at ca. 1640 cm<sup>-1</sup> originates from the H-O-H bending mode ( $\delta(\text{H-O-H})$ ) [162]. These two features increase as the Pd film is partially dissolved during potential cycling [75]. The sharp peak at 3644 cm<sup>-1</sup> is attributed to the  $\nu(\text{O-H})$  mode of water where hydrogen bond formation is inhibited in the presence of CO on the surface. This feature is also found in the absence of CO, but is less pronounced [163, 164]. The peak of the CO stripping current at 1100 mV in Figure 7.1 corresponds to the spectrum where there is only a small last trace of CO left (see Figure 7.2). In fact, while recording this spectrum the intensity of the CO peak decreased from one scan to the next. This demonstrates that through using this technique it is possible to observe the electrochemical oxidation of CO *in-situ*. The IR modes observed agree well with those reported previously on Pd films prepared and tested in a similar way [75].

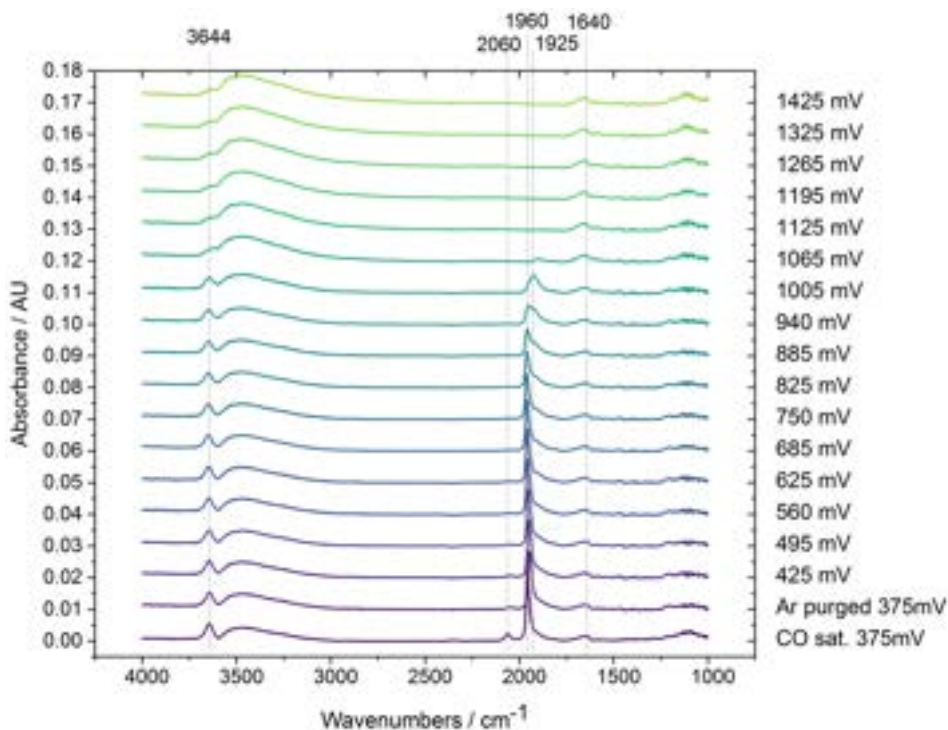


**Figure 7.2** CO stripping on a Pd SEIRAS film in 0.001 M HClO<sub>4</sub> + 0.099 M KClO<sub>4</sub>, pH 2.85: IR spectra during the first anodic sweep. Spectra were treated by removing the features of H<sub>2</sub>O vapor originating from the optical path, followed by baseline correction, as described in Section 3.5.

## 7.2 Allyl alcohol oxidation

From the product distribution determined after steady state propene oxidation presented in Chapter 5, we hypothesized that allyl alcohol is an intermediate when oxidizing propene to acrolein. This is in agreement with DFT calculations, which show that the insertion of oxygen into propene is the rate limiting step of this reaction (see also Paper I): As mentioned in Chapter 6, we assume the oxidation of propene occurs *via* a Langmuir-Hinshelwood mechanism. This means that surface-bound oxygen species are required to form allyl alcohol, which are a limiting factor on a surface highly covered with organic adsorbates. Further oxidation of allyl alcohol to acrolein only requires proton/electron transfers, but no insertion of oxygen.

To corroborate these results, I carried out steady state allyl alcohol experiments in the same way as the propene oxidation experiments. I used two different concentrations of allyl alcohol added to 0.1 M HClO<sub>4</sub>: 10 mM, which corresponds to the concentration of propene in propene saturated electrolyte at the reaction conditions [165], and 0.1 mM corresponding to the concentration of allyl alcohol observed during propene oxidation. The product distribution shown in Figure 7.3 b, shows a very high selectivity towards acrolein at high alcohol concentration, and towards acrolein and acrylic acid at low alcohol concentration. At high alcohol concentration the current density is significantly higher than in propene (shown in Figure 7.3 a), while at low concentration it is in the same order of magnitude.

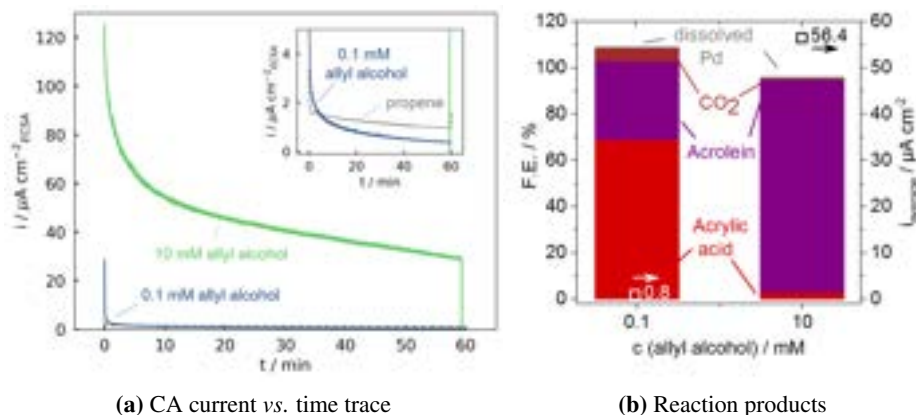


**Figure 7.3** Allyl alcohol oxidation at 0.8 V vs. RHE at 0.1 and 10 mM alcohol concentration in 0.1 M HClO<sub>4</sub>. Published in Paper I.

This agrees with the hypothesis displayed above, that oxygen insertion to form allyl alcohol is the rate limiting step in propene oxidation: Much higher reaction rates are possible, if oxygen is already part of the molecule, even if the reactant concentration in solution is the same. In principle, a similar argument could be used to rationalize the difference in product distribution between high and low allyl alcohol concentration. To form acrylic acid, another oxygen atom has to be inserted, which requires surface bound oxygen species. At the higher allyl alcohol concentration, the electrode surface is covered by organic species, while at lower concentration, oxygen is available and

formation of the acid possible. However, product analysis shows that over the course of the experiment, 90% of allyl alcohol are converted at low concentration (0.1 mM). This means that for a significant part of the duration of the experiment, the concentration of acrolein is higher than allyl alcohol, making it likely to get further oxidized to acrylic acid. At higher allyl alcohol concentration, the conversion is lower (70%), which agrees with the lower concentration of the secondary oxidation product acrylic acid. Experiments with lower overall conversion (*i.e.* shorter reaction times) would be necessary to differentiate whether the product distribution is determined by surface or bulk effects. Nonetheless, the high conversion of allyl alcohol highlights once more that the oxidation of the alcohol occurs much faster than of propene.

From the current time traces shown in Figure 7.3 it is clear that also for allyl alcohol oxidation the current decreases significantly with time. This is likely related to the depletion of the electrolyte of allyl alcohol. However, as literature suggests that surface poisoning plays a role [126], I carried out further allyl oxidation experiments in Ar saturated 0.001 M HClO<sub>4</sub> + 0.099 M KClO<sub>4</sub> containing 10 mM allyl alcohol using SEIRAS. Unfortunately, the Pd films were not very stable over time, especially during potential cycling. As mentioned before, Pd dissolution leads to an increase in the electrolyte related IR signals between 3000-3600 cm<sup>-1</sup> and around 1600 cm<sup>-1</sup>, as well as a signal at ca. 1260 cm<sup>-1</sup> (probably related to Si-O vibrations from the Si substrate [75]). At the same time, the baseline shifts dramatically which has been related to the oxidation of the surface which changes the reflectivity [162]. To highlight the effect of changing the potential on organic adsorbates rather than showing corrosion of the catalyst, instead of potential cycling like for CO stripping, a step-approach was pursued. The potential was first increased in 50 mV steps and then decreased in 100 mV steps. At each step the potential was held constant for ca. 5.5 min and an IR spectrum recorded in the beginning and after 5 min; between the steps, the potential was stepped down to the reference potential of 0.1 V *vs.* RHE for 2.5 min, where a reference spectrum was recorded. This procedure is illustrated in Figure 7.4.

During allyl alcohol oxidation at 150 mV, Arévalo et al. [126] observed the adsorption of a CO-like species at the Pd surface. By choosing 100 mV as reference potential, we could probe how stepping up to different potentials would affect this adsorbed species directly. At each potential step two spectra were recorded. Since Pd

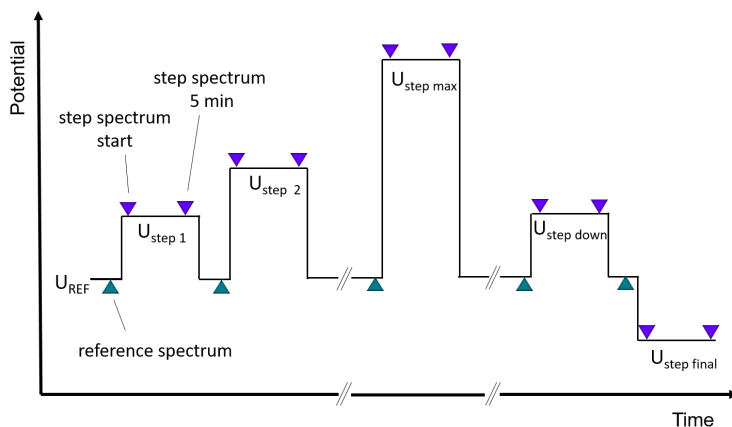


**Figure 7.4** Schematic of the potential profile for recording IR difference spectra. First a spectrum is recorded at a reference potential  $U_{\text{REF}}$ . Then the potential is stepped up to a step potential, where an IR spectrum is recorded immediately, and another one after 5 min. Then the potential is stepped back down to the reference potential and a new reference spectrum is recorded before stepping up to the next step potential. After reaching the maximum potential, the potential was stepped down again in a similar manner. While in allyl alcohol oxidation experiments 0.1 V was chosen as reference potential, 0.4 V was used for propene oxidation (Section 7.3).

dissolution significantly changes the background, spectral quality was worse after 5 min, so only the initial spectra are shown here. Some features related to the reaction of allyl alcohol changed over time; this is stated below. The spectra after 5 min are shown in Appendix A. For each step, the spectrum recorded at 100 mV directly before stepping up was subtracted from the spectra at the step potential.

The resulting difference spectra are shown in Figure 7.5. The corresponding electrochemical data is given in Appendix A. In the IR spectra, there are two regions where differences are observed: a smaller feature at  $3650\text{ cm}^{-1}$  and several positive and negative peaks in the range between  $1800\text{--}2000\text{ cm}^{-1}$ . The feature at  $3650\text{ cm}^{-1}$  appears at potentials starting from 0.6 V and decreases again above 0.85 V. The other group of features shows more complex behavior: At 0.3 V, there is a sharp positive peak at  $1922\text{ cm}^{-1}$  which shifts to higher wavenumbers up to ca. 0.8 V ( $1950\text{ cm}^{-1}$ ). Between 0.6 and 0.85 V, this peak is accompanied by a small negative feature with a minimum between  $1905$  and  $1910\text{ cm}^{-1}$ . A larger, broader negative feature at  $1843\text{ cm}^{-1}$  appears

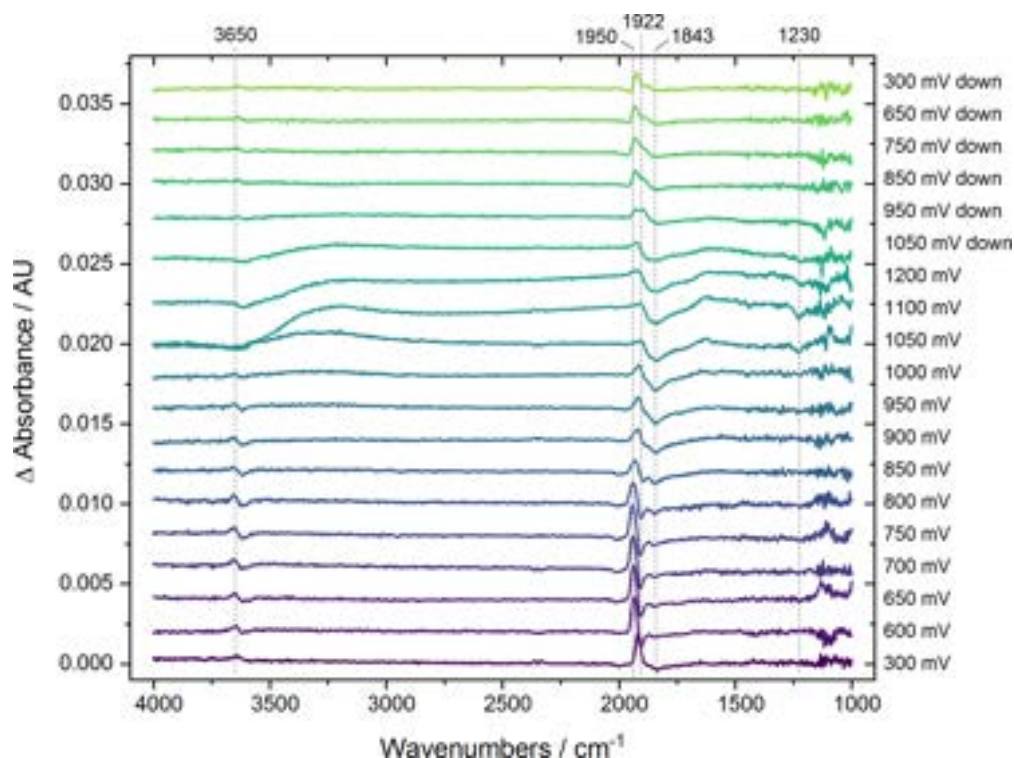


**Figure 7.5** SEIRAS difference spectra during allyl alcohol oxidation on Pd in 0.001 M HClO<sub>4</sub> + 0.099 M KClO<sub>4</sub>, pH 2.85 and 10 mM alcohol concentration. The differences were calculated between the step potential indicated at the right of the figure and reference spectra at 0.1 V recorded immediately prior to the potential step. For details see the text.

at 0.8 V and increases until 1.2 V, where it reaches its maximum. The positive feature disappears at this potential.

The peak at 3650 cm<sup>-1</sup> can be assigned to the  $\nu(\text{O}-\text{H})$  vibration of non-hydrogen bound H<sub>2</sub>O [75], as discussed above. The position of the other feature suggests that it is a convolution of the  $\nu(\text{C}-\text{O})$  mode of CO bound in different positions, as well as Stark shift of the adsorbed species when stepping up from 100 mV. Deconvolution would require additional experiments, and is out of the scope of this work. Nevertheless, the growth of the peak at 1950 cm<sup>-1</sup> is a clear indication that CO is being formed between 0.6 and 0.75 V in addition to the CO forming at 100 mV and that it binds in bridge position [75]. At higher potentials, less CO is present at the surface, which also manifests in the negative growth of the negative feature at ca. 1845 cm<sup>-1</sup>, which can be

assigned to the  $\nu(\text{C}-\text{O})$  mode of CO bound in a 3-fold hollow site. CO bound in this position being oxidized at the most positive potentials is in agreement with the spectra recorded in CO shown above.

At  $1230\text{ cm}^{-1}$  there is a weak negative peak visible at potentials above 1.050 V. A feature at this wavenumber has been assigned to the  $\delta(\text{O}-\text{H})$  mode of allyl alcohol [166], and is also present in the reference spectrum of pure allyl alcohol (see Appendix A). In the spectra recorded after 5 min several additional negative features appear at these potentials at 1440, 1235 and at  $1120\text{ cm}^{-1}$ , all of which can be assigned to allyl alcohol. This indicates that at such high potentials the surface gets depleted of allyl alcohol. On the other hand this also indicates that allyl alcohol is bound to the surface until this potential. The decrease in the feature at  $1230\text{ cm}^{-1}$  suggests that it is bound without abstraction of the alcohol proton.

### 7.3 Propene oxidation

Propene oxidation experiments were carried out essentially in the same way as the allyl oxidation experiments discussed in the previous section. Also here the potential was first stepped up, and then down, as schematically shown in Figure 7.4. In this case, 0.4 V was chosen as reference potential, where no reaction was expected to take place. From the EC-MS experiments shown in Chapter 6, we expected the surface to be covered by propene degradation species at this potential.

The IR difference spectra during propene oxidation are shown in Figure 7.6, the electrochemical data is given in Appendix A. The bottom spectrum corresponds to the first potential step. Again, there are two regions where changes are evident in the difference spectra: the region between  $3200$  and  $3600\text{ cm}^{-1}$ , and at wavenumbers below  $1700\text{ cm}^{-1}$ . Around  $3500\text{ cm}^{-1}$  a broad, negative peak starts to appear at ca. 750 mV and reaches its maximum intensity at the maximum potential of 1.2 V. A positive shoulder at  $3600\text{ cm}^{-1}$  is present between ca. 700 mV and 1000 mV, which is more pronounced in the spectra stepping down. Three features can be distinguished in the region between  $1300$  and  $1700\text{ cm}^{-1}$ : a positive peak at  $1630\text{-}1640\text{ cm}^{-1}$  pronounced between 800 and 1000 mV, a positive peak at  $1505\text{-}1520\text{ cm}^{-1}$  at potentials above

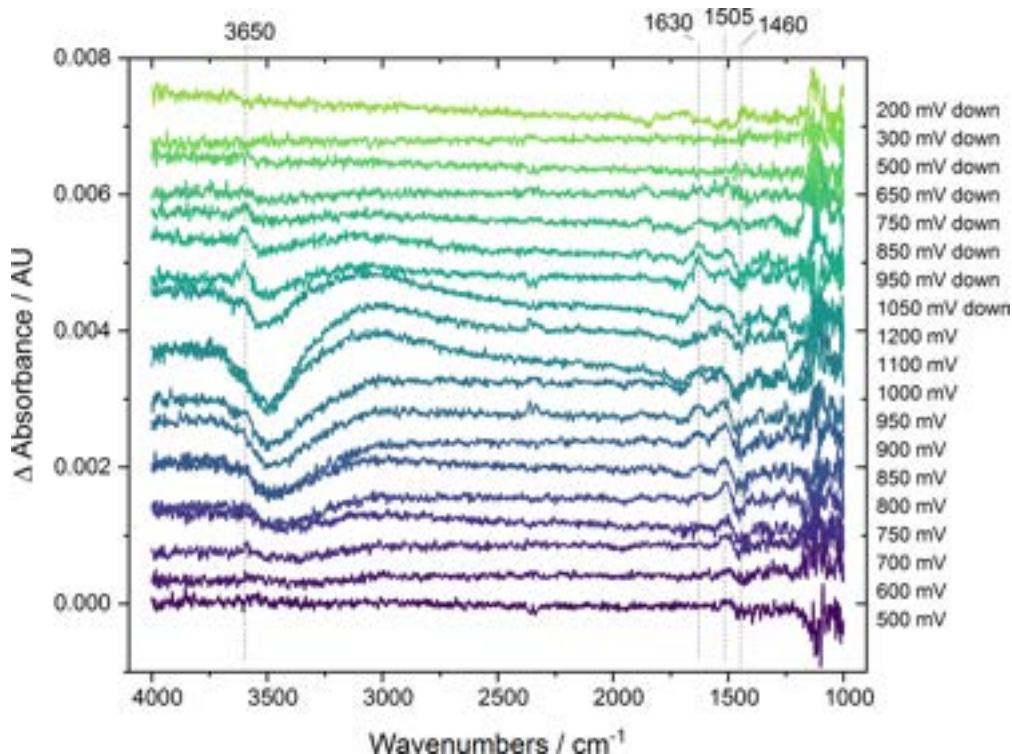


**Figure 7.6** SEIRAS difference spectra during propene oxidation on Pd in 0.001 M HClO<sub>4</sub> + 0.099 M KClO<sub>4</sub>, pH 2.85. The differences were calculated between the step potential indicated at the right of the figure and reference spectra at 0.4 V recorded immediately prior to the potential step. For details see the text.

ca 600 mV, and a negative feature at ca. 1460 cm<sup>-1</sup> which appears together with the positive peak at 1505-1520 cm<sup>-1</sup> and is most pronounced at the maximum potentials.

The peaks above 3000 cm<sup>-1</sup> can be assigned to potential dependent changes in the water structure [75, 164], like discussed above for allyl alcohol. The feature at 1630-1640 cm<sup>-1</sup> is assigned to the  $\delta(\text{H}-\text{O}-\text{H})$  mode of adsorbed water [162]. It appears at ca. 850 mV, which would agree with some of the surface adsorbate being stripped off and being replaced by water at the surface. At higher potentials, however, the water it is replaced by OH<sub>ad</sub> which does not exhibit this bending mode [167], leading to a decrease in peak intensity. The feature at 1505-1520 cm<sup>-1</sup> is likely related to the  $\delta(\text{H}-\text{O}-\text{H})$  of water which is more strongly adsorbed to the surface [163]. Some studies have assigned

features between 1490 and 1560 to the stretching mode of adsorbed enolate [167], however, this seems unlikely in acidic electrolyte. The negative feature at  $1460\text{ cm}^{-1}$  is probably related to the removal of organic adsorbates: features at these wavenumbers can be assigned to  $\delta(\text{CH}_2)$  and  $\delta(\text{CH}_3)$  modes [49, 166].

Peaks in the region between  $1000$  and  $1200\text{ cm}^{-1}$  have been assigned to adsorbed  $\text{HClO}_4$  [163], Si-O bonds [75], but also species related to several propene oxidation products [166]. However, no clear trends are visible, which suggests that the IR absorption of Si is too high in this region [162], and the signal-to-noise ratio not good enough to obtain meaningful information.

The features in these spectra are much lower in intensity than those recorded in the presence of allyl alcohol. C–O bond vibrations exhibit a much larger change in dipole moment than C–H and are therefore more intense. Also, CO binds to the surface such that the bond is normal to the surface plane, which maximized IR-absorption, while this is not necessarily the case for C–H bonds, resulting in even lower signal intensity.

From these results it is very clear that in contrast to allyl alcohol oxidation, CO is not a poisoning spectator species or reaction intermediate during oxidation of propene. This observation agrees with our hypothesis from DFT and EC-MS studies (see Chapter 6 and Paper I) that the surface is covered by propene degradation species enabling the insertion of O into the molecule and the formation of allyl alcohol. However, due to the presence of these species the dissociative adsorption of allyl alcohol is inhibited, and it is directly oxidized to acrolein and acrylic acid rather than forming CO.

## 7.4 Pd oxidation in Ar saturated electrolyte

As the signals seen during propene oxidation were very weak, the same potential step experiment was carried out on the same electrode in Ar saturated electrolyte, without propene. The difference IR spectra are shown in Figure 7.7. The applied potential and resulting current are shown in Appendix A. As in the case of propene, some changes in the spectra can be seen in the region between ca.  $3000$ - $3600\text{ cm}^{-1}$ , and between  $1500$ - $1700\text{ cm}^{-1}$ : A positive peak is present at  $3600\text{ cm}^{-1}$  between  $500$  and  $950\text{ mV}$ . From ca.  $900\text{ mV}$  a broad negative peak starts growing between  $3000$ - $3600\text{ cm}^{-1}$ , reaching its maximum intensity at the highest potential. The most pronounced feature in

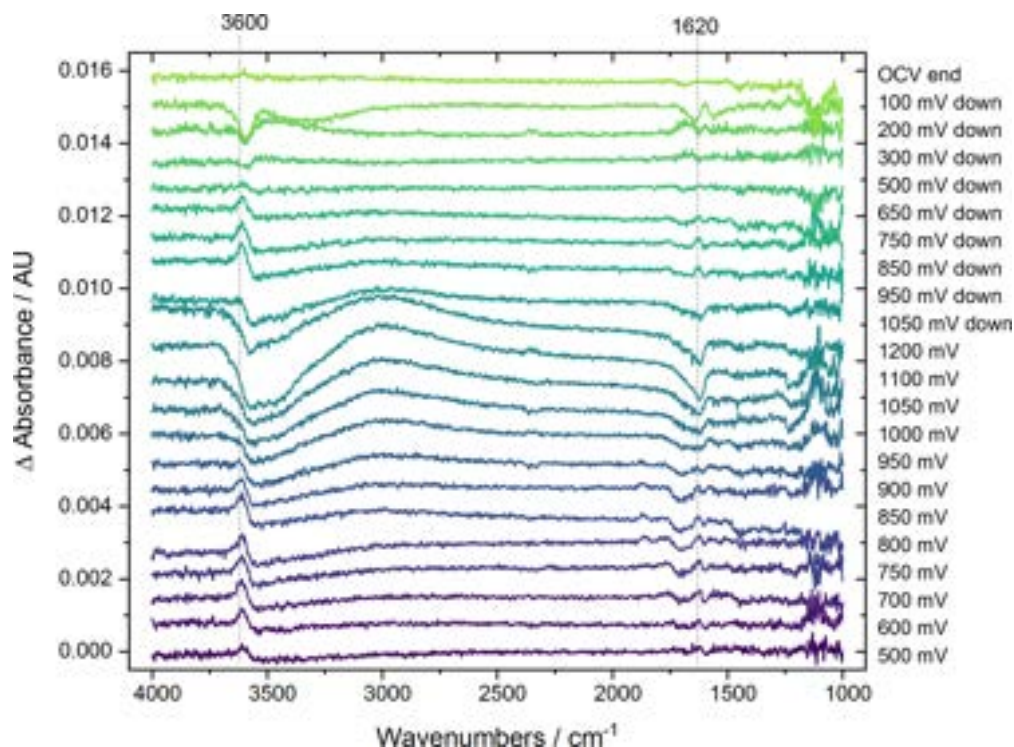


**Figure 7.7** SEIRAS difference spectra on Pd in Ar saturated electrolyte (0.001 M HClO<sub>4</sub> + 0.099 M KClO<sub>4</sub>, pH 2.85) for comparison with those recorded during propene oxidation. The differences were calculated between the step potential indicated at the right of the figure and reference spectra at 0.4 V recorded immediately prior to the potential step. For details see the text.

the lower wavenumber region is a negative peak at 1620 cm<sup>-1</sup> with maximum intensity at 1200 mV.

All these features were related to changes in the water structure, as discussed in detail in the previous sections. In Ar saturated electrolyte, these peaks are more pronounced (*i.e.* the absolute differences between the spectra and reference spectra are larger), indicating that in the presence of propene, the water structure is affected to a lesser degree, which could be related to the presence of surface adsorbates.

## 7.5 Propene displacement with CO

From EC-MS results shown in Chapter 6 and DFT results discussed in Paper I, we expect the surface to be completely covered with propene degradation species in the presence of propene at potentials below 0.9-1.0 V. However, the low intensity of propene-related signal in the IR spectra shown in the previous section hinders drawing conclusions about the surface coverage.

To further investigate the presence and type of adsorbate species, I performed a series of experiments where CO was used as a probe for free sites. Since the intensity of CO in SEIRAS is high, also low coverage should give observable signals. For all experiments, the electrolyte was first saturated with the test gas (Ar or propene), and thereafter saturated with CO at constant potential (400 mV and 800 mV), and a spectrum recorded. Then the excess CO was purged from solution, and a CO strip performed. The higher potential, 800 mV, was chosen as a compromise between an expected changed coverage of propene related surface adsorbates, and steady state oxidation of CO at higher potentials.

SEIRA spectra of CO introduced under different conditions are shown in Figure 7.8. Unlike initially expected, a clear CO peak was observed both in the presence of propene, and without. Nevertheless, propene has a significant influence on the CO peak. Without propene at 400 mV, the spectra resemble those observed during the CO-strip presented and discussed in Section 7.1. The main peaks in the range between 1500 and 2200 related to CO are given in Table 7.1 together with the respective assigned vibration modes. The features between 3000 and 3700  $\text{cm}^{-1}$  are related to changes in the water structure and have been discussed in the sections above. In all four cases there are two CO features visible while the electrolyte is CO saturated, which are attributed to on-top and bridge bound CO [75]. At 800 mV, CO at the surface is oxidized while purging out CO from the electrolyte. This has the effect that before the start of the CO strip, the peak in the spectra is reduced in intensity and shifted to lower wavenumbers, corresponding to the remaining CO moving to the 3-fold-hollow sites, as also seen during CO stripping (Figure 7.2). This effect is observed both with Ar and propene pre-treatment. The main difference between Ar and propene pre-saturated electrolyte is that in the presence of propene, the  $\nu(\text{C}-\text{O})$  bridge mode exhibits a large tail at lower

wavenumbers in the energy region of the  $\nu(\text{C}-\text{O})$  mode bound in a 3-fold-hollow site. This tail is present both at 400 and 800 mV. After the CO stripping, in all cases the CO-related features disappear and a feature at  $1650\text{ cm}^{-1}$  attributed to  $\delta(\text{H}-\text{O}-\text{H})$  appears. All four conditions shown above were recorded on the same electrode, to minimize differences in SEIRA activity. Similar experiments were also carried out on other samples showing the same effect.

**Table 7.1** IR peaks between  $1500\text{-}2000\text{ cm}^{-1}$  in the SEIRA spectra on Pd exposed to CO in the presence of Ar or propene, as shown in Figure 7.8. br = bridge, o.t. = on top, 3-f.h. = 3-fold-hollow. Peak assignment according to ref. [75]

Conditions	CO saturated		before CO strip	
	$\nu$ $\text{cm}^{-1}$	mode	$\nu$ $\text{cm}^{-1}$	mode
Ar, 400 mV	1960	$\nu(\text{C}-\text{O})$ br	1960	$\nu(\text{C}-\text{O})$ br
	2065-2088	$\nu(\text{C}-\text{O})$ o.t.		
Ar, 800 mV	1970	$\nu(\text{C}-\text{O})$ br	1905	$\nu(\text{C}-\text{O})$ 3-f.h.
	2078	$\nu(\text{C}-\text{O})$ o.t.		
$\text{C}_3\text{H}_6$ , 400 mV	1946-1690	$\nu(\text{C}-\text{O})$ br	1946-1690	$\nu(\text{C}-\text{O})$ br
	2065-2088	$\nu(\text{C}-\text{O})$ o.t.		
$\text{C}_3\text{H}_6$ , 800 mV	1968-1750	$\nu(\text{C}-\text{O})$ br	1913	$\nu(\text{C}-\text{O})$ 3-f.h.
	2080-2100	$\nu(\text{C}-\text{O})$ o.t.	1650	$\delta(\text{HOH})$
	1650	$\delta(\text{HOH})$		

To understand the observed behavior in the presence of propene better, additional experiments were carried out using the EC-MS setup. Due to experimental limitations, Pd foam electrodes were used, as in the EC-MS experiments shown in Chapter 6. In these experiments, the electrode was saturated with propene at constant potential (400 mV), until a characteristic adsorption current had decayed. Excess propene was removed from the electrolyte by purging with He. Then the gas was changed to CO, and  $m/z$  41, corresponding to propene, was monitored. The EC-MS plot showing mass and current traces is shown in Figure 7.9. A clear peak in  $m/z$  41 is visible, as soon as CO is introduced. At the same time a reductive current is observed. The integrated peak area of the  $m/z$  41 peak corresponds to a surface coverage of ca. 7% compared to the surface area determined from CO stripping in the absence of propene. A much

smaller propene peak was observed on Pd thin films with much smaller surface area, indicating that the feature originates from the electrode and not from parts of the setup. No feature was observed on Au foam, which does not adsorb CO as strongly and therefore is not expected to show such propene displacement. This confirms that the feature does not originate from propene trapped in the porous electrode. In Figure 7.9, just before switching carrier gas, masses 28 and 32 increase significantly, which is due to a small crack in the membrane chip through which air could seep in, when the pressure temporarily decreased during the gas changing process. Nonetheless, it is assumed not to have a large effect, as both CO and propene stripping experiments (not shown) showed similar behavior as on a fully intact chip.

Propene coming off the electrode indicates that the introduction of CO leads to the displacement of propene bound to the surface. Therefore, CO is still seen in the SEIRA spectra, despite the initial coverage of the surface. This means that there is some propene on the surface which has not degraded, and is less strongly bound than CO, so it can be displaced.

## 7.6 Summary

A combination of SEIRAS and EC-MS was used to determine the adsorbates on a Pd electrode during allyl alcohol and propene oxidation *in-situ*. Difference spectra between a low reference potential and a more oxidizing step potential were recorded to highlight the differences due to changes in surface adsorbates and minimize the effect of catalyst corrosion on the signal.

- There is clear evidence from SEIRAS that CO is present at the surface during allyl alcohol oxidation at potentials up to ca. 1050 mV. At these potentials, also the current density is the highest, and a decrease in allyl-alcohol related surface species is evident after 5 minutes of reaction time. At the same time the surface also gets oxidized, leading to distortion of the SEIRA difference spectra.
- During propene oxidation, the differences between the reference and the step potential are generally small. Two distinct features between 1500 and 1650  $\text{cm}^{-1}$  indicate a change in the water structure at the surface which is different from

the behavior the absence of propene. A negative peak at  $1460\text{ cm}^{-1}$  suggests the removal of adsorbed organic species already at potentials above 600 mV. In contrast to allyl alcohol, no CO was observed.

- When introducing CO to a propene saturated surface, part of the adsorbed propene is displaced by CO. This was observed first with SEIRAS, where a different peak shape indicates a different distribution of CO on the surface than on the pristine Pd electrode. EC-MS experiments show that propene is released from the electrode surface when introducing CO.

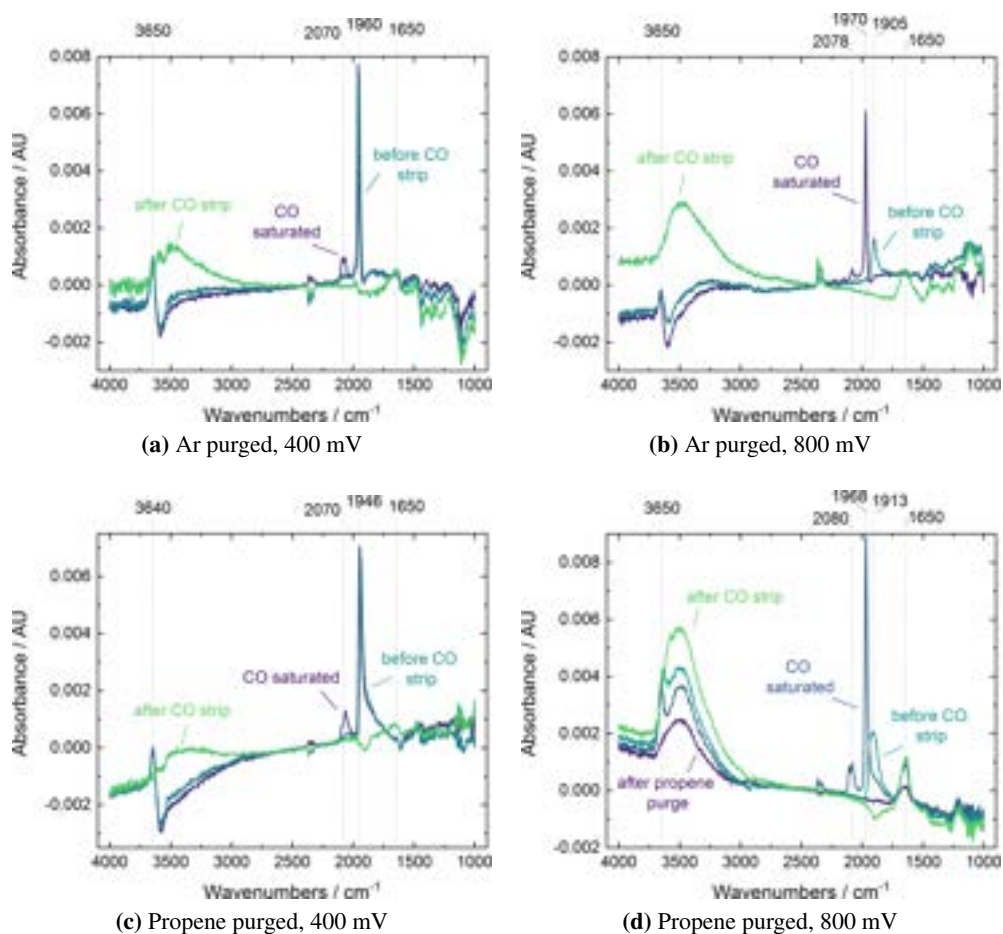


**Figure 7.8** SEIRA spectra on Pd in 0.001 M  $\text{HClO}_4$  + 0.099 M  $\text{KClO}_4$ , pH 2.85, where CO is used as a probe for available surface sites under different conditions. Spectra are shown as recorded. The feature at ca  $2300\text{ cm}^{-1}$  corresponding to  $\text{CO}_2$  is probably due to variations of  $\text{CO}_2$  in the optical system, rather than at the electrode. For details see the text.

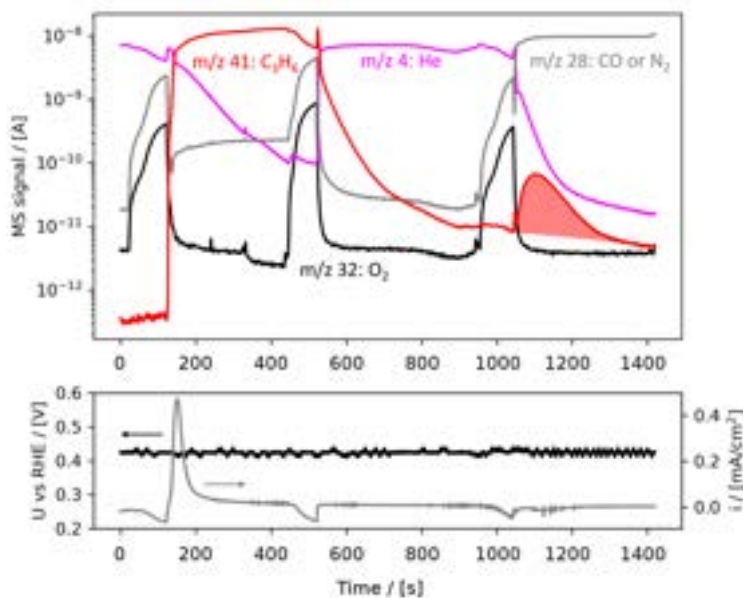


**Figure 7.9** EC-MS plot of the propene displacement experiment: Initially, the electrolyte is saturated with propene until the current stabilizes indicating saturation. Then propene is purged out by He, followed by the introduction of CO at ca. 1050 s, leading to the desorption of propene (filled peak). The mass signals shown are not calibrated. The increase of  $m/z$  28 and 32 before changing gases is due to a crack in the chip resulting in air seeping in during the gas changing process. This is assumed not to affect the experiment (see text).

# Chapter 8

## General discussion and conclusions

In the previous three chapters, I presented results using different experimental methods to study the electrochemical oxidation of propene. In the first part of this final chapter, I aim at relating these results in a general discussion. In the second part, I summarize the main conclusions and provide some ideas for future work.

### 8.1 General discussion

Propene oxidation on high surface area Pd electrodes at constant potential results in a mixture of several different products, with a complex dependency on the applied potential, as shown in Chapter 5. While current density is generally very low, there is a maximum in current density at ca. 0.9 V *vs.* RHE, which coincides with a high selectivity towards allyl oxidation products in the same potential range. DFT modeling of the reaction (see Paper I, Appendix B), suggests that on a clean Pd(111) surface there is a driving force for oxidative adsorption of propene by abstraction of an allylic proton, which is followed by coordination to the vinylic moiety. As a consequence, scission of C–C bonds becomes favorable, leaving behind strongly adsorbed C<sub>x</sub>H<sub>y</sub> species. Alternatively, the initial adsorption can be followed by further oxidation of the allylic position, abstraction of additional protons, and concurrent movement to a 3-fold hollow site. Kinetic barriers for oxidation of the allylic carbon by insertion of oxygen are very high on such a surface. Simulating a highly covered surface in the DFT

model by addition of CO as a model spectator species prevents propene degradation, and significantly lowers the barriers for allylic oxidation. We therefore propose that an *in-situ* formed surface adsorbate layer of propene degradation products enables the selective oxidation in the allylic position, by sterically hindering the energetically more favorable (co-) adsorption through the double bond, which requires more space available at the surface. Figure 8.1 summarizes this proposed mechanism schematically.

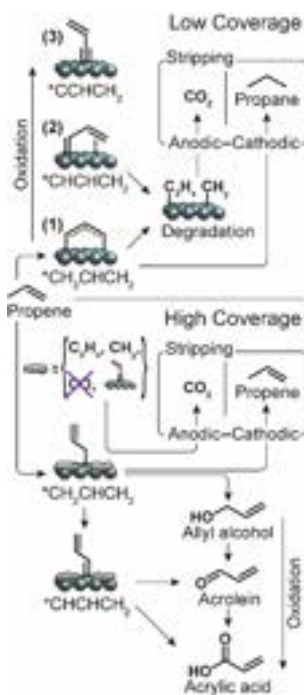


**Figure 8.1** Scheme of reaction mechanisms on Pd. The top part shows possible adsorption processes for a low coverage regime, and the resulting species desorbing in propene stripping experiments. The bottom part shows the same for a high coverage regime, where allylic oxidation is possible. Figure by Luca Silvioli, modified from Paper I. CO is crossed out, as I showed with SEIRAS that it is not present in any measurable amounts.

EC-MS experiments corroborate this proposed mechanism: Adsorption of propene at different potentials, followed by stripping of the adsorbate first cathodically then anodically, confirms the presence of a stably bound surface species. At lower purge potentials, the total amount of desorbing molecules suggests a coverage below the coverage of the electrode with CO. At the potentials where the highest selectivity for

allylic oxidation is observed, the coverage on a carbon atom basis is greater than the CO coverage, indicative of a highly populated surface under these conditions, in alignment with the DFT calculations. Further evidence for the effect of surface coverage on the mechanism comes from stripping experiments, where the coverage was controlled by partial stripping. Here the amount of propane desorption in the cathodic scan, indicative of vinylic binding, correlates with the amount of adsorbates previously removed in the form of CO<sub>2</sub>, while the amount of propene desorption is independent of the initial amount of surface adsorbate. This suggests that on a Pd surface the number of allylic adsorbates is not limited by simple availability of space, which is the case for vinylic adsorbates. Thus, we conclude that allylic adsorption is enabled by steric hindrance of other ways of coordination.

For electrochemical oxidation reactions, such a "third-body-effect" of an adsorbate steering the reaction mechanism is often talked about in the context of metal adsorbates, which are used to prevent degradation in alcohol oxidation reactions [30, 36, 37, 168]. Also in the field of selective reduction reactions, the effect of surface adsorbates is well known from Lindlar-type catalysts for the partial reduction of alkynes [169, 170]. For selective reduction of C=O bonds in the presence of C=C moieties, the effect of *in-situ* formed adsorbates [171, 172], and of added adsorbates, such as methanol, has been reported [173].

Based on this reaction mechanism, the dependence of the product distribution on the potential can be rationalized in the following way: At low potentials, there is not enough driving force for the reaction, therefore the current density is low. At intermediate potentials, there is a high enough driving force for oxidation, and partial coverage of the surface steers the reaction towards allylic oxidation, resulting in high activity and selectivity towards acrolein and acrylic acid. At high potentials, there is a lower selectivity towards acrolein due to lower surface coverage. At the same time, currents are lower, because of increased oxidation of the surface, which prevents further adsorption of propene, as commonly known for reactions following a Langmuir-Hinshelwood mechanism, such as CO-oxidation [136]. Propylene glycol is produced at higher potentials, where we expect a different reaction mechanism, involving interaction of the double bond with oxygen on the surface, to play a role.

Following from this adsorbate steered mechanism, I studied how the alloying of Pd with Au would affect surface adsorbates, as surrounding Pd atoms with Au was expected to prevent degradation and provide sites for allylic adsorption only. The observed effect of different amounts of Au in the surface on the binding of propene is sketched in Figure 8.2. I showed that the amount of  $\text{CO}_2$  per Pd atom coming off the surface in an anodic strip decreases with increasing Au content in the alloy, suggesting that already 10% Au in Pd is sufficient to reduce surface poisoning. At the same time, this surface is still covered enough to allow for adsorption in the allylic position. Interestingly, normalized to the number of Pd sites, the amount of propene bound in the allylic position seems to be significantly increased, suggesting a complex synergistic effect between adsorbate structure, sites for allylic coordination and the presence of Au on the surface. However, also the amount of propane bound in the vinylic position is increased. Based on this, I propose that alloying Pd with 10% Au improves activity, while not affecting the selectivity.

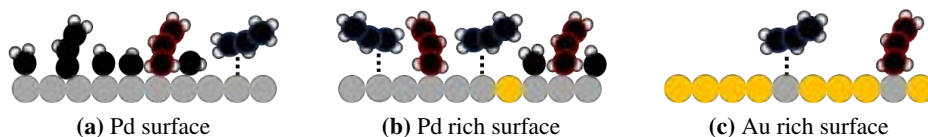


**Figure 8.2** Schematic of adsorption on different AuPd alloys. Atoms highlighted in red denote propene adsorbed in the allylic position, which desorbs cathodically as propene, while blue highlights denote vinylic adsorption, which desorbs cathodically as propane. The number of allylic and vinylic adsorbates on the different surfaces does not represent the absolute numbers observed experimentally.

The opposite case, a catalyst with 10% Pd in Au (Au rich), shows similar amounts of allylic coordination per Pd site as the Pd rich catalyst, but much more vinylic coordination, and no dependence on surface coverage. The ratio between propene and propane is roughly 1:20. For Pd and the Pd rich alloy, it is only between 1:5 to 1:8, while for Au, the ratio is the opposite, *i.e.* ca. 10 times more propene desorbs than propane. For Au, as I argued above, the amount of propane desorbing is limited by the availability of hydrogen on the surface rather than the coordination of propene to the surface. Therefore, a similar behavior would be expected in the presence of low amounts of Pd, as propene is expected to preferentially adsorb to the Pd atoms,

blocking them for hydrogen adsorption. The opposite is observed. An explanation for this behavior is not straightforward. A higher Au content in the alloy shifts the onset of propane evolution towards more negative potentials, and closer to the onset of HER, as discussed in Chapter 6, which suggests that binding of H to the surface influences propane desorption. H-binding is not expected to occur on Au atoms, especially since no propane evolution was seen on pure Au at the same potentials. However, island formation from dispersed Pd on the surface of a AuPd alloy has been observed at room temperature in the presence of CO [113]. A possible explanation of propane formation on the Au rich alloy is therefore the formation of Pd islands in the presence of propene, which are not large enough to provide sites for poisoning, but are large enough to enable propene hydrogenation. A comparison between the numbers of isolated Pd sites on the surface before and after the series of propene experiments (as determined from the ratio between CO stripping charge and hydrogen desorption in the absence of CO), indicates that there are more isolated Pd atoms after experiments with propene, which would disprove this hypothesis. However, the surface was cleaned by cycling the potential several times, during which the isolated Pd sites could have been re-established. The surface enrichment with Pd observed with XPS and ISS after the reaction is also an indication of high mobility of the atoms under reaction conditions. Still, this explanation is highly speculative and additional experiments are necessary to verify this. What is clear from the present results is that changes in surface composition induced by the potential [158], dissolution [112], or the interaction with surface adsorbates [113, 159, 174, 175] have to be considered when studying the reaction mechanism of propene oxidation on AuPd surfaces.

As opposed to measuring desorption products, SEIRAS provides a more direct way of observing surface adsorbates. However, the method requires a specific coordination geometry to be able to observe the bond vibrations of molecules bound to the surface. In the presence of propene, three features are observed on a Pd electrode, which are related to the change of the water structure in the vicinity of the electrode, probably due to the removal of organic adsorbates at oxidizing potential. Only a small negative peak is present, which can be assigned to a C–H vibration mode. Comparing this with the various adsorption geometries predicted by DFT (some are shown in the Supplementary Material of Paper I, Appendix A), this is not surprising: Most C–H bonds are parallel

or close to parallel to the surface, and also C–C bonds are generally oriented in low angles away from the surface, resulting in low IR absorption. In addition, the change in dipole moment for vibrations of these bonds is low, meaning that the IR absorption per molecule is naturally low. While the change in dipole moment for C–O bonds in intermediates after partial oxidation would be higher, the geometry is not favorable either, and their number at the surface is assumed to be low. This means that the absence of strong signals in the SEIRAS spectra does not necessarily disprove the presence of surface adsorbates. Contrarily, a further indication of their presence is that propene can be displaced from the surface by CO.

The comparison of propene and allyl alcohol spectra shows that there is a clear difference in the poisoning mechanism: In the presence of propene, no CO was observed, while with allyl alcohol in the electrolyte, CO is present on the surface. Considering the structure of the molecules, a main difference is that, in the case of allyl alcohol, oxygen is part of the molecule. To form CO, some bonds have to break, but no new ones have to be formed. According to the DFT calculations presented in Paper I, oxygen insertion to form allyl alcohol is the rate limiting step for propene oxidation; after formation, allyl alcohol will desorb, or be further oxidized to acrolein. However, this is only possible on an adsorbate covered surface. Therefore, in the presence of propene and at potentials where CO is stable, there are not enough free sites for allyl alcohol to adsorb and dissociate, hence no CO is detected. Without propene, allyl alcohol adsorbs and can dissociate under CO formation on the surface. It is known from alcohol oxidation that oxygen insertion is what makes full oxidation of methanol and ethanol more difficult than oxidation of formic acid [136]. My results are also in line with studies showing activity for allyl alcohol oxidation, but not for propene [46, 57].

## 8.2 Conclusions and outlook

### 8.2.1 Summary and conclusions

In this thesis, a thorough analysis of propene oxidation on Pd and AuPd alloys was presented, with focus on the effect of surface adsorbates on reaction mechanism and product distribution. The most important conclusions from this work can be summarized as follows:

- The observed product distribution is largely in agreement with literature [52, 53]. Besides the products described previously, allyl alcohol and propylene glycol were identified as propene oxidation products on Pd. The optimal potential for oxidation of the allylic position was found at ca. 0.9 V vs. RHE: The selectivity towards acrolein and acrylic acid is facilitated by surface adsorbates promoting allylic coordination by steric effects. At this potential, there is a balance between surface population by organic adsorbates and oxygen species, where the presence of the latter is required by the Langmuir-Hinshelwood-type reaction mechanism.
- The activity for propene oxidation can be significantly improved by adding 10% Au to Pd, while presumably maintaining the selectivity towards allylic oxidation.
- Due to adsorption geometry and generally low IR-activity of the adsorbed species, it is difficult to directly observe these using SEIRAS. Nevertheless, there is no evidence of poisoning by CO during propene oxidation, in contrast with the oxidation of allyl alcohol. This can be seen as a confirmation of oxygen insertion into the molecule being the rate limiting step.

Furthermore, a method for reliable quantification of reaction products was developed in the course of this work, as well as a versatile method for the preparation of high surface area Pd and Pd-Au alloy electrodes.

### 8.2.2 Outlook

Based on the work presented in this thesis, some questions regarding the reaction mechanism of propene oxidation could be answered, but these answers open up many more questions. The results presented in Chapters 6 and 7 are based on ongoing work,

which had not been completed in time to be included in this thesis. To answer some of the questions addressed in the first section of the present chapter, I will perform the following additional experiments in the near future:

- Determine the product distribution as a function of Au concentration in Pd using similar methods as for the results shown in Chapter 5.
- Determine the effect of CO displacement on desorption products using EC-MS.
- Determine whether it is possible to measure changes in Pd distribution on the surface in the presence of propene, for example by using EXAFS on thin films of a few nanometer thickness [137, 159].

More generally speaking, I think there are several directions in which future research should go, to further contribute to our understanding of the mechanisms behind electrochemical partial oxidation of hydrocarbons. The first direction I would suggest, is to study further how a surface can be engineered to give high selectivity for allylic oxidation while providing higher activity than pure Pd. To this end, surface modification of Pd by irreversible adsorption of for example Sn, Bi or Sb, which have proven to increase activity for alcohol oxidation, could provide a more well defined, stable surface structure, without the disadvantage of Au which is also catalytically active for propene oxidation.

As mentioned in Chapter 2, different products have been reported at different pH in different studies, but the effect of pH has to my knowledge never been tested on the same catalyst. In alkaline conditions, it is easier to adsorb OH to the surface, which could reduce surface poisoning. At the same time, the pH will also affect the stability of different products in solution.

While Pd exhibits high selectivity for allylic oxidation, propylene oxide and glycol are the more interesting products from a commercial point of view. Propylene glycol was observed at higher potentials, where surface oxidation was limiting the reaction rates. It could be worthwhile to test whether the limitation is due to low conductivity of the oxidized Pd surface, or adsorption of propene, for example by testing the reactivity of conductive oxides such as RuO<sub>2</sub> or IrO<sub>2</sub>.

Eventually, the understanding gained on propene could be extended to other hydrocarbons, both saturated and unsaturated ones, to further explore how the binding

---

configuration and geometry influences product distribution. Last but not least, tests in a fuel-cell-type reactor can be beneficial to avoid limitations due to the low solubility of propene in water, and the degradation of products in the electrolyte, if they can be separated in a shorter timescale using such a reactor.



# References

- [1] British Petroleum (BP). *BP Statistical Review of World Energy 2019*. Tech. rep. 2019. DOI: 10.2307/3324639. URL: <https://www.jstor.org/stable/3324639?origin=crossref>.
- [2] B. Burger. *Net Public Electricity Generation in Germany in 2018*. Tech. rep. Fraunhofer Institute ISE, 2019. URL: [https://www.energy-charts.de/downloads/electricity\\_production\\_germany\\_2018\\_2.pdf](https://www.energy-charts.de/downloads/electricity_production_germany_2018_2.pdf).
- [3] International Renewable Energy Agency (IRENA). *Renewable Power : Climate-Safe Energy competes on cost alone*. 2018. URL: [https://www.irena.org/-/media/Files/IRENA/Agency/Publication/2018/Dec/IRENA\\_COP24\\_costs\\_update\\_2018.pdf](https://www.irena.org/-/media/Files/IRENA/Agency/Publication/2018/Dec/IRENA_COP24_costs_update_2018.pdf).
- [4] Energistyrelsen. *Energistatistik 2017*. Tech. rep. 2017. URL: <https://ens.dk/service/statistik-data-noegletal-og-kort/maanedlig-og-aarlig-energistatistik>.
- [5] Danish Ministry of Climate Energy and Utilities. *Denmark's Draft Integrated National Energy and Climate Plan*. 2018. URL: [https://ens.dk/sites/ens.dk/files/EnergiKlimapolitik/denmarks\\_draft\\_integrated\\_energy\\_and\\_climate\\_plan.pdf](https://ens.dk/sites/ens.dk/files/EnergiKlimapolitik/denmarks_draft_integrated_energy_and_climate_plan.pdf).
- [6] N. Adaduldah, A. Dorsman, G. J. Franx, and P. Pottuijt. “The Influence of Renewables on the German Day Ahead Electricity Prices”. In: *Perspectives on Energy Risk*. Ed. by A. Dorsman, T. Gök, and M. B. Karan. Berlin, Heidelberg: Springer Berlin Heidelberg, 2014, pp. 165–182. DOI: 10.1007/978-3-642-41596-8\_10.
- [7] E. Fanone, A. Gamba, and M. Prokopczuk. “The case of negative day-ahead electricity prices”. In: *Energy Economics* 35.May 2008 (2013), pp. 22–34. DOI: 10.1016/j.eneco.2011.12.006.
- [8] Energinet.dk. *PtX i Danmark før 2030*. Tech. rep, Energinet, 2019. URL: <https://energinet.dk/Analyse-og-Forskning/Analyser/RS-Analyse-April-2019-PtX-i-Danmark-foer-2030>.
- [9] R. Schlögl. “Chemistry’s Role in Regenerative Energy”. English. In: *Ange wandte Chemie International Edition* 50.29 (2011), pp. 6424–6426. DOI: 10.1002/anie.201103415.

- [10] Energinet.dk. 2019. URL: <https://www.energidataservice.dk/dataset/electricitybalance>.
- [11] P. De Luna, C. Hahn, D. Higgins, S. A. Jaffer, T. F. Jaramillo, and E. H. Sargent. “What would it take for renewably powered electrosynthesis to displace petrochemical processes?” In: *Science* 364.6438 (2019). DOI: 10.1126/science.aav3506.
- [12] Z. W. Seh, J. Kibsgaard, C. F. Dickens, I. Chorkendorff, J. K. Nørskov, and T. F. Jaramillo. “Combining theory and experiment in electrocatalysis: Insights into materials design”. In: *Science* 355.6321 (2017), eaad4998. DOI: 10.1126/science.aad4998.
- [13] S. A. Nitopi, E. Bertheussen, S. B. Scott, X. Liu, K. Albert, S. Horch, B. Seger, I. E. L. Stephens, K. Chan, J. K. Nørskov, T. F. Jaramillo, and I. Chorkendorff. “Progress and Perspectives of Electrochemical CO<sub>2</sub> Reduction on Copper in Aqueous Electrolyte”. In: *Chemical Reviews* (2018). DOI: 10.1021/acs.chemrev.8b00705.
- [14] C. Reller, R. Krause, E. Volkova, B. Schmid, S. Neubauer, A. Rucki, M. Schuster, and G. Schmid. “Selective Electroreduction of CO<sub>2</sub> toward Ethylene on Nano Dendritic Copper Catalysts at High Current Density”. In: *Advanced Energy Materials* 7.12 (2017), p. 1602114. DOI: 10.1002/aenm.201602114.
- [15] M. Jouny, W. Luc, and F. Jiao. “General Techno-Economic Analysis of CO<sub>2</sub> Electrolysis Systems”. In: *Industrial and Engineering Chemistry Research* 57.6 (2018), pp. 2165–2177. DOI: 10.1021/acs.iecr.7b03514.
- [16] A. Wiebe, T. Gieshoff, S. Möhle, E. Rodrigo, M. Zirbes, and S. R. Waldvogel. “Electrifying Organic Synthesis”. In: *Angewandte Chemie - International Edition* 57.20 (2018), pp. 5594–5619. DOI: 10.1002/anie.201711060.
- [17] S. Möhle, M. Zirbes, E. Rodrigo, T. Gieshoff, A. Wiebe, and S. R. Waldvogel. “Modern Electrochemical Aspects for the Synthesis of Value-Added Organic Products”. In: *Angewandte Chemie - International Edition* 57.21 (2018), pp. 6018–6041. DOI: 10.1002/anie.201712732.
- [18] M. T. M. Koper. “Electrochemistry for the Production of Fuels, Chemicals and Materials”. In: *Catalysis in Chemistry and Biology*. World Scientific, 2018, pp. 229–232. DOI: 10.1142/9789813237179\_0033.
- [19] A. F. Lee, C. V. Ellis, J. N. Naughton, M. A. Newton, C. M. Parlett, and K. Wilson. “Reaction-driven surface restructuring and selectivity control in allylic alcohol catalytic aerobic oxidation over Pd”. In: *Journal of the American Chemical Society* 133.15 (2011), pp. 5724–5727. DOI: 10.1021/ja200684f.
- [20] N. S. Lewis and D. G. Nocera. “Powering the planet: Chemical challenges in solar energy utilization”. English. In: *Proceedings of the National Academy of Sciences* 103.43 (2006), pp. 15729–15735. DOI: 10.1073/pnas.0603395103.

- [21] N. Danilovic, K. E. Ayers, C. Capuano, J. N. Renner, L. Wiles, and M. Perotto. "(Plenary) Challenges in Going from Laboratory to Megawatt Scale PEM Electrolysis". In: *ECS Transactions* 75.14 (2016), pp. 395–402. DOI: 10.1149/07514.0395ecst.
- [22] BNP Paribas. *EROCI and the tough road ahead for oil*. 2019. URL: <https://docfinder.bnpparibas-am.com/api/files/1094E5B9-2FAA-47A3-805D-EF65EAD09A7F>.
- [23] British Petroleum (BP). *Energy demand by sector*. 2019. URL: <https://www.bp.com/en/global/corporate/energy-economics/energy-outlook/demand-by-sector.html>.
- [24] D. Victor, D. Zhou, E. H. M. Ahmed, P. K. Dadhich, J. G. J. Olivier, H.-H. Rogner, K. Sheikho, and M. Yamaguchi. "Introductory Chapter". In: *Climate Change 2014: Mitigation of Climate Change. Contribution of Working Group III to the Fifth Assessment Report of the Intergovernmental Panel on Climate Change*. Ed. by O. Edenhofer, R. Pichs-Madruga, Y. Sokona, E. Farahani, S. Kadner, K. Seyboth, A. Adler, I. Baum, S. Brunner, P. Eickemeier, B. Kriemann, J. Savolainen, S. Schlömer, C. von Stechow, T. Zwickel, and J. Minx. Cambridge, United Kingdom and New York, NY, USA: Cambridge University Press, 2014.
- [25] A Boulamanti and J. A. Moya. "Energy efficiency and GHG emissions: Prospective scenarios for the chemical and petrochemical industry". In: (2017). DOI: 10.2760/20486.
- [26] M. Nič, J. Jirát, B. Košata, A. Jenkins, and A. McNaught, eds. *IUPAC Compendium of Chemical Terminology*. Research Triangle Park, NC: IUPAC, 2009. DOI: 10.1351/goldbook.
- [27] I Chorkendorff and J. W. Niemantsverdriet. *Concepts of Modern Catalysis and Kinetics*. 2003. DOI: 10.1002/3527602658.
- [28] P. Sabatier. *La catalyse en chimie organique*. Librairie Polytechnique, Paris et Liège, 1920. DOI: 10.14375/np.9782369430186.
- [29] E. Skúlason, V. Tripkovic, M. E. Björketun, S. Gudmundsdóttir, G. Karlberg, J. Rossmeisl, T. Bligaard, H. Jónsson, and J. K. Nørskov. "Modeling the Electrochemical Hydrogen Oxidation and Evolution Reactions on the Basis of Density Functional Theory Calculations". In: *The Journal of Physical Chemistry C* 114.42 (2010), pp. 18182–18197. DOI: 10.1021/jp1048887.
- [30] V. Climent, N. Garca-Arez, and J. Feliu. "Clues for the Molecular-Level Understanding of Electrocatalysis on Single-Crystal Platinum Surfaces Modified by p-Block Adatoms". In: *Fuel Cell Catalysis: A Surface Science Approach*. Ed. by M. T. M. Koper. Hoboken, NJ, USA: John Wiley & Sons, Inc., 2009, pp. 209–244. DOI: 10.1002/9780470463772.ch7.

- [31] T Bligaard and J. K. Nørskov. “Ligand effects in heterogenous catalysis and electrochemistry”. In: *Electrochim. Acta* 52.18 (2007), pp. 5512–5516. DOI: 10.1016/j.electacta.2007.02.041.
- [32] V. Stamenkovic, B. S. Mun, K. J. J. Mayrhofer, P. N. Ross, N. M. Marković, J. Rossmeisl, J. Greeley, and J. K. Nørskov. “Changing the Activity of Electrocatalysts for Oxygen Reduction by Tuning the Surface Electronic Structure”. In: *Angewandte Chemie* 118.18 (2006), pp. 2963–2967. DOI: 10.1002/ange.200504386.
- [33] V. R. Stamenkovic, B Fowler, B. S. Mun, G Wang, P. N. Ross, C. A. Lucas, and N. M. Markovic. “Improved Oxygen Reduction Activity on Pt<sub>3</sub>Ni(111) via Increased Surface Site Availability”. In: *Science* 315.5811 (2007), pp. 493–497. DOI: 10.1126/science.1135941.
- [34] J Greeley, I. E. L. Stephens, a. S. Bondarenko, T. P. Johansson, H. a. Hansen, T. F. Jaramillo, J Rossmeisl, I Chorkendorff, and J. K. Nørskov. “Alloys of platinum and early transition metals as oxygen reduction electrocatalysts”. In: *Nature Chemistry* 1.7 (2009), pp. 552–556. DOI: 10.1038/nchem.367.
- [35] M. Escudero-Escribano, P. Malacrida, M. H. Hansen, U. G. Vej-Hansen, A. Velázquez-Palenzuela, V. Tripkovic, J. Schiøtz, J. Rossmeisl, I. E. Stephens, and I. Chorkendorff. “Tuning the activity of Pt alloy electrocatalysts by means of the lanthanide contraction”. In: *Science* 352.6281 (2016), pp. 73–76. DOI: 10.1126/science.aad8892.
- [36] E. Antolini. “Catalysts for direct ethanol fuel cells”. In: *Journal of Power Sources* 170.1 (2007), pp. 1–12. DOI: 10.1016/j.jpowsour.2007.04.009.
- [37] W. Li. “Anode Catalysts for Low-Temperature Direct Alcohol Fuel Cells”. In: *Materials for Low-Temperature Fuel Cells* (2015), pp. 69–110. DOI: 10.1002/9783527644308.ch04.
- [38] S. Siahrostami, A. Verdaguier-Casadevall, M. Karamad, D. Deiana, P. Malacrida, B. Wickman, M. Escudero-Escribano, E. A. Paoli, R. Frydendal, T. W. Hansen, I. Chorkendorff, I. E. L. S. Stephens, J. Rossmeisl, I. E. L. S. Stephens, and J. Rossmeisl. “Enabling direct H<sub>2</sub>O<sub>2</sub> production through rational electrocatalyst design”. In: *Nature Materials* 12.12 (2013), pp. 1137–1143. DOI: 10.1038/nmat3795.
- [39] A. J. Medford, A. Vojvodic, J. S. Hummelshøj, J. Voss, F. Abild-Pedersen, F. Studt, T. Bligaard, A. Nilsson, and J. K. Nørskov. “From the Sabatier principle to a predictive theory of transition-metal heterogeneous catalysis”. In: *Journal of Catalysis* 328 (2015), pp. 36–42. DOI: 10.1016/j.jcat.2014.12.033.
- [40] J. H. Montoya, L. C. Seitz, P. Chakthranont, A. Vojvodic, T. F. Jaramillo, and J. K. Nørskov. “Materials for solar fuels and chemicals”. In: *Nature Materials* 16.1 (2017), pp. 70–81. DOI: 10.1038/nmat4778.

- [41] A. J. Bard and L. R. Faulkner. *Electrochemical Methods: Fundamentals and Applications*. 2nd. New York: John Wiley & Sons, Inc., 2001, p. 833. DOI: 10.1016/B978-0-08-098353-0.00003-8.
- [42] L. L. Holbrook and H. Wise. “Electrooxidation of olefins at a silver electrode”. In: *Journal of Catalysis* 1-3 (), pp. 294–298. DOI: 10.1016/0021-9517(75)90090-1.
- [43] T.-C. Chou and J.-C. Chang. “Anodic oxidation of propylene on a screen electrode”. In: *Chemical Engineering Science* 35 (1980), pp. 1581–1590.
- [44] C. F. Oduoza and K. Scott. “Aspects of the Direct Electrochemical Oxidation of Propylene”. In: *ICHEME symposium series* 127.127 (1992), pp. 37–48.
- [45] K. Scott, C. Oduoza, and W. Hui. “Pilot scale electrosynthesis of alkene oxides by direct and indirect oxidation in a sieve plate electrochemical reactor”. In: *Chemical Engineering Science* 47.9-11 (1992), pp. 2957–2962. DOI: 10.1016/0009-2509(92)87158-M.
- [46] G. Göransson, J. S. Jirkovský, P. Krtil, and E. Ahlberg. “Oxidation of propenol on nanostructured Ni and NiZn electrodes in alkaline solution”. In: *Electrochimica Acta* 139 (2014), pp. 345–355. DOI: 10.1016/j.electacta.2014.06.169.
- [47] J. O. Bockris, H. Wroblowa, E. Gileadi, and B. J. Piersma. “Anodic oxidation of unsaturated hydrocarbons on platinized electrodes”. In: *Transactions of the Faraday Society* 61 (1965), p. 2531. DOI: 10.1039/tf9656102531.
- [48] M. Beltowska-Brzezinska, T. Łuczak, H. Baltruschat, and U. Müller. “Propene Oxidation and Hydrogenation on a Porous Platinum Electrode in Acidic Solution”. In: *The Journal of Physical Chemistry B* 107.20 (2003), pp. 4793–4800. DOI: 10.1021/jp021726f.
- [49] V. M. Schmidt and E. Pastor. “Electro-oxidation of propene on gold in acid solution studied by DEMS and FTIRS”. In: *Journal of Electroanalytical Chemistry* 401.1-2 (1996), pp. 155–161. DOI: 10.1016/0022-0728(95)04299-7.
- [50] J. L. Rodríguez, E. Pastor, and V. M. Schmidt. “Reactions of Unsaturated Hydrocarbons at the Gold/Electrolyte Interface in Acid Solution”. In: *The Journal of Physical Chemistry B* 101.23 (1997), pp. 4565–4574. DOI: 10.1021/jp962261u.
- [51] H. Kinza. “Zur elektrokatalytischen Oxydation von Propen mit molekularem Sauerstoff”. In: *Zeitschrift für Physikalische Chemie* 255.3 (1974), pp. 517–537.
- [52] G. R. Stafford. “The Electrogenative Partial Oxidation of Propylene”. In: *Electrochimica Acta* 32.8 (1987), pp. 1137–1143.
- [53] K. Otsuka, Y. Shimizu, I. Yamanaka, and T. Komatsu. “Wacker type and pi-allyl type oxidations of propylene controlled by fuel cell system in the gas phase”. In: *Catalysis Letters* 3 (1989), pp. 365–370.

- [54] K. Otsuka, T. Ushiyama, I. Yamanaka, and K. Ebitani. “Electrocatalytic synthesis of propylene oxide during water electrolysis”. In: *Journal of Catalysis* 157.2 (1995), pp. 450–460. DOI: 10.1006/jcat.1995.1310.
- [55] F Goodridge, S Harrison, and R. Plimley. “The electrochemical production of propylene oxide”. In: *Journal of Electroanalytical Chemistry and Interfacial Electrochemistry* 214.1-2 (1986), pp. 283–293. DOI: 10.1016/0022-0728(86)80103-6.
- [56] W. Hui. “The design of a sieve plate electrochemical reactor for epoxidation”. PhD thesis. University of Teesside, 1992.
- [57] A. Zimmer, D. Mönter, and W. Reschetilowski. “Catalytic epoxidation with electrochemically in situ generated hydrogen peroxide”. In: *Journal of Applied Electrochemistry* 33.10 (2003), pp. 933–937. DOI: 10.1023/A:1025881213041.
- [58] S. Hamakawa, T. Hayakawa, T. Tsunoda, K. Suzuki, K. Murata, and K. Takehira. “Partial Oxidation of Propene to Acrylaldehyde with an Electrochemical Membrane Reactor Coated with Yttria-Stabilized Zirconia”. In: *Electrochemical and Solid-State Letters* 1.5 (1999), p. 220. DOI: 10.1149/1.1390691.
- [59] F. W. Zemichael, A. Al-Musa, I. W. Cumming, and K. Hellgardt. “Propene partial oxidation over Au-Ag Alloy and Ag catalysts using electrochemical oxygen”. In: *Solid State Ionics* 179.27-32 (2008), pp. 1401–1404. DOI: 10.1016/j.ssi.2008.03.011.
- [60] Nexant. *Nexant Petroleum and Petrochemical Economics (PPE) Program*. Tech. rep. 2017.
- [61] C. J. Sullivan, A. Kuenz, and K.-D. Vorlop. “Propanediols”. In: *Ullmann’s Encyclopedia of Industrial Chemistry*. Weinheim, Germany: Wiley-VCH Verlag GmbH & Co. KGaA, 2018, pp. 1–15. DOI: 10.1002/14356007.a22\_163.pub2.
- [62] M. Weber, W. Pompetzki, R. Bonmann, and M. Weber. “Acetone”. In: *Ullmann’s Encyclopedia of Industrial Chemistry*. Weinheim, Germany: Wiley-VCH Verlag GmbH & Co. KGaA, 2014, pp. 1–19. DOI: 10.1002/14356007.a01\_079.pub4.
- [63] D. Arntz, A. Fischer, M. Höpp, S. Jacobi, J. Sauer, T. Ohara, T. Sato, N. Shimizu, and H. Schwind. “Acrolein and Methacrolein”. In: *Ullmann’s Encyclopedia of Industrial Chemistry*. Weinheim, Germany: Wiley-VCH Verlag GmbH & Co. KGaA, 2007. DOI: 10.1002/14356007.a01\_149.pub2.
- [64] W. G. Etzkorn. “Acrolein and Derivatives”. In: *Kirk-Othmer Encyclopedia of Chemical Technology*. Hoboken, NJ, USA: John Wiley & Sons, Inc., 2009, pp. 1–29. DOI: 10.1002/0471238961.0103181505202611.a01.pub3.
- [65] T. Ohara, T. Sato, N. Shimizu, G. Prescher, H. Schwind, O. Weiberg, K. Marten, and H. Greim. “Acrylic Acid and Derivatives”. In: *Ullmann’s Encyclopedia of Industrial Chemistry*. Weinheim, Germany: Wiley-VCH Verlag GmbH & Co. KGaA, 2011. DOI: 10.1002/14356007.a01\_161.pub3.

- [66] L. Krähling, J. Krey, G. Jakobson, J. Grolig, and L. Miksche. “Allyl Compounds”. In: *Ullmann's Encyclopedia of Industrial Chemistry*. Vol. 11. Weinheim, Germany: Wiley-VCH Verlag GmbH & Co. KGaA, 2000, pp. 122–123. DOI: 10.1002/14356007.a01\_425.
- [67] D. Trent. “Propylene oxide”. In: *Kirk-Othmer Encyclopedia of Chemical technology* (2001). DOI: 10.1002/0471238961.1618151620180514.a01.pub2.
- [68] W. L. Howard. “Acetone”. In: *Kirk-Othmer Encyclopedia of Chemical Technology*. Vol. 08. Hoboken, NJ, USA: John Wiley & Sons, Inc., 2011, pp. 1–15. DOI: 10.1002/0471238961.0103052008152301.a01.pub3.
- [69] T. A. Nijhuis, M. Makkee, J. A. Moulijn, and B. M. Weckhuysen. “The production of propene oxide: Catalytic processes and recent developments”. In: *Industrial and Engineering Chemistry Research* 45.10 (2006), pp. 3447–3459. DOI: 10.1021/ie0513090.
- [70] S. J. Khatib and S. T. Oyama. “Direct Oxidation of Propylene to Propylene Oxide with Molecular Oxygen: A Review”. In: *Catalysis Reviews* 57.3 (2015), pp. 306–344. DOI: 10.1080/01614940.2015.1041849.
- [71] F. Cavani and A. M. Gaffney. “Synthesis of Propene Oxide: A Successful Example of Sustainable Industrial Chemistry”. In: *Sustainable Industrial Chemistry*. Weinheim, Germany: Wiley-VCH Verlag GmbH & Co. KGaA, 2009, pp. 319–365. DOI: 10.1002/9783527629114.ch6.
- [72] C. A. Sequeira and D. M. Santos. “Electrochemical routes for industrial synthesis”. In: *Journal of the Brazilian Chemical Society* 20.3 (2009), pp. 387–406. DOI: 10.1590/S0103-50532009000300002.
- [73] R. Ojani, E. Hasheminejad, and J. B. Raoof. “Hydrogen evolution assisted electrodeposition of bimetallic 3D nano/micro-porous PtPd films and their electrocatalytic performance”. In: *International Journal of Hydrogen Energy* 39.16 (2014), pp. 8194–8203. DOI: 10.1016/j.ijhydene.2014.03.162. URL: <http://dx.doi.org/10.1016/j.ijhydene.2014.03.162>.
- [74] J. Liu, L. Cao, W. Huang, and Z. Li. “Direct electrodeposition of PtPd alloy foams comprised of nanodendrites with high electrocatalytic activity for the oxidation of methanol and ethanol”. In: *Journal of Electroanalytical Chemistry* 686 (2012), pp. 38–45. DOI: 10.1016/j.jelechem.2012.09.020.
- [75] H. Miyake, E. Hosono, M. Osawa, and T. Okada. “Surface-enhanced infrared absorption spectroscopy using chemically deposited Pd thin film electrodes”. In: *Chemical Physics Letters* 428.4-6 (2006), pp. 451–456. DOI: 10.1016/j.cplett.2006.07.063.
- [76] J. Shu, B. P. Grandjean, E. Ghali, and S. Kaliaguine. “Simultaneous deposition of Pd and Ag on porous stainless steel by electroless plating”. In: *Journal of Membrane Science* 77.2-3 (1993), pp. 181–195. DOI: 10.1016/0376-7388(93)85068-8.

- [77] D. Brandon and W. D. Kaplan. *Microstructural Characterization of Materials - 2nd Edition*. John Wiley & Sons Ltd., 2008.
- [78] W. J. Callister Jr. *Material Science and Engineering: An introduction*. 7th. John Wiley & Sons, Inc., 2006.
- [79] Metrohm Autolab B.V. *Basic overview of the working principle of a potentiostat/galvanostat (PGSTAT) – Electrochemical cell setup*. 2011.
- [80] E. Bertheussen, T. V. Hogg, Y. Abghoui, A. K. Engstfeld, I. Chorkendorff, and I. E. Stephens. “Electroreduction of CO on Polycrystalline Copper at Low Overpotentials”. In: *ACS Energy Letters* 3.3 (2018), pp. 634–640. DOI: 10.1021/acseenergylett.8b00092.
- [81] E. Bertheussen. “Electroreduction of carbon monoxide on copper electrodes”. PhD thesis. Technical University of Denmark, 2018.
- [82] X.-Z. Yuan, C. Song, H. Wang, and J. Zhang. *Electrochemical Impedance Spectroscopy in PEM Fuel Cells*. London: Springer London, 2010. DOI: 10.1007/978-1-84882-846-9.
- [83] T. Mittermeier, A. Weiß, H. A. Gasteiger, and F. Hasché. “Monometallic Palladium for Oxygen Reduction in PEM Fuel Cells: Particle-Size Effect, Reaction Mechanism, and Voltage Cycling Stability”. In: *Journal of The Electrochemical Society* 164.12 (2017), F1081–F1089. DOI: 10.1149/2.0561712jes.
- [84] A. Czerwiński. “The adsorption of carbon oxides on a palladium electrode from acidic solution”. In: *Journal of Electroanalytical Chemistry* 379.1-2 (1994), pp. 487–493. DOI: 10.1016/0022-0728(94)87173-6.
- [85] S. Zou, R. Gómez, and M. J. Weaver. “Infrared spectroscopy of carbon monoxide at the ordered palladium (110) - Aqueous interface: Evidence for adsorbate-induced surface reconstruction”. In: *Surface Science* 399.2-3 (1998), pp. 270–283. DOI: 10.1016/S0039-6028(97)00826-1.
- [86] S. Zou, R. Gómez, and M. J. Weaver. “Coverage-dependent infrared spectroscopy of carbon monoxide on palladium(100) in aqueous solution: adlayer phase transitions and electrooxidation pathways”. In: *Langmuir* 15.8 (1999), pp. 2931–2939. DOI: 10.1021/la9817720.
- [87] S. Zou, R. Gómez, and M. J. Weaver. “Infrared spectroscopy of carbon monoxide and nitric oxide on palladium(111) in aqueous solution: Unexpected adlayer structural differences between electrochemical and ultrahigh-vacuum interfaces”. In: *Journal of Electroanalytical Chemistry* 474.2 (1999), pp. 155–166. DOI: 10.1016/S0022-0728(99)00329-0.
- [88] M. Łukaszewski, M. Soszko, and A. Czerwiński. “Electrochemical methods of real surface area determination of noble metal electrodes - an overview”. In: *International Journal of Electrochemical Science* 11.6 (2016), pp. 4442–4469. DOI: 10.20964/2016.06.71.

- [89] M. Grdeń, M. Łukaszewski, G. Jerkiewicz, and A. Czerwiński. “Electrochemical behaviour of palladium electrode: Oxidation, electrodisolution and ionic adsorption”. In: *Electrochimica Acta* 53.26 (2008), pp. 7583–7598. DOI: 10.1016/j.electacta.2008.05.046.
- [90] C. W. Li and M. W. Kanan. “CO<sub>2</sub> reduction at low overpotential on Cu electrodes resulting from the reduction of thick Cu<sub>2</sub>O films”. English. In: *Journal of the American Chemical Society* 134.17 (2012), pp. 7231–7234. DOI: 10.1021/ja3010978.
- [91] M. Łukaszewski and A. Czerwiński. “Electrochemical behavior of palladium-gold alloys”. In: *Electrochimica Acta* 48.17 (2003), pp. 2435–2445. DOI: 10.1016/S0013-4686(03)00270-6.
- [92] M. Łukaszewski, K. Hubkowska, and A. Czerwiński. “Electrochemical absorption and oxidation of hydrogen on palladium alloys with platinum, gold and rhodium”. In: *Physical Chemistry Chemical Physics* 12.43 (2010), pp. 14567–14572. DOI: 10.1039/c0cp00542h.
- [93] D. C. Harris. *Quantitative Chemical Analysis*. 8th. New York, NY: W.H. Freeman and Company, 2010.
- [94] R. Sander. “Compilation of Henry’s law constants (version 4.0) for water as solvent”. In: *Atmospheric Chemistry and Physics* 15.8 (2015), pp. 4399–4981. DOI: 10.5194/acp-15-4399-2015. URL: <https://www.atmos-chem-phys.net/15/4399/2015/>.
- [95] M. Balci. *Basic <sup>1</sup>H- and <sup>13</sup>C-NMR Spectroscopy*. Ed. by M. B. T. B. H. Balci and C.-N. Spectroscopy. Amsterdam: Elsevier Science, 2005, p. 430. DOI: <https://doi.org/10.1016/B978-044451811-8.50002-4>.
- [96] J. A. C. Broekhaert. *Analytical Atomic Spectrometry with Flames and Plasmas*. Wiley-VCH Verlag GmbH & Co. KGaA, 2002.
- [97] G. Wedler. *Lehrbuch der Physikalischen Chemie*. 5th. Weinheim, Germany: Wiley-VCH Verlag GmbH & Co. KGaA, 2004.
- [98] P. R. Griffiths and J. A. de Haseth. *Fourier Transform Infrared Spectrometry*. 2nd. Wiley Interscience, John Wiley & Sons, Inc., 2007. DOI: 10.1007/s00216-008-2144-3. eprint: 1509.00722.
- [99] M. Osawa. “Surface-Enhanced Infrared Absorption”. In: *Near-Field Optics and Surface Plasmon Polaritons*. Vol. 81. Berlin, Heidelberg: Springer Berlin Heidelberg, 2001, pp. 163–187. DOI: 10.1007/3-540-44552-8\_9.
- [100] M. Osawa. “Surface-Enhanced Infrared Absorption Spectroscopy”. In: *Compendium of Surface and Interface Analysis*. Ed. by J. M. Chalmers. Singapore: Springer Singapore, 2018, pp. 697–706. DOI: 10.1007/978-981-10-6156-1\_113.
- [101] F. Menges. *Spectragryph - optical spectroscopy software*. URL: <http://www.effemm2.de/spectragryph/>.

- [102] O. Wolter and J. Heitbaum. “Differential Electrochemical Mass Spectroscopy (DEMS) - a New Method for the Study of Electrode Processes”. In: *Berichte der Bunsengesellschaft für physikalische Chemie* 88.1 (1984), pp. 2–6. DOI: 10.1002/bbpc.19840880103.
- [103] H. Baltruschat. “Differential electrochemical mass spectrometry”. In: *Journal of the American Society for Mass Spectrometry* 15.12 (2004), pp. 1693–1706. DOI: 10.1016/j.jasms.2004.09.011.
- [104] A. H. Wonders, T. H. Housmans, V. Rosca, and M. T. Koper. “On-line mass spectrometry system for measurements at single-crystal electrodes in hanging meniscus configuration”. In: *Journal of Applied Electrochemistry* 36.11 (2006), pp. 1215–1221. DOI: 10.1007/s10800-006-9173-4.
- [105] D. B. Trimarco, S. B. Scott, A. H. Thilsted, J. Y. Pan, T. Pedersen, O. Hansen, I. Chorkendorff, and P. C. Vesborg. “Enabling real-time detection of electrochemical desorption phenomena with sub-monolayer sensitivity”. In: *Electrochimica Acta* 268 (2018), pp. 520–530. DOI: 10.1016/j.electacta.2018.02.060.
- [106] D. B. Trimarco. “Real-time detection of sub-monolayer desorption phenomena during electrochemical reactions: Instrument development and applications”. PhD thesis. Technical University of Denmark, 2017.
- [107] S. B. Scott. “Isotope-Labeling Studies in Electrocatalysis for Renewable Energy Conversion”. PhD thesis. Technical University of Denmark, 2019.
- [108] NIST Mass Spectrometry Data Center, William E. Wallace, director. “Infrared Spectra”. In: *NIST Chemistry WebBook, NIST Standard Reference Database Number 69*. Ed. by P. Linstrom and W. Mallard. Gaithersburg MD, 20899: National Institute of Standards and Technology. DOI: doi.org/10.18434/T4D303.
- [109] N. W. Ashcroft and A. R. Denton. “Vegard’s Law”. In: *Physical Review A* 43.6 (1991), pp. 3161–3164.
- [110] Thermo Fisher Scientific. “XPS Knowledge”. In: *Thermo Advantage*. 2018.
- [111] CasaXPS. *Quantification using Asymmetric Line-Shapes*. 2005. URL: [http://www.casaxps.com/help\\_manual/manual\\_updates/calib\\_asymmetric\\_peaks.pdf](http://www.casaxps.com/help_manual/manual_updates/calib_asymmetric_peaks.pdf).
- [112] E. Pizzutilo, S. J. Freakley, S. Geiger, C. Baldizzone, A. Mingers, G. J. Hutchings, K. J. J. Mayrhofer, and S. Cherevko. “Addressing stability challenges of using bimetallic electrocatalysts: the case of gold–palladium nanoalloys”. In: *Catal. Sci. Technol.* 7.9 (2017), pp. 1848–1856. DOI: 10.1039/C7CY00291B.
- [113] K. Gossner and E. Mizera. “Investigations on the adsorption and electrocatalytic oxidation of carbon monoxide on gold + palladium alloys”. In: *Journal of Electroanalytical Chemistry and Interfacial Electrochemistry* 140.1 (1982), pp. 35–45. DOI: 10.1016/0368-1874(82)85297-0.

- [114] A. V. Naumkin, A. Kraut-Vass, S. W. Gaarenstroom, and C. J. Powell. *NIST X-ray Photoelectron Spectroscopy Database*. 2012.
- [115] M. Schmid. *LEIS Energy Calculator*. 2013. URL: <http://www.iap.tuwien.ac.at/www/surface/leis>.
- [116] C. Hahn, D. N. Abram, H. A. Hansen, T. Hatsukade, A. Jackson, N. C. Johnson, T. R. Hellstern, K. P. Kuhl, E. R. Cave, J. T. Feaster, and T. F. Jaramillo. “Synthesis of thin film AuPd alloys and their investigation for electrocatalytic CO<sub>2</sub>reduction”. In: *Journal of Materials Chemistry A* 3.40 (2015), pp. 20185–20194. DOI: 10.1039/c5ta04863j.
- [117] K. P. Kuhl, E. R. Cave, D. N. Abram, and T. F. Jaramillo. “New insights into the electrochemical reduction of carbon dioxide on metallic copper surfaces”. In: *Energy & Environmental Science* 5.5 (2012), p. 7050. DOI: 10.1039/c2ee21234j.
- [118] E. Bertheussen, A. Verdaguer-Casadevall, D. Ravasio, J. H. Montoya, D. B. Trimarco, C. Roy, S. Meier, J. Wendland, J. K. Nørskov, I. E. L. Stephens, and I. Chorkendorff. “Acetaldehyde as an Intermediate in the Electroreduction of Carbon Monoxide to Ethanol on Oxide-Derived Copper”. In: *Angewandte Chemie International Edition* 55.4 (2016), pp. 1450–1454. DOI: 10.1002/anie.201508851.
- [119] E. Bertheussen, Y. Abghoui, Z. P. Jovanov, A.-S. Varela, I. E. Stephens, and I. Chorkendorff. “Quantification of liquid products from the electroreduction of CO<sub>2</sub> and CO using static headspace-gas chromatography and nuclear magnetic resonance spectroscopy”. In: *Catalysis Today* 288 (2017), pp. 54–62. DOI: 10.1016/j.cattod.2017.02.029.
- [120] Y. Y. Birdja and M. T. M. Koper. “The Importance of Cannizzaro-Type Reactions during Electrocatalytic Reduction of Carbon Dioxide”. In: *Journal of the American Chemical Society* 139.5 (2017), pp. 2030–2034. DOI: 10.1021/jacs.6b12008.
- [121] B. J. V. Davies, M. Arenz, J. Rossmeisl, and M. Escudero-Escribano. “Electrochemical Synthesis of High-Value Chemicals: Detection of Key Reaction Intermediates and Products Combining Gas Chromatography–Mass Spectrometry and in Situ Infrared Spectroscopy”. In: *The Journal of Physical Chemistry C* (2019), acs.jpcc.9b01017. DOI: 10.1021/acs.jpcc.9b01017.
- [122] M. Hara, U. Linke, and T. Wandlowski. “Preparation and electrochemical characterization of palladium single crystal electrodes in 0.1 M H<sub>2</sub>SO<sub>4</sub> and HClO<sub>4</sub>. Part I. Low-index phases”. In: *Electrochimica Acta* 52.18 (2007), pp. 5733–5748. DOI: 10.1016/j.electacta.2006.11.048.
- [123] F. Hernandez and H. Baltruschat. “Electrochemical characterization of gold stepped surfaces modified with Pd”. In: *Langmuir* 22.10 (2006), pp. 4877–4884. DOI: 10.1021/la053257p.

- [124] N. Hoshi, K. Kagaya, and Y. Hori. "Voltammograms of the single-crystal electrodes of palladium in aqueous sulfuric acid electrolyte: Pd(S)-[n(111)×(111)] and Pd(S)-[n(100)×(111)]". In: *Journal of Electroanalytical Chemistry* 485.1 (2000), pp. 55–60. DOI: 10.1016/S0022-0728(00)00098-X.
- [125] N. Hoshi, M. Kuroda, and Y. Hori. "Voltammograms of stepped and kinked stepped surfaces of palladium: Pd(S)-[n(111)×(100)] and Pd(S)-[n(100)×(110)]". In: *Journal of Electroanalytical Chemistry* 521.1-2 (2002), pp. 155–160. DOI: 10.1016/S0022-0728(02)00687-3.
- [126] M. Arévalo, J. Rodríguez, and E. Pastor. "Elucidation of the reaction pathways of allyl alcohol at polycrystalline palladium electrodes". In: *Journal of Electroanalytical Chemistry* 505.1-2 (2001), pp. 62–71. DOI: 10.1016/S0022-0728(01)00457-0.
- [127] Y. Kwon, S. C. Lai, P. Rodriguez, and M. T. Koper. "Electrocatalytic oxidation of alcohols on gold in alkaline media: Base or gold catalysis?" In: *Journal of the American Chemical Society* 133.18 (2011), pp. 6914–6917. DOI: 10.1021/ja200976j.
- [128] P. Y. Bruice. *Organic Chemistry*. Pearson Education, 2007.
- [129] E. Pastor, S. González, and A. Arvia. "Electroreactivity of isopropanol on platinum in acids studied by DEMS and FTIRS". In: *Journal of Electroanalytical Chemistry* 395.1-2 (1995), pp. 233–242. DOI: 10.1016/0022-0728(95)04129-C.
- [130] A. Santasalo-Aarnio, Y. Kwon, E. Ahlberg, K. Kontturi, T. Kallio, and M. T. M. Koper. "Comparison of methanol, ethanol and iso-propanol oxidation on Pt and Pd electrodes in alkaline media studied by HPLC". In: *Electrochemistry Communications* 13.5 (2011), pp. 466–469. DOI: 10.1016/j.elecom.2011.02.022.
- [131] E. Negishi. *Handbook of Organopalladium Chemistry Handbook of Organopalladium Chemistry*. Vol. 2. 2002. DOI: 10.1002/0471212466.
- [132] M Pourbaix. *Atlas of electrochemical equilibria in aqueous solutions*. Pergamon Press, 1974.
- [133] J. P. Hoare. "The Effect of Metal Dissolution on the Rest Potential in the Palladium-Oxygen-Acid System". In: *Journal of the Electrochemical Society* 111.5 (1964), pp. 610–615. DOI: 10.1149/1.2426193.
- [134] L. H. Dall'Antonia, G. Tremiliosi-Filho, and G. Jerkiewicz. "Influence of temperature on the growth of surface oxides on palladium electrodes". In: *Journal of Electroanalytical Chemistry* 502.1-2 (2001), pp. 72–81. DOI: 10.1016/S0022-0728(00)00505-2.
- [135] R. Parsons and T. VanderNoot. "The oxidation of small organic molecules". In: *Journal of Electroanalytical Chemistry and Interfacial Electrochemistry* 257.1-2 (1988), pp. 9–45. DOI: 10.1016/0022-0728(88)87028-1.

- [136] M. T. Koper, S. C. Lai, and E. Herrero. "Mechanisms of the Oxidation of Carbon Monoxide and Small Organic Molecules at Metal Electrodes". In: *Fuel Cell Catalysis*. Hoboken, NJ, USA: John Wiley & Sons, Inc., 2009, pp. 159–207. DOI: 10.1002/9780470463772.ch6.
- [137] F. Gao and D. W. Goodman. "Pd-Au bimetallic catalysts: Understanding alloy effects from planar models and (supported) nanoparticles". In: *Chemical Society Reviews* 41.24 (2012), pp. 8009–8020. DOI: 10.1039/c2cs35160a.
- [138] P. Liu and J. K. Nørskov. "Ligand and ensemble effects in adsorption on alloy surfaces". In: *Physical Chemistry Chemical Physics* 3.17 (2001), pp. 3814–3818. DOI: 10.1039/b103525h.
- [139] M. Neurock and W. T. Tysoe. "Mechanistic insights in the catalytic synthesis of vinyl acetate on palladium and gold/palladium alloy surfaces". In: *Topics in Catalysis* 56.15-17 (2013), pp. 1314–1332. DOI: 10.1007/s11244-013-0153-8.
- [140] A. Hugon, L. Delannoy, J. M. Krafft, and C. Louis. "Selective hydrogenation of 1,3-butadiene in the presence of an excess of alkenes over supported bimetallic gold-palladium catalysts". In: *Journal of Physical Chemistry C* 114.24 (2010), pp. 10823–10835. DOI: 10.1021/jp100479b.
- [141] S. Pronkin, M. Hara, and T. Wandlowski. "Electrocatalytic properties of Au(111)-Pd quasi-single-crystal film electrodes as probed by ATR-SEIRAS". In: *Russian Journal of Electrochemistry* 42.11 (2006), pp. 1177–1192. DOI: 10.1134/S1023193506110048.
- [142] S. G. Sun, W. B. Cai, L. J. Wan, and M. Osawa. "Infrared absorption enhancement for CO adsorbed on Au films in perchloric acid solutions and effects of surface structure studied by cyclic voltammetry, scanning tunneling microscopy, and surface-enhanced IR spectroscopy". In: *Journal of Physical Chemistry B* 103.13 (1999), pp. 2460–2466. DOI: 10.1021/jp984028x.
- [143] C. H. Shue, L. Y. O. Yang, S. L. Yau, and K. Itaya. "In-Situ scanning tunneling microscopy of carbon monoxide adsorbed on Au(111) electrode". In: *Langmuir* 21.5 (2005), pp. 1942–1948. DOI: 10.1021/la047832l.
- [144] J. Lipkowski, Z. Shi, A. Chen, B. Pettinger, and C. Bilger. "Ionic adsorption at the Au(111) electrode". In: *Electrochimica Acta* 43.19-20 (1998), pp. 2875–2888. DOI: 10.1016/S0013-4686(98)00028-0.
- [145] J. Wang, B. M. Ocko, A. J. Davenport, and H. S. Isaacs. "In situ x-ray-diffraction and -reflectivity studies of the Au(111)/electrolyte interface: Reconstruction and anion adsorption". In: *Physical Review B* 46.16 (1992), pp. 10321–10338. DOI: 10.1103/PhysRevB.46.10321.
- [146] Z. Shi and J. Lipkowski. "Chloride adsorption at the Au(111) electrode surface". In: *Journal of Electroanalytical Chemistry* 403.1-2 (1996), pp. 225–239. DOI: 10.1016/0022-0728(95)04313-6.

- [147] M. Labayen and O. M. Magnussen. “In situ Video-STM study of the potential-induced  $(1 \times 1) \rightarrow$  “hex” transition on Au(1 0 0) electrode surfaces in  $\text{Cl}^-$  containing solution”. In: *Surface Science* 573.1 (2004), pp. 128–139. DOI: 10.1016/j.susc.2004.05.143.
- [148] U. E. Zhumaev, I. V. Pobelov, A. V. Rudnev, A. Kuzume, and T. Wandlowski. “Decoupling surface reconstruction and perchlorate adsorption on Au(111)”. In: *Electrochemistry Communications* 44 (2014), pp. 31–33. DOI: 10.1016/j.elecom.2014.04.009.
- [149] F. Maroun, F. Ozanam, O. M. Magnussen, and R. Behm. “The Role of Atomic Ensembles in the Reactivity of Bimetallic Electrocatalysts”. In: *Science* 293.5536 (2001), pp. 1811–1814. DOI: 10.1126/science.1061696.
- [150] E. Pastor, S. Wasmus, T. Iwasita, M. C. Arévalo, S. González, and A. J. Arvia. “DEMS and in-situ FTIR investigations of C3 primary alcohols on platinum electrodes in acid solutions.” In: *Journal of Electroanalytical Chemistry* 353.1-2 (1993), pp. 81–100. DOI: 10.1016/0022-0728(93)80288-S.
- [151] K. Mayrhofer, M. Arenz, B. Blizanac, V. Stamenkovic, P. Ross, and N. Markovic. “CO surface electrochemistry on Pt-nanoparticles: A selective review”. In: *Electrochimica Acta* 50.25-26 (2005), pp. 5144–5154. DOI: 10.1016/j.electacta.2005.02.070.
- [152] S. Cherevko, A. R. Zeradjanin, A. A. Topalov, N. Kulyk, I. Katsounaros, and K. J. J. Mayrhofer. “Dissolution of noble metals during oxygen evolution in acidic media”. English. In: *ChemCatChem* 6.8 (2014), pp. 2219–2223. DOI: 10.1002/cctc.201402194.
- [153] G. Bozzolo and J. Ferrante. “Composition dependence of bulk alloy properties”. In: *Physical Review B* 50.9 (1994), pp. 5971–5980. DOI: 10.1103/PhysRevB.50.5971.
- [154] Z. Kaszukur. “Direct observation of chemisorption induced changes in concentration profile in Pd-Au alloy nanosystems via in situ X-ray powder diffraction”. In: *Physical Chemistry Chemical Physics* 6.1 (2004), pp. 193–199. DOI: 10.1039/b308177j.
- [155] M. Ruff, N. Takehiro, P. Liu, J. K. Nørskov, and R. J. Behm. “Size-Specific Chemistry on Bimetallic Surfaces: A Combined Experimental and Theoretical Study”. In: *ChemPhysChem* 8.14 (2007), pp. 2068–2071. DOI: 10.1002/cphc.200700070.
- [156] T. Wei, J. Wang, and D. W. Goodman. “Characterization and chemical properties of Pd-Au alloy surfaces”. In: *Journal of Physical Chemistry C* 111.25 (2007), pp. 8781–8788. DOI: 10.1021/jp067177l.
- [157] A. E. Baber, H. L. Tierney, and E. C. H. Sykes. “Atomic-scale geometry and electronic structure of catalytically important Pd/Au alloys”. In: *ACS Nano* 4.3 (2010), pp. 1637–1645. DOI: 10.1021/nn901390y.

- [158] S. E. Weitzner and I. Dabo. “Voltage effects on the stability of Pd ensembles in Pd-Au/Au(111) surface alloys”. In: *Journal of Chemical Physics* 150.4 (2019). DOI: 10.1063/1.5054124.
- [159] M. Okube, V. Petrykin, J. E. Mueller, D. Fantauzzi, P. Krttil, and T. Jacob. “Topologically Sensitive Surface Segregations of Au-Pd Alloys in Electrocatalytic Hydrogen Evolution”. In: *ChemElectroChem* 1.1 (2014), pp. 207–212. DOI: 10.1002/celec.201300112.
- [160] J. Navarro-Ruiz, D. Cornu, and N. López. “Prevalence of trans-Alkenes in Hydrogenation Processes on Metal Surfaces: A Density Functional Theory Study”. In: *Journal of Physical Chemistry C* 122.44 (2018), pp. 25339–25348. DOI: 10.1021/acs.jpcc.8b06880.
- [161] C. J. Bondue and M. T. Koper. In: *Journal of Catalysis* 369 (2019), pp. 302–311. DOI: 10.1016/j.jcat.2018.11.019.
- [162] H. Miyake, T. Okada, G. Samjeské, and M. Osawa. “Formic acid electrooxidation on Pd in acidic solutions studied by surface-enhanced infrared absorption spectroscopy”. In: *Physical Chemistry Chemical Physics* 10.25 (2008), p. 3662. DOI: 10.1039/b805955a.
- [163] K. I. Ataka, T. Yotsuyanagi, and M. Osawa. “Potential-dependent reorientation of water molecules at an electrode/electrolyte interface studied by surface-enhanced infrared absorption spectroscopy”. In: *Journal of Physical Chemistry* 100.25 (1996), pp. 10664–10672. DOI: 10.1021/jp953636z.
- [164] A. Yamakata and M. Osawa. “Destruction of the water layer on a hydrophobic surface induced by the forced approach of hydrophilic and hydrophobic cations”. In: *Journal of Physical Chemistry Letters* 1.9 (2010), pp. 1487–1491. DOI: 10.1021/jz100424e.
- [165] J. C. G. Calado and A. M. F. Palavra. “Solubility of Propene in Water and in a Mineral Medium for the Cultivation of a Xanthobacter Strain”. In: *Journal of Solution Chemistry* 27.5 (1998). DOI: 10.1023/A:1022604705859.
- [166] K.-H. Dostert, C. P. O’Brien, F. Mirabella, F. Ivars-Barceló, and S. Schauer-mann. “Adsorption of acrolein, propanal, and allyl alcohol on Pd(111): a combined infrared reflection–absorption spectroscopy and temperature programmed desorption study”. In: *Physical Chemistry Chemical Physics* 18.20 (2016), pp. 13960–13973. DOI: 10.1039/C6CP00877A.
- [167] T. Okanishi, Y. Katayama, R. Ito, H. Muroyama, T. Matsui, and K. Eguchi. “Electrochemical oxidation of 2-propanol over platinum and palladium electrodes in alkaline media studied by in situ attenuated total reflection infrared spectroscopy”. In: *Physical Chemistry Chemical Physics* 18.15 (2016), pp. 10109–10115. DOI: 10.1039/C5CP07518A.

- [168] M. Beltowska-Brzezinska, T. Uczak, and R. Holze. “Electrocatalytic oxidation of mono- and polyhydric alcohols on gold and platinum”. In: *Journal of Applied Electrochemistry* 27.9 (1997), pp. 999–1011. DOI: 10.1023/A:1018422206817.
- [169] H. Lindlar. “Ein neuer Katalysator für selektive Hydrierungen”. In: *Helvetica Chimica Acta* 35.2 (1952), pp. 446–450. DOI: 10.1002/hlca.19520350205.
- [170] D. Albani, M. Shahrokhi, Z. Chen, S. Mitchell, R. Hauert, N. López, and J. Pérez-Ramírez. “Selective ensembles in supported palladium sulfide nanoparticles for alkyne semi-hydrogenation”. In: *Nature Communications* 9.1 (2018), p. 2634. DOI: 10.1038/s41467-018-05052-4.
- [171] K. H. Dostert, C. P. O'Brien, F. Ivars-Barceló, S. Schauer mann, and H. J. Freund. “Spectators Control Selectivity in Surface Chemistry: Acrolein Partial Hydrogenation over Pd”. In: *Journal of the American Chemical Society* 137.42 (2015), pp. 13496–13502. DOI: 10.1021/jacs.5b04363.
- [172] K. H. Dostert, C. P. O'Brien, F. Mirabella, F. Ivars-Barceló, S. Attia, E. Spadafora, S. Schauer mann, and H. J. Freund. “Selective Partial Hydrogenation of Acrolein on Pd: A Mechanistic Study”. In: *ACS Catalysis* 7.8 (2017), pp. 5523–5533. DOI: 10.1021/acscatal.7b01875.
- [173] G. Horányi and K. Torkos. “Effect of chemisorbed methanol on the rate and selectivity of electroreduction processes at a platinized platinum electrode”. In: *Journal of Electroanalytical Chemistry and Interfacial Electrochemistry* 111.2-3 (1980), pp. 279–286. DOI: 10.1016/S0022-0728(80)80048-9.
- [174] C. N. Brodsky, A. P. Young, K. C. Ng, C. H. Kuo, and C. K. Tsung. “Electrochemically induced surface metal migration in well-defined core-shell nanoparticles and its general influence on electrocatalytic reactions”. In: *ACS Nano* 8.9 (2014), pp. 9368–9378. DOI: 10.1021/nn503379w.
- [175] S. Venkatachalam and T. Jacob. “Hydrogen adsorption on Pd-containing Au(111) bimetallic surfaces”. In: *Physical Chemistry Chemical Physics* 11.17 (2009), p. 3263. DOI: 10.1039/b900250b.

# Appendix A

## Supporting information

### A.1 Materials

All solutions were prepared with high purity water from a millipore system (resistivity 18 M $\Omega$ ) For the experiments shown in Chapters 5 and 6, the electrolyte was prepared from 70% HClO<sub>4</sub> (suprapur, Merck) and NaClO<sub>4</sub> (99.99% trace metals basis, Sigma Aldrich). Electrode depositions were carried out on cleaned glassy carbon sheets (1 x 1.5 cm, HTW-Germany) or on glassy carbon disks (5 mm diameter, Pine Instruments) from a solution of PdCl<sub>2</sub> (99.999%, Sigma Aldrich) and/or KAuCl<sub>4</sub> (99%, Sigma Aldrich) in 2 M H<sub>2</sub>SO<sub>4</sub> (suprapur, Merck).

Standards for *ex-situ* product analysis were prepared from the pure substances: acrolein (analytical standard, Sigma Aldrich), acrylic acid (99%, Aldrich), allyl alcohol (>99%, Aldrich), propionaldehyde (>97%, Sigma Aldrich), propylene glycol (>99.5%, Sigma Aldrich), acetone (for analysis, EMSURE(R), Merck), and isopropanol (for analysis, EMSURE(R), Merck)

The electrolyte was sparged with high purity gases: Ar(5.0, AGA), propene (4.0, BOC), and CO (5.0, AGA).

For the experiments shown in Chapter 7 gases of similar purity, but from different suppliers were used: Ar (5.0, Praxair), propene (4.0, Praxair), CO (5.0, Advanced Specialty Gases). The electrolyte was prepared from 70% HClO<sub>4</sub> (Veritas double

distilled, GFS Chemicals) and  $\text{KClO}_4$  (99%, Alfa Aesar). Allyl alcohol (98+%, Alfa Aesar) was added to the electrolyte for allyl alcohol oxidation experiments.

## A.2 Experimental parameters

### A.2.1 Catalyst characterization methods

#### Scanning electron microscopy (SEM)

The majority of the SEM images shown in Chapter 4 were taken using a FEI Quanta 200 Cryo ESEM scanning electron microscope equipped with a field emission gun, Everhart-Thornley and solid-state BSE detectors, as well as EDS. Images were recorded using electron beam acceleration voltages between 10-20 kV at a pressure of ca.  $1 \cdot 10^{-5}$  mbar. The image of Au foam was recorded with a Quanta FEG 250 Analytical ESEM (also equipped with a field emission gun and similar detectors) at similar conditions. For the images of the SEIRAS films an FEI XL30 Sirion was used at 5 kV acceleration voltage.

#### X-ray diffraction (XRD)

The XRD patterns shown in Chapter 4 were recorded using a Malvern PANanalytical Empyrean x-ray diffractometer. The x-ray source is an Empyrean Cu LFF HR gun operated at 45 kV and 40 mA, the used wavelength  $K_\alpha = 1.5405980 \text{ \AA}$ . Thin film geometry was used with parallel beam optics to minimize the contribution from the substrate. The detector (PIXcel3D-Medipix3 1x1 detector) was operated with all channels open.

#### X-ray photoelectron spectroscopy (XPS)

The XPS spectra shown in Chapter 4 were recorded using a ThermoScientific Thetaprobe instrument equipped with an Al  $K_\alpha$  x-ray source. For survey spectra 20 scans were recorded with 50 ms dwell time per 1 eV step. For element detail scans 25-50 scans were recorded in 0.1 eV steps with 200 ms dwell time. The chamber pressure was in the range of  $10^{-9}$  mbar. The lateral resolution is 400  $\mu\text{m}$ . Ar sputtering was carried

out at an Ar pressure of ca.  $10^{-7}$  mbar at 4kV,  $1\mu\text{A}$ , on a 5 mm raster for 2.5 or 5 s per sputtering step (new and old filament, respectively) The SEIRAS electrode was analysed using a PHI Versaprobe. Data analysis was done using CasaXPS, version 2.3.19.

### **Low energy ion scattering (LEIS)**

The LEIS spectra were recorded using the same ThermoScientific Thetaprobe instrument used for XPS, at a He pressure of  $10^{-7}$  mbar with an ion energy of 1000 eV. The recorded energy range was from 0-1000 eV kinetic energy, at 50 ms dwell time, 1 eV step size and 2.5 retard ratio. 5 scans were averaged for each spot. Ar sputtering to clean the surface was carried out as for XPS analysts (described above)

### **Potentiostat**

All electrochemical measurements were carried out using different models of Bio-Logic potentiostats and the associated software EC-Lab: Model SP 150 was used for most experiments shown in Chapter 5 and all EC-MS experiments, VSP for the experiments in Chapter 5 at pH 3, and VMP3 for all SEIRAS experiments. In all cases, channels with EIS capability were used.

## **A.2.2 Product analysis methods**

### **Gas chromatography**

All GC analysis was carried out using an Agilent 7890A gas chromatograph equipped with a HP-PLOT Q column (45 m length, 0.53 mm diameter,  $40.0\ \mu\text{m}$  film thickness; flame ionization detector) and a Molsieve column (30 m length, 0.53 mm diameter,  $25.0\ \mu\text{m}$  film thickness; thermal conductivity detector). The inlet was a split/splitless inlet used with a split ratio of 0.5:1 (inlet temperature  $150\ ^\circ\text{C}$ ). For gas analysis, the following temperature program was used: 6 min at  $35\ ^\circ\text{C}$ , ramp with  $10\ ^\circ\text{C}/\text{min}$  to  $60\ ^\circ\text{C}$ , hold at  $60\ ^\circ\text{C}$  for 8 min. Each run was followed by a post run at  $230\ ^\circ\text{C}$  for 10 min. Calibration of the  $\text{CO}_2$  signal was done by oxidation of CO on Pt or Au foil and comparison of the charge with the signal intensity.

### **Static head-space gas chromatography**

The same GC used for gas analysis was also connected to an Agilent 7694E headspace sampler. 5 mL samples were filled into 10 mL glass vials and sealed. Gas was taken from the headspace after equilibration at 70 °C for 15 min. Loop and transfer line were kept at 110 °C and 120 °C, respectively. A HP-PLOT Q column was used (45m length, 0.53 mm diameter, 40.0  $\mu$ m film thickness; flame ionization detector). Injection was done into a split/splitless inlet at a 0.5:1 ratio at 150 °C. The temperature program was: initial hold 33 min at 120 °C, ramp with 10 °C/min to 230 °C, hold at 230 °C for 10 min. Each injection was followed by a post run at 230 °C for 10 min.

### **High performance liquid chromatography**

An Agilent 1200 series HPLC system was used, which is equipped with with autosampler, degasser, quaternary pump, a diode array detector (UV-VIS range), and a refractive index detector. A BIORAD, Aminex HPX-87H column was employed, heated externally to 50 °C. 5 mM H<sub>2</sub>SO<sub>4</sub> was used as eluent with a flow rate of 0.6 mL/min resulting in analysis times of ca. 40 min per injection. The injection volume was 30  $\mu$ L.

### **Nuclear magnetic resonance spectroscopy**

A Bruker AVANCEIII HD spectrometer (800.182 MHz) with a 5 mm TCI Cryoprobe (Bruker Biospin) was used for acquisition of all <sup>1</sup>H-NMR spectra. Water resonance was suppressed using a “perfect-echo” excitation sculpting pulse sequence (2000  $\mu$ s selective 180° inversion pulse). For each spectrum, 256 transient scans were acquired (acquisition time 3.4 s, interscan delay of 10 s). For NMR measurements, 475  $\mu$ L of the liquid sample were mixed with 100  $\mu$ L D<sub>2</sub>O and 25  $\mu$ L of 950  $\mu$ M DMSO in H<sub>2</sub>O as internal standard, resulting in a DMSO concentration corresponding to 50  $\mu$ M in the undiluted sample.

### **Inductively coupled plasma - mass spectrometry**

A iCAP-Q ICP-MS instrument was used for all measurements. The samples were diluted 1:10 or 1:100 with 0.67% to obtain concentrations between 1 and 10 ppb. Fresh

calibration samples were prepared for each set of measurements from 1000 mg<sub>metal</sub>/mL Pd or Au standards in HCl (SCP Science).

### Surface enhanced infrared absorption spectroscopy

A Thermo Nicolet iS50 FT-IR instrument was used, equipped with a MCT detector (cooled with liquid N<sub>2</sub>) and a PIKE VeeMAX III accessory for mounting an ATR crystal and an electrochemical cell. IR spectra were recorded at 4 cm<sup>-1</sup> resolution, 32 scans were averaged per spectrum.

## A.3 Additional figures

### A.3.1 Appendant to Chapter 3

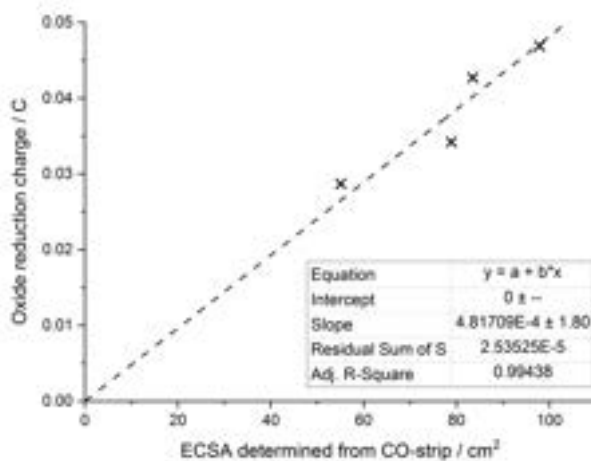


**Figure A.1** Calibration of surface area determined using the oxide reduction charge (at 50 mV/s) with the surface area determined from CO-stripping experiments on the same electrode. Measured on high surface area Pd electrodes in 0.1 M HClO<sub>4</sub>.

### A.3.2 Appendant to Chapter 7

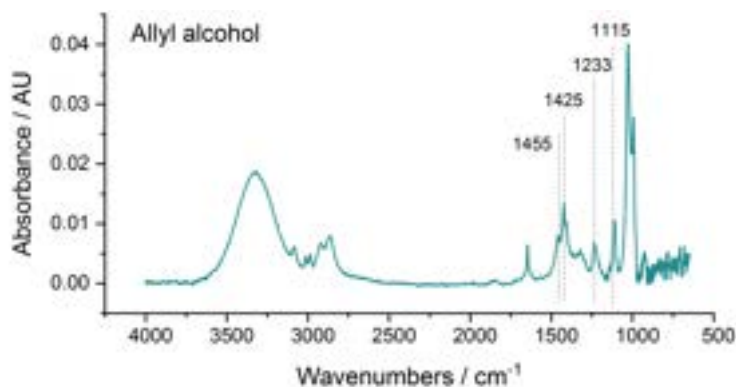


**Figure A.2** Reference spectrum of pure allyl alcohol directly applied to the Si prisma (no catalyst).

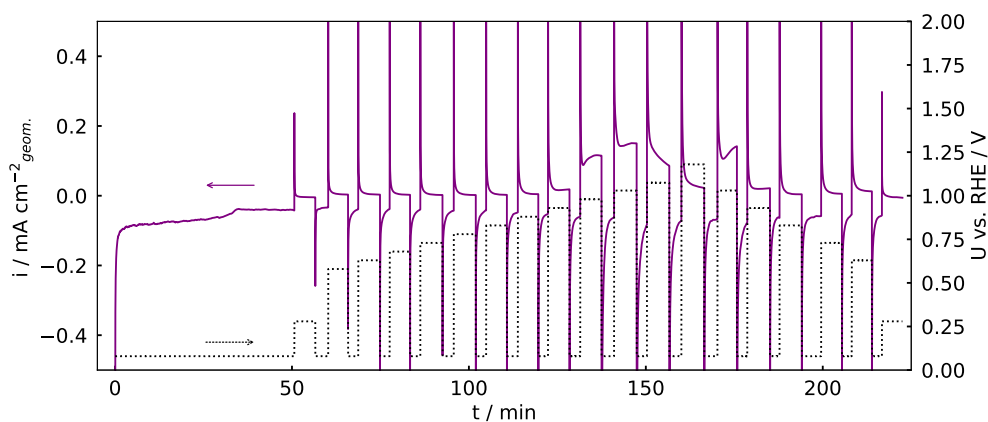


**Figure A.3** Allyl alcohol oxidation 0.001 M HClO<sub>4</sub> + 0.099 M KClO<sub>4</sub>, 10 mM allyl alcohol, Ar saturated: Potential applied (dotted line, right y-axis) and resulting current (full line, left y-axis). The maxima of the current spikes when changing potential are not shown for better visibility of steady-state current.

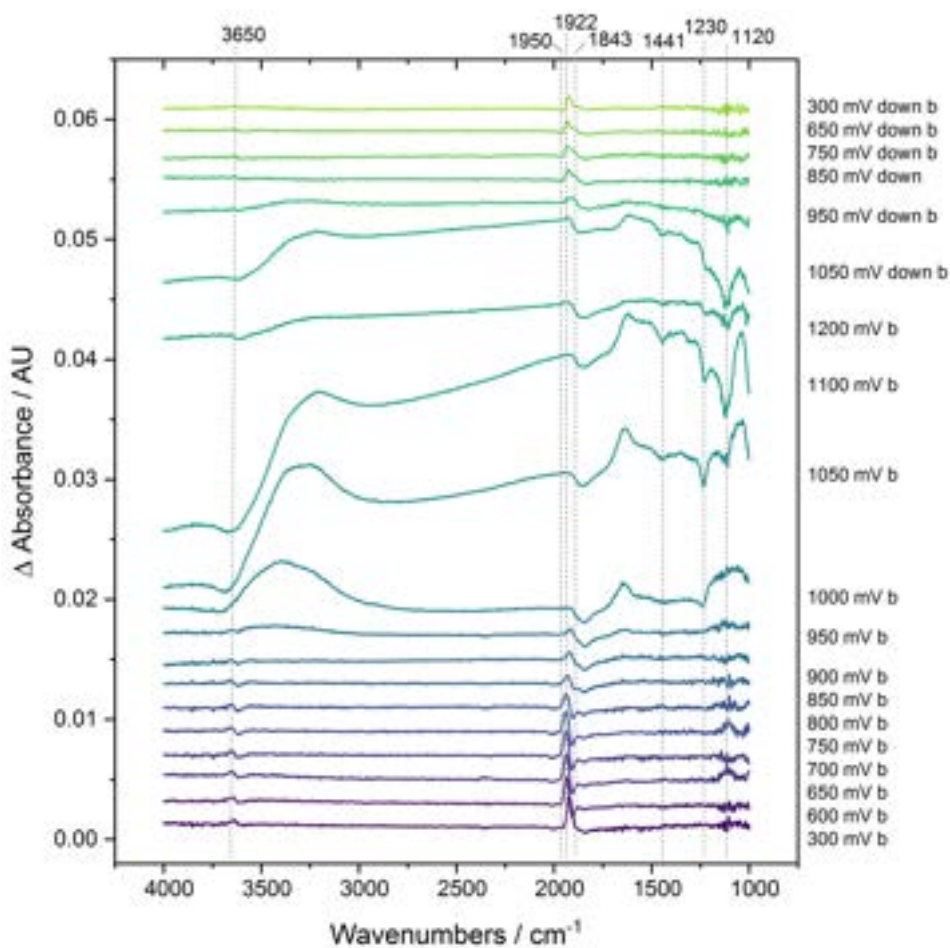


**Figure A.4** Spectra recorded during allyl alcohol oxidation 0.001 M  $\text{HClO}_4$  + 0.099 M  $\text{KClO}_4$  after 5 min at each potential step. Compare with Figure 7.5.

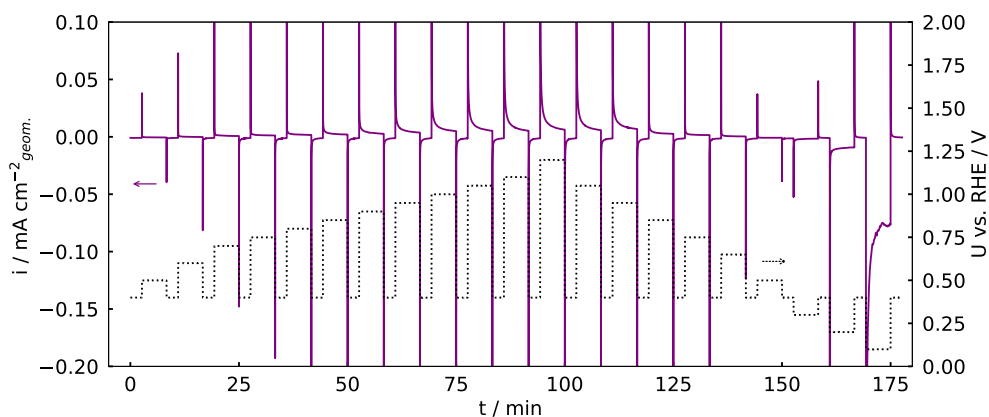


**Figure A.5** Propene oxidation in 0.001 M  $\text{HClO}_4$  + 0.099 M  $\text{KClO}_4$ : Potential applied (dotted line, right y-axis) and resulting current (full line, left y-axis). The maxima of the current spikes when changing potential are not shown for better visibility of steady-state current.

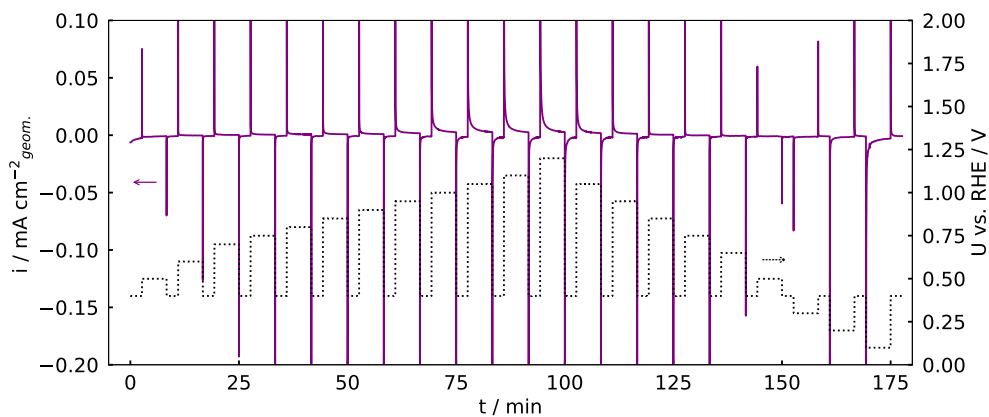


**Figure A.6** Pd oxidation in Ar saturated 0.001 M  $\text{HClO}_4$  + 0.099 M  $\text{KClO}_4$ : Potential applied (dotted line, right y-axis) and resulting current (full line, left y-axis). The maxima of the current spikes when changing potential are not shown for better visibility of steady-state current.

## **A.4 Previously published supporting information.**

In the following, selected parts of the Electronic Supplementary Material of Paper I are reprinted, which have been referred to throughout this thesis. The full document is available at [www.doi.org/10.1039/C8EE03426E](http://www.doi.org/10.1039/C8EE03426E).

Text and figures related to computational work (original page numbers S43 and S44) were prepared by Luca Silvioli.

## Product quantification –calibration and validation

Calibration standards for product quantification were prepared by dilution of the pure compounds with 0.1 M HClO<sub>4</sub>. Acrolein was first dissolved in 1 mL acetone to prevent polymerization on contact with water. Mixed standards containing at least three different compounds were used in all cases. Calibration lines were calculated by linear least square fitting of at least 5 different concentrations. The regression was first calculated without constraints. If the calculated y-intercept was smaller than the standard error (SE<sub>y</sub>), the regression was recalculated with a forced y-intercept of 0.

### *GC*

An Agilent 7890A instrument was used for both gas chromatography (GC), and static headspaces gas chromatography (HS-GC) measurements. The gas from the sample loop connected to the headspace of the electrochemical cell was injected into a HP-PLOT Q column (45m length, 0.53 mm diameter, 40.0 μm film thickness; flame ionization detector) and a Molsieve column (30m length, 0.53 mm diameter, 25.0 μm film thickness; thermal conductivity detector) in a ratio 0.5:1 (inlet temperature 150 °C). The temperature program for gas analysis was hold 6 min at 35 °C, ramp with 10 °C/min to 60 °C, hold at 60 °C for 8 min, followed by a post run at 230 °C for 10 min. The signal in the FID detector was used for the quantification of CO<sub>2</sub>. Calibration was done by oxidation of CO on Pt foil and comparison of the charge with the signal intensity.

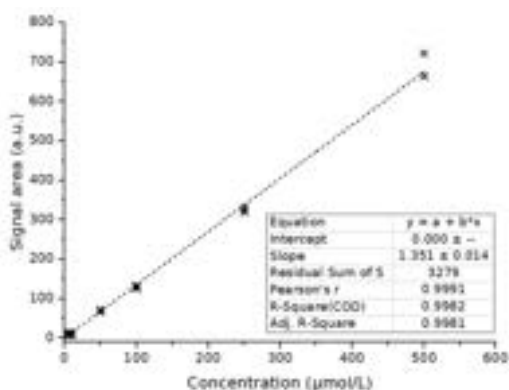
### *HS-GC*

The GC was coupled to an Agilent 7694E headspace sampler. 10 mL glass vials were filled with 5 mL electrolyte and sealed. Gas was taken from the headspace after equilibration at 70 °C for 15 min. Loop and transfer line were kept at 110 °C and 120 °C, respectively. Injection into a HP-PLOT Q column (45m length, 0.53 mm diameter, 40.0 μm film thickness; flame ionization detector) followed in a 0.5:1 ratio at

150 °C. The temperature program was hold 33 min at 120 °C, ramp with 10 °C/min to 230°C, hold at 230°C for 10 min, followed by a post run at 230 °C for 10 min.

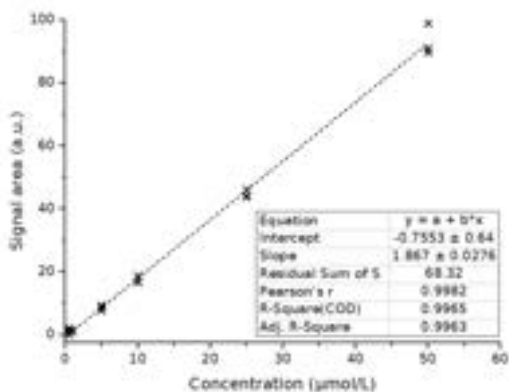
Duplicate measurements were attempted, but the fast degradation of the products at elevated temperatures in the autosampler lead to erroneous values.

HS-GC shows peaks for acetone, propanal, acrolein and isopropanol. We only used the method for the quantification of acetone and propanal as other methods proved to be more reliable/sensitive for the other compounds.



Given value	Average	Rel. STD (precision)	Rel deviation (accuracy)
µmol / L	µmol / L	%	%
10	8.79	7.45	-12.06
50	47.89	1.72	-4.22
100	89.39	10.14	-10.61
250	239.53	2.12	-4.19

Figure S13 Acetone calibration: Calibration line and statistical parameters (left) and details of the validation analysis (right). For the calibration, standards of 5 concentrations were prepared. Three individual samples of each standard were measured. For validation, standards of 4 different concentrations were prepared separately and again 3 individual samples each were measured. The rel. standard deviation between these 3 samples is given as an estimate for the precision of the method. The relative deviation of the average value from the given value can serve as estimate for the accuracy



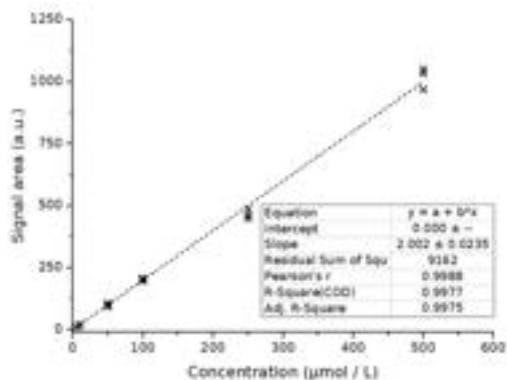
Given value	Average	Rel. STD (precision)	Rel deviation (accuracy)
µmol / L	µmol / L	%	%
10	9.08	10.76	-9.24
50	62.05	4.77	24.10
10	7.88	23.52	-21.20
50	50.70	6.12	1.40

Figure S14 Propanal calibration. See Figure S13 for details. Here validation was based on only two concentrations, but each prepared twice.

#### HPLC

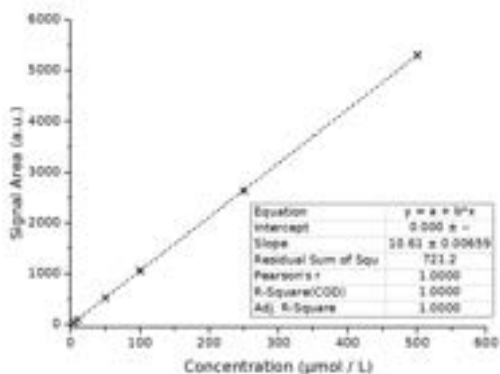
An Agilent 1200 series high performance liquid chromatograph was used, equipped with with autosampler, degasser, quaternary pump, and diode array detectors (UV-VIS range). A BIORAD, Aminex HPX-87H column was employed, heated externally to 50 °C. 5mM H<sub>2</sub>SO<sub>4</sub> (diluted from concentrated H<sub>2</sub>SO<sub>4</sub>, suprapur, Merck with ultrapure water) was used as eluent with a flow rate of 0.6mL/min. The injection volume was 30µL.

HPLC was used for only for acrolein and acrylic acid due to the need for sufficient absorption in the available UV-VIS range.



Given value	Average	Rel. STD (precision)	Rel deviation (accuracy)
µmol / L	µmol / L	%	%
5	5.91	7.19	18.22
50	56.58	4.47	13.16
250	275.23	4.53	10.09

Figure S15 Acrolein calibration. See Figure S13 for details. Validation is based on three injections of the same standard at three different concentrations.



Given value	Average	Rel. STD (precision)	Rel deviation (accuracy)
µmol / L	µmol / L	%	%
5	4.90	2.48	-2.09
10	9.89	1.14	-1.09
50	49.64	0.20	-0.72
100	100.79	1.00	0.79
250	249.04	0.09	-0.38

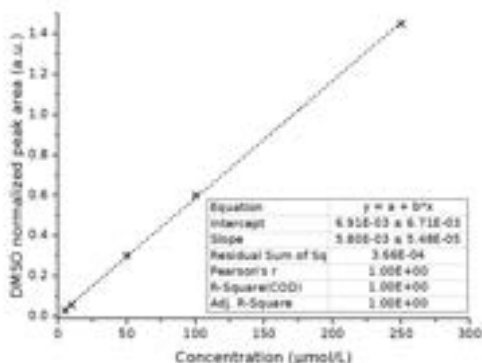
Figure S16 Acrylic acid calibration. See Figure S13 for details. Validation is based on three injections of the same standard at five different concentrations.

## NMR

The <sup>1</sup>H NMR spectra were acquired on a Bruker AVANCEIII HD spectrometer operating at a <sup>1</sup>H frequency of 800.182 MHz and equipped with a 5 mm TCI Cryoprobe (Bruker Biospin). The strong water resonance was suppressed utilizing a “perfect-echo” excitation sculpting pulse sequence (zgesgpp in the Bruker pulse sequence library) with a 2000 µs selective 180° inversion pulse. A total of 256 transient scans were

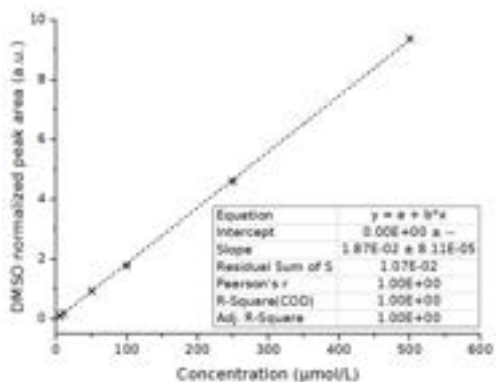
acquired for each spectrum with an acquisition time of 3.4 seconds and an interscan delay of 10 seconds. For each FID 64K complex points were acquired and the FID was then zero-filled to 64K real points before Fourier transformation (FT). An exponential apodization function with  $I_b = 0.3$  Hz was applied to the FID's prior to FT.

NMR samples were prepared by addition of 100  $\mu\text{L}$   $\text{D}_2\text{O}$  and 25  $\mu\text{L}$  of a 950  $\mu\text{M}$  DMSO in  $\text{H}_2\text{O}$  as internal standard to 475  $\mu\text{L}$  of the liquid sample, resulting in a DMSO concentration corresponding to 50  $\mu\text{M}$  in the undiluted sample. qNMR was used to quantify isopropanol, allyl alcohol and propylene glycol. For these compounds, external calibration lines were measured (see Figure S17, Figure S18 and Figure S19).



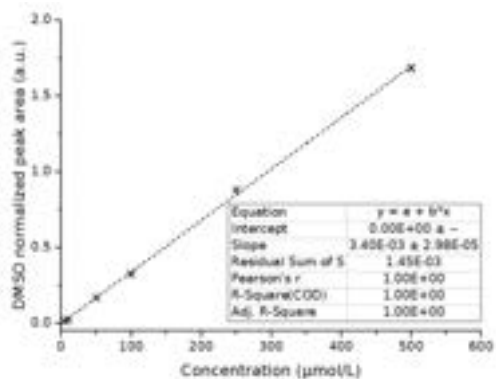
Given value	Average	Rel. STD (precision)	Rel deviation (accuracy)
$\mu\text{mol} / \text{L}$	$\mu\text{mol} / \text{L}$	%	%
5	3.93	-	-21.33
10	8.83	-	-11.71
50	49.92	-	-0.15
100	101.62	-	1.62

Figure S17 Allyl alcohol calibration: peak at 4.02ppm. See Figure S13 for details. Validation is based on the measurement of one individually prepared sample for each concentration.



Given value	Average	Rel. STD (precision)	Rel deviation (accuracy)
µmol / L	µmol / L	%	%
5	6.20	-	24.04
10	11.18	3.35	11.76
50	47.47	2.75	-5.05
100	96.43	1.85	-3.57
250	239.15	3.25	-4.34

Figure S18 Isopropanol calibration: peak at 1.07 ppm. See Figure S13 for details. Validation is based on the measurement of two individual samples with 10 µM analyte and four individual samples at three higher concentrations.



Given value	Average	Rel. STD (precision)	Rel deviation (accuracy)
µmol / L	µmol / L	%	%
5	6.05	-	20.93
10	11.23	5.18	12.26
50	50.63	7.07	1.26
100	106.77	5.04	6.77
250	264.38	6.29	5.75

Figure S19 Propylene glycol calibration: peak at 3.35 ppm. See Figure S13 for details. Validation is based on the measurement of two individual samples with 10 µM analyte and four individual samples at three higher concentrations.

Additional product analysis data at various conditions

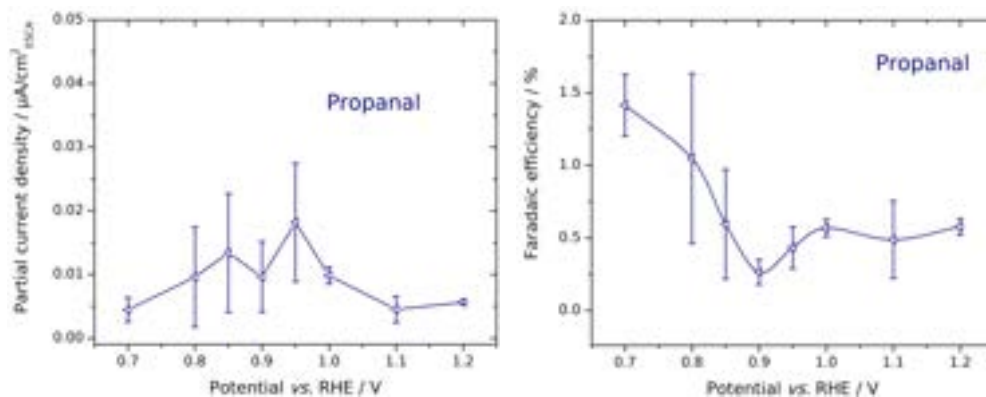


Figure S25 Partial current density and faradaic efficiency for propanal. The product concentration is very low resulting in large inaccuracies for the quantification.

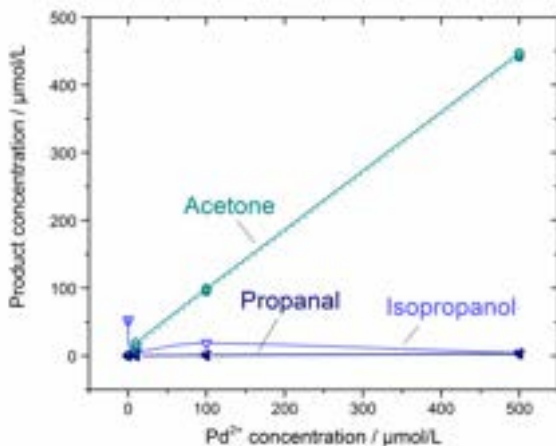


Figure S26 Product concentrations of propene oxidation in 0.1 M  $\text{HClO}_4$  containing different concentrations of  $\text{PdCl}_2$  without electrode (as shown in Figure 5 in the main text, empty symbols, full lines) compared with the concentrations obtained under the same conditions with glassy carbon electrode polarized to 0.9 V vs RHE added (half symbols, dotted lines).

## Calculation of reversible potentials

Table 2 Overview over thermochemical data used for the calculation of reversible potentials. The source refers to the source for the standard free enthalpy of formation and the standard entropy. All Henry constant data is taken from reference <sup>11</sup>. The free energy of solvation was calculated from the Henry's law constant according to equation (4) below. The free energy of formation was calculated from the standard free enthalpy and entropy of reactants and products

Compound	$\Delta_f H^\ominus$ (gas phase) / kJ/mol	S (gas phase) / J/K*mol	Henry constant $k_H^0$ / mol/kg*bar	$\Delta G_{sol}$ J/mol	$\Delta_f G^\ominus$ / kJ/mol	Source
H2	0	130.68				NIST <sup>7</sup>
O2	0	205.15				NIST <sup>7</sup>
C (s)		5.8				NIST <sup>7</sup>
H2O(l)	-285.83	69.95			-237.14	NIST <sup>7</sup>
CH2CHCHO (acrolein)	-84	281.12	230	-5275.50	-53.82	Smith <sup>8</sup>
CH2CHCO2H (acrylic acid)	-323.5	307.73	3100	-19293.20	-270.97	NIST <sup>7</sup>
CH3COCH3 (acetone)	-217.1	295.46	53	-8215.27	-152.53	NIST <sup>7</sup>
C3H6 (propene)	20.4	227	0.0092	13234.76	74.79	D'Ans Lax <sup>9</sup>
CH3CHOCH2 (propylene oxide)	-94.7	287.4	14	-4086.72	-27.73	NIST <sup>7</sup>
CH3CHOHCHOH (propylene glycol)	-429.8	288	76000	-12905.23	-293.46	NIST <sup>7</sup>
CH2CHCH2OH (allyl alcohol)	-123.6	-	430	-14851.76	-74.6	chemeo <sup>10</sup>
CH3CH2CHO (propanal)	-189	304	13	-6358.04	-126.98	NIST <sup>7</sup>
CO2 (g)	-393.5	213.8	Not used	8381.86	-394.35	NIST <sup>7</sup>

## Propene adsorption mechanism on Pd fcc111

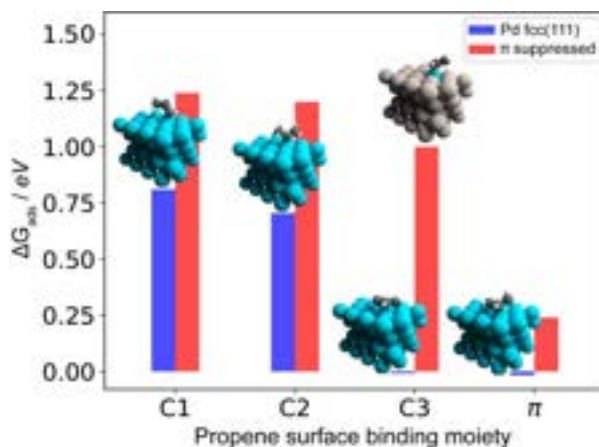


Figure S27 - Energetics for the possible adsorption mechanisms of propene on a fcc(111) slab surface. The vinylic and allylic contribution are decoupled in the red bar values.

In figure 27, C1, C2 and C3 refer to adsorption through proton/electron loss at the terminal unsaturated carbon, central unsaturated carbon and terminal saturated carbon, respectively.  $\pi$  refers to chemisorption by coordination of the double bond with a metal site, without proton/electron loss; this is a potential independent step, as no proton/electron couples are exchanged. Applying anodic potential lowers the oxidative adsorption energetics proportionally to the number of electron exchanged (hydrogen computational electrode); for this reason, C1 C2 C3 will bind stronger with applied potential maintaining the same relative energy gap, while  $\pi$  energy remains unchanged as potential independent. Furthermore, this figure illustrates the participation of double bond coordination to C3 adsorption. To isolate the contribution of double bond, we created a slab where a Pd site is surrounded by an inactive generic metal. Without neighbouring sites able to interact with the unsaturated bond, the adsorption energy value is due only to C3 adsorption. We found a relative destabilization of  $\sim 1\text{eV}$  for the C3 adsorption.

Propene degradation on Pd fcc111

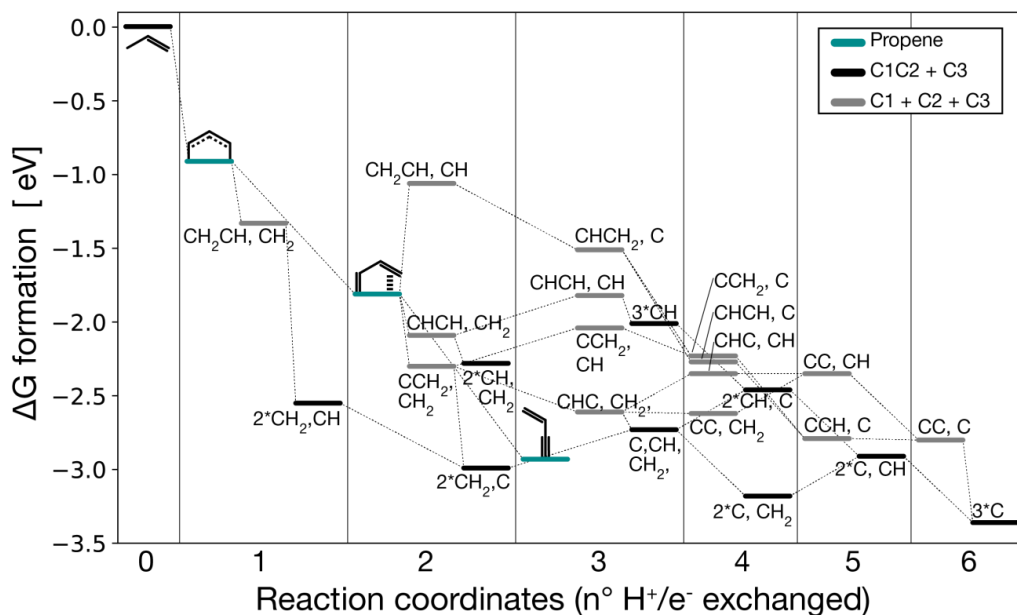


Figure S28 Computed energetics for the reaction of degradation of propene on a Pd fcc111 surface. There is indeed a strong driving force to crack the reactant to smaller carbon fractions, even on a relatively inert closely packed surface. These 1C fractions are then oxidized to  $\text{CO}_2$  when enough anodic potential is applied. Calculations fit the results of propene stripping experiments for the significant amount of  $\text{CO}_2$  recorded by MS.



## **Appendix B**

### **Appended publications**



## **Paper I**

### **Towards an atomistic understanding of electrocatalytic hydrocarbon oxidation: propene on palladium**

Anna Winiwarter\*, Luca Silvioli\*, Soren B. Scott, Kasper Enemark-Rasmussen, Manuel Saric, Daniel B. Trimarco, Peter C. K. Vesborg, Poul G. Moses, Ifan E. L. Stephens, Brian Seger, Jan Rossmeisl, and Ib Chorkendorff.

*Energy and Environmental Science*, 2019, **12**, 1055

\* these authors contributed equally



PAPER



Cite this: *Energy Environ. Sci.*,  
2019, 12, 1055

## Towards an atomistic understanding of electrocatalytic partial hydrocarbon oxidation: propene on palladium†

Anna Winiwarter,<sup>a</sup> Luca Silvili,<sup>b</sup> Soren B. Scott,<sup>a</sup> Kasper Enemark-Rasmussen,<sup>c</sup> Manuel Sariç,<sup>b</sup> Daniel B. Trimarco,<sup>d</sup> Peter C. K. Vesborg,<sup>a</sup> Poul G. Moses,<sup>e</sup> Ifan E. L. Stephens,<sup>f</sup> Brian Seger,<sup>a</sup> Jan Rossmeisl<sup>\*b</sup> and Ib Chorkendorff<sup>\*a</sup>

The efficient partial oxidation of hydrocarbons to valuable chemicals without formation of CO<sub>2</sub> is one of the great challenges in heterogeneous catalysis. The ever-decreasing cost of renewable electricity and the superior control over reactivity qualify electrochemistry as a particularly attractive means of addressing this challenge. Yet, to date, little is known about the factors regulating hydrocarbon oxidation at the atomic level. A relevant showcase reaction is propene electro-oxidation to key industrial commodity chemicals, such as acrolein, acrylic acid and propylene oxide. In this study, we investigate the partial electrochemical oxidation of propene on high-surface area Pd electrodes using a combination of electrochemical measurements, advanced product characterization and theoretical modeling. We report a new reaction product, propylene glycol, and high selectivity towards acrolein. We further identify key reaction intermediates and propose a mechanism dictated by the surface coverage of organic species formed *in situ*, where stable reactant adsorption at low coverage determines the selectivity towards allylic oxidation at high coverage. Our fundamental findings enable advances in partial hydrocarbon oxidation reactions by highlighting atomic surface structuring as the key to selective and versatile electrochemical catalyst design.

Received 22nd November 2018,  
Accepted 19th February 2019

DOI: 10.1039/c8ee03426e

rsc.li/ees

### Broader context

The transition from fossil to renewable energy sources must accelerate to mitigate the devastating effects of climate change. Within this context, society electrification is a highly regarded strategy, in which the industrial sectors are also expected to migrate to electrified manufacturing processes. Many thermocatalytic industrial chemical processes – some established for more than a century – are expensive and energetically inefficient and therefore require modernization. In many cases, electrochemistry has great potential for replacing outdated processes. Electrochemical reactions are inherently safer and allow fine selectivity control in optimized systems. They are also more versatile and scalable, and thus suited for decentralization and embedding in national energy grids, which will help compensate renewable energy fluctuations. In particular, a great opportunity lies in optimizing electrochemical partial oxidation reactions, which offer shortcuts to valuable products not accessible in the traditional chemical industry due to the tendency of carbon compounds to fully oxidize in thermally driven processes. Understanding the factors that control electrocatalytic reactions at the atomic level is the first step to creating efficient large scale electrochemical processes. Our work provides fundamental insights into the mechanism of hydrocarbon electro-oxidation through the study of a model, yet industrially relevant reaction: partial propene oxidation.

<sup>a</sup> SurfCat, Department of Physics, Technical University of Denmark, Fysikvej, Byg. 311, 2800 Kgs. Lyngby, Denmark. E-mail: ibchork@fysik.dtu.dk

<sup>b</sup> Nano-Science Center, Department of Chemistry, University of Copenhagen, Universitetsparken 5, 2100 Copenhagen, Denmark. E-mail: jan.rossmeisl@chem.ku.dk

<sup>c</sup> Department of Chemistry, Technical University of Denmark, Kemitorvet, Byg. 207, 2800 Kgs. Lyngby, Denmark

<sup>d</sup> Spectro Inlets, COBIS, Ole Maaløes Vej 3, 2200 Copenhagen, Denmark

<sup>e</sup> Haldor Topsoe A/S, Haldor Topsoes Allé 1, 2800 Kgs. Lyngby, Denmark

<sup>f</sup> Department of Materials, Imperial College London, Royal School of Mines, London, SW7 2AZ, UK

† Electronic supplementary information (ESI) available. See DOI: 10.1039/c8ee03426e

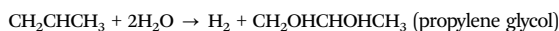
\* These authors contributed equally.

## 1. Introduction

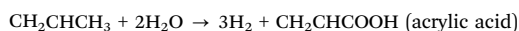
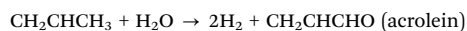
Wind and solar energy are increasingly outcompeting fossil fuels for electricity generation.<sup>1</sup> Increasing renewable electricity output calls for the electrochemical production of commodity chemicals, such as alcohols, aldehydes and acids.<sup>2–4</sup> Selective direct oxidation of hydrocarbons to partially oxidized products while avoiding full oxidation to CO<sub>2</sub>, the most thermodynamically favored product, remains elusive in gas phase heterogeneous catalysis.<sup>5–11</sup> Compared to thermal heterogeneous catalysis, an electrochemical approach to selective partial oxidation can

be advantageous. Mild oxidizing conditions and fine control over reaction parameters could direct the reaction to one specific product while preventing the formation of  $\text{CO}_2$ .<sup>12–14</sup> At the same time, electrochemical reactors based on fuel cell technology would allow for decentralized production with flexible feedstocks.<sup>15</sup>

Propene is an interesting model molecule for studying mechanisms concerning hydrocarbon selective oxidation. It provides two different reaction sites: the C–C double bond (vinyl group) and the allyl carbon. Oxidation of the double bond leads to the formation of 1,2-propylene oxide, which is hydrolyzed to propylene glycol in an aqueous environment.<sup>16</sup>



The allylic carbon, on the other hand, can be oxidized to produce allyl alcohol, acrolein, and acrylic acid.<sup>17</sup>



The structures of propene and relevant oxidation products are reported in Fig. 1.

High annual production capacities for several partial oxidation products of propene highlight the importance of this reaction; examples are propylene oxide (9.81 Mt, 2016),<sup>18</sup> propylene glycol (2.56 Mt, 2017 prognosis),<sup>19</sup> and acrylic acid (7.66 Mt, 2016).<sup>18</sup> Acetone, despite annual production volumes on the same order of magnitude as those mentioned,<sup>20</sup> is not considered hereafter a desired product, as it does not form electrocatalytically in our reaction system.

A few prior studies have examined the direct electrochemical oxidation of propene.<sup>21–27</sup> The most promising results have been reported on palladium electrodes in an acidic environment. Stafford<sup>28</sup> reported acrolein, acrylic acid, acetone and  $\text{CO}_2$  as the main products on palladium in an acidic aqueous electrolyte. Otsuka *et al.*<sup>29</sup> used a fuel cell set-up and found mainly acrolein and acrylic acid at lower cell voltage, but increasing amounts of acetone and  $\text{CO}_2$  at higher cell voltage. However, neither of these studies provide a full picture of faradaic efficiency *versus* potential, nor do they propose a mechanistic explanation for the observed selectivity towards allylic oxidation.

Herein, we present a systematic study of propene oxidation on high surface area palladium electrodes. We use dilute  $\text{HClO}_4$  as the electrolyte, known to be non-interacting with the electrode, to decouple electrolyte effects from surface dynamics.<sup>30</sup> We differentiate the electrocatalytic pathway from non-electrochemical side reactions, confirming that acetone is produced by a homogeneous reaction with  $\text{Pd}^{2+}$ .<sup>28,29</sup> We report the identification of a key electrochemical reaction intermediate, allyl alcohol, as well as an additional product, propylene glycol, which to the best of our knowledge has not been reported on this catalyst before. Using a combination of density functional theory

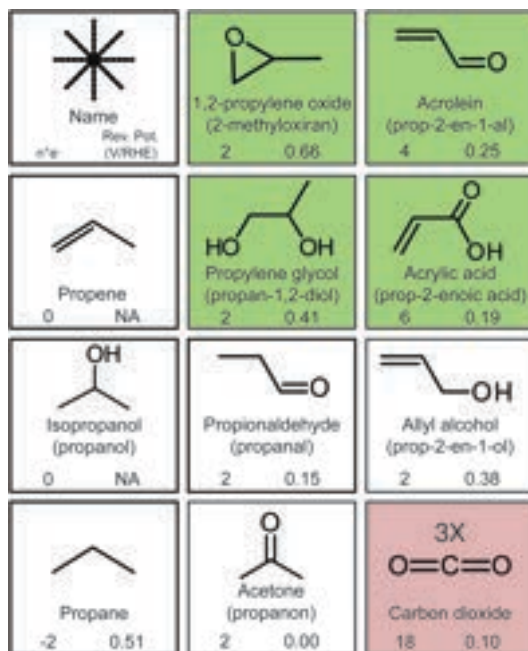


Fig. 1 Overview of propene and its main derivatives. A green background highlights industrially relevant products, while red denotes undesired compounds. The thermodynamic reversible potential for formation by propene oxidation was calculated from the reaction free energy, including solvation for all liquid products. Calculations details are reported in the ESI.†

(DFT) modeling and electrochemical mass spectrometry (EC-MS), we provide fundamental insights into the mechanism governing the changes in product distribution with potential in bulk experiments. The surface coverage plays a crucial role in steering the oxidation activity and selectivity: surface chemistry under reaction conditions forces reactants to weaker adsorption configurations, enabling selective oxidation of the allyl carbon.

## 2. Experimental methods

### Deposition of porous Pd

High surface area Pd electrodes were prepared by electrodeposition on glassy carbon sheets ( $1 \times 1.5$  cm, HTW-Germany) or on glassy carbon disks (5 mm diameter, Pine Instruments) for the EC-MS measurements. The sheets/disks were initially thoroughly polished with  $1/4 \mu\text{m}$  diamond on a polishing cloth (Stuers). Before each experiment the glassy carbon electrodes were cleaned of metal contamination by immersion in aqua regia, followed by repeated rinsing and sonication in ultrapure water. For the electrical contact, a Pt wire was attached to the glassy carbon and wrapped in Teflon tape to prevent contact with the electrolyte. The Pd deposition was carried out using a 2 mM  $\text{PdCl}_2$  solution (99.999%, Sigma Aldrich) in 2 M  $\text{H}_2\text{SO}_4$  (suprapur, Merck) in a 2-electrode setup with a Pt mesh (99.9%, GoodFellow) as a counter electrode. For optimal adhesion, a thin Pd layer was deposited at  $-1$  V vs. the counter

electrode for 1 min, followed by deposition at  $-4$  V *vs.* counter for 3 min with simultaneous  $H_2$  evolution (hydrogen bubble template method).<sup>31,32</sup> The electrode was thoroughly rinsed with ultrapure water before further use.

### Electrochemical experiments

Electrochemical experiments with product analysis were carried out in a 3-electrode setup in a 3-compartment glass cell (H-cell, see Fig. 2), as described previously.<sup>33</sup> The electrolyte was prepared by dilution of concentrated  $HClO_4$  (suprapur, Merck) in ultrapure water (18.2 M $\Omega$  resistivity, Millipore, Synergy UV system). A Pt mesh counter and a Hg/HgSO<sub>4</sub> reference electrode were employed. The reference electrode was calibrated regularly *versus* the RHE scale by measuring the open circuit voltage (OCV) at a Pt electrode in  $H_2$  saturated electrolyte until stable for at least 10 minutes. Gases (Ar 5.0, AGA or propene 4.0, BOC) were supplied through a glass frit, connected to a gas loop allowing for circulation of the gas during the reaction. Additional experiments were carried out in a conventional RDE setup.

For each measurement, a freshly prepared sample was placed in electrolyte and held at 0.4 V *vs.* RHE while the electrolyte was purged with propene. No electrochemical reaction is observed at this potential. The potential was then stepped up to the potential of interest and held for one hour.

The electrochemical surface area (ECSA) was determined after each experiment, using the PdO reduction peak in cyclic voltammograms. These CVs were measured in fresh electrolyte. Rather than assuming oxidation of a full monolayer of Pd, we calibrated the charge from PdO reduction with CO stripping experiments on the same electrode (for details see the ESI<sup>†</sup>).

All glassware was cleaned with aqua regia before use.

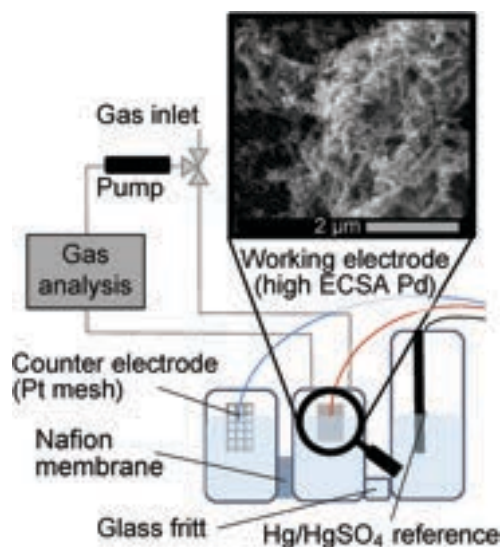


Fig. 2 Schematic of the 3-compartment cell used for bulk oxidation experiments. The inset shows a SEM image of a high surface area palladium electrode.

### Product analysis

Gaseous products were determined by gas chromatography (GC). Different methods were used for liquid product characterization: static headspace gas chromatography (HS-GC) for acetone and propanal, high pressure liquid chromatography (HPLC) for acrolein and acrylic acid, and quantitative nuclear magnetic resonance spectroscopy (qNMR) for allyl alcohol, isopropanol and propylene glycol. The Pd concentration in the electrolyte was determined with inductively coupled plasma-mass spectrometry (ICP-MS). For experimental details, see the ESI<sup>†</sup>.

### EC-MS

For electrochemistry-mass spectrometry (EC-MS) measurements, we used the setup and methodology described previously.<sup>34</sup> This setup uses a membrane microchip to interface the electrochemical environment and the vacuum system containing the mass spectrometer. CO and propene stripping experiments involved (1) dosing the reactant gas (CO or propene) through the membrane chip while holding the electrode at a constant potential, (2) flowing He through the chip until the mass spectrometer signal for the reactant gas returned to the baseline, and (3) cycling the electrode potential. All EC-MS measurements were performed in 1.0 M  $HClO_4$  in order to have sufficient electrolytic conductivity through the thin layer of electrolyte. Mass spectrometer signals were converted to amounts of propene, propane, and  $CO_2$  using internal calibration measurements (see the ESI<sup>†</sup> for details).

### DFT calculations

All ground state DFT and climbing image nudged elastic band (NEB) calculations were performed with the Grid-based Projector Augmented Wave (GPAW) program and the Atomic Simulation Environment (ASE) package.<sup>35–37</sup> The Kohn–Sham wavefunctions are represented on real-space uniform grids (finite difference mode); we used the BEEF-vdW exchange and correlation functional, a grid spacing of 0.18 Å and  $k$ -point sampling of  $(2 \times 2 \times 1)$ . For NEB calculations, the RPBE exchange and correlation functional was used instead to quantify the energy gap between initial and transition states in chemical reaction steps. More computational details and information on structures and reference compounds are reported in the ESI<sup>†</sup>.

## 3. Results and discussion

### Electrocatalytic activity

Cyclic voltammograms (CVs) of high surface area Pd in Ar and propene saturated 0.1 M  $HClO_4$  are shown in Fig. 3a (black and red line, respectively). The onset of Pd oxidation is at *ca.* 0.65 V *vs.* RHE; two oxidation waves can be distinguished with peaks around 0.8 and 1.1 V *vs.* RHE, suggesting a range of different facets are present on the Pd electrode.<sup>38–41</sup> In the cathodic scan a sharp reduction peak is present at *ca.* 0.7 V *vs.* RHE, where PdO is reduced. In propene saturated  $HClO_4$  the onset of oxidative current is shifted significantly to almost 0.9 V *vs.* RHE, followed by an oxidative peak with a significantly higher peak current than in Ar at a potential of *ca.* 1.1 V *vs.* RHE. We attribute this peak to the

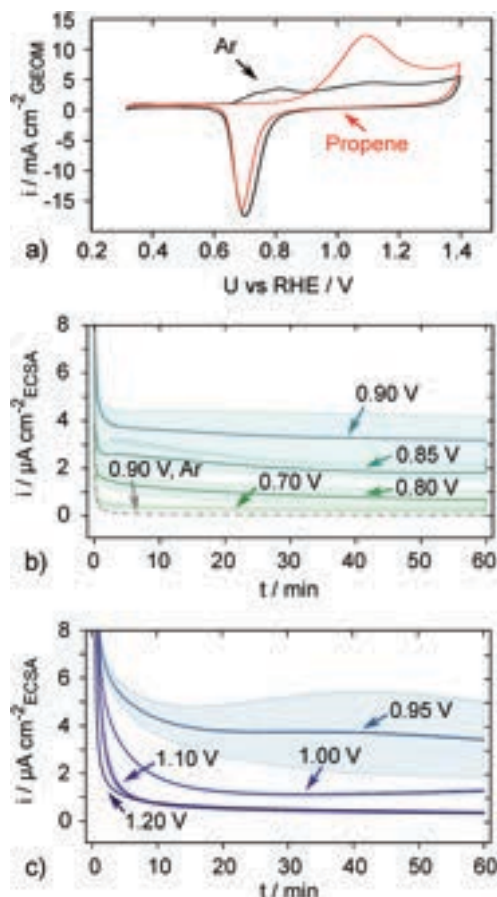


Fig. 3 (a) Cyclic voltammograms (stable) of high surface area Pd in 0.1 M  $\text{HClO}_4$  saturated with Ar (black) and propene (red), respectively, recorded at a scan rate of  $50 \text{ mV s}^{-1}$  in a rotating disc electrode setup (no rotation) while purging with gas. (b and c) Current–time traces of propene oxidation at constant potentials in 0.1 M  $\text{HClO}_4$ : average and standard deviations of three ( $E \leq 0.95 \text{ V}$ ) or two ( $E = 1.0 \text{ V}, 1.1 \text{ V}$ ) electrodes and a single, representative experiment for 1.2 V. The current–time trace in Ar saturated electrolyte at 0.9 V vs. RHE is shown for comparison. (b) Mildly oxidizing potentials, (c) strongly oxidizing potentials.

oxidation of propene in addition to PdO formation. The PdO reduction peak area is similar in the presence of propene, supporting the interpretation that the increased current in the anodic scan is in fact irreversible oxidation of propene rather than increased surface oxidation, as the latter would also manifest in a more pronounced reduction peak.

In order to investigate the selectivity for different products, we carried out chronoamperometry experiments in 0.1 M  $\text{HClO}_4$ . Products were accumulated for 1 h at a constant potential in order to reach high enough product concentrations for reliable product detection (see the Methods section for details). ECSA normalized current–time traces recorded during product accumulation are shown in Fig. 3b and c. In all cases, a significant

initial current drop is observed. For a more detailed analysis of the current–time traces, see Fig. S4 (ESI<sup>†</sup>). The highest current densities are observed at 0.90 and 0.95 V vs. RHE. At the same potentials, the variation between the individual experiments is also the largest. With the equilibrium potential for the oxidation of Pd at pH 1 being 0.91 V vs. RHE,<sup>42</sup> the high variability at these potentials is presumably related to the instability of the catalyst due to the surface redox and/or dissolution processes, which may modify the surface area to an unknown degree. The drop in current density at potentials larger than 0.95 V vs. RHE can be explained by the formation of passivating PdO on the surface.

### Product distribution and potential

**Primary oxidation products.** Fig. 4 shows the propene oxidation activity and product distribution as a function of potential. The faradaic efficiencies and partial current densities are shown for various products in Fig. 4a–c and Fig. 4d–f, respectively. The current was calculated based on the concentration at the end of the 1 h period. For better readability, the products are divided into three groups: the main target product acrolein, other propene oxidation products of interest (allyl alcohol, acrylic acid and propylene glycol), and undesired side products (acetone,  $\text{CO}_2$  and dissolved Pd).

The partial current density and faradaic efficiency for acrolein production are highest in the middle of the potential range studied, with maxima of  $2.1 \mu\text{A cm}^{-2}$  and 62%, respectively, at 0.9 V vs. RHE. At potentials above 1.1 V vs. RHE the concentration was too low for quantification. The trends for acrylic acid follow those for acrolein, reaching a maximum faradaic efficiency of 11% at 0.9 V vs. RHE. Allyl alcohol shows a similar dependency, except that the peak maximum is shifted to 0.85 V vs. RHE. Propylene glycol, on the other hand, is only produced at 1.0 V vs. RHE and more anodic, and both the specific current density and faradaic efficiency increase with increasing anodic potential. In addition to the mentioned products, small amounts of propanal were observed, but were too small to measure quantitatively (see Fig. S14 and S25, ESI<sup>†</sup>). The non-electrochemical product isopropanol was also observed in small quantities (1% of liquid products by mol at 0.9 V vs. RHE).

We attribute the high standard deviation in product faradaic efficiency below 0.9 V vs. RHE to the lack of significant quantities of products (see the ESI<sup>†</sup>); however, at 0.9 and 0.95 V vs. RHE we hypothesize the error is caused by the instability of the catalyst due to oxidation and dissolution processes as discussed above.

The overall faradaic efficiency considering only propene oxidation products is significantly less than 100% at strongly oxidizing potentials (Fig. 4), which may partially relate to oxidation of the surface and corrosion of the catalyst. Based on the charge required for the formation of one monolayer PdO (Fig. S4, ESI<sup>†</sup>), we estimated that at potentials more anodic than 0.95 V vs. RHE, Pd oxidation can account for up to 10–15% faradaic efficiency, increasing the total faradaic efficiency to at least 90%.

**Homogeneous reactions.** We noted undesired side reactions are taking place in the electrolyte. The acid catalyzed hydration of propene to isopropanol in the presence of water is well known<sup>43</sup> and was also observed in the electrolyte after purging with propene without an electrode (see the ESI<sup>†</sup>). Separate experiments with isopropanol added directly to the electrolyte showed no activity for

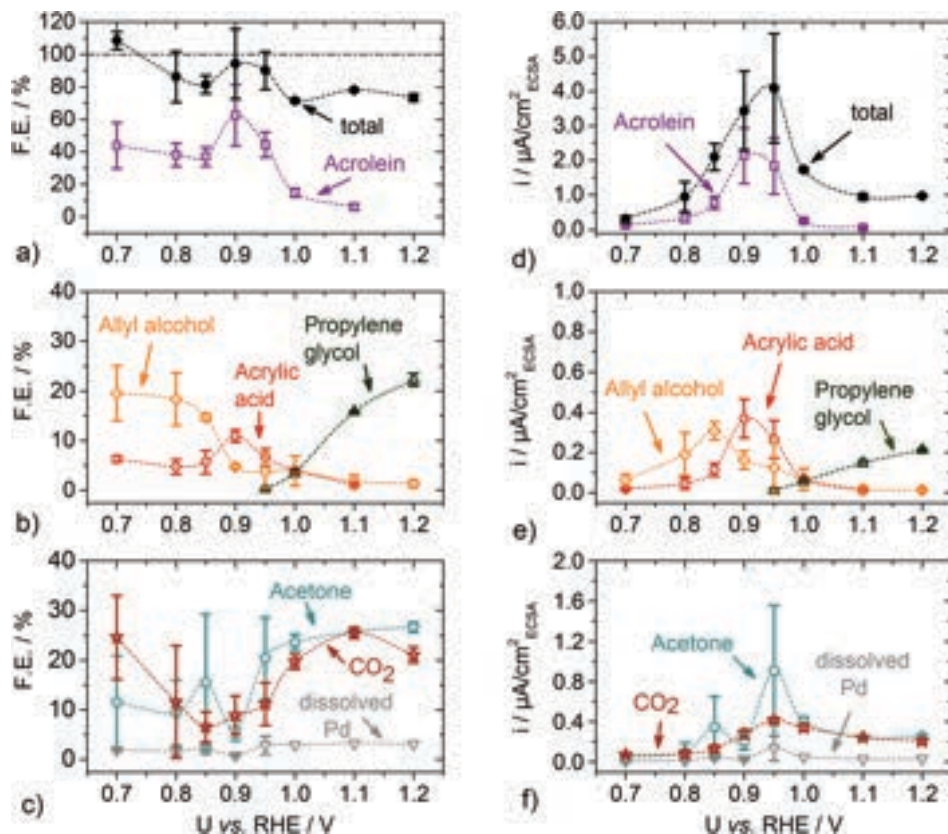


Fig. 4 Product distribution from chronoamperometry experiments presented in Fig. 3b and c as a function of potential: (a–c) faradaic efficiencies; (d–f) partial current densities. Additional undetected products were propanal (concentration unreliable as close to the quantification limit, see the ESI†) and isopropanol (chemical product, see the text).

electrochemical oxidation of the alcohol, excluding this compound from the primary reaction mechanism.

Previous studies on this system have reported homogeneous side reactions with  $\text{Pd}^{2+}$  in solution.<sup>28,29</sup> The concomitant increase of the acetone concentration with the Pd-ion concentration throughout the experiments suggests a direct relationship. In order to verify the role of  $\text{Pd}^{2+}$  as a catalyst/reactant for the oxidation to acetone, we analyzed the products formed when purging propene through a 0.1 M  $\text{HClO}_4$  solution containing different concentrations of  $\text{Pd}^{2+}$  ions (Fig. 5).

The concentration of the main product acetone linearly increases with Pd concentration with a slope close to one, indicating the role of  $\text{Pd}^{2+}$  in acetone production and suggesting that the  $\text{Pd}^{2+}$  ions are fully consumed within the reaction time. For  $\text{Pd}^{2+}$  concentrations of 100  $\mu\text{M}$  and above, the formation of metal nanoparticles was evident from discoloration of the solution and formation of a precipitate. The reaction is expected to proceed through a Wacker-type mechanism as follows ( $\Delta G = -167 \text{ kJ mol}^{-1}$ ):<sup>29</sup>

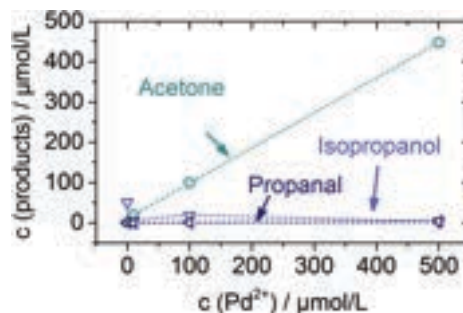
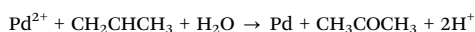


Fig. 5 Homogeneous reaction of propene in 0.1 M  $\text{HClO}_4$  with different concentrations of  $\text{PdCl}_2$ . All products formed under these conditions are shown in the figure.

While closing the catalytic cycle by re-oxidation of Pd at the electrode has been proposed,<sup>29</sup> we did not see evidence for this in our system (see Fig. S26, ESI†). Therefore we do not consider acetone as a desirable product.

**Product stability.** Degradation of products before quantification resulting in an underestimation of the amounts produced could explain the low total faradaic efficiencies in Fig. 4a. We therefore followed changes in product concentrations with time after the end of the experiment. We observed a significant decrease in acrolein concentration over time, which we could assign to the formation of hydration products 3-hydroxypropanal and propane-1,3,3-triol (see the ESI<sup>†</sup>). Despite our efforts to quantify acrolein and acrylic acid as fast as possible using HPLC, this might lead to a slight underestimation in their quantification.

### Surface chemistry and mechanistic analyses

In the following, we rationalize the observations in bulk oxidation tests with mechanistic analyses by means of DFT modeling and propene stripping experiments, proposing a reaction mechanism for the potential window in which the catalyst surface is metallic. We further provide insights into the relationship between surface population and catalytic activity, highlighting the correlation of surface coverage with the reaction outcome.

**Surface species, intermediates and reaction pathway – DFT.** Fig. 6 shows the energies of propene oxidation products, intermediates and transition states relative to water, propene, and the palladium fcc(111) surface, calculated by DFT and adjusted to +0.9 V vs. RHE using the computational hydrogen electrode reference system.<sup>44</sup> For the energy levels at 0.0 V vs. RHE, see Fig. S29 (ESI<sup>†</sup>). Fig. 6a reports the reaction energetics as calculated on a clean Pd slab (termed clean), while Fig. 6b shows the energy for the same intermediates adsorbed on a Pd slab with high surface coverage, mimicked by six CO spectator molecules adsorbed per unit cell (termed CO poisoned), contouring the intermediates' adsorption site(s). In Fig. 6, in addition to the energies of the intermediates, we report the initial states for chemical oxidation steps as half light/half teal blue lines, with energy values corresponding to the sum of the respective adsorbates' energy, and the calculated gas phase product reversible potentials. The kinetic reaction barriers are represented by dashed curves linking initial, transition and final states. The other dashed lines between intermediates indicate an elementary step of a (H<sup>+</sup>/e<sup>-</sup>) couple loss with negligible kinetic barrier.

The first catalytic step in propene electro-oxidation is adsorption of propene. Comparing the possible adsorption geometries, we find that adsorption *via* deprotonation of the allyl carbon is the most favorable for the potential range of interest (Fig. S27, blue bars, ESI<sup>†</sup>); additionally, propene activation in the allylic position is consistent with the observed product distribution. We therefore focus the mechanistic analysis on propene oxidative adsorption and reactivity *via* allylic carbon activation, followed by reaction with adsorbed \*OH or \*O. In Scheme 1, we report the elementary steps considered in the mechanistic study.

The consideration of elementary steps whereby adsorbed propene reacts with \*OH and \*O (Langmuir–Hinshelwood mechanism) is motivated by different factors. First, the onset of significant propene oxidation activity at about 0.7 V vs. RHE (Fig. 4) corresponds well with the DFT-calculated OH adsorption energy and OH adsorption features in the cyclic voltammogram in argon (Fig. 3a). Second, the

calculated adsorption energy of propene through the allyl carbon is significantly more exergonic than \*OH adsorption, suggesting the reason for the observed low activity is palladium's stronger affinity toward carbon as compared to oxygen. Third, the \*OH adsorption features of the cyclic voltammograms in Fig. 3a are suppressed in propene until the onset of propene oxidation, implying that water activation is limiting the working potential window and that \*OH adsorption is required for the oxidation of propene. This kind of competitive adsorption of two Langmuir–Hinshelwood reactants is familiar from CO electro-oxidation on platinum.<sup>34,45,46</sup>

The suppression of surface oxidation in the presence of propene also justifies our modeling of the reaction on metallic palladium fcc(111). Moreover, this facet has the lowest surface energy of all Pd surfaces, so we expect it to be the most abundant facet on polycrystalline Pd.<sup>47</sup> As explained in greater detail later, reactivity is limited by strong binding of propene, so we omit modeling facets more reactive than (111) as they would perform poorer in the reaction mechanism presented. Instead, we model the reaction by poisoning the catalyst with CO (Fig. 6b), to limit surface site accessibility and investigate the mechanism with destabilized intermediates.

Allylic propene adsorption on Pd begins with \*CH<sub>2</sub>CHCH<sub>2</sub> (1), which further deprotonates to \*CHCHCH<sub>2</sub> (2) or \*CCHCH<sub>2</sub> (3), if sites are available. The intermediates adsorb in atop, bridge and 3-fold hollow geometries, respectively; (1) and (2) are significantly stabilized on the clean surface through coordination of the vinyl group (Fig. S27, ESI<sup>†</sup>). At high surface coverage (Fig. 6b), vinylic coordination is hindered as it requires greater site availability than bare allylic adsorption. Adsorbed propene degradation is favorable on clean Pd (Fig. 6a), yielding adsorbed C1 and C2 species as reported with grey lines in Fig. 6 (the most thermodynamically favored degradations) and Fig. S28 (all degradation products, ESI<sup>†</sup>). Similarly to vinylic coordination, we observe that on the poisoned surface the degradation is inhibited, *i.e.* the energy levels for C1 and C2 species shift upwards relative to adsorbed propene. At the theoretical potential for water activation (0.7 V vs. RHE), \*O and \*OH calculated adsorption energies are roughly equivalent and the two coexist on the surface. At increasingly anodic potentials, \*O coverage progressively replaces \*OH on clean Pd, while on the CO poisoned surface \*OH remains the most stable source of oxygen over a wide potential range. For potentials higher than 1.1 V vs. RHE, experimentally we observe a significant activity drop, presumably because of catalyst surface oxidation with a different reaction mechanism involved, whose modeling is beyond the scope of this report.

At potentials above water activation (> 0.7 V vs. RHE), we cannot exclude a contribution from \*OH and \*O to propene proton abstraction; nonetheless we do not anticipate this phenomenon to make a significant contribution to the reaction mechanism: both theoretical simulations and electrochemical mass spectrometry (see below) suggest the oxidative adsorption of propene to occur at much more cathodic potentials.

We then investigate the kinetic barriers to products, calculating the relevant transition state energies on clean and CO poisoned Pd. We find significant activation barriers for all coupling steps

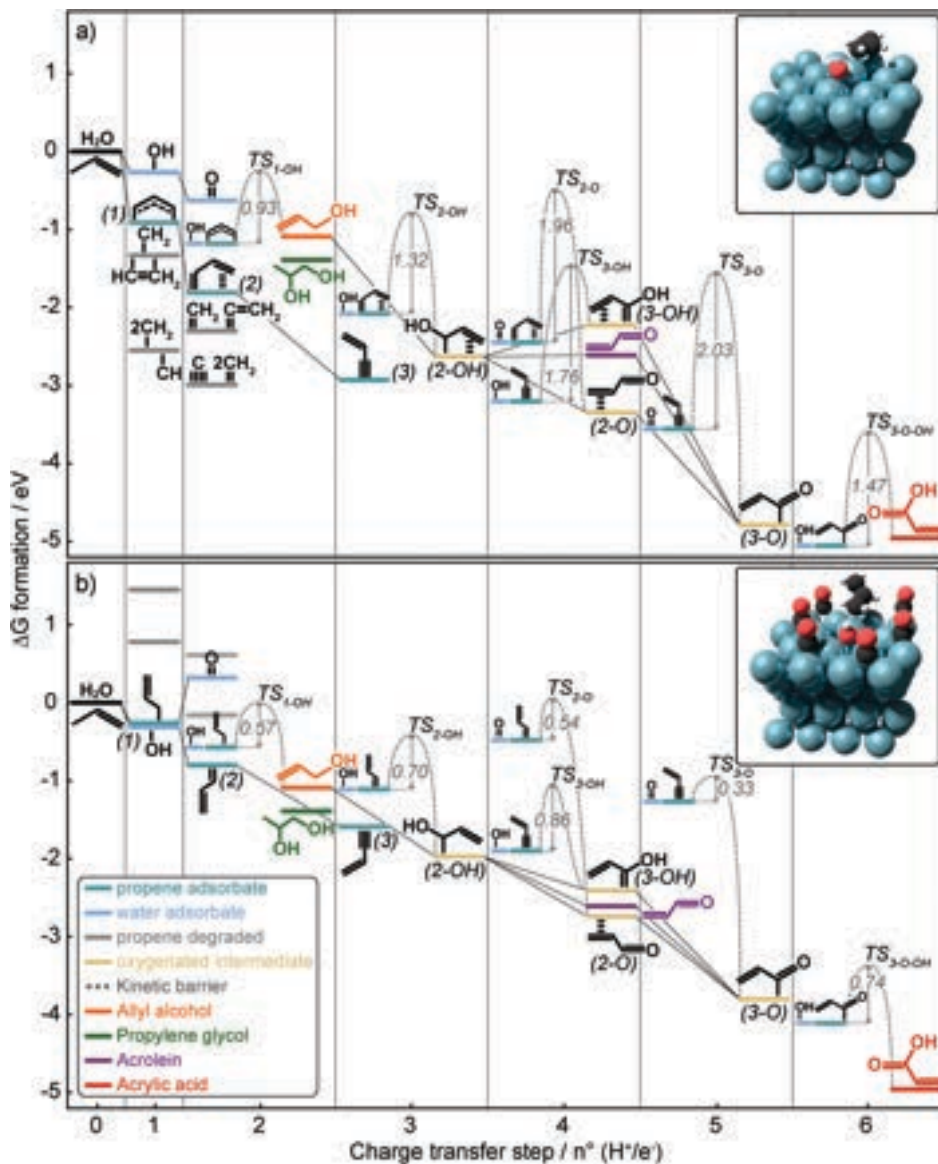


Fig. 6 Proposed reaction scheme for propene oxidation in water on (a) the clean Pd fcc(111) surface and (b) 6\*CO poisoned Pd fcc(111). The DFT Gibbs energy of formation for adsorbed intermediates and transition states at  $U = 0.9 \text{ V}$  vs. RHE are given as a function of the number of  $\text{H}^+ / \text{e}^-$  couples exchanged with the system. We assign labels in brackets to all intermediates for easier referencing in the text. The graphical insets provide visual examples of the model catalyst surface with adsorbates.

between adsorbed propene and \*O or \*OH, which we consider the reaction rate determining steps. Their transition states can be safely modelled since they all are potential independent, chemical reaction steps. In general, we predict high energy barriers if the intermediates react on a clean Pd surface, as reported in Fig. 6a. For (1) + OH coupling, required to form allyl alcohol, we calculate an activation energy close to 1 eV, which we consider virtually

unsurmountable at the experimental conditions tested. For all other steps, the kinetic barriers are even higher: For oxidation of (2) \*CHCHCH<sub>2</sub> and (3) \*CCHCH<sub>2</sub>, we find an unfavorable activation energy for oxygen incorporation of around 2 eV, both with \*O and \*OH. Besides, (3) is an intermediate that cannot convert to the primary product acrolein, as all allylic protons are lost. While (3) in theory can react to acrylic acid, its strong

Elementary step	$\Delta G^\ddagger$ (eV) @ 0.9 V vs. RHE	
	Clean	CO poisoned
$\text{CH}_2\text{CHCH}_3 + * \rightarrow * \text{CH}_2\text{CHCH}_3 + (\text{H}^+/\text{e})$ (propene) (1)	-0.91	-0.26
$* \text{CH}_2\text{CHCH}_3 \rightarrow * \text{CHCHCH}_3 + (\text{H}^+/\text{e})$ (1) (2)	-0.90	-0.54
$* \text{CHCHCH}_3 \rightarrow * \text{CCHCH}_3 + (\text{H}^+/\text{e})$ (2) (3)	-1.13	-0.79
$\text{H}_2\text{O} + * \rightarrow * \text{OH} + (\text{H}^+/\text{e})$	-0.27	-0.31
$* \text{OH} \rightarrow * \text{O} + (\text{H}^+/\text{e})$	-0.36	0.64
$* \text{CH}_2\text{CHCH}_3 + * \text{OH} \rightarrow \text{CH}_2\text{OHCHCH}_3 + 2*$ (1) (allyl alcohol)	0.09 <sup>a</sup>	-0.52 <sup>a</sup>
$* \text{CHCHCH}_3 + * \text{OH} \rightarrow * \text{CH(OH)CHCH}_3 + *$ (2) (2-OH)	-0.55 <sup>a</sup>	-0.66 <sup>a</sup>
$\text{CH}_2\text{OHCHCH}_3 + * \rightarrow * \text{CH(OH)CHCH}_3 + (\text{H}^+/\text{e})$ (allyl alcohol) (2-OH)	-1.54	-0.88
$* \text{CH(OH)CHCH}_3 \rightarrow * \text{C(OH)CHCH}_3 + (\text{H}^+/\text{e})$ (2-OH) (3-OH)	0.40	-0.44
$* \text{CH(OH)CHCH}_3 \rightarrow \text{CHOCHCH}_3 + * + (\text{H}^+/\text{e})$ (2-OH) (acrolein)	0.02	-0.64
$* \text{CH(OH)CHCH}_3 \rightarrow \text{CHOCH}_2\text{CH}_3 + (\text{H}^+/\text{e})$ (2-OH) (2-O)	-0.72	-0.77
$* \text{CHCHCH}_3 + * \text{O} \rightarrow \text{CHOCHCH}_3 + *$ (2) (2-O)	-0.92 <sup>a</sup>	-2.26 <sup>a</sup>
$* \text{CCHCH}_3 + * \text{OH} \rightarrow * \text{C(OH)CHCH}_3 + *$ (3) (3-OH)	0.97 <sup>a</sup>	-0.51 <sup>a</sup>
$\text{CHOCHCH}_3 \rightarrow \text{CHOCHCH}_3 + *$ (2-O) (acrolein)	0.74 <sup>a</sup>	0.13 <sup>a</sup>
$* \text{CCHCH}_3 + * \text{O} \rightarrow * \text{COCHCH}_3 + *$ (3) (3-O)	-1.23 <sup>a</sup>	-2.53 <sup>a</sup>
$* \text{C(OH)CHCH}_3 \rightarrow * \text{COCHCH}_3 + (\text{H}^+/\text{e})$ (3-OH) (3-O)	-2.56	-1.39
$\text{CHOCH}_2\text{CH}_3 \rightarrow * \text{COCH}_2\text{CH}_3 + (\text{H}^+/\text{e})$ (2-O) (3-O)	-1.44	-1.06
$* \text{COCH}_2\text{CH}_3 + * \text{OH} \rightarrow \text{COOHCH}_2\text{CH}_3 + 2*$ (3-O) (acrylic acid)	0.10 <sup>a</sup>	-0.85 <sup>a</sup>

<sup>a</sup> energy of chemical step, potential independent

**Scheme 1** Elementary reaction steps with relative free energy variation at 0.9 V vs. RHE for clean (Fig. 6a) and CO poisoned (Fig. 6b) catalytic substrates. The labels and colors correspond to those in Fig. 6.

interaction with the surface should block its participation in the reaction mechanism.

However, the reaction energetics significantly change if the adsorption geometry of adsorbates is restricted due to the high surface coverage modeled with \*CO. The intermediates' binding energies on the model CO poisoned surface are significantly weakened (Fig. 6b), while the transition states' energetics are only marginally affected. Such selective destabilization results

in the critical attenuation of the kinetic barriers, allowing for the reaction to proceed at room temperature. Similarly, adsorbed intermediates are destabilized relative to desorbed products, enabling an exergonic pathway to final products.

In propene electro-oxidation, a mechanistic model that neglects the effects of surface coverage has evident limitations, as it cannot explain the observed product distribution. By comparison between clean surface and \*CO hindered reactivity, we propose that propene electro-oxidation to allyl alcohol, acrolein and acrylic acid is enabled only in high surface coverage regimes. Notably, strong energetic drivers to propene degradation on clean Pd suggest not all the adsorbates are oxidized to a desorbing product, increasing the surface population. To test experimentally whether there is a high surface coverage under reaction conditions, we performed propene stripping experiments.

**Probing surface population – propene stripping.** We carried out propene stripping experiments in an electrochemistry-mass spectrometry (EC-MS) setup to test for the presence of surface adsorbates under reaction conditions. Fig. 7a shows the result of a propene stripping experiment as an EC-MS plot,<sup>34</sup> with calibrated mass spectrometer signals (propene = C<sub>3</sub>H<sub>6</sub> at  $m/z = 41$ , propane = C<sub>3</sub>H<sub>8</sub> at  $m/z = 29$ , and CO<sub>2</sub> at  $m/z = 44$ ) in the upper panel, and electrochemistry data in the lower panel. The propene is dosed before  $t = 0$  while the electrode is held at a constant dose potential (here +0.65 V vs. RHE) and then purged from the solution. The potential was then cycled, first cathodic to +0.1 V vs. RHE and then anodic to +1.4 V vs. RHE, while gaseous products were monitored with a mass spectrometer. The majority of desorption products come off during this first cycle (Fig. 7a). Thereafter, the electrode is cycled several times (see Fig. S10, ESI<sup>†</sup>), and the electrolyte is replaced to ensure a clean system for the next propene dose. This procedure was then repeated changing the dose potential.

Propene and propane desorb on the initial cathodic sweep, and CO<sub>2</sub> desorbs on the subsequent cathodic and anodic sweeps. Propene desorption likely represents propene in weak adsorption geometries which can be displaced by surface hydrogen adsorption. Propane is presumed to derive from the hydrogenation of propene adsorbed through vinylic coordination. The dip in the propene signal at the cathodic potential limit may indicate that weakly-adsorbed propene can also be reduced with sufficient overpotential. CO<sub>2</sub> desorption after the initial cathodic sweep indicates the presence of strongly bound adsorbates, which cannot be displaced by \*H or reduced to propane. Interestingly, a secondary CO<sub>2</sub> peak is observed in the subsequent cathodic scan, as has been observed previously in allyl alcohol stripping experiments.<sup>48,49</sup> A small amount of CO may have also been observed as a desorption product for some of the stripping experiments, but is challenging to quantify due to interference from both propane and CO<sub>2</sub> in its primary mass fragment,  $m/z = 28$ . In cyclic voltammetry without propene dosing, a much smaller amount (<5% ML) of CO<sub>2</sub> is observed in each anodic sweep and attributed to oxidation of residual carbon contamination from the air.

It should be noted that the EC-MS setup used here is not sensitive towards non-volatile, liquid products. Based on Fig. 4, we expect that significant liquid products are produced while

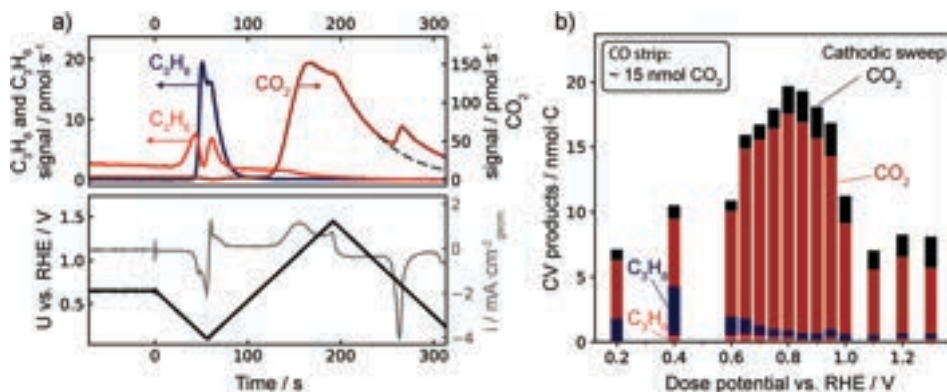


Fig. 7 Propene stripping experiments: (a) EC-MS plot of propene stripping. Propene has been dosed and purged at a dose potential of 0.65 V vs. RHE. Starting at  $t = 0$ , the potential is scanned cathodically to 0.1 V vs. RHE and then cycled between 0.1 V vs. RHE and 1.4 V vs. RHE while the desorption products propene ( $C_3H_6$ ), propane ( $C_3H_8$ ), and  $CO_2$  are monitored. (b) The amount of carbon desorbed in the form of the three observed desorption products during the first full cycle of the stripping experiments is plotted as a function of the potential at which propene was dosed.  $CO_2$  evolving during the first anodic and the subsequent cathodic scan is quantified separately as indicated.

propene is dosed for dosing potentials in the range 0.8–1.0 V vs. RHE. However, since the adsorbates remaining on the surface after propene is purged already had the chance to form liquid products during the stripping experiment itself is minor. Fig. 7b shows the integrated amount of each desorption product from successive propene stripping experiments as a function of the potential at which the propene was dosed. The products are added together based on the number of carbon atoms so that their proportions represent the portion of the adsorbed propene resulting in each stripping product. A broad maximum in the total amount of desorbates is observed in the range 0.7–0.9 V vs. RHE, where the primary desorption product is  $CO_2$ . The coverage (on a carbon-atom basis) in this potential range exceeds the saturation coverage of CO based on a CO stripping experiment on the same electrode (Fig. S9, ESI<sup>†</sup>). This confirms that under steady-state electrolysis, the electrode surface is largely poisoned by strongly-bound adsorbates, as predicted by the DFT model.

**Vinyl- vs. allyl-carbon adsorption mechanism.** DFT calculations for propene adsorption through allylic carbon deprotonation predict a contribution deriving from double bond coordination to the surface. Indeed, the adsorption geometry changes and the binding energy significantly weakens if the vinylic contribution is impeded (see Fig. S27, ESI<sup>†</sup>). The propene stripping experiment in Fig. 7 also suggests an active role of the unsaturated carbons in the molecule's coordination with the surface, as indicated by the significant amount of propane desorbing in a cathodic sweep. The propene desorption during the stripping experiment, on the other hand, may represent propene adsorbed through purely allylic coordination. Vinylic adsorption forces the molecule into a flat adsorption geometry, requiring the availability of more surface sites than solely allylic coordination. With the high carbon coverage regimes suggested by DFT under reaction conditions, this cumbersome adsorption mechanism might be hindered, while purely allylic

adsorption requiring less surface availability could become relatively more favorable.

To gain insights into the competition between vinyl coordination and other adsorption geometries, we designed and performed a modification of the propene stripping experiment. In these experiments, shown schematically in Fig. 8a, and exemplified in Fig. 8b, propane desorption is used as a probe for the amount of propene that can adsorb through the vinyl group. The potential at which we dose propene is the same each time, +0.4 V vs. RHE, at which no liquid products are formed, and at which the vinyl adsorbate that can be stripped off to propane is at its maximum coverage (Fig. 7b). After dosing and purging out the propene, the electrode is scanned cathodically to 0.1 V vs. RHE and then anodically up to a cleaning potential which is varied each time. The portion of strongly-adsorbed species that are oxidized off of the surface as  $CO_2$  increases with increasing cleaning potential (Fig. 8c, left y-axis). The cleaning potential thus controls the coverage of the surface prior to the next propene dose.

When propene is dosed now, it must compete with the remaining adsorbates for sites. According to our hypothesis, the coverage of vinyl-bound propene resulting from a propene dose that can desorb as propane in the cathodic scan after the dose should increase with the availability of sites for vinylic coordination, and thus with the cleaning potential. The integrated post-dose propane ( $C_3H_8$ ) and propene ( $C_3H_6$ ) is plotted as a function of the cleaning potential in Fig. 8c (right y-axis). To ensure that the changing amount of propane is a result of the surface coverage prior to the propene dose, we stepped up the cleaning potential and then repeated a few cleaning potentials stepping down. The post-dose propane follows the pre-dose  $CO_2$  desorption and the cleaning potential. This indicates that adsorption through the vinyl group is inhibited on a highly covered surface, confirming that the coverage directs the adsorption geometry. The propene ( $C_3H_6$ ) desorption on the other hand does not depend on the cleaning potential, indicating that the amount of propene

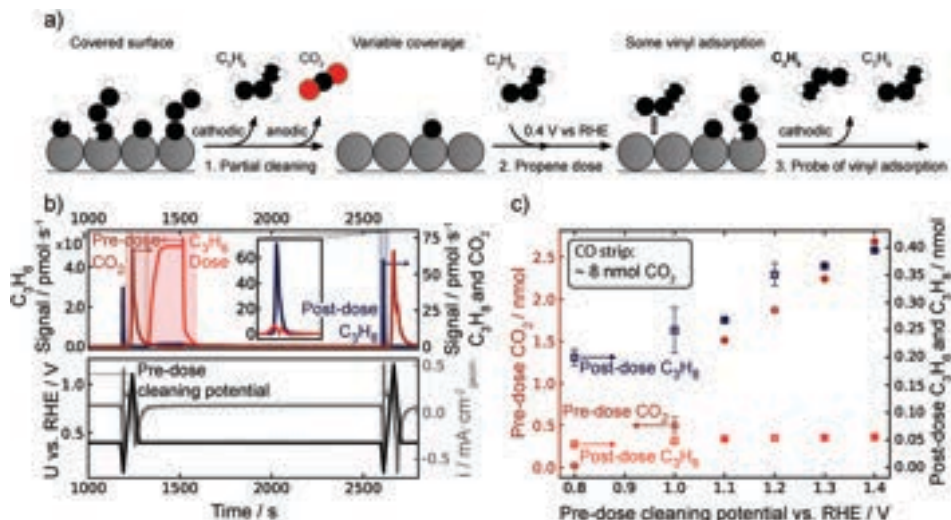


Fig. 8 EC-MS plot of propene stripping "site evacuation" experiments. A surface which has previously been covered by adsorbates by propene dosing (at  $t = 0$ ) is cleaned by scanning to an anodic potential (cleaning potential), stripping a portion of the strongly-adsorbed species off as  $\text{CO}_2$ . Propene is then dosed again and purged, and the sample is scanned cathodically to 0.1 V vs. RHE and back before starting the next experimental sequence. (a) Schematic. (b) Experimental data. The inset shows a zoom-in on the signals for propene and propane during the post-dose scan. (c) The integrated flux of  $\text{CO}_2$  (circles) from the scans prior to and  $\text{C}_2\text{H}_4$  and  $\text{C}_3\text{H}_6$  (squares) from the scans after each propene dose are plotted against the cleaning potential, which is stepped up and down. For values repeated while stepping down the cleaning potential (0.8, 1.0, and 1.2 V vs. RHE), the marker and error bars represent the mean and standard deviation of the measurements, respectively.

adsorbed exclusively through the allylic carbon is not influenced by the pre-dose coverage.

In our analysis, we do not explicitly consider steps and under-coordinated sites. These sites are more reactive than terraces and therefore we assume under reaction conditions these sites are readily passivated by carbon species and remain poisoned during catalytic activity, without participating in the proposed mechanism. Nevertheless, our results do not allow for definite exclusion of their role in the mechanism.

**Allyl alcohol conversion tests.** In the reaction scheme proposed above, the 2-electron partial oxidation product allyl alcohol is considered an intermediate in the production of the 4- and 6-electron partial oxidation products acrolein and acrylic acid. This is motivated by the fact that allyl alcohol has its peak production rate just cathodic of the latter products (Fig. 4). To test this hypothesis, we performed direct allyl alcohol oxidation experiments.

Fig. 9 shows the average total current density and the faradaic efficiency for direct oxidation of allyl alcohol on Pd at the intermediate potential 0.8 V vs. RHE for 60 min. Two different alcohol concentrations were tested; a 0.1 mM solution to represent the approximate concentration of allyl alcohol that was produced during 1 h of propene oxidation, and a 10 mM solution corresponding to the concentration of propene in the propene oxidation experiments. At the low concentration, the average current density was equivalent to the experiments in propene. At high concentration, it was increased more than 50-fold. Interestingly, the lower concentration experiment produced more of

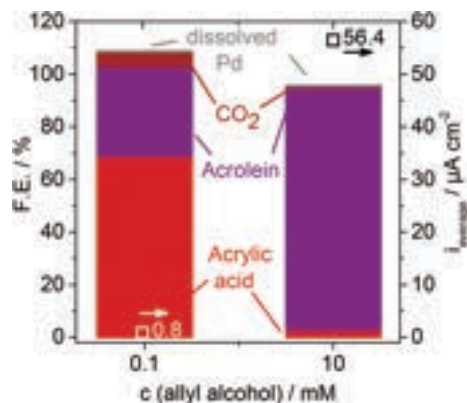


Fig. 9 Product distribution (faradaic efficiency, bar chart) for steady-state oxidation of different concentrations of allyl alcohol in 0.1 M  $\text{HClO}_4$  at 0.8 V vs. RHE for one hour. The average of the current density over the measurement time period is shown on the right axis (squares).

the further oxidized acrylic acid ( $4e^-$  process) whereas the higher concentration produces more of the less oxidized acrolein ( $2e^-$  process). Additional minor products are acrolein or acrylic acid, respectively,  $\text{CO}_2$  and traces of propanal. Dissolution of Pd was observed, but no acetone, as is expected in the absence of propene. The observed high current densities for allyl alcohol oxidation are in agreement with the theoretical hypothesis that oxygen incorporation is the rate determining step.

## Discussion

In steady-state propene oxidation experiments, we observed a complex potential dependence of the product distribution and high selectivity towards partial oxidation product acrolein, though with low ECSA-normalized current densities and signs of catalyst degradation. Reaction modeling predicts that on a clean surface the carbon intermediates bind too strongly and degrade rather than incorporate oxygen and convert to products. However, computed energies and propene stripping experiments indicate that the surface coverage of propene-derived species is high under reaction conditions and plays a key role in the adsorption mechanism. Hence, we propose a reaction scheme, summarized in Fig. 10. At low coverage, lack of spatial constraints promotes flat propene adsorption through combined allyl-vinyl binding. Depending on the potential, this adsorbate can degrade to smaller  $C_xH_y$  fractions and/or be oxidized further, deprotonating the allyl carbon and sinking into a 3-fold hollow site. DFT predicts these species to be highly stable and not to react further under steady-state conditions, increasing the surface coverage. They can however be stripped off as  $CO_2$  in an anodic sweep. The allyl-vinyl adsorbed propene can be reduced to propane in a cathodic sweep. At high carbon coverages, low site availability restricts

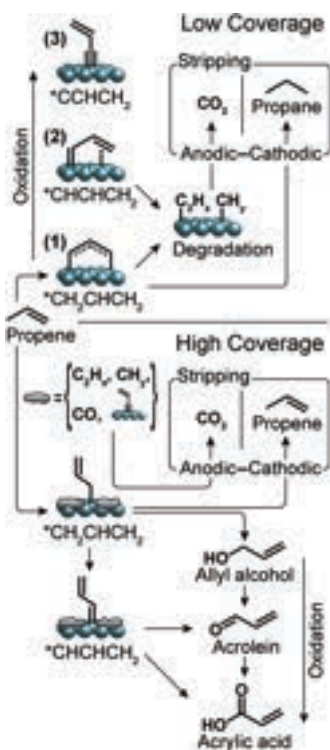


Fig. 10 Graphical representation of the proposed pathways for propene adsorption and conversion. The scheme is divided into two sectors, according to the coverage regime. In each sector, an inset addresses the desorbed species detected in propene stripping experiments.

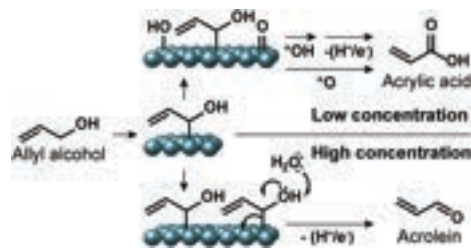


Fig. 11 Proposed mechanism for the oxidation of allyl alcohol at low (0.1 M, top) and high (10 M, bottom) concentrations, yielding two different product distributions.

the adsorption geometry to be primarily allylic and in the atop position. This induces the formation of weakly bound, reactive adsorbates, enabling steady-state conversion to the observed reaction products, though at the price of reduced activity due to partial poisoning. The forced displacement of reactants from a stabilized adsorption configuration to a more unstable, reactive position by surface adsorbates also causes a reduction in kinetic barriers, as shown with DFT. This resembles an effect known from Lindlar-type catalysts for selective hydrogenation of multiply unsaturated alkenes,<sup>50,51</sup> where partial poisoning of the surface, e.g. by methanol, destabilizes the adsorption of intermediates, preventing full hydrogenation.<sup>52</sup>

Interestingly, the propene oxidation product propylene glycol, which requires oxidation of the double bond, is only produced significantly at potentials anodic of 1.0 V vs. RHE. This could also be explained as a coverage effect. The lower coverage at high potentials, evidenced by the stripping experiments (Fig. 7b), enables coordination of the vinyl group. However, we do not exclude a different adsorption mechanism on an oxidized surface, though an extensive study on such oxidized surfaces is beyond the scope of this work. That said, the direct partial oxidation of propene to propylene glycol is of high industrial interest, since the existing pathways to propylene glycol (*via* propene oxide) have numerous disadvantages.<sup>53</sup>

The direct oxidation of allyl alcohol yielded different product concentrations depending on the concentration of allyl alcohol employed. This can be rationalized with a similar mechanistic approach to the oxidation of propene, as illustrated in Fig. 11: the adsorption of allyl alcohol is energetically favored, resulting in a high coverage at high concentrations, but lower coverage at the lower concentration we employed. While surface-bound oxygen species are required for the oxidation to acrylic acid, oxidation to acrolein can also occur by hydroxyl group deprotonation of allyl alcohol. Therefore, at high alcohol coverages, the dominating process will be formation of acrolein, due to the lack of surface oxygen species. At low coverage, surface oxygen species will be available, making way for the direct oxidation to acrylic acid.

## 4. Conclusions

In this study, using a combination of theoretical modeling and experimental techniques, we presented an in-depth analysis of

propene oxidation on high surface area polycrystalline Pd in 0.1 M HClO<sub>4</sub>.

The mechanistic findings in the report are the groundwork to efficient electrochemical conversion of propene. First, in propene oxidation steric effects at the surface regulate the reaction outcome by steering the adsorbate geometry. Thus, it is crucial to tune the catalyst surface population and coverage regimes. Second, with Langmuir–Hinshelwood kinetics on a carbophilic catalyst, the formation of oxygen species at the surface is rate limiting. Balancing oxygen and carbon adsorption while limiting vinylic coordination should ensure higher catalytic turnover, concurrently enabling selectivity towards allylic oxidation products. On the other hand, selective activation of the vinyl group on weaker adsorption sites would promote formation of other industrially relevant products, propylene oxide and propylene glycol, while minimizing degradation. Third, it is important to improve the catalyst stability under oxidative reaction conditions, either by engineering catalysts active at lower potentials, or by synthesis of catalytic materials resistant to anodic corrosion.

Through this work, we outline possible catalyst design strategies for propene partial electro-oxidation reactions and beyond. In practice, one could achieve greater surface coverage control *e.g.* by deposition of poisoning additives to form different atomic surface ensembles.<sup>54</sup> Alternatively, we are currently developing intermetallic catalysts with embedded carbophilic metals (Pd, Pt, Ru, Rh, and Ir) in inert or oxophilic matrices (Ag, Sn, Au, and graphite); this should activate specific reactant functionalities without prior poisoning, retaining all the mass activity of the precious metal used. Ultimately, the application of a multi-angle approach such as the one presented and a prudent generalization of our conclusions can support the study of other hydrocarbon partial oxidation reactions.

## Author contributions

A. W. and L. S. contributed equally. A.W., B. J. S., I. C. and I. E. L. S. designed the bulk electrolysis experiments. A. W. carried out the catalyst preparation, electrochemical experiments and product analysis. K. E.-R. designed and performed NMR characterization of products. S. B. S., D. B. T., P. C. K. V. and I. C. designed the stripping experiments, S. B. S. carried them out. J. R., L. S., M. S. and P. G. M. designed the DFT study, L. S. carried it out. A. W., L. S. and S. B. S. wrote the manuscript; all authors were involved in discussing and interpreting the results and editing the manuscript.

## Conflicts of interest

There are no conflicts to declare.

## Acknowledgements

We gratefully acknowledge the funding by Danmarks Innovationsfonden, part of the ProActive project (5160-00003B) and by Villum Fonden, part of the Villum Center for the Science of Sustainable Fuels and Chemicals (V-SUSTAIN grant 9455). 800 MHz NMR

spectra were recorded at the NMR Center at DTU supported by the Villum Foundation.

## References

- 1 N. S. Lewis and D. G. Nocera, *Proc. Natl. Acad. Sci. U. S. A.*, 2006, **103**, 15729–15735.
- 2 B. Lee, H. Naito, M. Nagao and T. Hibino, *Angew. Chem., Int. Ed.*, 2012, **51**, 6961–6965.
- 3 M. T. M. Koper, *Catalysis in Chemistry and Biology*, World Scientific, 2018, pp. 229–232.
- 4 C. Reller, R. Krause, E. Volkova, B. Schmid, S. Neubauer, A. Rucki, M. Schuster and G. Schmid, *Adv. Energy Mater.*, 2017, **7**, 1602114.
- 5 N. Agarwal, S. J. Freakley, R. U. McVicker, S. M. Althabhan, N. Dimitratos, Q. He, D. J. Morgan, R. L. Jenkins, D. J. Willock, S. H. Taylor, C. J. Kiely and G. J. Hutchings, *Science*, 2017, **358**, 223–227.
- 6 Z. Liang, T. Li, M. Kim, A. Asthagiri and J. F. Weaver, *Science*, 2017, **356**, 299–303.
- 7 K. T. Dinh, M. M. Sullivan, P. Serna, R. J. Meyer, M. Dincă and Y. Román-Leshkov, *ACS Catal.*, 2018, 8306–8313.
- 8 A. Marimuthu, J. Zhang and S. Linic, *Science*, 2013, **339**, 1590–1593.
- 9 M. D. Hughes, Y.-J. Xu, P. Jenkins, P. McMorn, P. Landon, D. I. Enache, A. F. Carley, G. A. Attard, G. J. Hutchings, F. King, E. H. Stitt, P. Johnston, K. Griffin and C. J. Kiely, *Nature*, 2005, **437**, 1132–1135.
- 10 B. K. Min and C. M. Friend, *Chem. Rev.*, 2007, **107**, 2709–2724.
- 11 Y. Choi, I. Sinev, H. Mistry, I. Zegkinoglou and B. Roldan Cuenya, *ACS Catal.*, 2016, **6**, 3396–3403.
- 12 Z. W. Seh, J. Kibsgaard, C. F. Dickens, I. Chorkendorff, J. K. Nørskov and T. F. Jaramillo, *Science*, 2017, **355**, eaad4998.
- 13 B. Lee and T. Hibino, *J. Catal.*, 2011, **279**, 233–240.
- 14 M. E. O'Reilly, R. S. Kim, S. Oh and Y. Surendranath, *ACS Cent. Sci.*, 2017, 2–7.
- 15 N. Danilovic, K. E. Ayers, C. Capuano, J. N. Renner, L. Wiles and M. Pertoso, *ECS Trans.*, 2016, **75**, 395–402.
- 16 S. J. Khatib and S. T. Oyama, *Catal. Rev.*, 2015, **57**, 306–344.
- 17 P. Sprenger, W. Kleist and J.-D. Grunwaldt, *ACS Catal.*, 2017, **7**, 5628–5642.
- 18 Nexant, Nexant Petroleum and Petrochemical Economics (PPE) Program, 2017.
- 19 C. J. Sullivan, A. Kuenz and K.-D. Vorlop, *Ullmann's Encyclopedia of Industrial Chemistry*, Wiley-VCH Verlag GmbH & Co. KGaA, Weinheim, Germany, 2018, pp. 1–15.
- 20 M. Weber, W. Pompetzki, R. Bonmann and M. Weber, *Ullmann's Encyclopedia of Industrial Chemistry*, Wiley-VCH Verlag GmbH & Co. KGaA, Weinheim, Germany, 2014, pp. 1–19.
- 21 J. O. Bockris, H. Wroblowa, E. Gileadi and B. J. Piersma, *Trans. Faraday Soc.*, 1965, **61**, 2531–2545.
- 22 M. Bęłowska-Brzezinska, T. Łuczak, H. Baltruschat and U. Müller, *J. Phys. Chem. B*, 2003, **107**, 4793–4800.

- 23 T.-C. Chou and J.-C. Chang, *Chem. Eng. Sci.*, 1980, **35**, 1581–1590.
- 24 K. Scott, C. Odouza and W. Hui, *Chem. Eng. Sci.*, 1992, **47**, 2957–2962.
- 25 G. Göransson, J. S. Jirkovský, P. Krtil and E. Ahlberg, *Electrochim. Acta*, 2014, **139**, 345–355.
- 26 L. L. Holbrook and H. Wise, *J. Catal.*, 1975, **38**, 294–298.
- 27 V. M. Schmidt and E. Pastor, *J. Electroanal. Chem.*, 1996, **401**, 155–161.
- 28 G. R. Stafford, *Electrochim. Acta*, 1987, **32**, 1137–1143.
- 29 K. Otsuka, Y. Shimizu, I. Yamanaka and T. Komatsu, *Catal. Lett.*, 1989, **3**, 365–370.
- 30 N. Markovic, *J. Electrochem. Soc.*, 1997, **144**, 1591.
- 31 R. Ojani, E. Hasheminejad and J. B. Raoof, *Int. J. Hydrogen Energy*, 2014, **39**, 8194–8203.
- 32 J. Liu, L. Cao, W. Huang and Z. Li, *J. Electroanal. Chem.*, 2012, **686**, 38–45.
- 33 E. Bertheussen, T. V. Hogg, Y. Abghoui, A. K. Engstfeld, I. Chorkendorff and I. E. L. Stephens, *ACS Energy Lett.*, 2018, **3**, 634–640.
- 34 D. B. Trimarco, S. B. Scott, A. H. Thilsted, J. Y. Pan, T. Pedersen, O. Hansen, I. Chorkendorff and P. C. K. Vesborg, *Electrochim. Acta*, 2018, **268**, 520–530.
- 35 J. Enkovaara, C. Rostgaard, J. J. Mortensen, J. Chen, M. Dulak, L. Ferrighi, J. Gavnholt, C. Glinsvad, V. Haikola, H. A. Hansen, H. H. Kristoffersen, M. Kuisma, A. H. Larsen, L. Lehtovaara, M. Ljungberg, O. Lopez-Acevedo, P. G. Moses, J. Ojanen, T. Olsen, V. Petzold, N. A. Romero, J. Stausholm-Møller, M. Strange, G. A. Tritsarlis, M. Vanin, M. Walter, B. Hammer, H. Häkkinen, G. K. H. Madsen, R. M. Nieminen, J. K. Nørskov, M. Puska, T. T. Rantala, J. Schiøtz, K. S. Thygesen and K. W. Jacobsen, *J. Phys.: Condens. Matter*, 2010, **22**, 253202.
- 36 A. Hjorth Larsen, J. Jørgen Mortensen, J. Blomqvist, I. E. Castelli, R. Christensen, M. Dulak, J. Friis, M. N. Groves, B. Hammer, C. Hargus, E. D. Hermes, P. C. Jennings, P. Bjerre Jensen, J. Kermod, J. R. Kitchin, E. Leonhard Kolsbjerg, J. Kubal, K. Kaasbjerg, S. Lysgaard, J. Bergmann Maronsson, T. Maxson, T. Olsen, L. Pastewka, A. Peterson, C. Rostgaard, J. Schiøtz, O. Schütt, M. Strange, K. S. Thygesen, T. Vegge, L. Vilhelmsen, M. Walter, Z. Zeng and K. W. Jacobsen, *J. Phys.: Condens. Matter*, 2017, **29**, 273002.
- 37 S. R. Bahn and K. W. Jacobsen, *Comput. Sci. Eng.*, 2002, **4**, 56–66.
- 38 M. Hara, U. Linke and T. Wandlowski, *Electrochim. Acta*, 2007, **52**, 5733–5748.
- 39 F. Hernandez and H. Baltruschat, *Langmuir*, 2006, **22**, 4877–4884.
- 40 N. Hoshi, K. Kagaya and Y. Hori, *J. Electroanal. Chem.*, 2000, **485**, 55–60.
- 41 N. Hoshi, M. Kuroda and Y. Hori, *J. Electroanal. Chem.*, 2002, **521**, 155–160.
- 42 M. Pourbaix, *Atlas of electrochemical equilibria in aqueous solutions*, Pergamon Press, 1974.
- 43 P. Y. Bruice, *Organic Chemistry*, Pearson Education, 2007.
- 44 J. K. Nørskov, J. Rossmeisl, A. Logadottir, L. Lindqvist, J. R. Kitchin, T. Bligaard and H. Jónsson, *J. Phys. Chem. B*, 2004, **108**, 17886–17892.
- 45 K. J. J. Mayrhofer, M. Arenz, B. B. Blizanac, V. Stamenkovic, P. N. Ross and N. M. Markovic, *Electrochim. Acta*, 2005, **50**, 5144–5154.
- 46 M. T. M. Koper, S. C. S. Lai and E. Herrero, *Fuel Cell Catalysis*, John Wiley & Sons, Inc., Hoboken, NJ, USA, 2009, pp. 159–207.
- 47 L. Vitos, A. V. Ruban, H. L. Skriver and J. Kollár, *Surf. Sci.*, 1998, **411**, 186–202.
- 48 E. Pastor, S. Wasmus, T. Iwasita, M. C. Arévalo, S. Gonzalez and A. J. Arvia, *J. Electroanal. Chem.*, 1993, **353**, 81–100.
- 49 M. C. Arévalo, J. L. Rodriguez and E. Pastor, *J. Electroanal. Chem.*, 2001, **505**, 62–71.
- 50 H. Lindlar, *Helv. Chim. Acta*, 1952, **35**, 446–450.
- 51 D. Albani, M. Shahrokhi, Z. Chen, S. Mitchell, R. Hauert, N. López and J. Pérez-Ramírez, *Nat. Commun.*, 2018, **9**, 2634.
- 52 G. Horányi and K. Torkos, *J. Electroanal. Chem. Interfacial Electrochem.*, 1980, **111**, 279–286.
- 53 T. A. Nijhuis, M. Makkee, J. A. Moulijn and B. M. Weckhuysen, *Ind. Eng. Chem. Res.*, 2006, **45**, 3447–3459.
- 54 D. Strmcnik, M. Escudero-Escribano, K. Kodama, V. R. Stamenkovic, A. Cuesta and N. M. Marković, *Nat. Chem.*, 2010, **2**, 880–885.



## **Paper II**

### **Tuning activity in electrochemical propene oxidation by alloying Pd with Au**

Luca Silvioli\*, [Anna Winiwarter](#)\*, Soren B. Scott, Ib Chorkendorff, Brian Seger, and Jan Rossmeisl.

*in preparation*

\* these authors contributed equally



# Tuning activity in electrochemical propene oxidation by alloying Pd with Au

Anna Winiwarter\*, Luca Silvioli\*, Soren B. Scott, Ib Chorkendorff, Brian Seger, and Jan Rossmeisl

\*these authors contributed equally

## Abstract

Selective partial oxidation of hydrocarbons to oxygenates plays a large role in the chemical industry and falling prices for electricity from renewable sources make electrification of such industrial chemical processes relevant. The oxidation of propene is an interesting model system as the model can be oxidized in two different positions, allowing for insights into the reaction mechanism. At the same time the reaction yields important commodity chemicals, such as acrolein, acrylic acid and propylene oxide. On Pd, a layer of adsorbents formed in-situ governs the reaction by steering the adsorption geometry such as to achieve high selectivity for allylic oxidation. In this study, we show how the in-situ formed adsorbent layer on the surface can be changed to improve activity while maintaining high selectivity by alloying Pd with Au. We use a combination of DFT based theoretical modelling, and electrochemical measurements with ex-situ product quantification and in-situ mass spectrometry. We explore how different Au:Pd ratios affect activity and selectivity by governing the nature, amount and coordination geometry of surface adsorbates. Our results are relevant for further development of selective catalysts for electrochemical hydrocarbon oxidation.



## **Paper III**

**Using SEIRAS and EC-MS for *in-situ* analysis of the surface adsorbates during electrochemical oxidation of propene and allyl alcohol**

Anna Winiwarter, Michael J. Boyd, Soren B. Scott, Brian Seger, Drew C. Higgins, Ib Chorkendorff, and Thomas F. Jaramillo

*in preparation*



# Using SEIRAS and EC-MS for in-situ analysis of the surface adsorbates during electrochemical oxidation of propene and allyl alcohol

Anna Winiwarter, Michael J. Boyd, Soren B. Scott, Brian Seger, Drew C. Higgins, Ib Chorkendorff, Thomas F. Jaramillo

## Abstract

Electrochemical partial oxidation of hydrocarbons for the synthesis of commodity chemicals has received increased attention in the light of falling prices for renewable electricity. A challenge for electrochemical oxidation of organic molecules is adsorption of non-reactive spectator species to the catalyst, which can lead to catalyst degradation, but also play an important role in the reaction mechanism. To elucidate the role of such adsorbates, it can be beneficial to observe them directly in-situ. In this study, we compare the adsorbates formed during oxidation of propene and allyl alcohol using a combination of SEIRAS and EC-MS. The visibility of propene adsorbates is limited, due adsorption geometry and nature of the intramolecular bonds. We devised a procedure to indirectly measure adsorbed species by displacement with CO, which binds more strongly to the surface than propene-derived species, and can be observed with SEIRAS. Propene desorption was confirmed by EC-MS measurements. A change in shape and position of the peak corresponding to CO indicates a different binding geometry in the presence of propene compared on a clean surface. We propose that this method can be useful for studying other systems where the adsorbed species is invisible due to fundamental limitations of IR spectroscopy.